# EFFEKT DES ZETAPOTENZIALS VON CHEMISCH MODIFIZIERTEN MATERIALOBERFLÄCHEN AUF DIE ZELLPHYSIOLOGIE UND MORPHOLOGIE VON OSTEOBLASTEN

**Kumulative Dissertation**

zur Erlangung des akademischen Grades

Doctor rerum humanarum (Dr. rer. hum.)

im Arbeitsbereich Zellbiologie

an der Medizinischen Fakultät der Universität Rostock

vorgelegt von Martina Grüning

Rostock, 2020

https://doi.org/10.18453/rosdok_id00003397

Gutachter:

Prof. Dr. Barbara Nebe, Universitätsmedizin Rostock, Arbeitsbereich Zellbiologie

Dr. Anika Jonitz-Heincke, Universitätsmedizin Rostock, Orthopädische Klinik

Prof. Dr. Jürgen Kolb, Universität Rostock, Institut für Physik; Leibniz-Institut für Plasmaforschung und Technologie e.V. Greifswald, Plasmen für Umwelt und Gesundheit

Jahr der Einreichung: 2020

Jahr der Verteidigung: 2021

**INHALTSVERZEICHNIS**

# 1 EINLEITUNG

Natürliche und synthetische Biomaterialien sind in der modernen Medizin längst nicht mehr wegzudenken. Maßgeschneidert für den Ersatz oder die Wiederherstellung von erkranktem und beschädigtem Gewebe wie Knochen, Zähne oder Gefäße interagieren sie im Körper mit dem biologischen System und steuern den therapeutischen Verlauf[1]. Bis zum vollständigen Verständnis der fundamentalen Prozesse an der Schnittstelle zwischen Biomaterial und Körper ist es allerdings noch ein weiter Weg[2]. Um diesen weiter zu beschreiten, steht in dieser Dissertation die Verknüpfung zweier Hauptaspekte im Vordergrund: Die Oberflächenladung abgeleitet vom Zetapotenzial (ζ), als eine Eigenschaft von Biomaterialien, und die Zellphysiologie und Morphologie, die die Auswirkung der Zell-Material-Interaktion beschreibt. Einleitend wird demnach im folgenden Abschnitt grundlegendes Wissen zu Biomaterialien und der Zell-Material-Interaktion vermittelt.

## 1.1 BIOMATERIALIEN – EIN KURZER EINBLICK IN EINE GIGANTISCHE BRANCHE

Der zunehmende Bedarf an Biomaterialien, der sich aus dem demografischen Wandel und dem Wunsch, Gesundheit und Wohlbefinden in der alternden Bevölkerung zu erhalten, ergibt, führt zu einem Wachstum des Biomaterialmarktes. Resultierend aus den zunehmenden Mitteln und Zuschüssen von Regierungseinrichtungen und Universitäten für die Entwicklung neuartiger Biomaterialien wird bis zum Jahr 2025 ein Anstieg des Volumens auf rund 250 Mrd. US $ erwartet[3]. Die Weltgesundheitsorganisation (WHO, engl. *world health organization*) schätzte schon 2015 die weltweit zur Verfügung stehenden generischen Produktgruppen auf ca. 10.000[4]. Hinter dieser rasanten Weiterentwicklung von Biomaterialien steckt eine interdisziplinäre Zusammenarbeit aus Bereichen wie Material- und Ingenieurswissenschaften, Physik, Chemie, Biologie und Medizin. Auf der anderen Seite schöpft sie Wissen aus einer jahrtausendalten und faszinierenden Historie, die den Grundstein für die Geburt der Biomaterialien gelegt hat[4–9]. Im Laufe der Zeit hat sich der Schwerpunkt bei der Entwicklung weg von der Gewebereparatur durch *biopassive Materialien* (eine möglichst minimale Interaktion mit dem umgebenden Gewebe eingehend) hin zur Geweberegeneration durch *bioaktive bzw. biointeraktive Materialien* (spezifische zelluläre Reaktionen auf molekularer Ebene stimulierend) verlagert. Dabei müssen im Wesentlichen die Anforderungen hinsichtlich klinischer (geeignete mechanische, physikochemische und biologische Eigenschaften), fertigungstechnischer (wie Sterilisierbarkeit) und wirtschaftlicher (Kosten, Marketing, Benutzer-freundlichkeit) Aspekte erfüllt werden[4].

### *1.1.1 TITAN ALS BELIEBTES BIOMATERIAL FÜR KNOCHENERSATZ*

Knochengewebe wird weltweit nach der Transfusion von Blut an zweithäufigster Stelle ausgetauscht[10]. Traumatische Knochenschäden oder Erkrankungen wie Osteoarthritis (Entzündung der Knochengelenke) und Osteoporose (Knochenschwund) führen zu einer Verschlechterung der mechanischen Knocheneigenschaften. Wenn konservative Behandlungen versagen, stellt der Ersatz des Knochengewebes durch ein Implantat eine gute Option dar[11]. Diese orthopädischen Implantate bestehen aufgrund ihrer hohen Stabilität und Haltbarkeit zu 95% aus metallischen Biomaterialien[12]. Insbesondere Titan (Ti), seine Legierungen und Ti-basierte

Verbundwerkstoffe finden seit den 1950ern große Beachtung[13,14]. Jährlich werden weltweit mehr als 1000 Tonnen Ti auf vielfältigste Weise für u.a. Zahnwurzelersatz, Hüft-, Knie-, Schulter- und Ellbogengelenk-ersatz sowie als Knochenschrauben und -platten oder zur Wirbelsäulenversteifung implantiert[13]. Dies entspricht etwa der Menge von 270 mg pro Person in Industrie- und Schwellenländern. Der Grund dafür liegt in der guten Akzeptanz des menschlichen Körpers für Ti. Die Elastizitätsmodule (Young' sche Module) von Ti-Legierungen liegen im Unterschied zu anderen Metallen deutlich näher an denen von Knochen[15,16]. Ti ist leicht, trotzdem extrem robust[13,15] und hat sich als biokompatibler[17] und dank seines passiven Ti-Oxidfilms als korrosionsbeständiger[18] als andere Metalle wie Edelstahl oder Kobalt-Chrom erwiesen. Daher ist Ti das gegenwärtig meistverwendete Material für lasttragende Implantate[19].

Dennoch steht all diesen Vorteilen ein entscheidender Nachteil gegenüber: Es handelt sich in jedem Fall um ein artifiziell hergestelltes Material, dessen Biofunktionalität im Allgemeinen schlecht ist, da es nicht direkt mit dem lebenden Gewebe verwächst. Fibröses Gewebe zwischen Implantat und Knochen führt dann zu einer unzureichenden Osseointegration, der direkten, strukturellen und funktionellen Verbindung zwischen lebendem Knochen und künstlicher Implantatoberfläche[20]. Eine daraus resultierende Implantatlockerung kann letztlich ein vorzeitiges Versagen des permanenten Implantats zur Folge haben[11]. Um dieses Risiko zu verringern, wurden viele Ansätze der Oberflächenmodifikation verfolgt, die die Osseointegration beschleunigen und verbessern sollen.

### *1.1.2 Oberflächenmodifikation zur Verbesserung der Osseointegration*

Das Ziel der Oberflächenmodifikation ist die chemische Bindung oder die mechanische Verankerung des Gewebes mit dem Metallsubstrat. Dabei ist die Biomimetik (das Übertragen von Naturphänomenen auf die Technik) die derzeit wichtigste treibende Kraft bei der Entwicklung von Biomaterialien[21]. Eine auf dieser Basis modifizierte orthopädische Oberfläche soll die Kontrolle der biologischen Reaktion des Körpers auf das Implantat ermöglichen. Allerdings ist die tatsächliche Anwendung solcher Modifikationen aufgrund von Problemen bei Umsetzung von Sicherheit und Qualitätserhaltung nicht so weit fortgeschritten wie die Forschung[12]. Kommerziell angewendete Oberflächenmodifikationen von Ti beschränken sich noch auf physikalische Behandlungen zur Veränderung der Oberflächenrauigkeit wie Sandstahlen, Säureätzen oder Anodisieren[11] und physikochemische Behandlungen wie die Beschichtung mit Hydroxylapatit[5] oder das Eintauchen in alkalische Natrium- oder Kaliumhydroxidlösungen zur Generierung einer Ti-Oxidgel-schicht[12,22]. Diese Methoden stimulieren die Osseointegration nur indirekt. Indessen zeigt der Fortschritt in der Forschung, dass die Osseointegration anhand von biochemischen und biologischen Beschichtungen direkt gefördert werden kann, indem diese die osteogene Differenzierung sowie Anlagerung und Proliferation von knochenbildenden Zellen (Osteoblasten) verbessern[19]. Hierzu zählen biomimetische Oberflächen-modifikationen durch Immobilisierung von bioaktiven Molekülen wie Peptiden, Proteinen und Polymeren, die das Verhalten der Zellen steuern können. Diese werden in zwei Kategorien eingeteilt: (1) Moleküle, die Signale

für die Knochenbildung erzeugen und (2) Moleküle, die den Zellen Adhäsionsstellen präsentieren[16]. Ersteres schließt beispielsweise Wachstumsfaktoren wie BMP-2 (engl. *bone morphorgenic protein-2*)[23] ein, die die Proliferation und Differenzierung von Stammzellen des Knochenmarks sowie Osteoblasten stimulieren. Zweiteres impliziert extrazelluläre Matrixproteine (EZM-Proteine) wie Kollagen I, Fibronektin, Vitronektin und RGD-haltige Oligopeptide, die über ihre Aminosäuresequenz aus Arginin, Glycin und Asparaginsäure (Arg-Gly-Asp, kurz RGD) Adhäsionsstellen für Osteoblasten schaffen und die Osseointegration initialisieren[11,16]. Die Proteine können entweder kovalent (durch funktionale Gruppen, spezielle Linkermoleküle oder plasmabasierte Gasphasenabscheidung) oder nicht kovalent durch Adsorption an der Oberfläche gebunden werden[16]. Diese Art der Beschichtung ist für eine gezielte Kontrolle der Zell-Material-Interaktion zwar vielversprechend, benötigt jedoch noch mehr Forschung und Entwicklungszeit[11,12,19].

## 1.2 ZELL-MATERIAL-INTERAKTION

Die frühe Osseointegration beginnt mit der Anlagerung, Adhäsion und Ausbreitung von Osteoblasten und beschreibt gleichzeitig die erste Phase der Zell-Material-Interaktion. Die Qualität dieser ersten Phase ist entscheidend, da sie die Proliferation und Differenzierung der Zellen beeinflusst[24]. Sie wird durch die physikalischen (Topographie, Elastizität) und chemischen (Benetzbarkeit, Ladung, Bioaktivität) Oberflächeneigenschaften gesteuert[25]. **Abbildung 1** stellt die wichtigsten Stufen der Zell-Material-Interaktion dar, die auf verschiedene Gruppen von Adhäsionsproteinen beruhen. Diese lassen sich gemäß des zeitlichen Ablaufs von Proteinadsorption bis zur Zellausbreitung in vier Kategorien einteilen: (1) Abscheidung von EZM-Proteinen wie Kollagen I, Fibronektin oder Vitronektin, (2) Ausprägung von Zelladhäsionsrezeptoren wie Integrine, (3) Expression von Adaptorproteinen wie Talin, Paxillin oder Vinkulin und (4) Bildung von Zytoskelettproteinen wie Aktin[25].

Lange bevor eine Adsorption der EZM-Proteine an der Materialoberfläche stattfindet, diffundieren Kationen und Anionen dissoziierter Salze aus dem Blut (*in vivo*-Situation) oder aus dem fötalen Kälberserum (FKS, *in vitro*-Situation) zur Oberfläche, sodass die geladenen funktionellen Gruppen einer Materialoberfläche, aber auch die der Proteine selbst, mit Gegenionen (Ionen mit entgegengesetzter Ladung zu der der Oberfläche) komplexiert werden[26]. Diese Gegenionen werden dann durch die Adsorption kleiner Proteine an der Materialoberfläche ausgetauscht. Eine Kombination aus kinetischen und thermodynamischen Wechselwirkungen führt letztlich zu einer stabil adsorbierten Monoschicht der größeren EZM-Proteinen, die stärker mit der Materialoberfläche interagieren und die anfänglich adsorbierten Proteine durch den sogenannten Vroman-Effekt[27,28] verdrängen. Sie übersetzen damit die fremde Oberfläche in eine für die Zelladhäsion „biologische Sprache“[29].

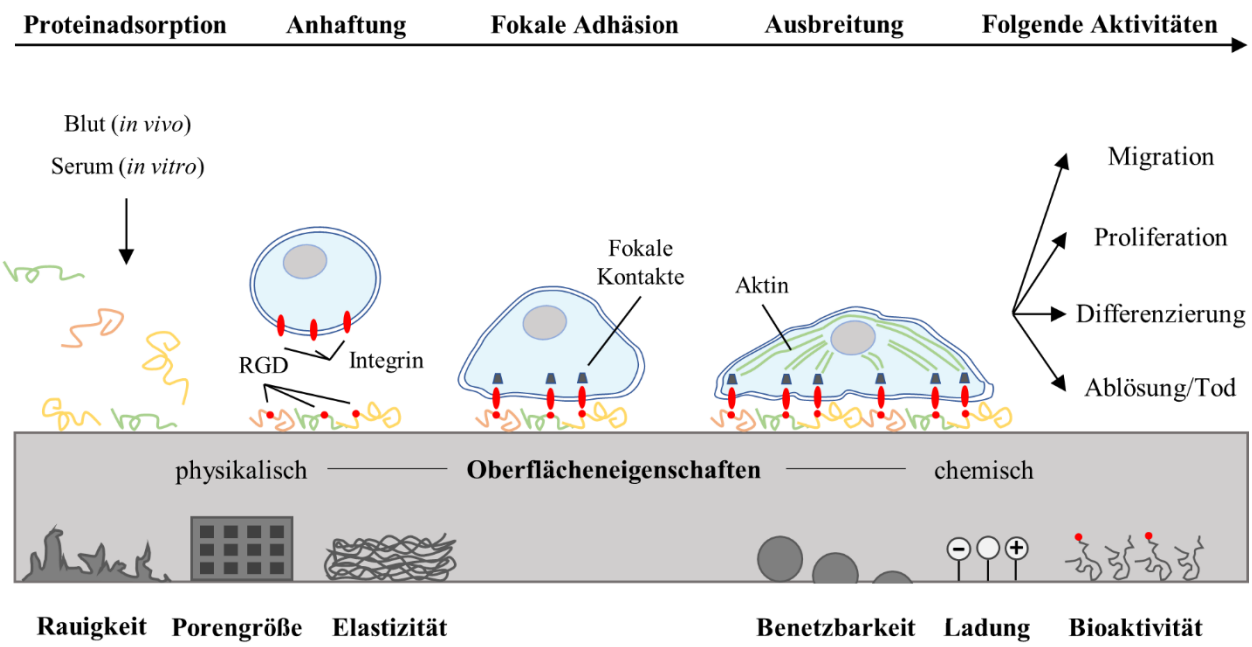


***Abbildung 1: Interaktion der Osteoblasten mit Oberflächen spezifischer physikalischer und chemischer Materialeigenschaften.*** *Während der Proteinadsorption lagern sich EZM-Proteine aus dem Blut auf der Oberfläche ab und vermitteln die Zelladhäsion. Diese wird in Zellanhaftung, fokale Adhäsion und Zellausbreitung unterteilt: Integrine erkennen RGD-Sequenzen der EZM-Proteine und veranlassen die Zell-Material-Verankerung. Fokale Kontakte, bestehend aus einem komplexen Netzwerk der Integrine, Adaptorproteine sowie kolokalisierten Kinasen und Phosphatasen, bilden das Bindeglied zwischen dem Aktinzytoskelett und der EZM. Die Zellen breiten sich auf dem Material aus. Nachfolgende Aktivitäten wie Migration, Proliferation und Differenzierung sind Teil der normalen Zellfunktionen. In Abhängigkeit von den Materialeigenschaften kann überdies das Ablösen der Zellen oder der Zelltod ausgelöst werden. Abbildung basierend auf Chen et al.[25], Ferrari et al.[30] und Khalili und Ahmad [31].*

Die Anhaftung der Zellen erfolgt kurz darauf und stellt die erste Interaktion zwischen Zellen und Material dar. Sie umfasst zunächst nur kurzfristige physikochemische Verbindungen durch beispielsweise ionische Kräfte und Van-der-Waals-Kräfte[32]. Aber auch elektrostatische Kräfte zwischen der Materialoberfläche und den Zellen spielen hierbei eine wichtige Rolle. Diese können insbesondere durch die negativ geladene perizelluläre Hyaluronsäurehülle der Osteoblasten entstehen[33], sodass eine schnelle Zellanhaftung vermittelt werden kann[34]. Daraufhin erkennen die transmembranen Integrinrezeptoren kurze Peptid-sequenzen der EZM-Proteine[35], wobei RGD die wichtigste Erkennungssequenz darstellt[36], und verankern die Zellen längerfristig mit der EZM und initiieren Signalwege für nachfolgende Zellreaktionen. Die Rekrutierung von Adaptorproteinen und die Bildung von fokalen Kontakten führen allmählich zu einer stabilen Adhäsion der Osteoblasten. Diese fokalen Kontakte, bestehend aus einem komplexen Netzwerk der transmembranen Integrine, Adaptorproteine und kolokalisierten Kinasen und Phosphatasen, die Signale zur Regulation der Genexpression an den Zellkern weiterleiten, bilden das Bindeglied zwischen dem Aktinzytoskelett und der EZM[37]. Durch die von den Integrinen aktivierte Signalübertragung, werden eine Reihe von Zytoskelett-proteinen aufgebaut. Die Zellen breiten sich fortlaufend auf dem Material aus, was zu einer Abnahme der Zellhöhe und einer Zunahme der Zell-

und Kontaktfläche mit verstärkter Adhäsionskraft führt[31]. Die Morphologie der Osteoblasten wechselt von kreisförmig zu langgestreckt, was unverzichtbar für eine normale Zellfunktion und eine erfolgreiche frühe Osseointegration ist[38]. Weitere Zellaktivitäten wie Migration, Proliferation, Differenzierung oder auch Apoptose (programmierter Zelltod) werden darauffolgend getriggert. Hierbei spielt $Ca^{2+}$ als Signalmolekül eine wichtige Rolle.

### 1.3 KALZIUM ($Ca^{2+}$) – EIN UNIVERSELLES SIGNALMOLEKÜL

Intrazelluläre Signalkaskaden schaffen die Verknüpfung zwischen den externen Signalen der Materialeigenschaften und der Zellantwort. Bis zu einem gewissen Grad werden alle physiologischen und pathologischen Prozesse in den Zellen von ionischen Veränderungen begleitet[39]. $Ca^{2+}$ ist solch ein Ion, das in der Biologie ein nahezu universelles Signalmolekül verkörpert[40], sowohl in Eukaryoten als auch in Prokaryoten[41]. In einer Vielzahl von Zelltypen, auch Osteoblasten[42], reguliert $Ca^{2+}$ die interzelluläre Kommunikation sowie zahlreiche intrazelluläre Prozesse wie die fokale Adhäsion, Proliferation oder Differenzierung, aber auch pathologische Ereignisse wie Zellschädigungen oder Zelltod[43]. Aufgrund der bemerkenswerten Bedeutung von $Ca^{2+}$ in der Biologie wurden zahlreiche Methoden zur Analyse der zellulären $Ca^{2+}$-Aktivität etabliert[44]. Die Entwicklung einer Methode zur Messung des zytoplasmatischen $Ca^{2+}$ mittels vorübergehend membrandurchlässiger fluoreszierender $Ca^{2+}$-Indikatoren[45,46] hat wesentlich zum Verständnis der normalen und abnormalen Zellfunktionen beigetragen[39].

Da $Ca^{2+}$ in viele verschiedene intrazelluläre Signalkaskaden integriert ist, ist eine Homöostase des intrazellulären $Ca^{2+}$-Spiegels von Bedeutung. Während der Metabolismus innerhalb von Sekunden umgestellt werden kann, müssen $Ca^{2+}$-Ionen in Zeitspannen von Minuten bis Stunden wirken, um Ereignisse wie Transkription oder Proliferation zu steuern[47]. Insofern wird die intrazelluläre $Ca^{2+}$-Konzentration von den Zellen streng kontrolliert. Hierzu dient eine Vielzahl von Regulationsmechanismen wie $Ca^{2+}$-Kanäle, -Pumpen, -Austauscher und -bindende Proteine[48,49], die als molekulare „Werkzeugkiste“ für die zelluläre $Ca^{2+}$-Dynamik zusammengefasst werden[47]. Jeder Zelltyp besitzt dabei ein spezifisches Komponentenset aus dieser „Werkzeugkiste“[47].

Während das extrazelluläre $Ca^{2+}$-Level im Knochen bei 1-2 mM liegt[42,50], sorgen verschiedene $Ca^{2+}$-Regulationsmechanismen der Osteoblasten für eine niedrige zytosolische $Ca^{2+}$-Konzentration von ~100 nM[42,48,51]. Ein Großteil des intrazellulären $Ca^{2+}$ ist allerdings in Organellen gespeichert. Dabei ist das endoplasmatische Retikulum (ER) mit 100–800 µM als größtes Depot bekannt[52]. Niedrigere Konzentrationen befinden sich in den Mitochondrien (100-200 nM[53]) und dem Golgiapparat (bis zu 300 µM[54]). Kommt es zu einer Aktivierung, steigt das zytosolische $Ca^{2+}$-Level auf 500–1.000 nM an[55]. Diese Konzentrationsänderung führt in der Zelle zur spezifischen Regulation der zellulären Prozesse[47]. Die Herkunft der $Ca^{2+}$-Ionen beruht dabei auf (1) einem $Ca^{2+}$-Einstrom aus dem extrazellulären Raum und/oder (2) einem $Ca^{2+}$-Ausstrom aus den

intrazellulären Speichern, vorwiegend aus dem ER[48,56]. Da die intrazelluläre $Ca^{2+}$-Dynamik hoch komplex ist, kann hier nur auf die wichtigsten Bestandteile eingegangen werden (**Abb. 2**).

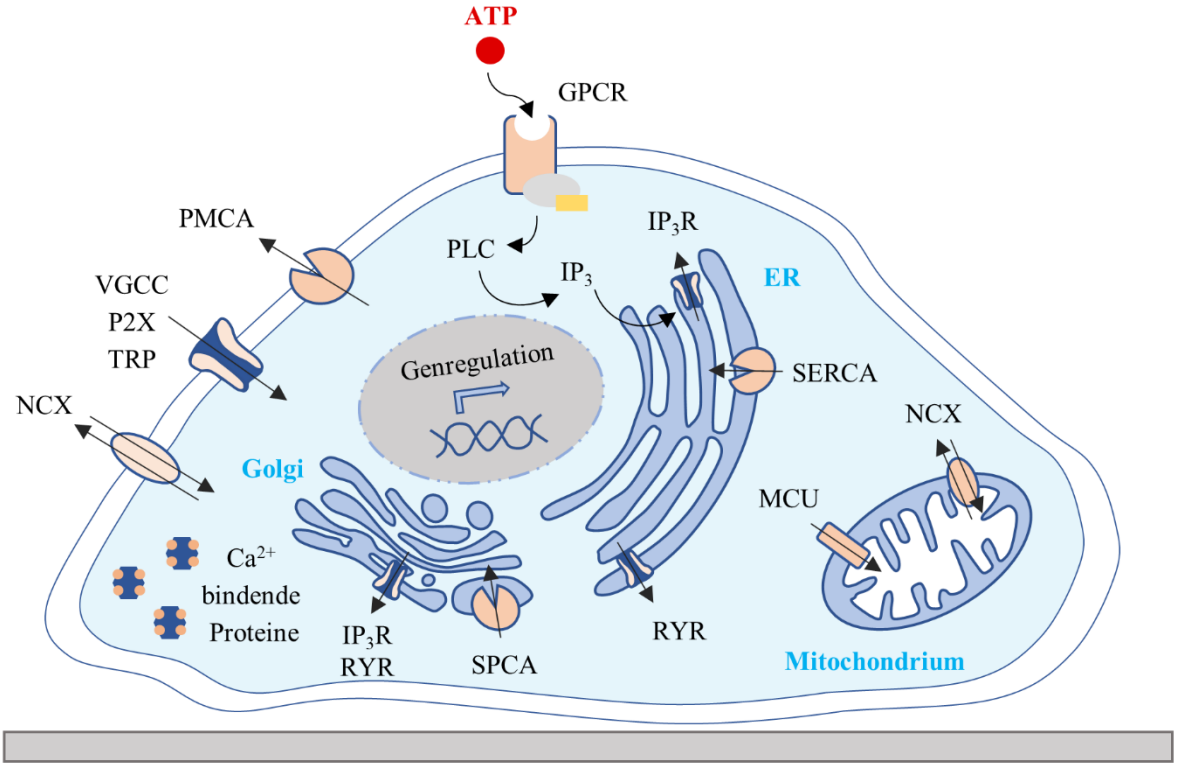


***Abbildung 2: Die intrazelluläre $Ca^{2+}$-Dynamik – ein wichtiger Bestandteil bei der Regulation der Zellfunktionen***. *Zu den wichtigsten $Ca^{2+}$-Kanälen und -Rezeptoren der Einstrommechanismen gehören diejenigen, die durch die Familie der $Ca^{2+}$-permeablen Ionenkanäle mit transientem Rezeptorpotenzial (TRP), spannungsgesteuerten $Ca^{2+}$-Kanälen (VGCC) und purinergen Rezeptoren (z.B. P2X) vermittelt werden. Die Aktivierung von speziellen Plasmamembran-lokalisierten G-Protein-gekoppelten Rezeptoren (GPCR) durch z.B. ATP führt zur Anschaltung des Phospholipase C (PLC) Signalwegs, der die Bildung von Inositoltriphosphat ($IP_3$) steigert. Die anschließende Stimulation von $IP_3$-Rezeptoren ($IP_3R$), die sich vor allem auf dem endoplasmatischen Retikulum (ER) befinden, führt zur Freisetzung von $Ca^{2+}$ aus den intrazellulären Speichern. Die am ER und Golgi lokalisierten Ryanodinrezeptoren (RYR) und der mitochondriale $Na^{+}/Ca^{2+}$-Austauscher (NCX) regulieren ebenfalls den $Ca^{2+}$-Ausstrom aus den Organellen. Weitere wie die Sarko/Endoplasmatische Retikulum-$Ca^{2+}$-ATPase (SERCA), die sekretorische Signalweg-$Ca^{2+}$-ATPase (SPCA) und der mitochondriale Uniporter (MCU) speichern zytosolisches $Ca^{2+}$ im ER, Golgi und den Mitochondrien, während $Ca^{2+}$-ATPasen der Plasmamembran (PMCA) aktiv $Ca^{2+}$ aus dem Zytosol in den extrazellulären Raum ausschleusen und zusammen mit NCX eine Rolle bei der Wiederherstellung der ruhenden intrazellulären $Ca^{2+}$-Konzentration von ~ 100 nM spielen. Das $Ca^{2+}$-Signal reguliert verschiedene $Ca^{2+}$-abhängige Transkriptionsfaktoren und kann zusätzlich durch $Ca^{2+}$-bindende Proteine wie Calmodulin gesteuert werden. Abbildung basierend auf Berridge et al.[47], Marchi und Pinton[48] und Stewart et al.[51].*

Der extrazelluläre Einstrom von $Ca^{2+}$ in das Zytoplasma wird durch den elektrochemischen Gradienten entlang der Plasmamembran angetrieben und mit Hilfe der Aktivierung von verschiedenen Eintrittskanälen ermöglicht[47]. Hierzu zählen unter anderem spannungsabhängige $Ca^{2+}$-Kanäle (VGCC, engl. *voltage gated $Ca^{2+}$ channel*) und ligandengesteuerte Kationenkanäle wie die durch Adenosintriphosphat (ATP) aktivierten ionotropen Purinozeptoren vom Typ P2X[48].

Die Aktivierung von G-Protein gekoppelten Rezeptoren (GPCR, engl. *G-protein coupled receptor*) etwa durch ATP wie der Purinozeptor Typ $P2Y_2$[57] reguliert den zytosolischen $Ca^{2+}$-Einstrom aus dem intrazellulären ER-Speicher über den Phospholipase C Signalweg. Dieser ermöglicht die Spaltung von Phosphatidylinositol-4,5-Bisphosphat ($PIP_2$) in Inositoltriphosphat ($IP_3$) und Diacylglycerin (DAG)[58,59]. Während DAG die Proteinkinase C aktiviert[60], dockt $IP_3$ im ER an $IP_3$-Rezeptoren ($IP_3R$) an und löst die $Ca^{2+}$-Ausschüttung aus[61]. Die erschöpften Vorräte des ER können durch extrazelluläres $Ca^{2+}$ hauptsächlich über Sarco/Endoplasmatische Retikulum $Ca^{2+}$-ATPasen (SERCA) wieder aufgefüllt werden[62]. Dies trägt zur Ausschaltung des $Ca^{2+}$-Signals bei[48].

Die Wiederherstellung des normalen zytoplasmatischen $Ca^{2+}$-Levels erfolgt zusätzlich durch das Ausschleusen über die $Ca^{2+}$-ATPasen der Plasmamembran (PMCA) und die Pufferwirkung der Mitochondrien[63], die einen Großteil der vom ER ausgeschütteten Ionen über den mitochondrialen $Ca^{2+}$-Uniporter (MCU) aufnehmen[64]. Diese werden nur allmählich über $Na^+/Ca^{2+}$-Austauscher (NCX) in das Zytoplasma zurückgegeben[48], um dann von SERCA und PMCA kontrolliert aus der Zelle transportiert zu werden[47]. $Ca^{2+}$ reguliert hier die mitochondriale Atmung und die ATP-Synthese; eine mitochondriale $Ca^{2+}$-Überlastung kann überdies Apoptose auslösen[49]. Im Golgiapparat wird die Aufrecht-erhaltung des $Ca^{2+}$-Spiegels vorwiegend über SPCA (engl. *secretory-pathway $Ca^{2+}$-ATPases*) sowie $IP_3R$ reguliert[65]. Dort ist $Ca^{2+}$ von entscheidender Bedeutung für die enzymatische Aktivität bei der Modifikation, dem Transport und der Sekretion von Proteinen und Lipiden[65].

Aufgrund dieser fundamentalen zellphysiologischen Aufgaben ist die Beeinflussung der $Ca^{2+}$-Dynamik durch Eigenschaften der Materialoberfläche von besonderem Forschungsinteresse. In der vorliegenden Arbeit wurde sich dieser komplexen Dynamik vor allem durch Messung der intrazellulären Fähigkeit zur $Ca^{2+}$-Mobilisierung durch externe ATP-Stimulation auf Materialbeschichtungen verschiedener ζ-Potenziale genähert, um Aussagen über den Einfluss von Oberflächenladungen auf die Zellphysiologie treffen zu können.

## 2 FRAGESTELLUNG UND UNTERSUCHUNGSZIEL

Die Entwicklung und Anwendung von orthopädischen und dentalen Biomaterialien erfordert eine umfangreiche Kenntnis von Materialeigenschaften sowie ein Verständnis zu Wechselwirkungen von Materialien mit dem biologischen System. Die vorliegende Arbeit ist im Rahmen des Teilprojektes A03 des von der Deutschen Forschungsgemeinschaft geförderten Sonderforschungsbereichs (SFB) 1270/1 ELAINE „Elektrisch Aktive Implantate“ entstanden (www.elaine.uni-rostock.de, 299150580). Ziel dieser Dissertation war es, die Zellphysiologie und Morphologie von Osteoblasten durch gezielte Materialoberflächenladungen, abgeleitet vom ζ-Potenzial, zu verbessern.

Es besteht Grund zur Annahme, dass Oberflächenladungen eine entscheidende Rolle bei der Zell-Material-Interaktion spielen. Die Oberfläche von Osteoblasten ist aufgrund ihrer Hyaluronsäurehülle negativ geladen. Man kann davon ausgehen, dass eine positiv geladene Materialoberfläche für die elektrostatischen Wechselwirkungen bei der ersten Zellbegegnung attraktiv ist. Folgende Fragen sollten daher in dieser Arbeit beantwortet werden:

(I) Ist das ζ-Potenzial der Materialoberfläche ein entscheidender Faktor für die Zell-Material-Interaktion?

(II) Können positive Ladungen generell Zellfunktionen begünstigen? Oder gibt es einen bestimmten Bereich des ζ-Potenzials der von Osteoblasten bevorzugt wird?

Um diese zu beantworten, waren systematische Experimente mit diversen chemischen Modifikationen von planaren Ti-Oberflächen erforderlich. In enger Kooperation mit dem SFB Teilprojekt A04 der Universität Greifswald (Prof. C. A. Helm), dem Leibniz-Institut für Plasmaforschung und Technologie e. V. (INP) in Greifswald (Dr. K. Fricke), der Industrieforschungseinrichtung INNOVENT e. V. in Jena (Dr. M. Schnabelrauch) und der Universität Regensburg (Prof. R. Müller) wurden die Oberflächen mit Aminopolymeren, EZM-Proteinen und Peptidmotiven, Polyelektrolytmultischichten sowie mit Gold funktionalisiert und charakterisiert. Um das Zellverhalten auf den negativ und positiv geladenen Materialoberflächen zu erfassen, wurde die Zellmorphologie, die intrazelluläre $Ca^{2+}$-Dynamik und die Zellviabilität analysiert.

# 3 METHODEN

Im Folgenden werden diejenigen Methoden aufgeführt, die für die jeweiligen Publikationen eigenhändig durchgeführt wurden. Detaillierte Protokolle sind in den Publikationen zu finden (ab Seite 49).

## 3.1 OBERFLÄCHENMODIFIKATIONEN

Als Basismaterial und Negativkontrolle für die Publikationen II, IV und V wurden planare Silizium-Oberflächen des Zentrums für Mikrotechnologien (ZfM) verwendet, die mit 100 nm Ti besputtert wurden (nachfolgend als Ti-Oberflächen bezeichnet). Für die Zellexperimente und Bestimmung der Benetzbarkeit wurden Oberflächen mit einer Größe von 1 × 1 × 0,075 cm (Länge × Breite × Tiefe) und für die ζ-Potenzial-analyse Oberflächen mit einer Größe von 2 × 1 × 0,075 cm eingesetzt. Durch die Kooperationen der oben aufgelisteten Institutionen konnten diverse Modifikationen aus den Kategorien (i) Aminopolymere, (ii) EZM-Proteine & Peptidmotive, (iii) Polyelektrolytmultischichten (PEM), und (iv) „Sonstige“ erzeugt und für Zellexperimente genutzt werden. **Tabelle** 1 fasst die Oberflächenmodifikationen der Ti-Proben zusammen und verweist auf deren Hersteller sowie die Datenveröffentlichung der Ergebnisse.

***Tabelle 1. Kooperationen zur Herstellung unterschiedlich geladener Oberflächen***

| Oberfläche | | Hersteller | | Datenveröffentlichung |
|---|---|---|---|---|
| | | Name | Institution | |
| Kontrollen | Ti | Norbert Zichner | ZfM Chemintz, *Schichtabscheidung* | Publikation II, IV, V |
| Amino-polymere | PPAAm | Katja Fricke | INP Greifswald, *Bioaktive Oberflächen* | Publikation II, IV, V |
| | APTES | Manuela Dubs | Innovent Jena, *Biomaterialien* | Publikation V |
| | PEI | Jutta Lehnfeld | UR, *Kolloid- und Grenzflächenchemie* | Publikation V |
| | PPI-G4 | | | Publikation V |
| | PPI-G2 | | | Mendeley Data[66] |
| EZM-Proteine & Peptid-motive | Col I | Martina Grüning | UMR, *Zellbiologie* | Publikation V |
| | Matrigel | | | Publikation V |
| | RGD | Manuela Dubs | Innovent Jena, *Biomaterialien* | Publikation V |
| PEM | $PSS_{3\ DS}$ | Sven Neuber | UHGW, *Weiche Materie und Biophysik* | Publikation IV, V |
| | $PDADMA_{10.5\ DS}$ | | | Publikation IV, V |
| Sonstige | Au | Regina Lange | UHRO, *Oberflächen – und Grenzflächenphysik* | Mendeley Data[66] |

Abkürzungen: APTES, 3-Aminopropyltriethoxysilan; Col I, Kollagen Typ I; DS, Doppelschicht; EZM-Proteine, Extrazelluläre Matrix Proteine; INP, Leibniz-Institut für Plasmaforschung und Technologie; PEI, Polyethylenimin; PEM, Polyelektrolytmultischichten; PDADMA, Polydiallyldimethylammoniumchlorid; PPAAm, Plasma polymerisiertes Allylamin; PPI-G2/4, Polypropylenimin Dendrimere (Generation 2/4); PSS, Polystyrolsulfonat; RGD, Arginin-Glycin-Aspartat Sequenz; Ti, Titan; UHGW, Universität Greifswald; UHRO, Universität Rostock; UMR, Universitätsmedizin Rostock; UR, Universität Regensburg; ZfM, Zentrum für Mikrotechnologien.

## 3.2 OBERFLÄCHENCHARAKTERISIERUNG

Die Modifikationen wurden anhand der Oberflächenladung mittels ζ-Potenzialmessung (Publikation III, IV, V) und der Benetzbarkeit anhand der Bestimmung des Wasserkontaktwinkels θ (WCA, engl. *water contact angle*) und der freien Oberflächenenergie (SFE, engl. *surface free energy*) (Publikation II, IV, V) charakterisiert. Folgend werden Grundlagen des ζ-Potenzials und des WCA, sowie der SFE dargelegt.

### *3.2.1 ζ-POTENZIAL*

Das ζ-Potenzial (elektrokinetisches Potenzial) beschreibt das Ladungsverhalten an der Schnittstelle der Materialoberfläche zur Flüssigkeit und ist ein Indikator für die Oberflächenladung. Alle Materialien erhalten spontan eine oberflächenelektrische Ladung im Kontakt mit Wasser. Dies erfolgt hauptsächlich durch Säure-Base-Reaktionen auf beschichteten Oberflächen zwischen den funktionalen Gruppen von Proteinen, Polymeren oder Polyelektrolyten und Wasser oder durch Adsorption von Wasserionen auf Oberflächen ohne funktionale Gruppen. Saure Gruppen wie Carbonsäure-, Sulfonsäure- oder Hydroxylgruppen dissoziieren in Wasser und sind somit negativ geladen. Basische Gruppen wie Aminogruppen werden protoniert und nehmen eine positive Ladung an. Hierbei spielt der pH-Wert eine entscheidende Rolle.

Anhand des Models der elektrischen Doppelschicht (EDL, engl. *electrical double layer*) lässt sich das Phänomen vereinfacht darstellen (**Abb. 3A**). Die Materialoberflächenladung wird durch spezifisch adsorbierende Gegenionen neutralisiert. Dieser der Oberfläche am nächstliegenden Bereich wird als stationäre Phase bezeichnet und gilt als unbeweglich. Die darauffolgende diffuse Phase zeichnet sich durch die Diffusion und thermische Bewegung zufällig verteilter Ionen aus. Die Grenze zwischen dem Rand der stationären und diffusen Schicht wird als Scherungs- oder Abscherschicht bezeichnet. Das elektrische Potenzial sinkt erst linear, dann exponentiell in der diffusen Schicht auf null ab. Während das tatsächliche Oberflächenpotenzial Ψo unzugänglich ist, kann das ζ-Potenzial in der Abscherschicht bestimmt werden[67].

Bei der Messung zweier sich gegenüberliegenden Oberflächen am elektrokinetischen SurPASS™ Messgerät (Anton Paar GmbH) bewegt sich die wässrige Lösung aufgrund eines angelegten Drucks in der Messzelle und Scherkräfte wirken auf die Gegenionen. Durch die Ladungstrennung entsteht ein Strömungspotenzial, das mittels Elektroden ermittelt werden kann. (**Abb. 3B**). Anhand der Formel von Hermann von Helmholtz und Marian von Smoluchowski berechnet die Attract Software (Anton Paar GmbH) das ζ-Potenzial:

$$\zeta = \frac{dl_{str}}{dp} \times \frac{\eta}{\varepsilon \times \varepsilon_0} \times \frac{L}{A}, \qquad \textit{(Helmholtz Smoluchowski Gleichung)}$$

wobei, $l_{str}$ das Strömungspotenzial, p der Druck, η die Viskosität und ε die Dielektrizitätskonstante der wässrigen Lösung, L die Länge und A die Weite x Höhe der Messkammer ist.

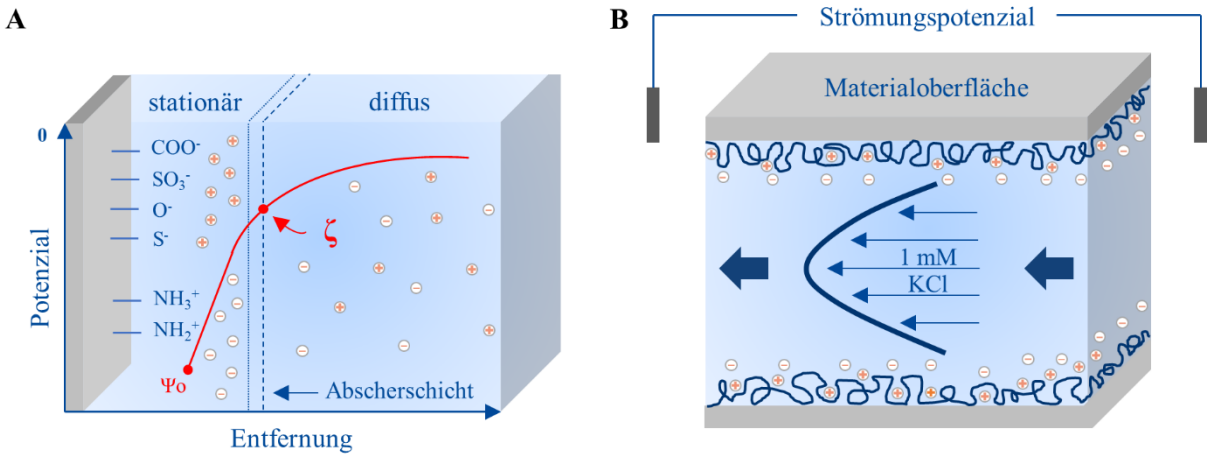


***Abbildung 3: Bestimmung des ζ-Potenzials als ein Indikator für die Oberflächenladung.*** *(A) Das ζ-Potenzial ist das elektrische Potenzial an der Abscherschicht zwischen der für Gegenionen unbeweglichen stationären und für Ionen beweglichen diffusen Phase der elektrischen Doppelschicht. Das tatsächliche Oberflächenpotenzial Ψo ist unzugänglich. (B) Aufgrund des angelegten Durchflusses einer wässrigen Lösung wirken Scherkräfte auf die Gegenionen der Oberflächenladung, resultierend in einer Ladungstrennung. Das so entstandene Strömungspotenzial wird mittels Elektroden gemessen und anhand der Helmholtz Smoluchowski Gleichung in das ζ-Potenzial umgerechnet. Abbildung basierend auf Ferraris et al.*[67] *und LLS Health CDMO Website*[68].

### *3.2.2 WASSERKONTAKTWINKEL UND FREIE OBERFLÄCHENENERGIE*

Der WCA ist ein Maß für die Benetzbarkeit einer Oberfläche durch Wasser. Bei vollständiger Benetzung ergibt sich ein WCA von 0°. Zwischen 0° und 90° gilt die Oberfläche als hydrophil, über 90° als hydrophob. Ultrahydrophobe Materialien mit dem sogenannten „Lotuseffekt“ nähern sich dem theoretischen Grenzwert des WCA von 180°[69]. Gemäß der Young’schen Gleichung resultiert der WCA aus einem vorherrschenden Kräftegleichgewicht dreier Komponente:

$$\sigma_s = \sigma_{ls} + \sigma_l \times \cos\theta\,, \qquad \textit{(Young'sche Gleichung)}$$

wobei $\sigma_s$ (s, engl. *solid*) die freie Oberflächenenergie, $\sigma_l$ (l, engl. *liquid*) die Oberflächenspannung der Flüssigkeit und $\sigma_{ls}$ die Grenzflächenspannung zwischen Materialoberfläche und Flüssigkeit ist (**Abb. 4**). Er wird mittels Tropfenkonturanalyse (DSA, engl. *drop shape analysis*) der ADVANCE Software (Krüss GmbH) bestimmt, bei der anhand der Auswertung der Grauwerte des aufgenommenen Bildes eines liegenden Tropfens zum einen die Basislinie (Kontakt zwischen Tropfen und Materialoberfläche) und zum anderen der Tropfenumriss erkannt wird.

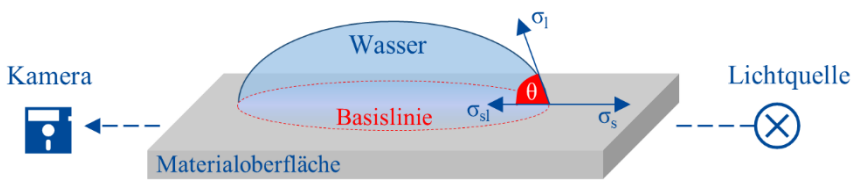

***Abbildung 4: Messung des Kontaktwinkels zur Bestimmung der Benetzbarkeit einer Oberfläche mittels Tropfenkonturanalyse.*** *Der Kontaktwinkel θ ist ein Maß für das Vermögen einer Flüssigkeit (hier: Wasser) eine Materialoberfläche zu benetzen. Die Form, die ein Tropfen auf der Fläche annimmt, hängt von der freien Oberflächenenergie ($\sigma_s$), der Oberflächenspannung der Flüssigkeit ($\sigma_l$) und der Grenzflächenspannung zwischen Materialoberfläche und Flüssigkeit ($\sigma_{ls}$) ab. Der Kontaktwinkel wird anhand eines durch eine Kamera aufgenommenen Bildes eines liegenden Tropfens an der Grenze zwischen der Tropfenkontur und dem Oberflächenrand (Basislinie) gemessen. Abbildung basierend auf DataPhysics Instruments Website*[69].

Während der WCA alleine nur einen Hinweis auf die Benetzung der Materialoberfläche gibt, ist die SFE ein quantitatives Maß für die intermolekularen Kräfte an der Materialgrenzfläche. Zu diesen Kräften zählen dispersive van-der-Waals-Kräfte wie Londonsche Dispersions- und Debye-Wechselwirkungen sowie polare Wasserstoffbrückenbindungen und Dipol-Dipol-Wechselwirkungen. Ist die SFE hoch, wird das Material leicht von jeder Flüssigkeit benetzt. Um die SFE zu bestimmen, wird am häufigsten das Modell nach Owens, Wendt, Rabel und Kaelble (OWRK) angewendet, das mit Kontaktwinkeln zweier Flüssigkeiten mit bekannten polaren und dispersiven Anteilen der Oberflächenspannung auskommt (typischerweise Wasser und Diiodomethan).

## 3.3 ZELLBIOLOGISCHE UNTERSUCHUNGEN

Für die zellbiologischen Untersuchungen auf den Oberflächen wurden humane MG-63 Osteoblasten (ATCC®, CRL1427™) verwendet, die sich zur Untersuchung der Zell-Material-Interaktion eignen[70] und deren Eigenschaften den der primären Osteoblasten ähneln[71,72].

### *3.3.1 ZELLMORPHOLOGIE*

Anhand der Zellmembranmarkierung mit dem rot fluoreszierenden Farbstoff PKH26, der sich mit langen aliphatischen Schwänzen stabil in die Lipidregionen der Zellmembran einbaut, konnte die Zellfläche und Kreisförmigkeit nach 1, 3 und 12 h Kultivierung (Publikation IV) mittels Photoshop CC 2017 ausgemessen werden. Dabei berechnet die Software die Kreisförmigkeit K wie folgt:

$$\boldsymbol{K = \frac{4\,\pi \times A_C}{U_C^2}}, \qquad \textit{(Kreisförmigkeit)}$$

wobei $A_C$ die Zellfläche und $U_C$ der Zellumfang ist (C, engl. *cell*). Ein perfekter Kreis wird durch einen Wert von 1,0 und ein zunehmend lang gestrecktes Polygon durch einen gegen 0 konvergierenden Wert beschrieben. Zusätzlich konnte die Zellfläche und Kreisförmigkeit nach einem Kultivierungszeitraum von 24 h von vital mit dem $Ca^{2+}$-Indikator Fluo-3 gefärbten Zellen mit Photoshop ermittelt werden (Publikation IV, V). Rasterelektronenmikroskopische (REM) Aufnahmen dienten zur genaueren Betrachtung der Zellmorphologie nach 24 h Kultivierung (Publikation V).

### *3.3.2 INTRAZELLULÄRE $Ca^{2+}$-DYNAMIK*

#### *(1) Voruntersuchungen: ATP-Rezeptoren, ATP-Konzentration, $Ca^{2+}$-Ursprung (Publikation V)*

Intrazelluläres $Ca^{2+}$ kann durch externe ATP-Stimulation mobilisiert werden. Daher wurde für die $Ca^{2+}$-Mobilisierungsversuche in Publikation V zunächst der Nachweis von G-Protein-gekoppelten ATP-Rezeptoren

($P2Y_2$) und ATP-abhängigen Liganden-gesteuerten Ionenkanälen ($P2X_7$) mittels immunzytochemischer Färbung in Zusammenarbeit mit Dr. Susanne Stählke (UMR, Zellbiologie) erbracht. Zusätzlich wurde anhand eines Zellviabilitätstests (MTS, siehe 3.3.3) überprüft, welche ATP-Konzentration für die Stimulation der $Ca^{2+}$-Mobilisierung geeignet ist. Zudem können die mobilisierten $Ca^{2+}$-Ionen extrazellulären oder intrazellulären Ursprungs sein. Dies wurde anhand von ATP-Stimulation (siehe 3.3.2 (3)) in $Ca^{2+}$-haltigem Puffer oder in Abwesenheit von $Ca^{2+}$ (Ausschluss des extrazellulären Einstroms) ermittelt.

### *(2) $Ca^{2+}$- Aktin Vitalfärbung (BacMam)*

Das intrazelluläre basale $Ca^{2+}$-Signal wurde nach einem Kultivierungszeitraum von 1 h mittels vitaler Fluo-3- und Hoechst-Färbung untersucht (Publikation V). Um das basale $Ca^{2+}$-Signal nach 24 h Zellkultivierung zu visualisieren, erfolgte die Doppelfärbung von Fluo-3 und Hoechst an Aktin-RFP (RFP, engl. *red fluorescent protein*) transfizierten Zellen (Publikation I, V). Diese Transfektion erfolgte mit Hilfe der *BacMam*-Technologie, welche auf dem Gentransfer von *Bac*uloviren in *Mam*malia-Zellen basiert, um das gewünschte Zielprotein (hier: Aktin) zu exprimieren. Hierfür sind die Baculoviren mit einem von Säugetierzellen erkennbaren Promoter oberhalb des Zielgens modifiziert. Die Genexpression in den Zellen beginnt 4-6 h nach Transfektion und ist innerhalb von 24 h maximal. Allerdings werden wie bei jeder Transfektionstechnik nicht alle Zellen gleich effiziert transfiziert. Für ein optimales Expressionslevel wurde die Zellzahl sowie das bei Zellaussaat zugegebene Volumen der BacMam-Lösung adjustiert.

### *(3) $Ca^{2+}$-Mobilisierung (Publikation V)*

Die intrazelluläre $Ca^{2+}$-Dynamik in Abhängigkeit unterschiedlicher Oberflächenladungen wurde mittels $Ca^{2+}$-Imaging Technik untersucht (Publikation V). **Abbildung 5** zeigt die methodischen Hauptschritte von Zelleinsaat bis zur Berechnung der mittlere Fluoreszenzintensität ($MFI_C$; engl. *mean fluorescent intensity of cells*) der Fluo-3 gefärbten Zellen. Nach einer Kultivierung von 24 h wurden die Zellen mittels des nicht-ratiometrischen $Ca^{2+}$-Indikators Fluo-3 grün gefärbt. $Ca^{2+}$-Indikatoren sind Moleküle, die zur Darstellung räumlicher Dynamiken von $Ca^{2+}$-Signalen verwendet werden. Im Ruhe- und $Ca^{2+}$-freien Zustand weisen sie minimale Fluoreszenz auf. Diese erhöht sich um mehr als das 100-fache, wenn sie $Ca^{2+}$ binden[73]. Fluo-3 zählt zu den geeignetsten $Ca^{2+}$-Indikatoren für die konfokale Laser-Scanning-Mikroskopie (LSM)[39], wenn die Wirkung externer Reize ohne eine absolute Konzentrationsbestimmung untersucht wird[44]. Der Indikator ist an ein Acetoxymethyl (AM)-Ester gebunden, was eine passive Diffusion in die Zellen ermöglicht. Intrazelluläre Esterasen spalten die AM-Gruppe ab und schließen somit den Farbstoff in der Zelle ein. Unter dem inversen konfokalen LSM wurden die Zellen mit ATP stimuliert (**Abb. 5A**), während eine Zeitserie über 8 min aufgenommen und so das basale $Ca^{2+}$-Signal und die $Ca^{2+}$-Mobilisierung nach ATP-Stimulation bei 180 s erfasst wurde (**Abb. 5B**). Hierbei wurde mit einer maximal geöffneten Lochblende (engl. *pinhole*) gearbeitet, um das gesamte $Ca^{2+}$-Signal verlustfrei zu dokumentieren.

Zur quantitativen Ermittlung der $Ca^{2+}$-Signal-Rohdaten wurden 10 Kästchen pro Oberfläche (1 Kästchen pro Zelle mit einer definierten Fläche $A_{ROI}$ von 100 µm²) über die Aufnahmen gelegt und mittels „Mean ROI"-Funktion (ROI, engl. *region of interest*) der ZEN blue Software analysiert (**Abb. 5C**). Diese MFI innerhalb der Kästchen wird als $MFI_{ROI}$ bezeichnet und beinhaltet die $Ca^{2+}$-Signale der 10 Zellen über die gesamte Aufnahmedauer von 8 min (siehe Diagramm in **Abb. 5C**). Für die weitere Auswertung wurden die $MFI_{ROI}$-Werte in den Bereichen *vor* (0-170 s) und *nach* der ATP-Stimulation (maximales Signal zwischen 190-240 s) als $MFI_B$ (B für *basal*) und $MFI_A$ (A für engl. *after*) definiert.

Aufgrund von Unterschieden in der Zellfläche, die das $Ca^{2+}$-Signal beeinflussen können, wurde im letzten Schritt die gemittelte Zellfläche $A_C$ (in µm²) in der Berechnung der $MFI_C$ berücksichtigt (**Abb. 5D**). Im Vergleich zu einer flach ausgebreiteten Zelle ist das $Ca^{2+}$-Signal einer kugelförmigen Zelle auf eine kleinere Fläche konzentriert (mehr Zellvolumen unter der Fläche, da die Zellhöhe entsprechend größer ist), was bei einer maximal geöffneten Lochblende zu erhöhten $MFI_{ROI}$-Werten führt. Zur Veranschaulichung lässt sich dieser Effekt mit einer Punktlichtquelle (kugelige Zelle) und einem großflächigen Scheinwerferlicht (flach ausgebreitete Zelle) vergleichen. Unter der Annahme, dass das $Ca^{2+}$-Signal in der Zelle gleichmäßig verteilt ist (d.h., dass die $MFI_{ROI}$-Werte unabhängig von der Kästchenpositionierung in der Zelle sind), wurden alle MFI-Werte auf $A_C$ der jeweiligen Oberfläche und der definierten Fläche von $A_{ROI}$ normiert. Der Anstieg des $Ca^{2+}$-Signals ($Ca^{2+}$-Mobilisierung, $MFI_{A-B}$) auf den Oberflächen berechnete sich letztendlich aus der Differenz von $MFI_A$ und $MFI_B$.

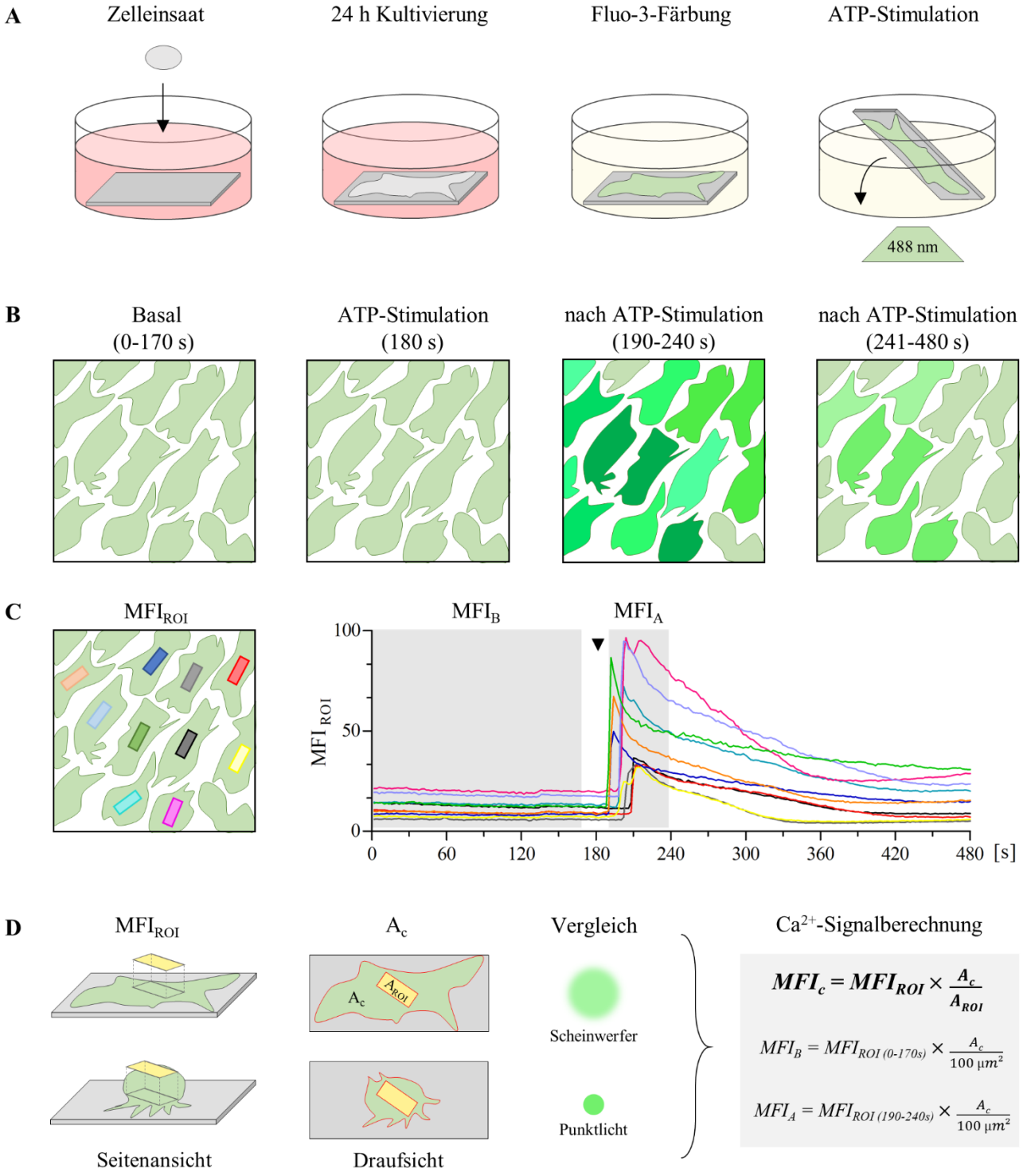


***Abbildung 5: Messung der intrazellulären $Ca^{2+}$-Dynamik mittels $Ca^{2+}$-Imaging Technik.*** *(A) Zellbehandlung: Nach einer Kultivierung von 24 h werden die Zellen mit dem $Ca^{2+}$-Indikator Fluo-3 gefärbt und mit ATP stimuliert. (B) Aufnahme am LSM780: Die $Ca^{2+}$-Mobilisierung wird über eine Zeitserie von 8 min dokumentiert. Dabei wird zunächst das basale $Ca^{2+}$-Signal (0-170 s) aufgenommen. Nach 180 s erfolgt die ATP-Stimulation der Zellen, wobei die maximale Zellreaktion zwischen 190 und 240 s liegt. (C) Rohdatengenerierung: Die mittlere Fluoreszenzintensität (MFI) von 10 Kästchen/10 Zellen wird anhand der ZEN blue Funktion „Mean ROI" ermittelt ($MFI_{ROI}$) und teilt sich in die Bereiche $MFI_B$ (basal, 0-170 s) und $MFI_A$ (nach ATP-Stimulation, 180-240 s). (D)*

*Berechnung des $Ca^{2+}$-Signals: $MFI_{ROI}$ ist von der Zellgröße abhängig. Im Gegensatz zu einer flach ausgebreiteten Zelle (Vergleich Scheinwerferlicht) ist das $Ca^{2+}$-Signal einer kugelförmigen Zelle (Vergleich Punktlichtquelle) auf eine kleinere Fläche konzentriert. Um die MFI der Zellen ($MFI_C$) zu erhalten, werden daher die $MFI_{ROI}$-Werte auf die mittlere Zellfläche $A_C$ und die definierte Kästchengröße von 100 µm² ($A_{ROI}$) normiert.*

### *3.3.3 ZELLVIABILITÄT*

Untersuchungen zur Zellviabilität (Publikation V) fanden anhand drei verschiedener Messprinzipien statt. Der kolorimetrische Stoffwechselaktivitätstest (MTS) weist NADH(P)H-abhängige Dehydrogenasen in mitochondrial aktiven und lebensfähigen Zellen nach, indem diese Enzyme gelbes MTS-Tetrazolium zu violettem Formazan reduzieren. Mit Hilfe der fluoreszenzmikroskopischen Lebend/Tot-Färbung konnten die Esteraseaktivität (Calcein) und Membranintegrität (Ethidium-Homodimer) erfasst werden. Zudem konnte anhand der durchflusszytometrischen Zellzyklusanalyse die proliferative Phase PP, basierend auf der mit Propidiumiodid angefärbte DNA-Menge, wie folgt berechnet werden:

$$\boldsymbol{PP = S + G2/M}\,, \qquad \textit{(Proliferative Phase)}$$

wobei während der S-Phase (S, engl. *synthesis*) die Replikation der DNA und in der G2-Phase (G, engl. *gap*) Qualitätskontrollen und Vorbereitungen auf die bevorstehende Zellteilung (M, Mitose) stattfinden, sodass hier ein tetraploider Chromosomensatz vorliegt.

## 3.4 STATISTIK

Die statistische Auswertung und Darstellung der Daten erfolgte mit der Software GraphPad Prism Version 6.05 für Windows. Da die Daten nicht normalverteilt vorlagen (D'Agostino-Pearson Omnibus und Shapiro-Wilk-Test), wurde zum einen der nichtparametrische Kruskal-Wallis-Test gefolgt von Dunn´s Post-hoc-Test mit dem Signifikanzwert $p < 0,05$ für Werte der Zellfläche (Publikation IV), der Morphologie/ Kreisförmigkeit, der $Ca^{2+}$-Mobilisierung und Proliferation (Publikation V) durchgeführt. Zum anderen wurde der Mann-Whitney-U-Test für Werte des $Ca^{2+}$-Ursprungs und der gepaarter Wilcoxon-Rangsummen-Test für Werte der Zellviabilität (MTS) (Publikation V) mit dem Signifikanzwert $p < 0,05$ angewendet. Die Daten der Zellfläche (siehe Publikation VI) wurden als Boxplots mit Median, Interquartilsabstand (IQR, engl. *interquartile range*), sowie Minimal- und Maximalwert dargestellt. Daten in Publikation V wurden als (i) Mittelwert ± sem (Standardfehler, engl. *standard error of the mean*) für $MFI_C$-Werte, (ii) Mittelwert ± SD (Standardabweichung, engl. *standard deviation*) für Proliferations- und Zellflächenwerte, sowie für WCA-, SFE- und ζ-Potenzial-Werte, und (iii) Median ± IQR für Kreisförmigkeits- und MTS-Werte dargelegt.

Für die zusammenfassenden **Abbildungen 7** und **9** in dieser Arbeit wurden die Werte mittels Mann-Whitney-U-Test auf Signifikanzen geprüft ($p < 0,05$).

# 4 ERGEBNISSE

In diesem Abschnitt werden die Publikationen in Form von Kurzfassungen mit Hintergrund, Ergebnissen, Fazit und persönlichem Beitrag vorgestellt. Publikationen I und II (Nebe et al. 2019, Staehlke et al. 2018) eröffnen Grundlagen für Publikationen IV und V (Gruening et al. 2020, Gruening et al. 2020), die die Eigen- und Hauptarbeit dieser Dissertation darstellen. Publikation III (Lehnfeld et al. 2020) entstand aus der Kooperation zur Universität Regensburg. Detaillierte Ergebnisse können in den jeweiligen Publikationen eingesehen werden (ab Seite 49). Zudem werden bei Publikationen IV und V auf zusätzliche zum Teil in Mendeley Data veröffentlichte Daten verwiesen, die nicht Teil der Manuskripte waren.

## 4.1 PUBLIKATION I: DIE ZELLATTRAKTIVE PPAAM NANOSCHICHT

*HINTERGRUND:* Orthopädische permanente Implantate sollen spezifische zelluläre Reaktionen mit dem Ziel der Geweberegeneration und der Integrationsbeschleunigung unterstützen. In vorangegangener Forschung wurde gezeigt, dass eine stabile und ɣ-sterilisierbare Oberflächenmodifikation mit plasmapolymerisiertem Allylamin (PPAAm) nicht nur eine erhöhte Zellaktivität *in vitro*, sondern auch eine verbesserte Osseointegration *in vivo* fördern kann[74]. Die homogene Nanoschicht trägt aufgrund von Aminogruppen eine positive Oberflächenladung und wechselwirkt somit elektrostatisch mit der negativen Ladung humaner Osteoblasten, die durch die Carboxylgruppen der Hyaluronsäurehülle hervorgerufen wird[33]. Infolgedessen entstand die Annahme, dass eine positive Ladung an der Materialoberfläche generell die initiale Zelladhäsion vorantreiben könnte. Die Beschichtung wurde auf unterschiedlichen Biomaterialien wie Ti, Ti-Legierungen, Kalziumphosphat-Gerüsten oder elektrogesponnenen Polylactid-Fasernetzen angewendet. In diesem Kontext fasst die Studie die bisherig erzielten Ergebnisse mit PPAAm zusammen. Zudem wurde die Eignung der Beschichtung (15 s bis 960 s Plasmabehandlung) für die Steigerung der Attraktivität rauer und glatter Keramikoberflächen für Dentalimplantate mit Yttriumoxid-stabilisiertem tetragonalem Zirkoniumoxid untersucht.

*ERGEBNISSE:* Die PPAAm-Beschichtung ließ sich für die Bioaktivierung von Keramikoberflächen unter Aufrechterhaltung der tetragonalen Kristallstruktur nutzen. Es konnte ein quasi-lineares Schichtwachstum bei einer Plasmabehandlung von 15 s bis 480 s beobachtet werden. Der Wasserkontaktwinkel (WCA) lag schon nach einer Plasmabehandlung von 15 s (Schichtdicke < 10 nm) im optimal hydrophilen Bereich zwischen 40° und 60°, während sich die freie Oberflächenenergie (SFE) auf ~50 mN/m (bei 120 s und 960 s Plasmabehandlung) erhöhte und die Oberflächenladung (ζ-Potenzial) bei pH 6 im positiven Bereich lag (+ 33 mV). Humane MG-63 Osteoblasten zeigten einen sehr gut ausgebreiteten und extrem an die Materialoberfläche angeschmiegten Phänotyp. Die Adhäsion (10 min nach Zelleinsaat) konnte durch die Oberflächenmodifizierung mit PPAAm deutlich verbessert werden.

*FAZIT:* Die PPAAm-Beschichtung eignet sich auf verschiedenen Materialien für die orthopädische und dentale Implantologie. Die positiv geladene Nanoschicht zeichnet sich durch eine außergewöhnlich zell-attraktive

Eigenschaft aus, begründet in diverser physiologischer Hinsicht, wie z.B. Zellmigration und Vinkulinmobilität (**Abb. 6**). Dementsprechend wurde PPAAm als Positivkontrolle für die Zellversuche der Publikationen VI und V dieser Dissertation eingesetzt.

*PERSÖNLICHER BEITRAG:* Etablierung, Optimierung und Durchführung der BacMam-Methode (Transfektion von Aktin-RFP (RFP, engl. *red fluorescent protein*)) am Laser-Scanning-Mikroskop LSM780 mit gleichzeitiger Vitalfärbung von Fluo-3 ($Ca^{2+}$-Indikator) und Hoechst (dsDNA) zur Visualisierung des basalen $Ca^{2+}$-Signals und des Aktinzytoskeletts nach 24 h Zellkultivierung auf Ti und PPAAm-modifiziertem Ti; Manuskript Review.

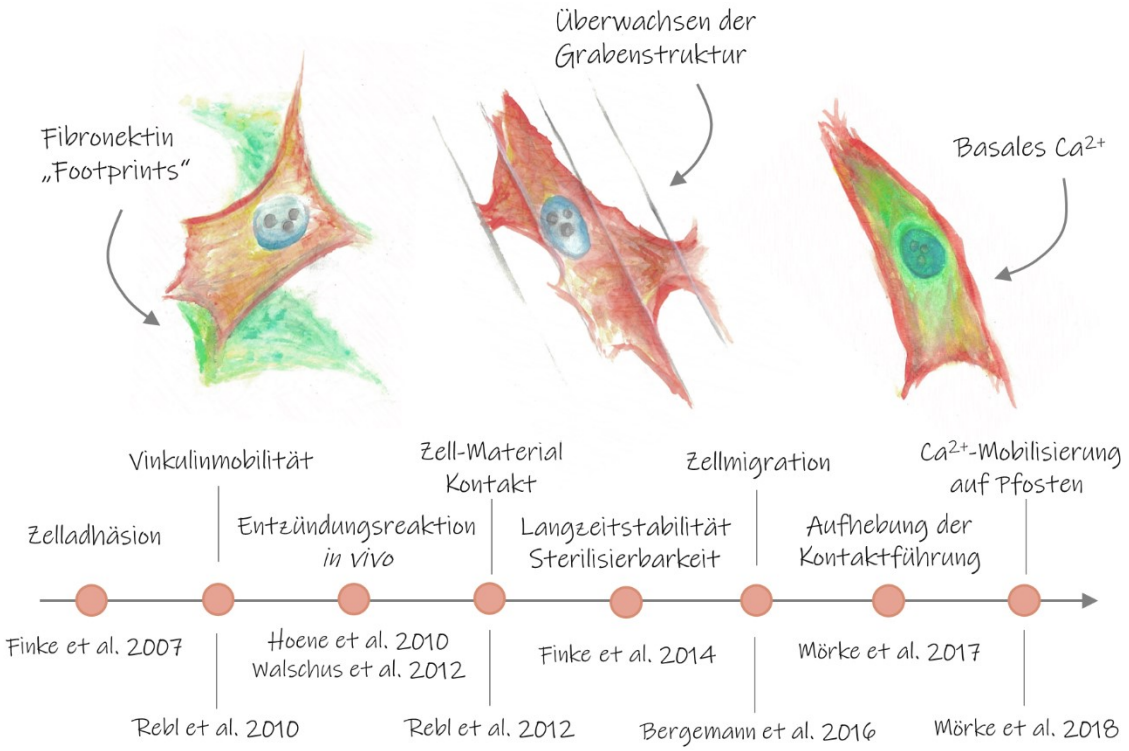


***Abbildung 6: Eine einzigartige zellattraktive Beschichtung – Rückblick auf die Besonderheiten des Nanolayers PPAAm.*** *Die Nanobeschichtung eignet sich auf verschiedensten Materialien. Sie ist stabil, sterilisierbar, hydrophil und trägt eine positive Oberflächenladung[75]. Sie ist in der Lage die Zellaktivität und -funktion zu erhöhen: PPAAm verbessert die Zelladhäsion und -ausbreitung sowie die Organisation der Adhäsionskomponente wie Aktin oder Vinkulin[34,76]. Zellen weisen auf PPAAm eine erhöhte Migration[77](Zelle links) und einen extrem flachen Phänotyp auf[78]. Erstaunlicherweise setzt die Nanoschicht die darunterliegende Topographie außer Kraft und lässt die Zellen die Kontaktführung „vergessen"[79] (Zelle mittig). Auf Pfostenstukturen hebt PPAAm die eingeschränkte Zellfunktion auf und erhöht die $Ca^{2+}$-Mobilisierung[80] (Zelle rechts). Zudem kann durch PPAAm die Osseointegration verbessert werden[74]. Illustration der Zellen von Dr. Nana-Maria Grüning und Helena Noall.*

## 4.2 PUBLIKATION II: $Ca^{2+}$-MOBILISIERUNG ALS INDIKATOR FÜR DIE ZELLPHYSIOLOGIE

*HINTERGRUND:* Die Oberflächeneigenschaften der Biomaterialmodifikationen sind ausschlaggebend für die Zell-Material-Interaktion und somit für die Integration in das Biosystem. Zellen sind in der Lage diese Eigenschaften wahrzunehmen; die dadurch ausgelösten physiologischen Prozesse sind allerdings unzureichend beschrieben. Bisherige Forschung zeigte, dass definiert geometrische Pfostenstrukturen nachteilige zellphysiologische Prozesse bedingten, welche sich auch durch eine reduzierte intrazelluläre $Ca^{2+}$-Mobilisierung nach ATP-Stimulation kennzeichneten. Zellen auf PPAAm-beschichteten Pfostenstrukturen hingegen waren aktiver und reagierten mit einer erhöhten $Ca^{2+}$-Mobilisierung nach ATP-Zugabe. In diesem Zusammenhang wurde in dieser Studie die Bedeutung der intrazellulären $Ca^{2+}$-Dynamik für die Charakterisierung der Zell-Material-Interaktion auf verschiedenen Oberflächen (Ti, PPAAm, Collagen Typ I, IBIDI Zellkulturplastik) in Verbindung mit der Zellviabilität humaner Osteoblasten untersucht.

*ERGEBNISSE:* Die Charakterisierung der Oberflächeneigenschaften mittels WCA-Messungen zeigte hydrophilere Werte aller Oberflächen (60°-73°) im Vergleich zu unbeschichtetem Ti (85°). Die Oberflächenmodifizierung mit PPAAm führte zu einer positiv geladenen Oberfläche im physiologischen Bereich bei pH 7,4 (ζ-Potenzial +8.6 mV). Diese Oberfläche resultierte in einer signifikant erhöhten Zellviabilität und in einer verbesserten intrazellulären $Ca^{2+}$-Mobilisierung nach externer ATP-Stimulierung sowohl in MG-63 Zellen, als auch in primären humanen Osteoblasten.

*FAZIT:* Die intrazelluläre $Ca^{2+}$-Dynamik ist ein sensitiver Parameter, der die Zellphysiologie auf Biomaterialoberflächen reflektiert. Diese Studie unterstützt somit die Annahme, dass die $Ca^{2+}$-Signalkaskade bei der Transmission externer Signale in die Zelle von wesentlicher Bedeutung ist. Das positive ζ-Potenzial scheint hierbei für die $Ca^{2+}$-Mobilisierung eine wichtige Rolle zu spielen. Folglich wurde dieses *in vitro*-Verfahren als Hauptmethode für den Vergleich verschiedener Oberflächenladungen in dieser Dissertation (Publikation V) angewendet und kann für die Bewertung neuer Biomaterialien von Nutzen sein.

*PERSÖNLICHER BEITRAG:* Bestimmung der WCA-Werte von Ti, PPAAm-modifiziertem Ti, Collagen Typ I-modifiziertem Ti sowie IBIDI Zellkulturplastik am Drop Shape Analyzer DSA-25 mittels Tropfenkonturanalyse der ADVANCE Software (Krüss GmbH); Manuskript Review.

### 4.3 PUBLIKATION III: ζ-POTENZIAL ABHÄNGIGE PROTEINADSORPTION

*HINTERGRUND:* Die Proteinadsorption ist einer der ersten Prozesse nach der Implantation eines Biomaterials und kann die weitere Zell-Material-Interaktion beeinflussen. Daher ist es wichtig, den Prozess der Proteinadsorption zu verstehen und unspezifische Proteinablagerungen zu verhindern. In dieser Studie wurden auf Grundlage von Polyaminen und Polyamidoaminen (PAMAM) unterschiedliche Strukturen (Dendrimere, Oligomere, Polymere) synthetisiert und in Hinblick auf die Proteinadsorption mit Einzel-proteinen (Humanserumalbumin (HSA) und Lysozym) sowie komplexen physiologischen Flüssigkeiten (fötales Kälberserum (FKS) und menschlicher Speichel) untersucht. Um letztlich Aufschluss über das Proteinverhalten geben zu können, wurde die Proteinadsorption mit den physikochemischen Eigenschaften der Oberflächen (ζ-Potenzial, WCA, SFE) korreliert.

*ERGEBNISSE:* Alle Modifikationen konnten als hydrophil eingestuft werden (WCA <60°) und besaßen ähnliche freie Oberflächenenergien (SFE ~46-54 mN/m), während ihre Amingruppendichten und Oberflächenladungen unter physiologischem pH 7,4 stark variierten (ζ-Potenzial: Strömungspotenzial zwischen -90 und +48 mV). Hinsichtlich der Benetzbarkeit (WCA, SFE) wurde keine Korrelation festgestellt. Vielmehr korrelierte die Menge an adsorbiertem Protein stark mit dem ζ-Potenzial der Oberflächen-beschichtungen. Für die HSA-, Speichel- und FKS-Lösungen (hauptsächlich negativ geladene Proteine) konnte ein nahezu linearer Anstieg der Proteinadsorption mit zunehmend positiverem ζ-Potenzial der Materialoberflächen beobachtet werden. Für das positiv geladene Lysozym konnte ein entgegengesetztes Verhalten (d.h. abnehmende Adsorption mit steigendem ζ-Potenzial) beobachtet werden.

*FAZIT:* Die Proteinadsorption an den Oberflächen wird hauptsächlich durch elektrostatische Effekte dominiert und ist somit stark vom ζ-Potenzial abhängig. Je positiver das ζ-Potenzial, desto mehr Proteine der physiologischen FKS-Lösung, die standardmäßig als Medienzusatz bei der Zellkultivierung eingesetzt wird, adsorbieren auf der Materialoberfläche.

*PERSÖNLICHER BEITRAG:* Durchführung der ζ-Potenzial-Messungen (Strömungspotenzial) der Oberflächen-modifikationen am elektrokinetischen SurPASS™ Messgerät (Anton Paar GmbH) mit Polypropylenimin (PPI) Dendrimeren der Generationen 2 und 4 sowie Polyethylenimin (PEI) Polymeren; Manuskript Review.

## 4.4 PUBLIKATION IV: ζ-POTENZIAL ABHÄNGIGE ZELLAUSBREITUNG

*HINTERGRUND:* Um geeignete Beschichtungen für Biomaterialien zu entwickeln, ist ein fundiertes Wissen zur Zell-Material-Interaktion unerlässlich. Obwohl sich zahlreiche Forschungsgruppen mit diesem Thema beschäftigen, ist der "Zell-Material-Kommunikationscode" nicht vollständig entschlüsselt. Betrachtet man beispielsweise die Benetzbarkeit einer Oberfläche, so weist die Literatur darauf hin, dass hydrophile Oberflächen die Zelladhäsion fördern. Jedoch werden auch kontroverse Ergebnisse berichtet. In dieser Studie wurde das Augenmerk auf das ζ-Potenzial gelegt, als ein möglicher dominierender Faktor für das Zellverhalten an der Materialgrenzfläche. Es sollten erste Hinweise gesammelt werden, ob positive Ladungen generell Zellfunktionen begünstigen können. Daher wurde der zeitliche Verlauf der Zellausbreitung humaner Osteoblasten von 1 h bis 24 h auf funktionalisierten Ti-Oberflächen mit unterschiedlichen Oberflächenladungen untersucht und Daten beispielhafter Oberflächen mit negativer (Ti, PSS), moderat positiver (PPAAm) und stark positiver Ladung (PDADMA) publiziert. Im Folgenden werden die Ergebnisse aller 12 untersuchten Oberflächen beschrieben.

*ERGEBNISSE:* Die Zellausbreitung der MG-63 Osteoblasten richtete sich stark nach dem ζ-Potenzial der Oberflächen (**Abb. 7**). **Abbildung 7A** zeigt die Zellfläche nach 1 h und 24 h auf unterschiedlich geladenen Oberflächen, **Abbildung 7B** die Kreisförmigkeit. Hierbei wird ein perfekter Kreis durch einen Wert von 1,0 und ein zunehmend lang gestrecktes Polygon durch einen gegen 0 konvergierenden Wert beschrieben. Nach 1 h Kultivierung zeigten Oberflächen mit moderat positivem ζ-Potenzial (+1 mV bis +10 mV) die größte Zellfläche, während die Kreisförmigkeit der Zellen noch auf allen Oberflächen erhöht war (0,6 bis 0,8). Nach 24 h wiesen Oberflächen mit negativen (-120 mV bis -3 mV) und moderat positiven Ladungen kaum Unterschiede in der Zellfläche auf, wohingegen sich die Fläche auf stark positiven Oberflächen (+50 mV bis +55 mV), nach anfänglich besserer Ausbreitung als auf negativen Oberflächen, drastisch reduzierte. Die Kreisförmigkeit lag zwischen 0,7 und 0,8 (im Vergleich zu 0,3 bis 0,5 der negativen und moderat positiven Oberflächen). Der Rückgang der Zellfläche auf PPI-G4-modifizierten Oberflächen war im Zeitraum von 12 h bis 24 h am deutlichsten (0,3-fach, **Abb. 8**). Bei PDADMA-modifizierten Oberflächen erfolgte die Abnahme der Zellfläche bereits nach 1 h. Hier war der Flächenverlust zwischen 1 h und 3 h am stärksten (0,5-fach, Publikation IV).

*FAZIT:* Das ζ-Potenzial spielt für die zeitliche Zellausbreitung und die Zellform eine entscheidende Rolle. Humane MG-63 Osteoblasten scheinen hierbei jedoch nur einen bestimmten Bereich des ζ-Potenzials im moderat Positiven zu favorisieren. Die Oberflächenbenetzbarkeit (WCA, SFE) stellt eine eher untergeordnete Rolle dar.

*PERSÖNLICHER BEITRAG:* Versuchsplanung und -durchführung, Datenerhebung, -auswertung und -visualisierung von insgesamt 12 Materialoberflächen (davon vier in Publikation IV veröffentlicht); Koordination der Kooperationen mit dem SFB Teilprojekt A04 der Universität Greifswald (Prof. C. A. Helm),

dem Leibniz-Institut für Plasmaforschung und Technologie e. V. (INP) in Greifswald (Dr. K. Fricke), der Industrieforschungseinrichtung INNOVENT e. V. in Jena (Dr. M. Schnabelrauch) und der Universität Regensburg (Prof. R. Müller); Manuskriptpräparation.

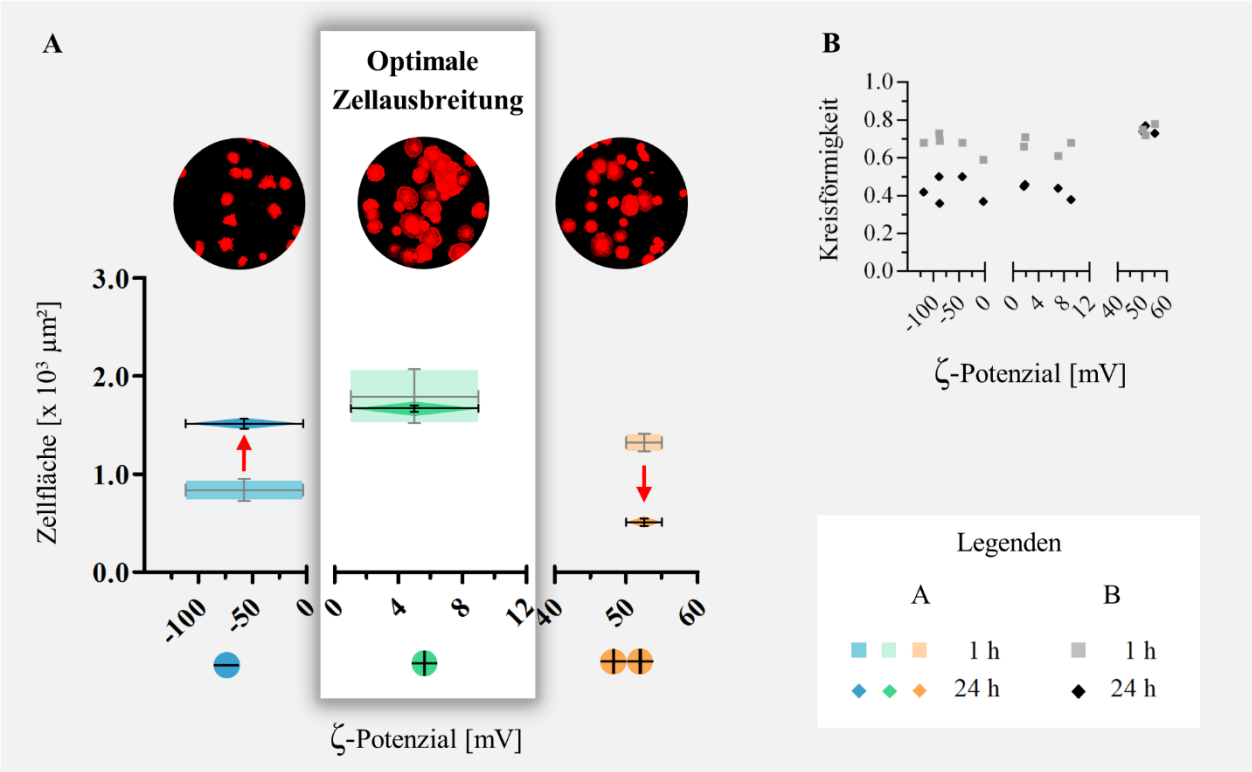


***Abbildung 7: ζ-Potenzial abhängiger Verlauf der zeitlichen Zellausbreitung.*** *(A) Osteoblasten auf moderat positiven Oberflächen (+1 mV bis +10 mV) weisen nach 1 h die höchste Zellfläche auf (1791 ± 275 µm²). Diese Zellfläche ändert sich innerhalb von 24 h nur geringfügig (1669 ± 66 µm²). Zellen auf negativ geladenen Oberflächen (-120 mV bis -3 mV) besitzen zunächst eine geringere Zellfläche nach 1 h (838 ± 114 µm²), breiten sich jedoch innerhalb von 24 h so aus, dass sie das gleiche Niveau der Zellen auf moderat positiven Oberflächen erreichen (roter Pfeil, 1513 ± 108 µm² nach 24 h). Zellen auf stark positiven Oberflächen (+50 mV bis +55 mV) zeigen eine anfängliche signifikant bessere Ausbreitung (1321 ± 89 µm²) als auf negativen Oberflächen, doch nimmt die Fläche innerhalb von 24 h stark ab (roter Pfeil, 510 ± 65 µm² nach 24 h). (B) Während die Zellform auf negativen und moderat positiv geladenen Oberflächen innerhalb von 24 h von kreisförmig zu einer langgestreckteren Form wechselt, weisen Zellen auf stark positiv geladenen Oberflächen eine gestörte Zellausbreitung auf und behalten ihre kreisförmige Morphologie bei. Darstellung: Beispielhafte mikroskopische Aufnahmen PKH26 gefärbter Zellen nach 1 h auf Ti, PPAAm und PDADMA; Zellfläche nach 1 h und 24 h sowie ζ-Potenziale in Mittelwerte ± SD; Kreisförmigkeit nach 1 h und 24 h in Mediane; negativ geladene Oberflächen: Au, PSS, Ti, Matrigel und Col I; moderat positiv geladene Oberflächen: RGD, APTES, PPAAm und PEI; stark positiv geladene Oberflächen: PPI-G4, PDADMA und PPI-G2. (Statistik nicht in Abbildung enthalten: Mann-Whitney-U Test, $p < 0.05$, Signifikanzen nach 1 h: - vs. + und - vs. ++; Signifikanzen nach 24 h: - vs. ++ und + vs. ++).*

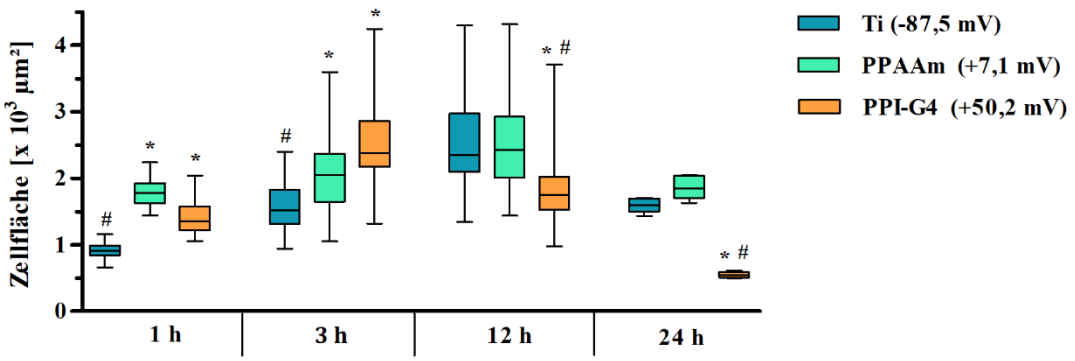


***Abbildung 8: Zeitlicher Verlauf der Zellausbreitung auf PPI-G4 im Vergleich zu Ti und PPAAm in Anlehnung der Publikation IV.*** *Zellen auf PPI-G4 breiten sich nach 1 h signifikant besser aus als auf Ti. Ab 3 h tritt jedoch eine drastische Reduktion der Zellfläche ein. (Darstellung: Mediane ± IQR mit Maximum und Minimum; Kruskal-Wallis + Dunn's, $p < 0.05$, * Signifikanz zu Ti und # Signifikanz zu PPAAm; n = 3 unabhängige Experimente).*

### 4.5 PUBLIKATION V: ζ-POTENZIAL ABHÄNGIGE $Ca^{2+}$-MOBILISIERUNG UND ZELLVIABILITÄT

*HINTERGRUND:* Die vorherige Studie IV zeigte, dass positive Ladungen an der Materialgrenzfläche nicht generell die Zellausbreitung begünstigen können. Daher bestand Grund zur Annahme, dass dies auch auf weitere Zellaktivitäten zutrifft. In dieser Studie wurde daher die intrazelluläre $Ca^{2+}$-Dynamik, metabolische Aktivität, Membranintegrität und Proliferation humaner MG-63 Osteoblasten nach einer Kultivierungsdauer von 24 h auf funktionalisierten Ti-Oberflächen (Aminopolymere, EZM-Proteine & Peptidmotive, PEM) mit einem breiten Spektrum an ζ-Potenzialen vom Negativen (-90 mV bis -3 mV), moderat Positiven (+1 mV bis +10 mV) bis zum stark Positiven (~50 mV) untersucht. Nachfolgend werden die $Ca^{2+}$-Mobilisierungsergebnisse bezüglich eines ζ-Potenzialbereichs von -120 mV bis +55 mV dargestellt (zusätzliche Daten der Ti-Modifikationen mit Au (- 120 mV) und PPI-G2 (+ 55 mV) sind im verlinkten Mendeley Dataset[66] zu finden).

*ERGEBNISSE:* Ein Anstieg des intrazellulären $Ca^{2+}$-Signals ($Ca^{2+}$-Mobilisierung, $MFI_{A-B}$) auf den Oberflächen wurde durch externe ATP-Stimulation ausgelöst und berechnete sich aus der Differenz der mittleren Fluoreszenzintensität *nach* Stimulation ($MFI_A$, A für engl. *after*) und der mittleren *basalen* Fluoreszenzintensität ($MFI_B$, B für *basal*). Eine signifikante Verbesserung der intrazellulären $Ca^{2+}$-Mobilisierung wurde auf Oberflächen mit moderat positiven (955 ± 146 $MFI_{A-B}$) im Vergleich zu negativen ζ-Potenzialen (426 ± 55 $MFI_{A-B}$) erreicht (**Abb. 9**). Dramatische Verluste der Zellaktivität wurden auf Oberflächen mit einem stark positiven ζ-Potenzial beobachtet. Auf diesen Oberflächen war die $Ca^{2+}$-Dynamik deutlich gestört; die Zellen konnten kaum auf eine externe ATP-Stimulation reagieren (52 ± 68 $MFI_{A-B}$). Darüber hinaus wies der MTS-Test auf eine Reduktion der metabolischen Aktivität zwischen 10% (PPI-G4) und 23% (PDADMA) im Vergleich zu Ti hin. Die Lebend/Tot-Färbung zeigte, dass einige Zellen auf PPI-G4- und PDADMA-funktionalisierten Oberflächen ihre Membranintegrität verloren. Zusätzlich konnte dokumentiert werden, dass die Proliferation im Vergleich zu Ti zwischen 12% (PPI-G4) und 40% (PDADMA) abnahm, während der Zellanteil in der G1-Phase um 14% (PPI-G4) beziehungsweise 40% (PDADMA) stieg und somit ein G1-Arrest vorlag.

*FAZIT:* Diese systematische Studie bestätigt die Vermutung, dass Zellen keine positiven Ladungen im Allgemeinen, sondern nur moderat positive ζ-Potenziale favorisieren. Das Zellverhalten der MG-63 Osteoblasten hängt stark von dem ζ-Potenzial der Materialoberfläche, weniger von der Benetzbarkeit (WCA, SFE), ab. Schlussfolgernd erscheint das ζ-Potenzial als einer der Schlüsselparameter für die Zellinteraktion an der Biomaterialgrenzfläche und sollte bei der Entwicklung neuer Beschichtungen für dentale und orthopädische Implantate berücksichtigt werden.

*PERSÖNLICHER BEITRAG:* Versuchsplanung und -durchführung, Datenerhebung, -auswertung und -visualisierung von insgesamt 12 Materialoberflächen (davon 10 in Publikation V veröffentlicht); Koordination der Kooperationen mit dem SFB Teilprojekt A04 der Universität Greifswald (Prof. C. A. Helm), dem Leibniz-Institut für Plasmaforschung und Technologie e. V. (INP) in Greifswald (Dr. K. Fricke), der

Industrieforschungseinrichtung INNOVENT e. V. in Jena (Dr. M. Schnabelrauch) und der Universität Regensburg (Prof. R. Müller); Manuskriptpräparation.

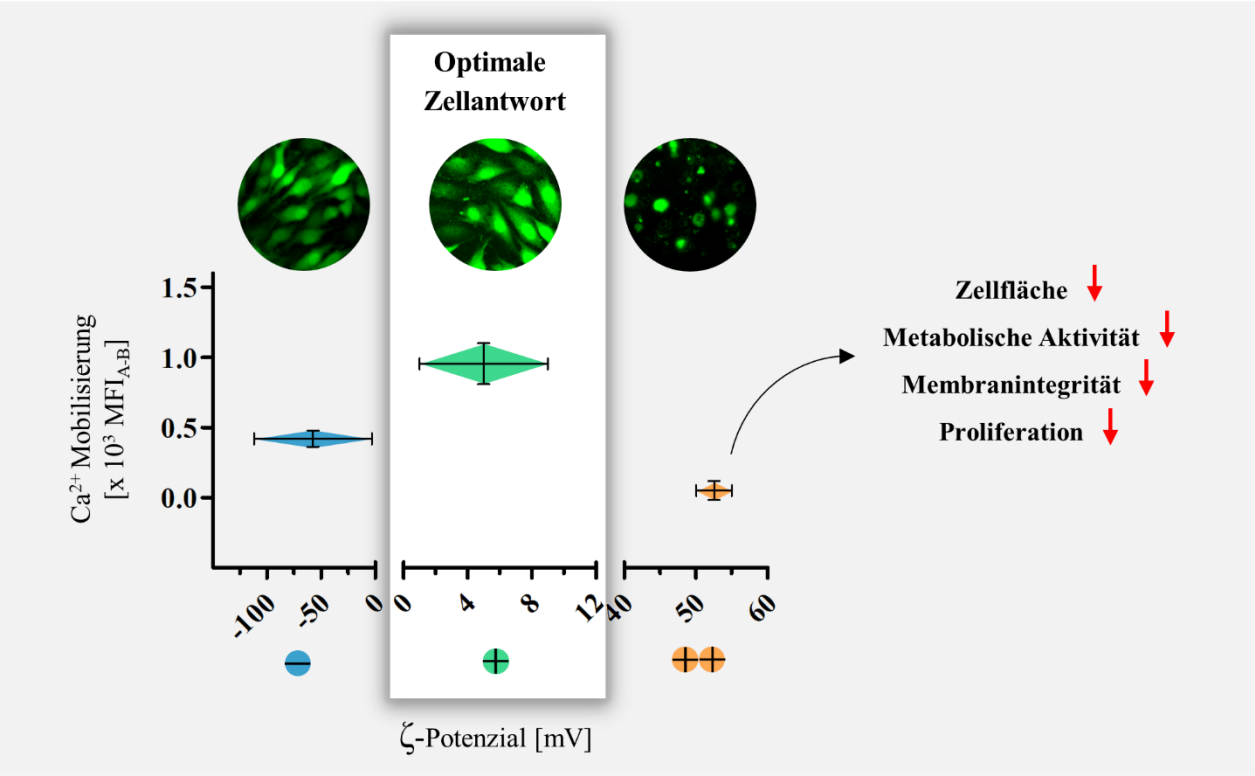


***Abbildung 9: ζ-Potenzial abhängige $Ca^{2+}$-Dynamik und Zellviabilität.*** *Zellen auf moderat positiven Oberflächen (+1 mV bis +10 mV) weisen eine signifikant bessere intrazelluläre $Ca^{2+}$-Mobilisierung nach ATP-Stimulation auf, als Zellen auf negativ geladenen Oberflächen (-120 mV bis -3 mV). Stark positive Oberflächenladungen (+50 mV bis +55 mV) führen zu dramatischen Verlusten der Zellaktivität und gestörten Zellfunktionen. Dies manifestiert sich in einer signifikant reduzierten $Ca^{2+}$-Mobilisierung sowie einer Reduktion der Zellfläche, Viabilität, Membranintegrität und Proliferation. Darstellung: Beispielhafte mikroskopische Aufnahmen Fluo-3 gefärbter Zellen nach 24 h; $Ca^{2+}$-Mobilisierung in Mittelwerte ± sem und ζ-Potenziale in Mittelwerte ± SD; negativ geladene Oberflächen: Au, PSS, Ti, Matrigel und Col I; moderat positiv geladene Oberflächen: RGD, APTES, PPAAm und PEI; stark positiv geladene Oberflächen: PPI-G4, PDADMA und PPI-G2. (Statistik nicht in Abbildung enthalten: Mann-Whitney-U-Test, $p < 0.05$, alle paarweisen Vergleiche zeigten Signifikanzen).*

# 5 DISKUSSION

Oberflächeneigenschaften beeinflussen das Schicksal der Zellen, indem sie initiale zelluläre Prozesse wie Anhaftung, Adhäsion und Ausbreitung an der Grenzfläche steuern[24]. Diese wirken sich weiter auf andere Zellaktivitäten wie Proliferation, Differenzierung[81] und intrazelluläre Signalübertragung[82,83] aus. Die Stimulation des Zellverhaltens durch Modifikation der Oberflächeneigenschaften wie Topographie, Elastizität, Benetzbarkeit und Bioaktivität stellt eine gute Möglichkeit dar, die Knochenregeneration zu beschleunigen[30]. Frühere Studien haben gezeigt, dass Osteoblasten nur bestimmte Bereiche dieser Eigenschaften bevorzugen[25], wie eine der Knochenoberfläche ähnliche Rauigkeit im Nanometer-bereich[11,84–86], Porengrößen von 100 bis 700 µm[19,87], eine mäßig hydrophile Benetzbarkeit mit Kontakt-winkeln zwischen 40 und 65°[78,79,81] oder auch spezifische EZM-Proteine wie Kollagen, Fibronektin, Laminin und Vitronektin[25,88,89], ihre RGD-Sequenz[79] sowie Zytokine wie bFGF (engl. *basic fibroblast growth factor*)[90].

Welchen Effekt aber hat die Oberflächenladung auf die Zell-Material-Interaktion? Dies wurde in der vorliegenden Arbeit anhand eines breiten Spektrums an ζ-Potenzialen durch chemische Modifikationen eines Ti-basierten Materials untersucht. Zellen in lebendem Knochengewebe sind von einem elektrisch geladenen, organisch-anorganischen Festkörper umgeben, durchdrungen von einem mit ionischer Lösung gefüllten komplexen Kanalsystem[91]. Daher kann die Physiologie der Knochenzellen auch auf künstlichen Materialoberflächen durch elektrische Signale beeinflusst werden. Wie Massen ein Schwerefeld, heiße Körper ein Temperaturfeld und Wasserquellen ein Strömungsfeld generieren, so erzeugen Ladungen ein elektrisches Feld in ihrer Umgebung[92]. Bei der Annäherung zweier geladener Oberflächen (Material- und Zelloberfläche) wird eine Kraft zwischen ihnen erzeugt. Oberflächen, die die gleiche Polarität aufweisen, stoßen einander ab, und diejenigen, die eine entgegengesetzte Polarität aufweisen, ziehen einander an (Coulomb-Kraft[93]). Dabei ist die elektrische Kraft zwischen ihnen wesentlich größer als die Gravitation[92]. Insofern erscheint es nur logisch, dass elektrostatische Kräfte für die Zellanhaftung und -adhäsion auf Materialoberflächen von großer Bedeutung sind[94].

Die am häufigsten verwendete[94] und gut geeignete Technik[67], um die Materialoberflächenladung zu bestimmen, ist die Messung des ζ-Potenzials, dass das Ladungsverhalten an der Grenze zwischen Materialoberfläche und wässriger Phase beschreibt. Frühere Studien haben sich meist entweder mit einem begrenzten Bereich des ζ-Potenzials befasst[95–97] oder eine eindeutige Bestimmung der Ladung fehlte[98–101], sodass detaillierte Aussagen über dessen Einfluss auf die Zell-Material-Interaktion bis jetzt nicht möglich waren.

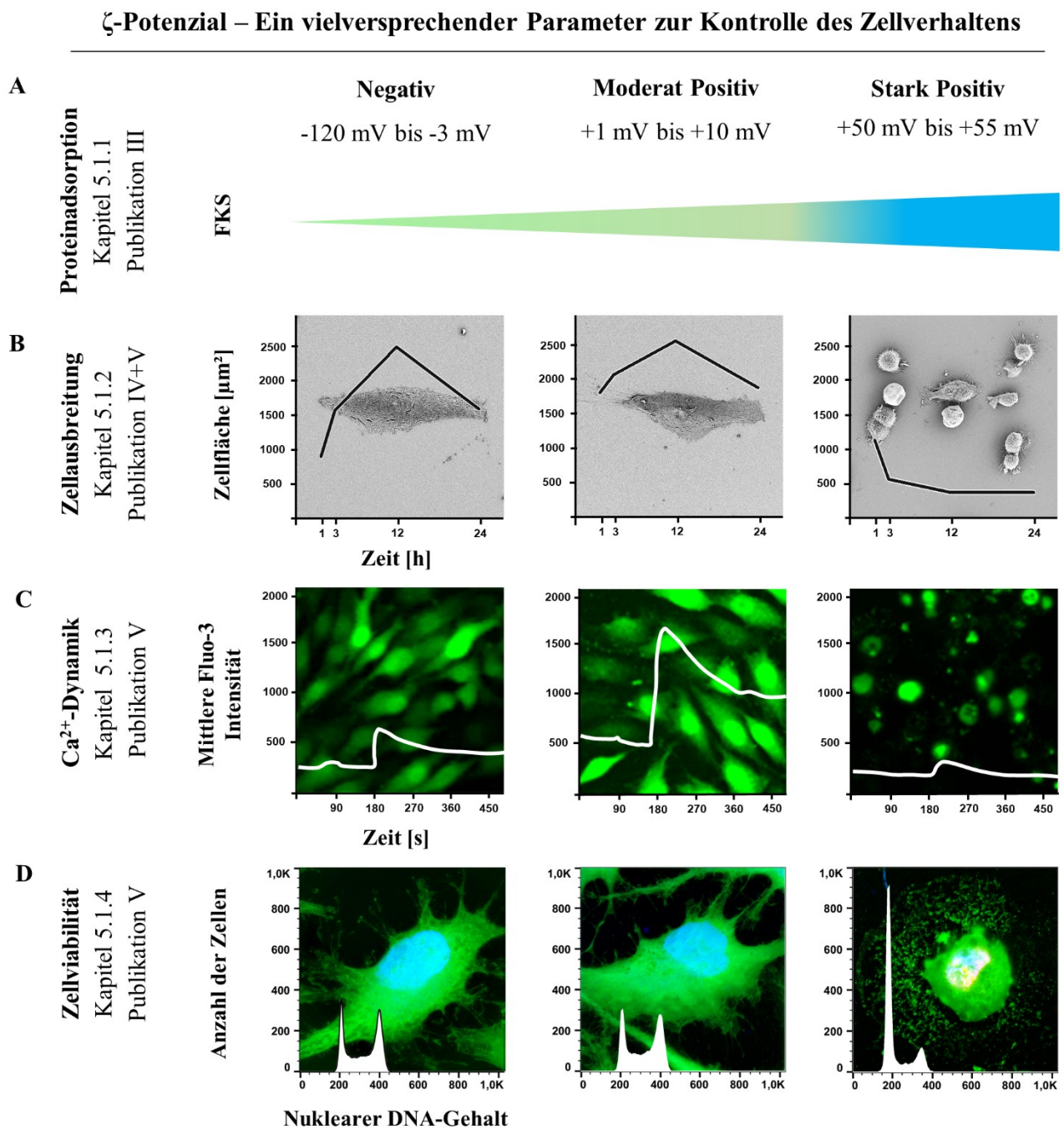


***Abbildung 10:*** **Übersicht der Diskussionsthemen zum Effekt des ζ-Potenzials auf die Proteinadsorption sowie die Zellphysiologie und -morphologie von Osteoblasten.** *Hier zusammengefasst sind die Ergebnisse im Bereich von -120 mV bis +55 mV der (A) Proteinadsorption am Beispiel von FKS (BCA-Assay durchgeführt von Jutta Lehnfeld, Uni Regensburg), der (B) Zellmorphologie nach 24 h (REM-Aufnahmen) sowie des Verlaufs der Zellausbreitung von 1 bis 24 h (PKH26-Membranfärbung, Fluo-3-Färbung), der (C) $Ca^{2+}$-Dynamik nach 24 h ($Ca^{2+}$-Imaging Technik am LSM von vitalen Fluo-3 gefärbten Zellen: basales $Ca^{2+}$-Signal bis 180 s und intrazelluläre $Ca^{2+}$-Mobilisierung nach ATP-Stimulation zum Zeitpunkt von 180 s) und (D) der Zellviabilität (Zellzyklus-Histogramm mittels Durchflusszytometrie mit LSM-Aufnahmen der Membranintegrität von Calcein und EtHD-1 gefärbten Zellen). Die zellbiologischen Ergebnisse in B-D sind auf Ti, PPAAm und PDADMA als Repräsentation der negativ, moderat positiv und stark positiv geladenen Oberflächen dargestellt.*

## 5.1 ζ-Potenzial – Ein vielversprechender Parameter zur Kontrolle des Zellverhaltens

Jahrelange Forschung mit einer außergewöhnlich zellattraktiven plasmapolymerisierten Nanoschicht aus Allylamin (PPAAm) zeigte, dass diese Modifikation auf verschiedensten Materialien zu einem positiven ζ-Potenzial und einer verbesserten Zellantwort führte (**Publikation I**). Daher entstand die Frage, ob das ζ-Potenzial ein entscheidender Faktor für die Zell-Material-Interaktion ist und ob positive Oberflächen generell die Zellfunktionen verbessern. Oder gibt es auch hier nur einen bestimmten optimalen Bereich des ζ-Potenzials für Osteoblasten? Die zellbiologischen Untersuchungen haben gezeigt, dass man die Oberflächenladungen anhand der Zellreaktionen in 3 Kategorien einteilen konnte: negativ (-120 bis -3 mV), moderat positiv (+1 bis +10 mV) und stark positiv (+ 50 bis +55 mV). Die Ergebnisse werden im Folgenden bezüglich des Effekts auf die Proteinadsorption, Zellausbreitung (Zellfläche und Zellform), $Ca^{2+}$-Dynamik sowie Zellviabilität (Metabolismusaktivität, Membranintegrität, Zellzyklus) diskutiert (**Abb. 10**).

### *5.1.1 Vermehrte Proteinadsorption von FKS mit zunehmend positivem ζ-Potenzial*

Bevor Zellen die Oberfläche erreichen, findet eine Adsorption von Proteinen wie Fibronektin, Kollagen oder Albumin aus der physiologischen Lösung statt, die als Signalgeber fungieren und die Anheftung und Proliferation von Zellen vermitteln[102]. Die Proteinadsorption wurde quantitativ von Jutta Lehnfeld an der Universität Regensburg in Bezug auf ein ζ-Potenzialbereich (Strömungspotenzial) von -90 bis +48 mV mittels BCA Test (engl. *bicinchoninic acid*) in einfacher Form mit Modelproteinen in gepufferter Salzlösung (HSA und Lysozym) und in viel komplexerer Form mit physiologischen Lösungen (Speichel und FKS), die Hunderte von verschiedenen Proteintypen enthalten[26], bestimmt (**Publikation III**).

Es konnte gezeigt werden, dass die Proteinadsorption an der Oberfläche (Proteinmenge und -population) hauptsächlich durch elektrostatische Effekte dominiert wird und stark vom ζ-Potenzial abhängig ist. Tendenziell gilt für physiologische Lösungen mit vorwiegend negativ geladenen Proteinen wie FKS (ungebundene Proteine mit Ladungen von -7 mV[103]): Je positiver das ζ-Potenzial der Oberfläche, desto stärker die Proteinadsorption. Dies konnte auch für Einzelproteine wie Fibronektin[104] oder BSA (engl. *bovine serum albumin*)[105,106], einer der Hauptbestandteile von FKS[107], gezeigt werden.

Hinsichtlich der Benetzbarkeit (WCA, SFE) konnte in dieser Studie keine Korrelation zur Proteinmenge beobachtet werden. Nichtsdestoweniger ist bekannt, dass die Benetzbarkeit einen Einfluss auf die Konformation der Proteine hat. Diese liegen auf hydrophilen Oberflächen in einer nativen und flexiblen Konformation vor[108], die für die Integrine gut zugänglich ist[81], während hydrophobe Oberflächen zur Proteinentfaltung führen können[109,110], bei der RGD-Sequenzen für die Integrine nicht oder nur begrenzt präsentiert werden[81]. Dies kann dann in einer instabilen Schicht auf der Materialoberfläche mit unnatürlichen Proteinstrukturen resultieren, die eine fibröse Einkapslung des Implantats verursachen kann[16]. Auch Ladungen

an der Materialoberfläche können die spezifische Struktur der adsorbierenden Proteine durch Wechselwirkungen mit Wasserstoff- und Salzbrücken verändern und zu einer Proteinentfaltung führen[26].

Was letztendlich an der Materialoberfläche passiert ist allerdings nicht so trivial und einfach vorherzusagen[111]. Denn die Ladung der ionisierbaren Gruppen der Proteine ist nicht konstant, sondern wird durch die lokale elektrostatische Umgebung beeinflusst[112–114]. Sind die Ionen in der entfernteren Lösung und nahe der Materialgrenzfläche ungleichmäßig verteilt, verschiebt sich der pH-Wert. Dies führt zu einer anderen Proteinladung nahe der Materialoberfläche als aufgrund der Proteineigenschaften in entfernterer Lösung erwartet. Infolgedessen resultiert eine andere elektrostatische Affinität des Proteins zur Oberfläche[112].

### *5.1.2 OPTIMALE ZELLAUSBREITUNG IM BEREICH DES MODERAT POSITIVEN ζ-POTENZIALS*

Die Zellanhaftung und -ausbreitung ist entscheidend für das weitere Zellverhalten. Um die Fragen zu beantworten, ob positive Oberflächenladungen generell Zellfunktionen begünstigen oder ob ein bestimmter Bereich des ζ-Potenzials von Osteoblasten bevorzugt wird, wurde im ersten Schritt dieser Arbeit die Zellmorphologie (Größe und Form) anhand einer 24-stündigen Analyse PKH26 (1-12 h) und Fluo-3 (24 h) gefärbter Zellen untersucht (**Publikationen IV, V**). Nach 24 h erfolgten zusätzlich REM-Aufnahmen der Zellen auf ausgewählten Oberflächen (**Publikation V**).

Es konnte gezeigt werden, dass MG-63 Osteoblasten grundsätzlich eine anfängliche Tendenz zur schnelleren Ausbreitung auf positiv geladenen im Vergleich zu negativ geladenen Oberflächen aufwiesen. Im Frühstadium der Osseointegration können Osteoblasten mit ihrer negativ geladenen Hyaluronsäurehülle[33] an den positiv geladenen Materialoberflächen anhaften. Aber nicht nur Osteoblasten sind negativ geladen[33], sondern Säugetierzellen im Allgemeinen besitzen aufgrund geladener Bestandteile der Glykolipide und -proteine in der Glykokalyx eine negative Nettoladung[115,116]. Daher ist es nicht verwunderlich, dass in der Literatur auch bei anderen Zelltypen eine Verstärkung der Zelladhäsion und -ausbreitung durch positive Oberflächenladungen zu finden ist. Chang et al.[97] dokumentierten die stärkere Ausbreitung von NIH/3T3-Fibroblasten mit steigendem ζ-Potenzial von -187 mV und +6 mV auf SAM-modifizierten Au-Substraten. Auch endotheliale HEC-Zellen auf Polymeroberflächen (ζ-Potenzial: +4 mV und +5 mV vs. -41 mV)[117] und humane mesenchymale Stammzellen auf PAMAM modifizierten alginat-basierten Hydrogelen (ζ-Potenzial: +12 mV vs. -22 mV)[103] zeigten eine ähnlich gute Zellausbreitung auf den positiv geladenen Oberflächen. Jedoch beinhaltet keine dieser Studien Daten zur Zellausbreitung auf Oberflächen in dem hier definierten stark positiven ζ-Potenzialbereich (+ 50 bis +55 mV).

Interessanterweise konnte in dieser Arbeit bei Osteoblasten auf stark positiven Oberflächen eine drastische Reduktion der Zellfläche innerhalb von 24 h gezeigt werden, während auf negativen und moderat positiven Oberflächen nach 24 h ein langgestreckt ausgebreiteter Phänotyp mit ähnlichen Zellflächen vorzufinden war. Dies lieferte erste Hinweise, dass Zellfunktionen nicht generell durch positive Ladungen gefördert werden, sondern die Zellphysiologie auf stark positiv geladenen Oberflächen eingeschränkt wird.

Die Zellen wiesen auf stark positiven Oberflächenladungen vorwiegend eine kreisförmige bis kugelige Morphologie auf, bei Letzteren teilweise mit fehlender Mikrovillistruktur (beobachtet bei PDADMA). Apikale Mikrovilli sind mit Aktin durchzogene membranöse Fortsätze der Zellmembran und dienen normalerweise der Oberflächenvergrößerung für wichtige Sekretions-, Transport- und Enzymaktivitäten[118]. Bei Osteoblasten sind sie vor allem für die Mineralisierung während der Knochenbildung und -entwicklung wichtig[121]. Während verkürzte Mikrovilli auf eine Reduktion der metabolischen Aktivität hinweisen können[121], wird ein dauerhaftes Verschwinden dieser Strukturen als eines der frühen Ereignisse in der Apoptose angesehen[119,122].

### *5.1.3 Gesteigerte $Ca^{2+}$-Mobilisierung im Bereich des moderat positiven ζ-Potenzials*

Als sekundärer Botenstoff reguliert $Ca^{2+}$ auch in Osteoblasten[42] zahlreiche zelluläre Prozesse wie die Ausbildung fokaler Adhäsionen, Proliferation oder Differenzierung, aber auch pathologische Ereignisse wie Zellschädigung oder Apoptose[43]. Die Messung von zytoplasmatischem $Ca^{2+}$ kann wesentlich zum Verständnis von normalen und abnormalen Zellfunktionen beigetragen[39].

In **Publikation II** konnte gezeigt werden, dass die intrazelluläre $Ca^{2+}$-Dynamik ein sensitiver Parameter ist, der die Zellphysiologie auf Biomaterialoberflächen reflektieren kann. $Ca^{2+}$-Signalkaskaden sind bei der Transmission externer Reize in die Zelle für die zellphysiologischen Prozesse von wesentlicher Bedeutung. In vorangegangenen Studien wurden Osteoblasten auf topographischen Pfostenstrukturen kultiviert und zeigten Veränderungen im Aufbau des Aktinzytoskeletts, welches geclustert auf den Pfosten vorlag, sowie eine reduzierte Zellaktivität, die durch ein verringertes $Ca^{2+}$-Mobilisierungsvermögen nach ATP-Stimulation widergespiegelt werden konnte[83]. Mörke et al.[123] fanden heraus, dass es sich hierbei um eine versuchte Phagozytose der fixierten Pfosten durch die Zellen handelte – ein sehr energieaufwendiger und stress-induzierender Prozess mit Auswirkungen auf die Zellaktivität. Beschichtete man allerdings diese Pfostenstrukturen mit PPAAm wurden die eingeschränkten Zellfunktionen gemildert, was sich wiederum in einer gesteigerten $Ca^{2+}$-Mobilisierung bemerkbar machte[80]. Osteoblasten reagierten auch auf eine Modifizierung planarer Ti-Oberflächen mit PPAAm im Vergleich zur unbeschichteten Ti-Kontrolle mit einer erhöhten Zellaktivität, begleitet durch eine gesteigerte $Ca^{2+}$-Mobilisierung sowohl in MG-63 als auch in primären Osteoblasten (**Publikation II**).

Folglich wurde im zweiten Schritt dieser Arbeit die Fähigkeit zur intrazellulären $Ca^{2+}$-Mobilisierung auf verschiedenen Oberflächenladungen analysiert, um den Effekt des ζ-Potenzials auf die Zellphysiologie weiter zu untersuchen. Hierfür konnte in **Publikation V** zunächst die $Ca^{2+}$-Messmethode in Bezug auf den Einsatz der ATP-Konzentration als Stimulanz, den Nachweis von ATP-Rezeptoren in der Zellmembran ($P2Y_2$ und $P2X_7$) sowie die Herkunft der $Ca^{2+}$-Ionen nach ATP-Stimulation (extrazellulär oder intrazellulär) näher spezifiziert werden. Anschließend erfolgte die Untersuchung des basalen $Ca^{2+}$-Signals auf den Kontrolloberflächen Ti und PPAAm nach 1 h und 24 h mittels BacMam-Methode (Vitalfärbung von $Ca^{2+}$, Aktin und dsDNA). Die intrazelluläre $Ca^{2+}$-Mobilisierung in vitalen Fluo-3 gefärbten Zellen wurde auf allen

Oberflächenmodifikationen am LSM analysiert, um tiefere Einblicke in die Wirkung der Oberflächen-ladungen auf die Zellphysiologie zu gewinnen. Im Folgenden werden die Ergebnisse diskutiert.

Zahlreiche Substanzen (darunter beispielsweise das Nebenschilddrüsenhormon PTH, Vitamin D3 oder Prostaglandin), die den Knochenumbau beeinflussen, können die intrazelluläre $Ca^{2+}$-Konzentration in Osteoblasten verändern[124]. Es wird jedoch angenommen, dass extrazelluläres ATP eine wichtige Rolle in der Knochenbiologie spielt, indem es die Funktion der Osteoblasten durch Erhöhung des zytosolischen $Ca^{2+}$-Spiegels moduliert[125,126]. Extrazelluläres ATP übt seine Wirkung über eine spezielle Rezeptorfamilie namens P2-Purinozeptoren aus[127,128], bestehend aus zwei Unterfamilien: P2Y (G-Protein-gekoppelte Rezeptoren) und P2X (ligandengekoppelte Kationenkanäle)[57]. Um eine direkte intrazelluläre $Ca^{2+}$-Reaktion auszulösen, wurden für die $Ca^{2+}$-Mobilisierungsversuche eine extrazelluläre ATP-Konzentration von 0,5 mM verwendet. Der MTS-Test zeigte, dass eine 20-minütige Inkubation dieser ATP-Konzentration keinen Einfluss auf die Zellviabilität der MG-63 Osteoblasten hatte. Die Ergebnisse wurden dadurch also nicht beeinflusst.

Immunzytochemische Färbungen zeigten sowohl die Anwesenheit von $P2Y_2$- als auch von $P2X_7$-Rezeptoren in MG-63 Zellen. ATP induzierte jedoch die Mobilisierung des intrazellulären $Ca^{2+}$ vorwiegend durch die Aktivierung von $P2Y_2$-Rezeptoren, die apikal exprimiert[129] werden und bekanntermaßen durch Kopplung an Gq-Proteine die Phospholipase $C_\beta$ aktivieren und somit die Produktion von $IP_3$ vermitteln[130,131]. Denn obwohl bei den Osteoblasten auch der ionotrope Purinozeptor $P2X_7$ nachgewiesen wurden, konnten die Mobilisierungsversuche auf Ti unter Ausschluss von extrazellulärem $Ca^{2+}$ im Medium keinen signifikanten Unterschied im Anstieg des freigesetzten intrazellulären $Ca^{2+}$ zeigen.

Es wurde nachgewiesen, dass das ζ-Potenzial einen enormen Effekt auf die intrazelluläre $Ca^{2+}$-Dynamik hat. Oberflächen mit moderat positiven Ladungen fördern die $Ca^{2+}$-Mobilisierung signifikant stärker als negativ geladene Oberflächen. Ein höheres basales $Ca^{2+}$-Level in Zellen auf PPAAm im Vergleich zu unbeschichtetem Ti konnte schon nach 1 h festgestellt werden. Zellen sind in der Lage auf Oberflächen im moderat positiven ζ-Potenzialbereich effektiver auf ihre intrazellulären $Ca^{2+}$-Speicher nach einem externen Stimulus zuzugreifen, sind somit aktiver, können besser auf ihre Umgebung reagieren und mit dem benachbarten Gewebe kommunizieren. Im Gegensatz dazu, stellen stark positive ζ-Potenziale offensichtlich zellphysiologisch große Herausforderungen dar. Zellen konnten diese hohen Ladungen nicht tolerieren und zeigten eine stark gehemmte $Ca^{2+}$-Mobilisierung, was eine Einschränkung der Zellfunktionen betont.

Durch Stress oder Beschädigung der Zelle wird übermäßig viel $Ca^{2+}$ aus dem ER in die Mitochondrien übertragen, was zu einer mitochondrialen $Ca^{2+}$-Überlastung[132,133] und der Freisetzung pro-apoptotischer Faktoren in das Zytosol führen kann[48]. Im folgenden Abschnitt wird der Einfluss der stark positiven Ladungen auf die Zellphysiologie näher diskutiert.

### *5.1.4 Reduzierte Zellviabilität im Bereich des stark positiven ζ-Potenzials*

Um den negativen Effekt von stark positiven Oberflächenladungen weiter zu konkretisieren wurde die Zellviabilität auf den Oberflächen Ti, PPAAm und PPI-G4/PDADMA, die jeweils negative, moderat positive und stark positive ζ-Potenziale verkörpern, mittels MTS-Tests (metabolische Aktivität), Lebend/Tod-Färbung (Membranintegrität) und Zellzyklusanalyse (Proliferation) untersucht (**Publikation V**).

Es konnte die durch die Reduktion der Zellfläche und der $Ca^{2+}$-Mobilisierung vermutete Einschränkung der Zellfunktionen auf stark positiven Oberflächen bestätigt werden. Hier liegt zusätzlich eine verringerte metabolische Aktivität und Proliferation nach 24 h vor. In der Literatur geht man davon aus, dass positive Oberflächenladungen, die in den hier definierten moderaten Bereich fallen, zur Erhöhung der Proliferation und osteogenen Differenzierung beitragen[134,135,103,136]. Dahingegen wurde der Rückgang der Zell-proliferation auf stark positiven Oberflächen durch einen beachtlichen Anstieg der Zellzahl in der G1-Phase begleitet. Während des Zellzyklus verhindern Kontrollpunkte in der G1- und G2-Phase die weitere Proliferation, wenn beispielsweise eine Zellschädigung durch Akkumulation reaktiver Sauerstoffspezies (ROS)[137] oder inadäquate Umweltbedingungen wie bakterielle Infektionen[138], Hypoxie[139] oder Nahrungsmangel[140] vorliegen. Zellen, die diese Sicherheitskontrollen nicht bestehen, gehen in die nicht-proliferative ruhende G0/G1-Phase (Zellzyklus-Arrest) oder sogar in die permanente Seneszenz über[140,141]. Überdies zeigen Guo et al.[142], dass auch bei Fibroblasten nach 24 h auf kationischen Polymerfilmen mit ζ-Potenzialen von +50 mV und +62 mV keine weitere Proliferation erfolgte.

Die stark positive Oberflächenladung führt zu einer intensiven Wechselwirkung mit der negativ geladenen Zelloberfläche[33]. Diese wird als Ursache für geschädigte Lipiddoppelschichten angesehen, da neue vesikuläre Strukturen um die kationischen Moleküle herum entstehen und Löcher in der Zellmembran verursachen[143]. Dies konnte durch die Lebend/Tot-Färbung unterstützt werden, die eine aufgehobene Membranintegrität in noch vitalen Zellen auf stark positiven Oberflächen zeigte – ein Hinweis auf den möglicherweise bevorstehenden Zelltod.

Dieser kann in zwei Klassen unterteilt werden: Apoptose und Nekrose. Bei der energieaufwendigen Apoptose schrumpft die Zelle und die chromosomale DNA sowie der Zellkern werden fragmentiert ohne eine Beschädigung der Plasmamembran. Die tote Zelle wird letztlich in apoptotische Vesikel verpackt und durch phagozytäre Zellen entfernt. Somit ist die Apoptose für das Ausbleiben von Entzündungsreaktionen bekannt. Die Nekrose dagegen ist das Endergebnis einer „bioenergetischen Katastrophe“[144], die aus einer ATP-Erschöpfung resultiert und durch zelluläre Signalwege als Reaktion auf externe Reize wie Zell-beschädigungen oder toxische Einflüsse ausgelöst wird. Die Zellen schwellen an und es kommt zum Zusammenbruch der Membranintegrität. Durch die Freisetzung des Zellinhaltes und proinflammatorischer Moleküle wird eine Entzündungsreaktion induziert[144]. In der vorliegenden Arbeit konnten keine apoptotischen Ereignisse anhand der Zellzyklusanalyse gemessen werden. Allerdings wäre mittels Durchflusszytometrie nur eine späte Apoptosephase bei Vorliegen einer fragmentierten DNA quantifizierbar. Es ist nicht auszuschließen, dass nicht

erfasste frühe apoptotische Events in den geschrumpften Zellen stattfanden, wie das erwähnte Verschwinden der Mikrovillistrukturen bei mehreren Zellen auf PDADMA andeutete. Nichtsdestotrotz könnte man auch von nekrotischen Abläufen ausgehen, da die Membranintegrität einiger Zellen auf Oberflächen mit stark positivem ζ-Potenzial aufgehoben wurde. Tatsächlich waren Membran-überreste der Zellen auf diesen Oberflächen nachzuweisen wie **Abbildung 11** am Beispiel von PDADMA Oberflächen zeigt.

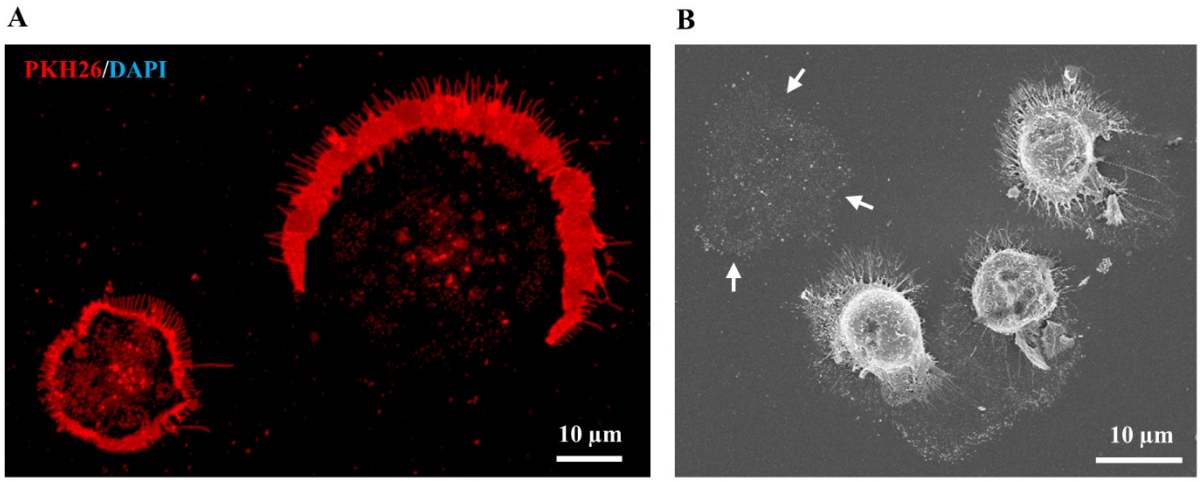


***Abbildung 11: Überreste der Zellen auf PDADMA.*** *(A) Bereits nach 1h können Membranüberreste der PKH26 gefärbten Osteoblasten in Abwesenheit von Zellkernen (fehlende DAPI-Färbung) nachgewiesen werden (Mikroskopische LSM780-Aufnahme mittels C-Apochromat 40x/1.20W Korr M27 Objektiv und ZEN black Software 2011 SP4, Carl Zeiss).(B) Nach 24 h sind die Membranüberreste sowohl bei Zellen mit reduzierter Zellfläche als auch nach kompletter Zellablösung (weiße Pfeile) zu erkennen (REM-Aufnahme mittels FE-SEM Merlin VP compact, InlenseDuo Scanner, Vergrößerung 500x).*

Da apoptotische Zellen in Abwesenheit von Phagozytose in eine sekundäre Nekrose übergehen, die viele morphologische Merkmale der primären nekrotischen Zellen aufweist, wie das Anschwellen des ER, der Mitochondrien und des Zytoplasmas, ist es allerdings oft schwer diese beiden Prozesse voneinander zu unterscheiden. Zudem haben sekundär nekrotische Zellen bereits ein apoptotisches Stadium durchlaufen und besitzen kondensierte oder fragmentierte Zellkerne.[145]

Einen kleinen Einblick in den möglichen Ablauf beim Einsatz von stark positiv geladenen Biomaterial-oberflächen in einer *in vivo*-Situation könnte folgende Studie[146] geben, in der Wistar-Ratten durch die Injektion von PPI-G5-Dendrimeren nach 24 h Hämolyse und Gewebedegeneration durch Membran-destabilisierung[147] aufwiesen. Die Zellen und das umliegende Gewebe würden also dramatisch und irreversibel beschädigt.

## 5.2 Fazit und Ausblick

Eine zentrale Frage in der Biomaterialforschung zum Ersatz von Knochengewebe dreht sich um die Verbesserung der Zell-Material-Interaktion und letztlich der Osseointegration mithilfe chemischer Modifikationen der Implantatoberflächen. Eine schnelle und stabile Zelladhäsion und -ausbreitung sowie ein hohes Reaktions- und Kommunikationsvermögen sorgen für eine erfolgreiche Zellansiedlung und Einwachsen des Biomaterials. Als generelles Fazit der vorliegenden Daten gilt, dass die Oberflächenladung, abgeleitet vom ζ-Potenzial, angesichts ihres enormen Effekts auf die Zellphysiologie und –morphologie, ein fundamentaler Faktor für die Zell-Material-Interaktion ist und somit bei der Entwicklung neuer Biomaterialien beachtet werden sollte. In Abhängigkeit von der zellphysiologischen Antwort auf die unterschiedlichen Oberflächenladungen konnten erstmals drei Bereiche des ζ-Potenzials identifiziert werden: negativ (-120 mV bis -3 mV), moderat positiv (+1 mV bis +10 mV) und stark positiv (+50 mV bis +55 mV). Es zeigte sich, dass nicht generell positiv geladene Oberflächen die Zellfunktionen begünstigen, sondern der optimale Bereich für die Zellantwort nur im moderat Positiven liegt.

Das ζ-Potenzial kann zwar als fundamentaler aber nicht als alleiniger, ausschlaggebender Faktor gelten, da die Prozesse an der Schnittstelle zwischen Biomaterial und Organismus sehr komplex und noch nicht vollkommen verstanden sind. Zukünftige Forschungsarbeiten sollten sich daher auf die zugrundeliegenden molekularen Strukturen und Mechanismen konzentrieren, die zu der durch Oberflächenladungen beeinflussten Zellreaktion führen. Dazu könnten folgende Aspekte beitragen:

(I) Erweiterung des ζ-Potenzialbereichs

Ab welcher positiven Ladung tritt der negative Effekt auf die Zellphysiologie ein? Hierzu könnten polyelektrolytische Multischichten dienen, deren Vorteil in einer variablen Schichtanzahl liegt. Während eine PDADMA-endende Multischicht aus nur 3,5 Doppelschichten noch zu einem negativen ζ-Potenzial führt, weist PDADMA mit 10,5 Schichten ein stark positives ζ-Potenzial auf. Man könnte durch Variation der Schichtanzahl somit den Zellen unterschiedliche Oberflächenladungen anbieten und den untersuchten positiven ζ-Potenzialbereich erweitern.

(II) Zusammenhang zwischen Oberflächenladung und Proteinadsorption

Die Adsorption geladener Proteine könnte das ζ-Potenzial der Materialoberfläche beeinflussen. Mit welchen Oberflächenladungen interagieren die Zellen nach Proteinadsorption? ζ-Potenzialmessungen vor und nach Proteinadsorption aus physiologischen Lösungen an modifizierten Oberflächen könnten mehr Klarheit über die Wechselwirkung der Ladung und Proteinadsorption bringen, die letztlich die Zellreaktionen beeinflussen.

(III) Rolle und Ablauf des Zelltods auf Oberflächen mit stark positivem ζ-Potenzial

Die Bestimmung der zytosolischen ATP-Konzentration könnte Aufschluss über den energetischen Zustand der Zellen auf unterschiedlich geladenen Oberflächen geben. Um einen apoptotischen und nekrotischen Zelltod auf

stark positiven Ladungen zu unterscheiden, bedarf es allerdings zeitabhängiger Analysen der Zelltodparameter auf verschiedenen Leveln (morphologisch und biochemisch). Mikroskopische Zeitraffer-aufnahmen der Fluoreszenz von Zellen hinsichtlich spezieller Marker für die Membranintegrität, lysosomale Integrität oder die mitochondriale Depolarisierung könnten den Verlauf der morphologischen und biochemischen Veränderungen festhalten. Des Weiteren können spezifische zelluläre Marker für Apoptose wie die Zytochrom C Freisetzung, die Produktion des Spaltprodukts tBid („*truncated*“ Bid) sowie die Aktivierung der Kaspasen-3/7 oder Marker für Nekrose wie Prokaspasen-3/7, Zytokeratin 18 und das High-Mobility-Group-Protein B1 (HMGB-1) im Überstand der Zellen untersuchen werden.

(IV) Einfluss von Oberflächen mit stark positivem ζ-Potenzial auf die $Ca^{2+}$-Dynamik

Welche Komponenten der $Ca^{2+}$-Dynamik werden durch stark positive Oberflächenladungen gehemmt? Neben der gezielten Inhibition von wichtigen Komponenten wie die Sarko/Endoplasmatische Retikulum-$Ca^{2+}$-ATPase (z.B. durch Thapsigargin) oder $IP_3$-Rezeptoren (durch z.B. Xestospongin C), sind $Ca^{2+}$-sensitive Aequorin-Photoproteine vielversprechende Targets, um spezifische Organellen wie das ER, die Mitochon-drien und den Golgi-Apparat zu adressieren und verschiedene Aspekte der $Ca^{2+}$-Homöostase fluoreszenz-mikroskopisch zu verfolgen.

Diese Arbeit zeigt auf, dass durch eine gezielte Oberflächenmodifikation das ζ-Potenzial als „Fine Tuning“-Werkzeug eingesetzt werden kann, um eine präzisere Zellreaktion zu erhalten. Letztlich könnte dies zu einer erfolgreicheren Implantatintegration und einer längeren Verweildauer des Implantats beitragen.

# 6 ZUSAMMENFASSUNG

Ein tiefgreifendes Verständnis der Prozesse an der Schnittstelle zwischen Biomaterial und Gewebe des Organismus ist entscheidend für die Weiterentwicklung von orthopädischen und dentalen Implantaten. Permanente Implantate sollen spezifische zelluläre Reaktionen mit dem Ziel der Geweberegeneration und der Integrationsbeschleunigung unterstützen. Chemische Oberflächenmodifikationen, die eine Oberflächenladung besitzen, wie die positiv geladene zellattraktive Nanoschicht aus plasmapolymerisiertem Allylamin können Zellfunktionen fördern (Publikation I, II). Die komplexen Zusammenhänge zwischen der Oberflächenladung und dem Zellverhalten wurden jedoch noch nicht vollständig aufgeklärt.

Die vorliegende Arbeit befasste sich daher mit dem Einfluss der Oberflächenladung, abgeleitet vom ζ-Potenzial, auf die Proteinadsorption und insbesondere auf die Interaktion von humanen MG-63 Osteoblasten mit chemisch modifizierten Titan-Oberflächen. Es konnte gezeigt werden, dass die Proteinadsorption hauptsächlich durch elektrostatische Effekte dominiert wird und somit stark vom ζ-Potenzial abhängig war. Je höher das ζ-Potenzial der Oberflächen, desto mehr Proteine der physiologischen FKS-Lösung adsorbierten auf der Materialoberfläche (Publikation III). Dagegen wurde weder für die Proteinadsorption noch für das Zellverhalten ein klarer Zusammenhang mit der Benetzbarkeit der Oberflächen gefunden. Das ζ-Potenzial konnte erstmals in Abhängigkeit von der zellulären Reaktion auf die Ladungen (Zellausbreitung, Zellviabilität, intrazelluläre $Ca^{2+}$-Mobilisierung) in drei Kategorien eingeteilt werden: negativ (-120 bis -3 mV), moderat positiv (+1 bis +10 mV) und stark positiv (+50 bis +55 mV). Für die zeitliche Zellausbreitung, die Zellform und Zellphysiologie spielte das ζ-Potenzial eine entscheidende Rolle. Nach 1 h Kultivierung zeigten Osteoblasten auf Oberflächen mit moderat und stark positivem ζ-Potenzial eine stärkere Zellausbreitung als auf negativ geladenen Oberflächen. Interessanterweise verkleinerte sich jedoch die Zellfläche signifikant auf stark positiv geladenen Oberflächen im zeitlichen Verlauf bis 24 h (Publikation IV). Da die intrazelluläre $Ca^{2+}$-Dynamik ein sensitiver Parameter ist, der die Zellphysiologie auf Biomaterialoberflächen reflektiert (Publikation II), konnte der Effekt des ζ-Potenzials weiter spezifiziert werden. Eine signifikante Verbesserung der intrazellulären $Ca^{2+}$-Mobilisierung nach 24 h wurde auf Oberflächen mit moderat positiven im Vergleich zu negativen ζ-Potenzialen erreicht. Dramatische Verluste der $Ca^{2+}$-Freisetzung wurden auf Oberflächen mit stark positiven ζ-Potenzialen beobachtet. Die deutlich gestörte $Ca^{2+}$-Dynamik korrelierte mit einer Reduktion der metabolischen Aktivität, einer Aufhebung der Membranintegrität und mit einer Proliferationsabnahme bedingt durch einen G1-Arrest (Publikation V).

Diese systematische Arbeit mit insgesamt 12 Oberflächenmodifikationen zeigt die Bedeutung des ζ-Potenzials für die Osteoblastenphysiologie und -funktion. Zusammenfassend konnte gezeigt werden, dass Zellen nur den moderat positiven ζ-Potenzialbereich favorisieren. Das ζ-Potenzial erscheint als einer der Schlüsselparameter für die Zellinteraktion an der Biomaterialgrenzfläche und kann als „Fine Tuning"-Werkzeug eingesetzt werden. Daher sollte es bei der Entwicklung und Charakterisierung neuer Implantatbeschichtungen Berücksichtigung finden.

# 7 SUMMARY

A profound understanding of the processes at the interface between biomaterial and body is crucial for the further development of orthopedic and dental implants. Permanent implants are intended to support specific cellular reactions with the aim of tissue regeneration and acceleration of integration. Chemical surface modifications resulting in a surface charge, such as the positively charged cell-attractive PPAAm nanolayer can promote cell functions (publication I, II). However, the complex relationships between surface charge and cell behavior have not yet been fully elucidated.

Therefore, the present work addressed the impact of the surface charge, deduced from ζ-potentials, on protein adsorption, but especially on the interaction of human MG-63 osteoblasts with chemically modified titanium surfaces. It could be demonstrated that protein adsorption is mainly dominated by electrostatic forces and was therefore strongly dependent on the ζ-potential. The higher the ζ-potential of the surfaces, the more proteins of the physiological FKS solution adsorbed on the material surface (publication III). No correlation could be found for either protein adsorption or cell behavior with the wettability of the surfaces. In contrast, the ζ-potential could for the first time be classified into three categories depending on the cellular response to the charges (cell spreading, cell viability, intracellular $Ca^{2+}$ mobilization): negative (-120 to -3 mV), moderately positive (+1 to +10 mV) and highly positive (+50 to +55 mV). The ζ-potential played a decisive role for the time-related cell spreading, the cell shape and physiology. After 1 h of cultivation osteoblasts on surfaces with moderately and highly positive ζ-potentials displayed a significantly enhanced cell spreading than on negatively charged surfaces. However, it could be shown that the spreading behavior on surfaces with highly positively charged potentials was strongly inhibited in the time course of 24 h. This resulted in a significant reduction of surface area (publication IV). Since the intracellular $Ca^{2+}$ dynamics is a sensitive parameter reflecting the cell physiology on biomaterial surfaces (publication II), the effect of the ζ-potential could be further specified via ATP stimulation. A significant improvement of intracellular $Ca^{2+}$ mobilization after 24 h was achieved on surfaces with moderately positive compared to negative ζ-potentials. Dramatic losses of cell activity were observed on surfaces with highly positive ζ-potentials: A significantly impaired $Ca^{2+}$ dynamic occurred along with a reduction in metabolic activity, a loss of membrane integrity and a decline in proliferation due to increasing G1 arrest (publication V).

This systematic work with a total of 12 surface modifications emphasizes the importance of the ζ-potential for the osteoblastic physiology and function. In summary, it was revealed that cells favor only the moderately positive ζ-potential range. The ζ-potential appears as one of the key parameters for cell interaction at the biomaterial interface and can be used as a "fine tuning" tool. It should therefore be considered in the development and characterization of new implant coatings.

# 8 LITERATURVERZEICHNIS


1. Elsevier Science Pub. Co - Biomaterials. Biomaterials Definition. (**2020**). Auf <https://www.journals.elsevier.com/biomaterials>
2. Deutsche Gesellschaft für Materialkunde e.V. (DGM). Biomaterialien. (**2020**). Auf <https://www.dgm.de/netzwerk/fachausschuesse-gesamtuebersicht/biomaterialien/?tx_management_board%5BboardPk%5D=186765CCB30C4071A81E6DFF48200B99&tx_management_board%5BboardName%5D=Biomimetische Biomaterialien&tx_management_board%5Baction%5D=list&tx_manage>
3. Zion Market Research. Global Biomaterials Market 2016-2026. (**2020**). Auf <https://www.zionmarketresearch.com/market-analysis/global-biomaterials-market>
4. Kulinets, I. in *Regul. Aff. Biomater. Med. Devices* (Hrsg. Amato, S. F. & Ezzell Jr, R. M.) 1–10 (Woodhead Publishing, 2015). ISBN: 9780857095428
5. Migonney, V. in *Biomaterials* 1–10 (John Wiley & Sons, Inc., 2014). ISBN: 9781119043553
6. Rajput, R., Chouhan, Z., Sindhu, M., Sundararajan, S. & Chouhan, R. R. S. A Brief Chronological Review of Dental Implant History. *Int. Dent. J. Students Res.* Volume 4**,** 105–107 (**2016**).
7. Qu, H., Fu, H., Han, Z. & Sun, Y. Biomaterials for bone tissue engineering scaffolds: a review. *RSC Adv.* 9**,** 26252–26262 (**2019**).
8. Im, G.-I. Biomaterials in orthopaedics: the past and future with immune modulation. *Biomater. Res.* 24**,** 7 (**2020**).
9. Marin, E., Boschetto, F. & Pezzotti, G. Biomaterials and biocompatibility: An historical overview. *J. Biomed. Mater. Res. Part A* 108**,** 1617–1633 (**2020**).
10. Campana, V., Milano, G., Pagano, E., Barba, M., Cicione, C., Salonna, G., Lattanzi, W. & Logroscino, G. Bone substitutes in orthopaedic surgery: from basic science to clinical practice. *J. Mater. Sci. Mater. Med.* 25**,** 2445–2461 (**2014**).
11. Stepanovska, J., Matejka, R., Rosina, J., Bacakova, L. & Kolarova, H. Treatments for enhancing the biocompatibility of titanium implants. *Biomed. Pap.* 164**,** 23–33 (**2020**).
12. Hanawa, T. in *Titan. Med. Dent. Appl.* (Hrsg. Froes, F. H. & Qian, M.) 95–113 (Woodhead Publishing, 2018). ISBN: 9780128124567
13. Froes, F. H. S. in *Titan. Med. Dent. Appl.* (Hrsg. Froes, F. H. & Qian, M.) 3–21 (Woodhead Publishing, 2018). ISBN: 9780128124567
14. Zhang, L. & Chen, L. A Review on Biomedical Titanium Alloys: Recent Progress and Prospect. *Adv. Eng. Mater.* 21**,** 1801215 (**2019**).
15. Niinomi, M. Mechanical properties of biomedical titanium alloys. *Mater. Sci. Eng. A* 243**,** 231–236 (**1998**).
16. Stewart, C., Akhavan, B., Wise, S. G. & Bilek, M. M. M. A review of biomimetic surface functionalization for bone-integrating orthopedic implants: Mechanisms, current approaches, and future directions. *Prog. Mater. Sci.* 106**,** 100588 (**2019**).
17. Chen, Q. & Thouas, G. A. Metallic implant biomaterials. *Mater. Sci. Eng. R Reports* 87**,** 1–57 (**2015**).
18. Antunes, R. A. & de Oliveira, M. C. L. Corrosion fatigue of biomedical metallic alloys: Mechanisms and mitigation. *Acta Biomater.* 8**,** 937–962 (**2012**).
19. Liu, Y., Rath, B., Tingart, M. & Eschweiler, J. Role of implants surface modification in osseointegration: A systematic review. *J. Biomed. Mater. Res. Part A* 108**,** 470–484 (**2020**).
20. Brånemark, R., Brånemark, P., Rydevik, B. & Myers, P. Osseointegration in skeletal reconstruction and rehabilitation: a review. *J. Rehabil. Res. Dev.* 38**,** 175–181 (**2001**).
21. Green, D. W., Watson, G. S., Watson, J. A., Lee, D.-J., Lee, J.-M. & Jung, H.-S. Diversification and enrichment of clinical biomaterials inspired by Darwinian evolution. *Acta Biomater.* 42**,** 33–45 (**2016**).
22. Kim, H. M., Miyaji, F., Kokubo, T. & Nakamura, T. Preparation of bioactive Ti and its alloys via simple chemical surface treatment. *J. Biomed. Mater. Res.* 32**,** 409–17 (**1996**).
23. Kim, S. E., Song, S.-H., Yun, Y. P., Choi, B.-J., Kwon, I. K., Bae, M. S., Moon, H.-J. & Kwon, Y.-D. The effect of immobilization of heparin and bone morphogenic protein-2 (BMP-2) to titanium surfaces on inflammation and osteoblast function. *Biomaterials* 32**,** 366–373 (**2011**).

24. von der Mark, K. & Park, J. Engineering biocompatible implant surfaces: Part II: Cellular recognition of biomaterial surfaces: Lessons from cell–matrix interactions. *Prog. Mater. Sci.* 58**,** 327–381 (**2013**).
25. Chen, S., Guo, Y., Liu, R., Wu, S., Fang, J., Huang, B., Li, Z., Chen, Z. & Chen, Z. Tuning surface properties of bone biomaterials to manipulate osteoblastic cell adhesion and the signaling pathways for the enhancement of early osseointegration. *Colloids Surfaces B Biointerfaces* 164**,** 58–69 (**2018**).
26. Latour, R. A. Fundamental Principles of the Thermodynamics and Kinetics of Protein Adsorption to Material Surfaces. *Colloids Surfaces B Biointerfaces* 191**,** 110992 (**2020**).
27. Vroman, L. Finding seconds count after contact with blood (and that is all I did). *Colloids Surfaces B Biointerfaces* 62**,** 1–4 (**2008**).
28. Slack, S. M. & Horbett, T. A. in *Proteins Interfaces II* (Hrsg. Horbett, T. A. & Brash, J. L.) 112–128 (ACS Symposium Series, 1995). ISBN: 9780841215276
29. Wilson, C. J., Clegg, R. E., Leavesley, D. I. & Pearcy, M. J. Mediation of Biomaterial–Cell Interactions by Adsorbed Proteins: A Review. *Tissue Eng.* 11**,** 1–18 (**2005**).
30. Ferrari, M., Cirisano, F. & Morán, M. C. Mammalian Cell Behavior on Hydrophobic Substrates: Influence of Surface Properties. *Colloids and Interfaces* 3**,** 48 (**2019**).
31. Khalili, A. & Ahmad, M. A Review of Cell Adhesion Studies for Biomedical and Biological Applications. *Int. J. Mol. Sci.* 16**,** 18149–18184 (**2015**).
32. Anselme, K. Osteoblast adhesion on biomaterials. *Biomaterials* 21**,** 667–681 (**2000**).
33. Rebl, H., Finke, B., Schmidt, J., Mohamad, H. S., Ihrke, R., Helm, C. A. & Nebe, J. B. Accelerated cell-surface interlocking on plasma polymer-modified porous ceramics. *Mater. Sci. Eng. C* 69**,** 1116–1124 (**2016**).
34. Finke, B., Luethen, F., Schroeder, K., Mueller, P. D., Bergemann, C., Frant, M., Ohl, A. & Nebe, B. J. The effect of positively charged plasma polymerization on initial osteoblastic focal adhesion on titanium surfaces. *Biomaterials* 28**,** 4521–4534 (**2007**).
35. Shekaran, A. & Garcia, A. J. Nanoscale engineering of extracellular matrix-mimetic bioadhesive surfaces and implants for tissue engineering. *Biochim. Biophys. Acta - Gen. Subj.* 1810**,** 350–360 (**2011**).
36. LeBaron, R. G. & Athanasiou, K. A. Extracellular matrix cell adhesion peptides: functional applications in orthopedic materials. *Tissue Eng.* 6**,** 85–103 (**2000**).
37. Kanchanawong, P., Shtengel, G., Pasapera, A. M., Ramko, E. B., Davidson, M. W., Hess, H. F. & Waterman, C. M. Nanoscale architecture of integrin-based cell adhesions. *Nature* 468**,** 580–4 (**2010**).
38. Yang, S. & Kim, H.-M. The RhoA-ROCK-PTEN pathway as a molecular switch for anchorage dependent cell behavior. *Biomaterials* 33**,** 2902–2915 (**2012**).
39. Takahashi, A., Camacho, P., Lechleiter, J. D. & Herman, B. Measurement of intracellular calcium. *Physiol. Rev.* 79**,** 1089–125 (**1999**).
40. Gilabert, J. A. in *Calcium Signaling. Adv. Exp. Med. Biol.* (Hrsg. Islam, M.) 1131: 163–182 (Springer, Cham, 2020). auf <http://link.springer.com/10.1007/978-3-030-12457-1_7>
41. Dominguez, D. C. Calcium signalling in bacteria. *Mol. Microbiol.* 54**,** (**2004**).
42. Duncan, R. L., Akanbi, K. A. & Farach-Carson, M. C. Calcium signals and calcium channels in osteoblastic cells. *Semin Nephrol.* 18**,** 178–90 (**1998**).
43. Berridge, M. J., Bootman, M. D. & Lipp, P. Calcium - a life and death signal. *Nature* 395**,** 645–648 (**1998**).
44. Bruton, J., Cheng, A. J. & Westerblad, H. in 7–26 (Springer, Cham, 2020). doi:10.1007/978-3-030-12457-1_2
45. Tsien, R. Y. A non-disruptive technique for loading calcium buffers and indicators into cells. *Nature* 290**,** 527–528 (**1981**).
46. Tsien, R. Y., Pozzan, T. & Rink, T. J. Calcium homeostasis in intact lymphocytes: cytoplasmic free calcium monitored with a new, intracellularly trapped fluorescent indicator. *J. Cell Biol.* 94**,** 325–334 (**1982**).
47. Berridge, M. J., Bootman, M. D. & Roderick, H. L. Calcium signalling: dynamics, homeostasis and remodelling. *Nat. Rev. Mol. Cell Biol.* 4**,** 517–529 (**2003**).
48. Marchi, S. & Pinton, P. Alterations of calcium homeostasis in cancer cells. *Curr. Opin. Pharmacol.* 29**,** 1–6 (**2016**).
49. Islam, M. S. in *Calcium Signaling. Adv. Exp. Med. Biol.* (Hrsg. Islam, M.) 1131: 1–6 (Springer, Cham, 2020). ISBN: 978-3-030-12457-1

50. Machaca, K. Ca2+ signaling, genes and the cell cycle. *Cell Calcium* 49**,** 323–330 (**2011**).
51. Stewart, T. A., Yapa, K. T. D. S. & Monteith, G. R. Altered calcium signaling in cancer cells. *Biochim. Biophys. Acta - Biomembr.* 1848**,** 2502–2511 (**2015**).
52. Carreras-Sureda, A., Pihán, P. & Hetz, C. Calcium signaling at the endoplasmic reticulum: fine-tuning stress responses. *Cell Calcium* 70**,** 24–31 (**2018**).
53. Xu, Z., Zhang, D., He, X., Huang, Y. & Shao, H. Transport of Calcium Ions into Mitochondria. *Curr. Genomics* 17**,** 215–9 (**2016**).
54. Pinton, P., Pozzan, T. & Rizzuto, R. The Golgi apparatus is an inositol 1,4,5-trisphosphate-sensitive Ca2+ store, with functional properties distinct from those of the endoplasmic reticulum. *EMBO J.* 17**,** 5298–308 (**1998**).
55. Zayzafoon, M. Calcium/calmodulin signaling controls osteoblast growth and differentiation. *J. Cell. Biochem.* 97**,** 56–70 (**2006**).
56. Vetter, I., Carter, D., Bassett, J., Deuis, J. R., Tay, B., Jami, S. & Robinson, S. D. in *Calcium Signaling. Adv. Exp. Med. Biol.* (Hrsg. Islam, M.) 1131: 27–72 (Springer, Cham, 2020). ISBN: 978-3-030-12457-1
57. Abbracchio, M. P. & Burnstock, G. Purinoceptors: Are there families of P2X and P2Y purinoceptors? *Pharmacol. Ther.* 64**,** 445–475 (**1994**).
58. Berridge, M. J. Inositol trisphosphate and diacylglycerol as second messengers. *Biochem. J.* 220**,** 345–60 (**1984**).
59. Michell, R. H. Inositol phospholipids and cell surface receptor function. *Biochim. Biophys. Acta - Rev. Biomembr.* 415**,** 81–147 (**1975**).
60. Nishizuka, Y. Intracellular signaling by hydrolysis of phospholipids and activation of protein kinase C. *Science* 258**,** 607–14 (**1992**).
61. Berridge, M. J. Inositol trisphosphate and calcium signalling. *Nature* 361**,** 315–325 (**1993**).
62. Shen, W.-W., Frieden, M. & Demaurex, N. Remodelling of the endoplasmic reticulum during store-operated calcium entry. *Biol. Cell* 103**,** 365–380 (**2011**).
63. Rizzuto, R., De Stefani, D., Raffaello, A. & Mammucari, C. Mitochondria as sensors and regulators of calcium signalling. *Nat. Rev. Mol. Cell Biol.* 13**,** 566–578 (**2012**).
64. Marchi, S. & Pinton, P. The mitochondrial calcium uniporter complex: molecular components, structure and physiopathological implications. *J. Physiol.* 592**,** 829–839 (**2014**).
65. Pizzo, P., Lissandron, V., Capitanio, P. & Pozzan, T. Ca2+ signalling in the Golgi apparatus. *Cell Calcium* 50**,** 184–192 (**2011**).
66. Gruening, M. Enhancement of Intracellular Calcium Ion Mobilization by Surface Charges. *Mendeley Data* 3**,** (**2020**).
67. Ferraris, S., Cazzola, M., Peretti, V., Stella, B. & Spriano, S. Zeta Potential Measurements on Solid Surfaces for in Vitro Biomaterials Testing: Surface Charge, Reactivity Upon Contact With Fluids and Protein Absorption. *Front. Bioeng. Biotechnol.* 6**,** 60 (**2018**).
68. LLS Health CDMO. Zeta Potential (ZP): An Overview and ZP Guide. (**2020**). Auf <https://lubrizolcdmo.com/technical-briefs/overview-of-the-zeta-potential/>
69. DataPhysics Instruments GmbH. Kontaktwinkel. (**2020**). Auf <https://www.dataphysics-instruments.com/de/wissen/grenzflaechen-verstehen/kontaktwinkel/>
70. Staehlke, S., Rebl, H. & Nebe, B. Phenotypic stability of the human MG-63 osteoblastic cell line at different passages. *Cell Biol. Int.* 43**,** 22–32 (**2019**).
71. Clover, J. & Gowen, M. Are MG-63 and HOS TE85 human osteosarcoma cell lines representative models of the osteoblastic phenotype? *Bone* 15**,** 585–591 (**1994**).
72. Czekanska, E. M., Stoddart, M. J., Ralphs, J. R., Richards, R. G. & Hayes, J. S. A phenotypic comparison of osteoblast cell lines versus human primary osteoblasts for biomaterials testing. *J. Biomed. Mater. Res. Part A* 102**,** 2636–2643 (**2014**).
73. Paredes, R. M., Etzler, J. C., Watts, L. T., Zheng, W. & Lechleiter, J. D. Chemical calcium indicators. *Methods* 46**,** 143–151 (**2008**).
74. Gabler, C., Zietz, C., Göhler, R., Fritsche, A., Lindner, T., Haenle, M., Finke, B., Meichsner, J., Lenz, S., Frerich, B., Lüthen, F., Nebe, J. & Bader, R. Evaluation of Osseointegration of Titanium Alloyed Implants Modified by Plasma Polymerization. *Int. J. Mol. Sci.* 15**,** 2454–2464 (**2014**).
75. Finke, B., Rebl, H., Hempel, F., Schäfer, J., Liefeith, K., Weltmann, K.-D. & Nebe, J. B. Aging of Plasma-

Polymerized Allylamine Nanofilms and the Maintenance of Their Cell Adhesion Capacity. *Langmuir* 30**,** 13914–13924 (**2014**).

76. Rebl, H., Finke, B., Ihrke, R., Rothe, H., Rychly, J., Schroeder, K. & Nebe, B. J. Positively Charged Material Surfaces Generated by Plasma Polymerized Allylamine Enhance Vinculin Mobility in Vital Human Osteoblastss. *Adv. Eng. Mater.* 12**,** B356–B364 (**2010**).
77. Bergemann, C., Cornelsen, M., Quade, A., Laube, T., Schnabelrauch, M., Rebl, H., Weißmann, V., Seitz, H. & Nebe, B. Continuous cellularization of calcium phosphate hybrid scaffolds induced by plasma polymer activation. *Mater. Sci. Eng. C. Mater. Biol. Appl.* 59**,** 514–523 (**2016**).
78. Rebl, H., Finke, B., Lange, R., Weltmann, K.-D. & Nebe, J. B. Impact of plasma chemistry versus titanium surface topography on osteoblast orientation. *Acta Biomater.* 8**,** 3840–3851 (**2012**).
79. Mörke, C., Rebl, H., Finke, B., Dubs, M., Nestler, P., Airoudj, A., Roucoules, V., Schnabelrauch, M., Körtge, A., Anselme, K., Helm, C. A. & Nebe, J. B. Abrogated Cell Contact Guidance on Amino-Functionalized Microgrooves. *ACS Appl. Mater. Interfaces* 9**,** 10461–10471 (**2017**).
80. Moerke, C., Staehlke, S., Rebl, H., Finke, B. & Nebe, J. B. Restricted cell functions on micropillars are alleviated by surfacenanocoating with amino groups. *J. Cell Sci.* 131**,** (**2018**).
81. Bacakova, L., Filova, E., Parizek, M., Ruml, T. & Svorcik, V. Modulation of cell adhesion, proliferation and differentiation on materials designed for body implants. *Biotechnol. Adv.* 29**,** 739–767 (**2011**).
82. Anselme, K., Ponche, A. & Bigerelle, M. Relative influence of surface topography and surface chemistry on cell response to bone implant materials. Part 2: biological aspects. *Proc. Inst. Mech. Eng. H.* 224**,** 1487–507 (**2010**).
83. Staehlke, S., Koertge, A. & Nebe, B. Intracellular calcium dynamics dependent on defined microtopographical features of titanium. *Biomaterials* 46**,** 48–57 (**2015**).
84. Park, J., Bauer, S., von der Mark, K. & Schmuki, P. Nanosize and Vitality: TiO2 Nanotube Diameter Directs Cell Fate. *Langmiur* 7**,** 1686–1691 (**2007**).
85. Puckett, S., Pareta, R. & Webster, T. J. Nano rough micron patterned titanium for directing osteoblast morphology and adhesion. *Int. J. Nanomedicine* 3**,** 229–41 (**2008**).
86. Gongadze, E., Kabaso, D., Bauer, S., Slivnik, T., Schmuki, P., van Rienen, U. & Iglič, A. Adhesion of osteoblasts to a nanorough titanium implant surface. *Int. J. Nanomedicine* 6**,** 1801–1816 (**2011**).
87. Stamp, R., Fox, P., O'Neill, W., Jones, E. & Sutcliffe, C. The development of a scanning strategy for the manufacture of porous biomaterials by selective laser melting. *J. Mater. Sci. Mater. Med.* 20**,** 1839–1848 (**2009**).
88. Müller, R., Abke, J., Schnell, E., Scharnweber, D., Kujat, R., Englert, C., Taheri, D., Nerlich, M. & Angele, P. Influence of surface pretreatment of titanium- and cobalt-based biomaterials on covalent immobilization of fibrillar collagen. *Biomaterials* 27**,** 4059–4068 (**2006**).
89. Rico, P., Hernández, J. C. R., Moratal, D., Altankov, G., Pradas, M. M. & Salmerón-Sánchez, M. Substrate-Induced Assembly of Fibronectin into Networks: Influence of Surface Chemistry and Effect on Osteoblast Adhesion. *Tissue Eng. Part A* 15**,** 3271–3281 (**2009**).
90. Cao, C., Song, Y., Yao, Q., Yao, Y., Wang, T., Huang, B. & Gong, P. Preparation and preliminary in vitro evaluation of a bFGF-releasing heparin-conjugated poly(ε-caprolactone) membrane for guided bone regeneration. *J. Biomater. Sci. Polym. Ed.* 26**,** 600–616 (**2015**).
91. Chakkalakal, D. A. Mechanoelectric transduction in bone. *J. Mater. Res.* 4**,** 1034–1046 (**1989**).
92. Meschede, D. in *Gerthsen Phys. Springer-Lehrbuch.* (Hrsg. Vogel, H.) 293–351 (Springer, Berlin, Heidelberg, 2002). ISBN: 978-3-662-07460-2
93. Shech, E. & Hatleback, E. The Material Intricacies of Coulomb's 1785 Electric Torsion Balance Experiment. (**2014**). Auf <http://philsci-archive.pitt.edu/11048/>
94. Metwally, S. & Stachewicz, U. Surface potential and charges impact on cell responses on biomaterials interfaces for medical applications. *Mater. Sci. Eng. C* 104**,** 109883 (**2019**).
95. Altankov, G., Richau, K. & Groth, T. The role of surface zeta potential and substratum chemistry for regulation of dermal fibroblasts interaction. *Materwiss. Werksttech.* 34**,** 1120–1128 (**2003**).
96. Iwai, R., Nemoto, Y. & Nakayama, Y. The effect of electrically charged polyion complex nanoparticle-coated surfaces on adipose-derived stromal progenitor cell behaviour. *Biomaterials* 34**,** 9096–9102 (**2013**).
97. Chang, H.-Y., Huang, C.-C., Lin, K.-Y., Kao, W.-L., Liao, H.-Y., You, Y.-W., Lin, J.-H., Kuo, Y.-T., Kuo, D.-Y. & Shyue, J.-J. Effect of Surface Potential on NIH3T3 Cell Adhesion and Proliferation. *J. Phys. Chem. C* 118**,** 14464–14470 (**2014**).

98. Lee, J. H., Jung, H. W., Kang, I.-K. & Lee, H. B. Cell behaviour on polymer surfaces with different functional groups. *Biomaterials* 15**,** 705–711 (**1994**).

99. Bacakova, L., Svorcik, V., Rybka, V., Micek, I., Hnatowicz, V., Lisa, V. & Kocourek, F. Adhesion and proliferation of cultured human aortic smooth muscle cells on polystyrene implanted with N+, F+ and Ar+ ions: correlation with polymer surface polarity and carbonization. *Biomaterials* 17**,** 1121–1126 (**1996**).

100. Webb, K., Hlady, V. & Tresco, P. A. Relative importance of surface wettability and charged functional groups on NIH 3T3 fibroblast attachment, spreading, and cytoskeletal organization. *J. Biomed. Mater. Res.* 41**,** 422–430 (**1998**).

101. Lesný, P., Přádný, M., Jendelová, P., Michálek, J., Vacík, J. & Syková, E. Macroporous hydrogels based on 2-hydroxyethyl methacrylate. Part 4: Growth of rat bone marrow stromal cells in three-dimensional hydrogels with positive and negative surface charges and in polyelectrolyte complexes. *J. Mater. Sci. Mater. Med.* 17**,** 829–833 (**2006**).

102. Yang, Y., Cavin, R. & Ong, J. L. Protein adsorption on titanium surfaces and their effect on osteoblast attachment. *J. Biomed. Mater. Res.* 67A**,** 344–349 (**2003**).

103. Schulz, A., Katsen-Globa, A., Huber, E. J., Mueller, S. C., Kreiner, A., Pütz, N., Gepp, M. M., Fischer, B., Stracke, F., von Briesen, H., Neubauer, J. C. & Zimmermann, H. Poly(amidoamine)-alginate hydrogels: directing the behavior of mesenchymal stem cells with charged hydrogel surfaces. *J. Mater. Sci. Mater. Med.* 29**,** 105 (**2018**).

104. Cai, K., Frant, M., Bossert, J., Hildebrand, G., Liefeith, K. & Jandt, K. D. Surface functionalized titanium thin films: Zeta-potential, protein adsorption and cell proliferation. *Colloids Surfaces B Biointerfaces* 50**,** 1–8 (**2006**).

105. Krajewski, A., Malavolti, R. & Piancastelli, A. Albumin adhesion on some biological and non-biological glasses and connection with their Z-potentials. *Biomaterials* 17**,** 53–60 (**1996**).

106. Krajewski, A., Piancastelli, A. & Malavolti, R. Albumin adhesion on ceramics and correlation with their Z-potential. *Biomaterials* 19**,** 637–641 (**1998**).

107. Loughney, J. W., Lancaster, C., Ha, S. & Rustandi, R. R. Residual bovine serum albumin (BSA) quantitation in vaccines using automated Capillary Western technology. *Anal. Biochem.* 461**,** 49–56 (**2014**).

108. Latour, R. A. Perspectives on the simulation of protein–surface interactions using empirical force field methods. *Colloids Surfaces B Biointerfaces* 124**,** 25–37 (**2014**).

109. Sanfeld, A., Royer, C. & Steinchen, A. Thermodynamic, kinetic and conformational analysis of proteins diffusion–sorption on a solid surface. *Adv. Colloid Interface Sci.* 222**,** 639–660 (**2015**).

110. Anand, G., Sharma, S., Dutta, A. K., Kumar, S. K. & Belfort, G. Conformational Transitions of Adsorbed Proteins on Surfaces of Varying Polarity. *Langmuir* 26**,** 10803–10811 (**2010**).

111. Hartvig, R. A., van de Weert, M., Østergaard, J., Jorgensen, L. & Jensen, H. Protein Adsorption at Charged Surfaces: The Role of Electrostatic Interactions and Interfacial Charge Regulation. *Langmuir* 27**,** 2634–2643 (**2011**).

112. Biesheuvel, P. M., van der Veen, M. & Norde, W. A Modified Poisson−Boltzmann Model Including Charge Regulation for the Adsorption of Ionizable Polyelectrolytes to Charged Interfaces, Applied to Lysozyme Adsorption on Silica. *J. Phys. Chem. B* 109**,** 4172–4180 (**2005**).

113. Ståhlberg, J. & Jönsson, B. Influence of Charge Regulation in Electrostatic Interaction Chromatography of Proteins. *Anal. Chem.* 68**,** 1536–1544 (**1996**).

114. Lund, M., Åkesson, T. & Jönsson, B. Enhanced Protein Adsorption Due to Charge Regulation. *Langmuir* 21**,** 8385–8388 (**2005**).

115. Ozkan, M., Pisanic, T., Scheel, J., Barlow, C., Esener, S. & Bhatia, S. N. Electro-Optical Platform for the Manipulation of Live Cells. *Langmuir* 19**,** 1532–1538 (**2003**).

116. Van Damme, M. P., Tiglias, J., Nemat, N. & Preston, B. N. Determination of the charge content at the surface of cells using a colloid titration technique. *Anal. Biochem.* 223**,** 62–70 (**1994**).

117. van Wachem, P. ., Hogt, A. ., Beugeling, T., Feijen, J., Bantjes, A., Detmers, J. . & van Aken, W. . Adhesion of cultured human endothelial cells onto methacrylate polymers with varying surface wettability and charge. *Biomaterials* 8**,** 323–328 (**1987**).

118. Nowrouzi, A. & Yazdanparast, R. G1 phase arrest and apoptosis induction in human thyroid cancer cell line Thr.C1.PI33 by 3-hydrogenkwadaphnin isolated from Dendrostellera lessertii. *Iran. Biomed. J.* 11**,** 215–21 (**2007**).

119. Thouverey, C., Strzelecka-Kiliszek, A., Balcerzak, M., Buchet, R. & Pikula, S. Matrix vesicles originate from apical membrane microvilli of mineralizing osteoblast-like Saos-2 cells. *J. Cell. Biochem.* 106**,** 127–138 (**2009**).

120. Thouverey, C., Malinowska, A., Balcerzak, M., Strzelecka-Kiliszek, A., Buchet, R., Dadlez, M. & Pikula, S. Proteomic characterization of biogenesis and functions of matrix vesicles released from mineralizing human osteoblast-like cells. *J. Proteomics* 74**,** 1123–1134 (**2011**).

121. Hoentsch, M., Bussiahn, R., Rebl, H., Bergemann, C., Eggert, M., Frank, M., von Woedtke, T. & Nebe, B. Persistent Effectivity of Gas Plasma-Treated, Long Time-Stored Liquid on Epithelial Cell Adhesion Capacity and Membrane Morphology. *PLoS One* 9**,** e104559 (**2014**).

122. Laster, S. M. & Mackenzie, J. M. Bleb formation and F-actin distribution during mitosis and tumor necrosis factor-induced apoptosis. *Microsc. Res. Tech.* 34**,** 272–80 (**1996**).

123. Moerke, C., Mueller, P. & Nebe, B. Attempted caveolae-mediated phagocytosis of surface-fixed micro-pillars by human osteoblasts. *Biomaterials* 76**,** 102–114 (**2016**).

124. Meszaros, G. J. & Karin, N. J. Inhibitors of ER Ca2+-ATPase activity deplete the ATP- and thrombin-sensitive Ca2+ pool in UMR 106-01 osteosarcoma cells. *J. Bone Miner. Res.* 10**,** 704–710 (**2009**).

125. Orriss, I. R., Burnstock, G. & Arnett, T. R. Purinergic signalling and bone remodelling. *Curr. Opin. Pharmacol.* 10**,** 322–330 (**2010**).

126. Reimer, W. J. & Dixon, S. J. Extracellular nucleotides elevate [Ca2+]i in rat osteoblastic cells by interaction with two receptor subtypes. *Am. J. Physiol.* 263**,** C1040-8 (**1992**).

127. Nakamura, E., Uezono, Y., Narusawa, K., Shibuya, I., Oishi, Y., Tanaka, M., Yanagihara, N., Nakamura, T. & Izumi, F. ATP activates DNA synthesis by acting on P2X receptors in human osteoblast-like MG-63 cells. *Am. J. Physiol. Physiol.* 279**,** C510–C519 (**2000**).

128. Alqallaf, S., Evans, B. & Kidd, E. Atypical P2X7 receptor pharmacology in two human osteoblast-like cell lines. *Br. J. Pharmacol.* 156**,** 1124–1135 (**2009**).

129. Wolff, S. C., Qi, A.-D., Harden, T. K. & Nicholas, R. A. Polarized expression of human P2Y receptors in epithelial cells from kidney, lung, and colon. *Am. J. Physiol. Physiol.* 288**,** C624–C632 (**2005**).

130. Murthy, K. S. & Makhlouf, G. M. Coexpression of ligand-gated P2X and G protein-coupled P2Y receptors in smooth muscle. Preferential activation of P2Y receptors coupled to phospholipase C (PLC)-beta1 via Galphaq/11 and to PLC-beta3 via Gbetagammai3. *J. Biol. Chem.* 273**,** 4695–704 (**1998**).

131. Erb, L., Liao, Z., Seye, C. I. & Weisman, G. A. P2 receptors: intracellular signaling. *Pflügers Arch. - Eur. J. Physiol.* 452**,** 552–562 (**2006**).

132. Bonora, M., Bononi, A., De Marchi, E., Giorgi, C., Lebiedzinska, M., Marchi, S., Patergnani, S., Rimessi, A., Suski, J. M., Wojtala, A., Wieckowski, M. R., Kroemer, G., Galluzzi, L. & Pinton, P. Role of the c subunit of the F $_O$ ATP synthase in mitochondrial permeability transition. *Cell Cycle* 12**,** 674–683 (**2013**).

133. Morciano, G., Giorgi, C., Bonora, M., Punzetti, S., Pavasini, R., Wieckowski, M. R., Campo, G. & Pinton, P. Molecular identity of the mitochondrial permeability transition pore and its role in ischemia-reperfusion injury. *J. Mol. Cell. Cardiol.* 78**,** 142–153 (**2015**).

134. Staehlke, S., Lehnfeld, J., Schneider, A., Nebe, J. B. & Müller, R. Terminal chemical functions of polyamidoamine dendrimer surfaces and its impact on bone cell growth. *Mater. Sci. Eng. C* 101**,** 190–203 (**2019**).

135. Tan, F., Xu, X., Deng, T., Yin, M., Zhang, X. & Wang, J. Fabrication of positively charged poly(ethylene glycol)-diacrylate hydrogel as a bone tissue engineering scaffold. *Biomed. Mater.* 7**,** 055009 (**2012**).

136. De Luca, I., Di Salle, A., Alessio, N., Margarucci, S., Simeone, M., Galderisi, U., Calarco, A. & Peluso, G. Positively charged polymers modulate the fate of human mesenchymal stromal cells via ephrinB2/EphB4 signaling. *Stem Cell Res.* 17**,** 248–255 (**2016**).

137. Muller, F. L., Lustgarten, M. S., Jang, Y., Richardson, A. & Van Remmen, H. Trends in oxidative aging theories. *Free Radic. Biol. Med.* 43**,** 477–503 (**2007**).

138. Kato, T., Tsuda, T., Inaba, H., Kawai, S., Okahashi, N., Shibata, Y., Abiko, Y. & Amano, A. Porphyromonas gingivalis gingipains cause G(1) arrest in osteoblastic/stromal cells. *Oral Microbiol. Immunol.* 23**,** 158–64 (**2008**).

139. Zou, W., Yang, S., Zhang, T., Sun, H., Wang, Y., Xue, H. & Zhou, D. Hypoxia enhances glucocorticoid-induced apoptosis and cell cycle arrest via the PI3K/Akt signaling pathway in osteoblastic cells. *J. Bone Miner. Metab.* 33**,** 615–624 (**2015**).

140. Blagosklonny, M. V. Cell cycle arrest is not senescence. *Aging (Albany. NY).* 3**,** 94–101 (**2011**).

141. Terzi, M. Y., Izmirli, M. & Gogebakan, B. The cell fate: senescence or quiescence. *Mol. Biol. Rep.* 43**,** 1213–1220 (**2016**).

142. Guo, S., Kwek, M. Y., Toh, Z. Q., Pranantyo, D., Kang, E.-T., Loh, X. J., Zhu, X., Jańczewski, D. & Neoh, K. G. Tailoring Polyelectrolyte Architecture To Promote Cell Growth and Inhibit Bacterial Adhesion. *ACS Appl. Mater. Interfaces* 10**,** 7882–7891 (**2018**).

143. Mecke, A., Majoros, I. J., Patri, A. K., Baker, J. R., Banaszak Holl, M. M. & Orr, B. G. Lipid Bilayer Disruption by Polycationic Polymers: The Roles of Size and Chemical Functional Group. *Langmuir* 21**,** 10348–10354 (**2005**).

144. Edinger, A. L. & Thompson, C. B. Death by design: apoptosis, necrosis and autophagy. *Curr. Opin. Cell Biol.* 16**,** 663–669 (**2004**).

145. Krysko, D. V., Berghe, T. Vanden, Parthoens, E., D'Herde, K. & Vandenabeele, P. Chapter 16 Methods for Distinguishing Apoptotic from Necrotic Cells and Measuring Their Clearance. *Methods Enzymol.* 442**,** 307–341 (**2008**).

146. Dutta, T., Garg, M., Dubey, V., Mishra, D., Singh, K., Pandita, D., Singh, A. K., Ravi, A. K., Velpandian, T. & Jain, N. K. Toxicological investigation of surface engineered fifth generation poly (propyleneimine) dendrimers *in vivo*. *Nanotoxicology* 2**,** 62–70 (**2008**).

147. Jang, W.-D., Kamruzzaman Selim, K. M., Lee, C.-H. & Kang, I.-K. Bioinspired application of dendrimers: From bio-mimicry to biomedical applications. *Prog. Polym. Sci.* 34**,** 1–23 (**2009**).

# 9 ABKÜRZUNGSVERZEICHNIS

| | |
|---|---|
| $A_C$ | mittlere Zellfläche |
| AM | Acetoxymethylester |
| APTES | 3-Aminopropyltriethoxysilan |
| ATP | Adenosintriphosphat |
| Au | Gold |
| BCA | Bicinchoninsäure |
| BSA | Bovin Serumalbumin |
| $Ca^{2+}$ | Kalziumion |
| Col I | Kollagen Typ I |
| DAG | Diacylglycerin |
| DS | Doppelschicht |
| dsDNA | doppelsträngige DNA |
| EDL | elektrische Doppelschicht |
| ER | endoplasmatisches Retikulum |
| EZM | extrazelluläre Matrix |
| FKS | fötales Kälberserum |
| Fluo-3 | {[2-(2-{2-[Bis(carboxymethyl) amino]-5-(2,7-dichlor-6-hydroxy-3-oxo-3H-xanthen-9-yl)phenoxy} ethoxy)-4-methylphenyl] (carboxymethyl)amino} essigsäure |
| G1/2 | Gap-Phasen |
| GPCR | G-Protein gekoppelter Rezeptor |
| HMGB-1 | High-Mobility-Group-Protein B1 |
| HOB | primäre humane Osteoblasten |
| HSA | Humanserumalbumin |
| INP | Leibniz-Institut für Plasma-forschung und Technologie e. V. |
| $IP_3$ | Inositoltriphosphat |
| $IP_3R$ | $IP_3$-Rezeptor |
| IQR | Interquartilsabstand |
| LSM | Laser-Scanning Mikroskop |
| MCU | mitochondriale Uniporter |
| MFI | mittlere Fluoreszenzintensität |
| $MFI_A$ | MFI nach ATP Stimulation (190-240 s) |
| $MFI_{A-B}$ | Anstieg des $Ca^{2+}$-Signals |
| $MFI_C$ | mittlere Fluoreszenzintensität der Zellen |
| $MFI_{ROI}$ | MFI innerhalb der ROI Kästchen |
| MTS | ((3-(4,5-Dimethylthiazol-2-yl)-5-(3-Carboxy methoxyphenyl)-2-(4-sulfophenyl)-2H-tetrazolium salz) |
| NCX | $Na^+/Ca^{2+}$-Austauscher |
| P2X | ionotroper Purinozeptor Typ P2X |
| P2Y | G-Protein-gekoppelter Purinozeptor Typ P2Y |
| PAMAM | Polyamidoamin |
| PDADMA | Polydiallyldimethylammonium chlorid |
| PEI | Polyethylenimin |
| PEM | Polyelektrolytmultischicht |
| PMCA | Plasmamembran $Ca^{2+}$-ATPasen |
| PP | proliferative Phase |
| PPAAm | Plasma polymerisiertes Allylamin |
| PPI-G2/4/5 | Polypropylenimin Dendrimer Generation 2/4/5 |
| PSS | Polystyrolsulfonat |
| REM | Rasterelektronenmikroskopie |
| RFP | rot fluoreszierendes Protein |
| RGD | Arginin-Glycin-Aspartat Sequenz |
| ROI | Region of Interest |
| RYR | Ryanodinrezeptor |
| S | Synthesephase |
| SAM | Self-assembled Monolayer |
| SD | Standardabweichung |
| sem | Standard error of the mean |
| SERCA | Sarko/Endoplasmatische Retikulum-$Ca^{2+}$-ATPase |
| SFB | Sonderforschungsbereich |
| SFE | freie Oberflächenenergie |
| SPCA | sekretorische Signalweg-$Ca^{2+}$-ATPase |
| tBid | truncated BH3 interacting domain death agonist |
| Ti | Titan |
| TRP | Ionenkanäle mit transientem Rezeptorpotenzial |
| UHGW | Universität Greifswald |
| UHRO | Universität Rostock |
| UMR | Universitätsmedizin Rostock |
| UR | Universität Regensburg |
| VGCC | spannungsgesteuerte $Ca^{2+}$-Kanäle |
| WCA | Wasserkontaktwinkel |
| ZfM | Zentrum für Mikrotechnologien |
| ζ | Zetapotenzial |

# 10 ANHANG

## 10.1 WISSENSCHAFTLICHE AKTIVITÄTEN

### *10.1.1 PUBLIKATIONEN*

- **Gruening M**, Neuber S, Nestler P, Lehnfeld J, Dubs M, Fricke K, Schnabelrauch M, Helm CA, Müller R, Staehlke S, Nebe JB. Enhancement of intracellular calcium ion mobilization by moderately but not highly positive material surface charges. Frontiers in Bioengineering and Biotechnology 8: 1016 (2020). doi: 10.3389/fbioe.2020.01016. IF 3.644
- **Gruening M**, Neuber S, Fricke K, Helm CA, Nebe B. Cell-material interaction - Spreading course correlates with surface charge. American Journal of Biomedical Research 9: 1 (2020). doi: 10.34297/AJBSR.2020.09.001341. IF 0.823
- **Gruening M.** Enhancement of intracellular calcium ion mobilization by surface charges. Mendeley Dataset Version 3 (2020). doi: 10.17632/H8RS6V4DGT.3
- Lehnfeld J, **Gruening M**, Kronseder M, Mueller R. Comparison of protein-repellent behavior of linear versus dendrimer-structured surface-immobilized polymers. Langmuir 36 (21): 5880–5890 (2020). doi: 10.1021/acs.langmuir.0c00625. IF 3.557
- Nebe B, Rebl H, Schlosser M, Staehlke S, **Gruening M**, Weltmann KD, Walschus U, Finke B. Plasma polymerized allylamine – the unique cell-attractive nanolayer on biomaterials. Polymers 11: 1004 (2019). doi: 10.3390/polym11061004. IF 3.164
- Staehlke S, Rebl H, Finke B, Mueller P, **Gruening M** and Nebe B. Enhanced calcium ion mobilization in osteoblasts on amino group containing plasma polymer nanolayer. Cell & Bioscience 8: 22 (2018). doi: 10.1186/s13578-018-0220-8. IF 3.294
- Rakers S, Ondrusch AK, **Gruening M**, Adamek M, Moeckel B, Gebert M. Monitoring changing cellular characteristics during the development of a fin cell line from Cyprinus carpio. Comp. Biochem. Physiol. B, Biochem. Mol. Biol. 225: 1–12 (2018).
  doi: 10.1016/j.cbpb.2018.06.003. IF 1.684

### *10.1.2 KONGRESSE UND WORKSHOPS*

- **Teilnahme**. 5. und 8. Forschungscamp der Universität Rostock, November 2017, 2020
  **Posterpräsentation**. 6. und 7. Forschungscamp der Universität Rostock, November 2018/2019
- **Teilnahme**. 8.-11. Forschungsworkshop der Universitätsmedizin Rostock, November 2017/2018/ 2019/2020
- **Teilnahme**. 5.-7. Graduiertenworkshop des Departments Life, Light & Matter der Universität Rostock, Januar 2018/2019/2020

- **Posterpräsentation**. 9. Internationaler Kongress Nanotechnologie in Biologie & Medizin (BioNanoMed), Graz/Österreich, April 2018
- **Teilnahme**. IRTG Summer School "Clinical Needs for Electrically Active Implants", Hasenwinkel, Mai 2018
- **Posterpräsentation**. Forschungsworkshop des Departments Life, Light & Matter der Universität Rostock, Juni 2018
- **Posterpräsentation**. 29. Jahreskonferenz der Europäischen Gesellschaft für Biomaterialien (ESB), Maastricht/Niederlande, September 2018
- **Vortrag**. Electrical stimulation with human osteoblasts (*in vitro*). IRTG Basics and Trends Workshop, Parin, November 2018
- **Posterpräsentation**. Internationales Symposium Grenzflächenbiologie von Implantaten (IBI), Warnemünde, Mai 2019
- **Posterpräsentation (Auszeichnung Poster Award)**. Europäisches Symposium Intelligente Materialien (IM), Kiel, Juni 2019
- **Posterpräsentationen (2)**. Jahreskonferenz der Europäischen Gesellschaft für Biomaterialien (ESB) & Jahrestagung der Deutschen Gesellschaft für Biomaterialien (DGBM), Dresden, September 2019
- **Vorträge (3)**. Material surface charges and their influence on cell physiology and morphology. SFB ELAINE Retreat, Göhren und Hasenwinkel September 2018/2019, virtuell 2020
- **Vortrag**. Zeta potential – A key property for the development of functional biomaterials? Weltkongress für Biomaterialien (WBC), virtuell, Dezember 2020

### *10.1.3 GRADUIERTENAKADEMIE UND SEMINARE*

- **Gute wissenschaftliche Praxis**. Dr. Gerald Jurasinski, Graduiertenakademie der Universität Rostock, November 2017
- **Bildbearbeitung mit Adobe Photoshop CC** (Kurs 35). Kerstin Baier, Universität Rostock, März 2018
- **Academic Writing in natural sciences**. Lorraine Mannion, Graduiertenakademie der Universität Rostock, Juni 2018
- **Rhetoric & Presenting Skills**. Kira Ludwig, Graduiertenakademie der Universität Rostock, Juni 2018
- **Praxiskurs Galvanotaxis**. Prof. Dr. Rüdiger Köhling/Dr. Christian Bahls, Universitätsmedizin Rostock, September/Oktober 2018
- **Introduction to working with alternating current**. Stephan Graunke, Universität Rostock, März 2019
- **Grundlagen der angewandten Statistik**. Dr. Kerstin Schmidt/Paul Schmidt (BioMath GmbH), Graduiertenakademie der Universität Rostock, Dezember 2019
- **Successful writing of grant proposals**. Prof. Dr. Olaf Wolkenhauer, Universität Rostock, Januar 2020

- **Bewerben in 4 Schritten für Doktorand*innen und PostDocs**. Bianca Sievert (beruf & leben GbR), Graduiertenakademie der Universität Rostock, März 2020
- **Improved Reading: Read scientific texts fast and efficiently**. Friedrich Hasse (Improved Reading GmbH), Graduiertenakademie der Universität Rostock, März 2020
- **Mentales Stressmanagement**. Marina Wenzl (Moove GmbH), virtuell, Mai 2020
- **Disputationstraining**. Dr. Daniela Twilfer (Kommunikationstrainerin, Münster), Graduiertenakademie der Universität Rostock, virtuell, August/September 2020

## 10.2 VERWENDETE ORIGINALARBEITEN ZUR KUMULATIVEN DISSERTATION

- **Publikation I: Seiten 49 – 68**

  Nebe B, Rebl H, Schlosser M, Staehlke S, Gruening M, Weltmann KD, Walschus U, Finke B. Plasma polymerized allylamine – the unique cell-attractive nanolayer on biomaterials. Polymers 11: 1004 (2019).
- **Publikation II: Seiten 69 – 79**

  Staehlke S, Rebl H, Finke B, Mueller P, Gruening M and Nebe B. Enhanced calcium ion mobilization in osteoblasts on amino group containing plasma polymer nanolayer. Cell & Bioscience 8: 22 (2018).
- **Publikation III: Seiten 80 – 90**

  Lehnfeld J, Gruening M, Kronseder M, Mueller R. Comparison of protein-repellent behavior of linear versus dendrimer-structured surface-immobilized polymers. Langmuir 36 (21): 5880–5890 (2020).
- **Publikation IV: Seiten 91 – 93**

  Gruening M, Neuber S, Fricke K, Helm CA, Nebe B. Cell-material interaction - Spreading course correlates with surface charge. American Journal of Biomedical Research 9: 1 (2020).
- **Publikation V: Seiten 94 – 111**

  Gruening M, Neuber S, Nestler P, Lehnfeld J, Dubs M, Fricke K, Schnabelrauch M, Helm CA, Müller R, Staehlke S, Nebe JB. Enhancement of intracellular calcium ion mobilization by moderately but not highly positive material surface charges. Frontiers in Bioengineering and Biotechnology 8: 1016 (2020).
- **Publikation V (Supplementary Material): Seiten 112 – 119**

polymers

MDPI

*Publikation I: Article*

# Plasma Polymerized Allylamine – The Unique Cell-Attractive Nanolayer for Dental Implant Materials

**J. Barbara Nebe [1,2,*], Henrike Rebl [1], Michael Schlosser [3,4], Susanne Staehlke [1], Martina Gruening [1], Klaus-Dieter Weltmann [5], Uwe Walschus [4] and Birgit Finke [5]**

[1] Department of Cell Biology, Rostock University Medical Center, Schillingallee 69, 18057 Rostock, Germany; henrike.rebl@med.uni-rostock.de (H.R.); susanne.staehlke@med.uni-rostock.de (S.S.); martina.gruening@med.uni-rostock.de (M.G.)

[2] Department Life, Light & Matter, University of Rostock, Albert-Einstein-Str. 25, 18059 Rostock, Germany

[3] Department of Surgery, University Medical Center Greifswald, 17475 Greifswald, Germany; schlosse@uni-greifswald.de

[4] Department of Medical Biochemistry and Molecular Biology, University Medical Center Greifswald, 17475 Greifswald, Germany; uwe.walschus@uni-greifswald.de

[5] Leibniz Institute for Plasma Science and Technology (INP), Felix-Hausdorff-Str. 2, 17489 Greifswald, Germany; weltmann@inp-greifswald.de (K.-D.W.); finke-hgw@t-online.de (B.F.)

* Correspondence: barbara.nebe@med.uni-rostock.de; Tel.: +49-381-494-7771; Fax: +49-381-494-7764

Received: 18 April 2019; Accepted: 31 May 2019; Published: 5 June 2019

**Abstract:** Biomaterials should be bioactive in stimulating the surrounding tissue to accelerate the ingrowth of permanent implants. Chemical and topographical features of the biomaterial surface affect cell physiology at the interface. A frequently asked question is whether the chemistry or the topography dominates the cell-material interaction. Recently, we demonstrated that a plasma-chemical modification using allylamine as a precursor was able to boost not only cell attachment and cell migration, but also intracellular signaling in vital cells. This microwave plasma process generated a homogenous nanolayer with randomly distributed, positively charged amino groups. In contrast, the surface of the human osteoblast is negatively charged at −15 mV due to its hyaluronan coat. As a consequence, we assumed that positive charges at the material surface—provoking electrostatic interaction forces—are attractive for the first cell encounter. This plasma-chemical nanocoating can be used for several biomaterials in orthopedic and dental implantology like titanium, titanium alloys, calcium phosphate scaffolds, and polylactide fiber meshes produced by electrospinning. In this regard, we wanted to ascertain whether plasma polymerized allylamine (PPAAm) is also suitable for increasing the attractiveness of a ceramic surface for dental implants using Yttria-stabilized tetragonal zirconia.

**Keywords:** plasma polymerized allylamine; zirconia; surface characteristics; XPS; water contact angle; zeta potential; cell adhesion; osteoblasts; actin cytoskeleton; cell signaling

## 1. Introduction

Novel biomaterials in orthopedic or dental surgery should actively promote the osseointegration of implants. Both surface roughness and chemical modification can influence the interaction of osteoblasts with biomaterial surfaces. In implantology, titanium (Ti) and its alloys are often used because of their excellent biocompatibility and their mechanical properties. However, they are relatively inert and therefore new functionalization strategies are needed.

Consequently, it is essential to understand the initial reactions of cells at the material interface, including the organization of focal adhesion contacts that link the extracellular space and intracellular signaling processes. Human osteoblasts possess a net negative charge (−15 mV) [1] due to their hyaluronan coat [2], with carboxyl groups in the glycosaminoglycan chain. As a result, we assumed that positive charges at the material surface are attractive for the first cell attachment. We, therefore, developed a positively charged plasma polymerized nanolayer of allylamine (PPAAm) [2,3], which was deposited using physical low-pressure gas-discharge plasma in a microwave reactor. These processes are highly applicable, extremely effective, and valuable for the improvement of implant performance. There are, however, high demands in terms of process guidance and film quality—still a technological challenge even today. The PPAAm coating should adhere well and, thus, be mechanically stable; cross-linked and also stable in different aqueous media, resistant to hydrolysis and delamination, and equipped with a sufficient density of positively charged amino groups. Furthermore, the sterilizability of the plasma polymerized implant surfaces and their long-term storage characteristics are very important features, which have to be carefully evaluated before being used in implantology. For later applications, it was of interest to assess the applicability of this PPAAm layer on different material surfaces.

In recent years, we and other working groups [4–9] have thoroughly characterized this PPAAm layer containing amino groups in regard to its physico-chemical characteristics as well as cell biological outcomes after the modification of a variety of material substrates (Table 1) [10–18]. In general, this plasma polymer nanolayer showed cell-attractive characteristics that could not be achieved by coatings with extracellular matrix proteins, e.g., collagen type I or arginine-glycin-aspartic acid (Arg-Gly-Asp, RGD) (Table 1).

PPAAm was deposited on smooth and rough surfaces like polished, machined, or corundum-blasted titanium (Ti) [15] or titanium alloy [13,19], electrospun polylactide fiber meshes [14], β-tricalcium phosphate scaffolds [12], as well as a µm-thick, porous calcium phosphate layer [11]. The final plasma process conditions were chosen so as to yield substrate surfaces completely covered by a thin (>20 nm) PPAAm plasma polymer film. In this way, the chemical surface properties of the original substrate surface were completely replaced by the properties of PPAAm, whereby the mechanical properties of the bulk material were retained.

### *1.1. PPAAm Layer Characteristics—An Overview*

Under the plasma-chemical deposition conditions [3,13,18,20] employed here, PPAAm films are mechanically stable and highly adhesive (80 N/mm$^2$) [21]. A qualitative scratch test, a quantitative standard adhesive bonding strength test according to DIN EN 582 [22], and a wear test using artificial bone (30 pcf Sawbones and Palacos bone cement (PMMA)) [22] were carried out. An explanation for the excellent adhesion and robustness of the plasma polymer films deposited on zirconium/titanium substrates was given by the group of Bilek [23]: Metallic carbide and oxycarbide bonds were formed during the initial film formation by a two-dimensional-like, layer by layer (Frank-van der Merve) growth mode.

PPAAm coatings have, in general—regardless of the substrate—a positive zeta potential from +7.7 mV (pH 6) [18] to +8.6 mV (pH 7.4) [10] to +14 mV (pH 6) [16], and +26.3 mV (pH 6), also after long-term storage in ambient air for up to 200 days [13]. The total surface energy of the PPAAm film is 52 ± 8 mN/m, the polar part 22 ± 8 mN/m (Table 1). The XPS surface elemental composition of PPAAm is 30 ± 2% for N/C and near the theoretical N/C value of allylamine of 33%. O/C as a contamination is <10%. The amino group density $NH_2$/C varies between 2–4%.

These surface properties and also the cell-attractive properties seem to be independent of the film thickness produced by different treatment times under the same pulse/pause ratio of the plasma.

The wettability of PPAAm-covered surfaces seems to be optimal for cell responses, with water contact angles (WCA) between 45°–68° (Table 1) [24]. Our deposited, very well cross-linked PPAAm films are stable in aqueous media [18]. This is a precondition for the layer effectiveness and stability in cell culture, in animal evaluations, or for later applications in human tissue.

**Table 1.** Overview of plasma polymerized allylamine (PPAAm) surface coating of diverse bulk materials, their physico-chemical characteristics, and cell biological outcomes [10–18].

| Materials | Chemistry | WCA (°) | Zeta Potential (Mv) | XPS (%) | Surface Energy (mN/m) | In Vitro Cell Behavior | Published |
|---|---|---|---|---|---|---|---|
| Silicon-titanium microgrooves, 20 × 2 μm (ZfM) | PPAAm; methyl-carboxyl-plasma polymer, COL-I, RGD; 480 s gross | 57° | +**8.6** at pH 7.4 | N/C 31<br>O/C 4 | – | Abrogated MG-63 cell contact guidance; randomly oriented actin stress fibers, PPAAm vs. all coatings | Moerke C et al., ACS Applied Material Interfaces, 2017 [10] |
| Ti-6Al-4V plasma chemical oxidation (PCO) | PPAAm; 60 s gross, 960 s gross | 57–60° | positively charged, by AFM | N/C 32<br>O/C 2<br>$NH_2$/C 2.8 | polar 16<br>disperse 30<br>total 46 | Accelerated MG-63 cell-surface interlocking, actin formation around the pores of porous ceramics; 3-fold increase of cell area (30 min) | Rebl H et al., Materials Science and Engineering C, 2016 [11] |
| β-tricalcium phosphate hybrid scaffolds | PPAAm; 960 s gross | – | – | N/C 29<br>O/C 10<br>$NH_2$/C 2.5 | – | Continuous cellularization of hybrid 3D scaffolds (14 day); DNA concentration at the bottom 7.7-fold higher; MG-63 cell migration enhanced | Bergemann C et al., Materials Science and Engineering C, 2016 [12] |
| Ti-6Al-4V, cp, grade 2, polished | PPAAm; 960 s gross | 47° after prep.<br>40–50° after 360 days storage on air | +**13.9** (2 days)<br>+**20.9** (20 days)<br>+**26.3** (200 days)<br>at pH 6 | N/C 27<br>O/C 6<br>$NH_2$/C 2.5 | polar 25<br>disperse 29<br>total 54 | Aging and γ-sterilization of PPAAm; maintenance of cell adhesion capacity up to 360 day<br>2.2-fold and 1.6-fold increased cell areas (30 min, 24 h, resp.); cell area still visibly larger after 360 days of storage in air (5, 10, 30, 60 min, 24 h) | Finke B et al., Langmuir, 2014 [13] |
| Electrospun poly(L-lactide-co-D/L-lactide) mesh | PPAAm; (preactivation in Ar/$O_2$ plasma) 480 s gross | 5° | – | N/C 28<br>O/C 5<br>$NH_2$/C 2.5 | polar 40<br>disperse 28<br>total 68 | SV40-HUC-1 uroepithelial cells, Ca9-22 gingiva epithelial cells: enhanced cell integration in PLA fiber meshes; SV40-HUC-1 cell area: 1.26-fold, Ca9-22 cell area: 1.35-fold (both 30 min), spreading not influenced by γ-sterilization | Schnabelrauch M et al., International Journal of Polymer Science, 2014 [14] |
| Ti, cp, grade 2, P—polished, M—machined, CB—corund. blasted | PPAAm; PEG DA-COL-I, GDA-COL-I, 960 s gross | 47° P-PPAAm<br>56° M-PPAAm<br>41° CB-PPAAm | – | – | P-PPAAm total 55<br>M-PPAAm total 50<br>CB-PPAAm total 57 | Impact of plasma chemistry versus Ti surface topography: MG-63 cells literally melt into the groove structure; fewer elongated cells; 4.7-fold increased cell adhesion (5 min); 2.3-fold increased cell area (30 min) | Rebl H et al., Acta Biomaterialia, 2012 [15] |
| Borofloat glass | PPAAm; COL-I; 960 s gross | 50° | +**14** at pH 6 | N/C 20<br>O/C 11<br>$NH_2$/C 2–3 | – | Enhanced vinculin mobility (1.5-fold, nm/min) in vital MG-63 cells; 1.5-fold increased vinculin contact length; 3.7-fold increase of cell area (30 min); all vs. COL-I | Rebl H et al., Advanced Engineering Materials, 2010 [16] |
| Bionas® 2500 metabolic sensor chips SC 1000 | PPAAm; 120 s gross | 45° | +**14** at pH 6 | N/C 20<br>O/C 14 | polar 27<br>disperse 27<br>total 54 | MG-63 cell coverage of chips 2-fold, 72%; cell area increased 1.9-fold (4 h); vital cell adhesion significantly higher (0–24 h), e.g., 2.31-fold (2 h); acidification and oxygen consumption not influenced | Rebl H et al., International Journal of Artificial Organs, 2010 [17] |
| Ti, cp, grade 2 polished | PPAAm, PEG DA-COL-I, COL-I; 960 s gross | 48° | +**7.7** at pH 6 | N/C 28<br>O/C 4<br>$NH_2$/C 2.5 | – | Hyaluronan-mediated MG-63 cell adhesion; cell adhesion increased 7-fold (15 min); accelerated formation of actin cytoskeleton and paxillin and vinculin (60 min), vs. Ti-P, comparable with collagen coatings | Finke B et al., Biomaterials, 2007 [18] |

*1.2. In Vitro Outcome*

The plasma-chemical modification with PPAAm of all these different biomaterial surfaces enormously improved initial cell adhesion, spreading, organization of adhesion-related components, and the cell ingrowth into the structured material surfaces (Table 1) [10–18]. The cells were strongly attached to the surface; this was detected by a spinning disk device [25]. Whereas the bone cell (MG-63) adherence was lowest on uncoated Ti6Al4V disks (44.2 ± 9.0 N/m$^2$), on PPAAm-coated (66.8 ± 12.0 N/m$^2$) and plasma polymerized ethylenediamine (PPEDA)-coated (53.2 ± 8.3 N/m$^2$) Ti6Al4V disks, a significantly higher shear stress was necessary to detach the cells from the PPAAm/PPEDA surface, indicating a stronger cell attachment (after 18 h of cell growth).

The osteoblasts displayed an extremely flattened phenotype and the cells seemed to merge with the topography of the surface. These highly cell-attractive characteristics of the PPAAm layer remain even after long-term storage up to one year or after γ-sterilization [13]. If cells grow on micro-grooved surfaces, the cells were aligned parallel to the grooves; this is called "contact guidance". The functionalization of geometrically micro-grooved surfaces (20 µm groove width) with PPAAm resulted in an astonishing cell behavior: Although PPAAm is only a nanolayer, the cells were no longer able to "feel" the underlying grooves and the contact guidance was abrogated due to the chemistry on the surface [10]. We could observe this behavior also on PPAAm-coated, machined Ti surfaces: MG-63 cells could overcome the restrictions of the stochastically grooved surface and spread out over a large area [15]. However, the actin fibers of the cells on machined Ti + PPAAm were not arranged in parallel; instead, their actin fibers could also overcome the alignment (Figure 1).

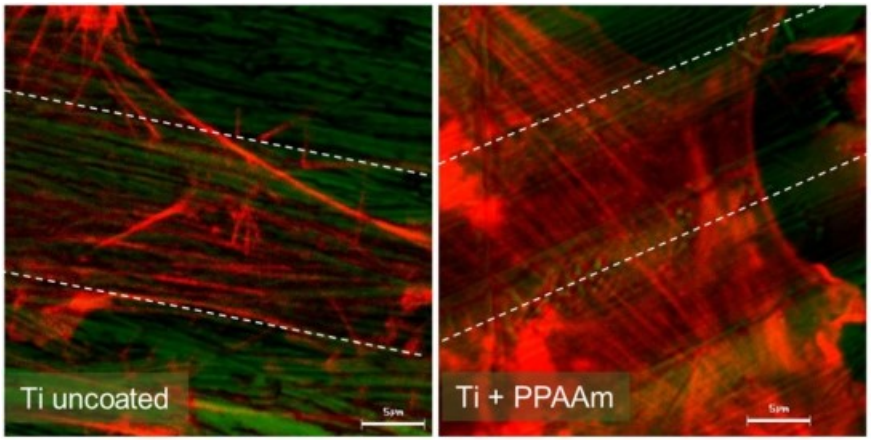


**Figure 1.** Cell alignment on stochastically structured Ti surfaces (Ti cp, grade 2, Ra 0.315 µm, [15]). Left: The actin filaments are aligned in the direction of the striations (dashed lines in grey) caused by machining. Right: Abrogated alignment due to PPAAm nanolayer coating of Ti (960 s gross) [15]. Technical description: Confocal laser scanning microscopy (LSM 410, Carl Zeiss AG, Oberkochen, Germany), scale bar 5 µm, actin staining (red) with Alexa Fluor 546 phalloidin, Ti surface in reflection mode false colored in green.

Our latest investigations by Moerke et al. [26] revealed that the restricted functions of osteoblasts on Ti micropillars (dimension 5 × 5 × 5 µm) are alleviated by nanocoating the surface with PPAAm. Human MG-63 cells growing on Ti micropillars normally express less mRNA of collagen type I, osteocalcin, and fibronectin after 24 h. This could be attenuated by coating of the micropillars with PPAAm. Although PPAAm is only a nanolayer, the influence was impressive and significant. At the same time, we saw cells very sensitive to the kinetics of calcium signaling on PPAAm-coated micropillars: After ATP stimulation, the intracellular calcium ion level increased impressively. The basal calcium ion content of cells on PPAAm was also significantly higher compared with uncoated Ti surfaces [26] as seen in the depiction (Figure 2). This is an indication that

cells on PPAAm are very active in their cell physiology and it could explain why all the adhesion-related cell functions are accelerated.

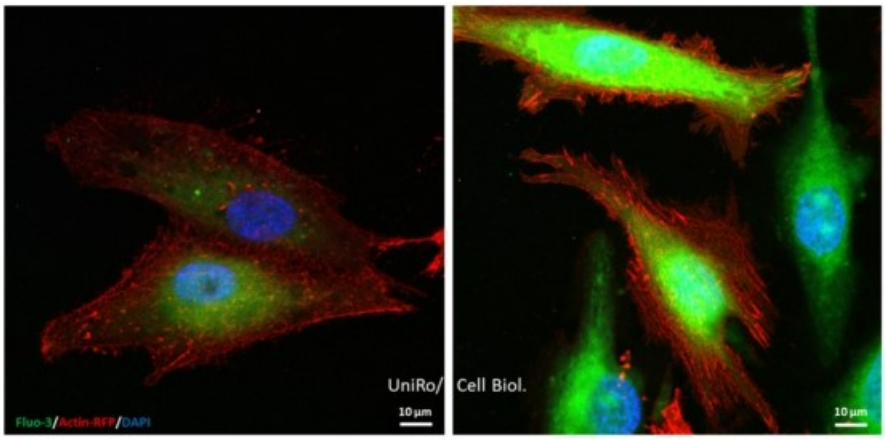


**Figure 2.** Basal calcium ion levels (green) in living MG-63 osteoblasts (red for actin, blue for nucleus) 24 h on planar Ti, either uncoated (**left**) or coated with a nanolayer of the plasma polymer (PPAAm, 480 s gross) (**right**). Note that on PPAAm, the intracellular basal $Ca^{2+}$ ion level is elevated, indicating higher cellular activity. Live-cell staining: 50,000 cells/$cm^2$ Ti wafer in DMEM with 10% FCS, staining with 20 µL BacMam 2.0 reagent (red) (actin-RFP, Life Technologies Corporation, Eugene, Oregon, USA) at 37 °C, 5 µM calcium indicator Fluo-3/AM (green) (Life Technologies Corporation) [27,28], and 1:1000 Hoechst 33342 (blue) (Thermo Fisher Scientific, Waltham, Massachusetts, USA) in isotonic HEPES buffer. Confocal laser scanning microscopy (LSM 780, Carl Zeiss Microscopy GmbH, Jena, Germany) with a plan-apochromat 63× oil immersion objective (Carl Zeiss, 1.40. Oil DIC M27), excitation at 405, 488, and 561 nm; scale bars 10 µm.

### *1.3. In Vivo Outcome*

The inflammatory response after implantation plays a central role for the in vivo biocompatibility of an implant, with macrophages and other immune cells being of central importance [29].

To examine the influence of PPAAm films on the inflammatory response, Ti plates were coated with PPAAm and implanted intramuscularly in a rat model [30]. In this study, each animal simultaneously received an uncoated Ti implant and three Ti implants with PPAAm films created with different plasma process parameters. After 7, 14, and 56 days, the implants were removed together with the peri-implant tissue to quantify the number of total and tissue macrophages as well as total T-lymphocytes and MHC class II positive antigen-presenting cells following immunohistochemical staining. Based on experience from other studies, the different implantation periods were chosen to represent the acute phase of inflammation (day 7), the transition from acute to chronic inflammation (day 14), and the chronic phase of inflammation (day 56) typical for implant-related inflammation. On day 14, all three PPAAm-coated sample series demonstrated a significantly lower response of total macrophages than the uncoated samples. On day 56, the two-sample series that received a PPAAm variant with a shorter gross processing time still had a significantly lower number of total macrophages than the untreated samples (Figure 3). Taken together with the data from the physico-chemical analysis, these results indicate that different plasma process parameters lead to variations in the PPAAm film properties which influence the local inflammatory reactions.

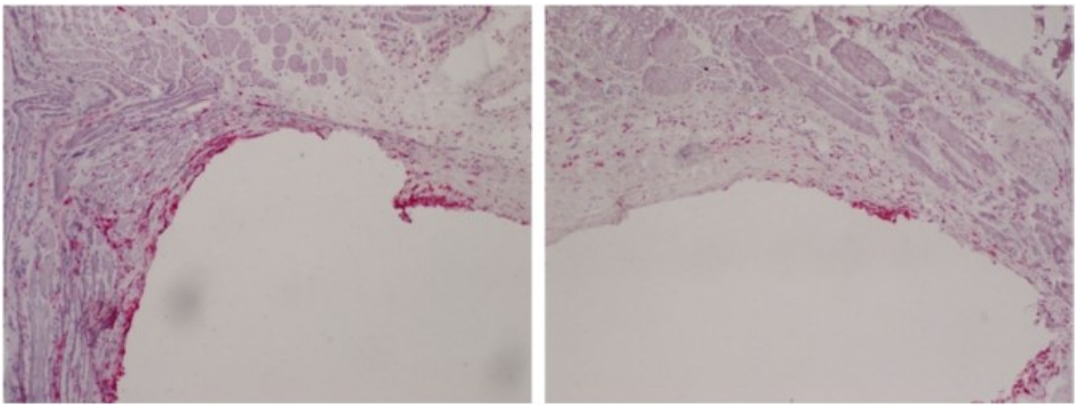

**Figure 3.** Total monocytes/macrophages ($CD68^+$) in the peri-implant tissue 56 days after intramuscular implantation into rats of an unmodified Ti plate (**left**) vs. a PPAAm-coated Ti plate (**right**). Note the reduced macrophage response for PPAAm samples. Method: Peri-implant tissue samples were immediately shock-frozen after explantation and, following careful removal of the Ti plates, processed as cryosections (5 µm) and stained with monoclonal antibody ED1 (mouse anti-CD68); image magnification 125×.

Antibacterial surface modifications could prevent infections frequently associated with the implantation of biomaterials. In this regard, a surface modification with copper (Cu) could be an interesting approach. A surface treatment called plasma immersion ion implantation of copper (Cu-PIII) resulted in incorporation of copper ions into the topmost $TiO_2$ layer. While implants treated with Cu-PIII had antibacterial properties in vitro, preliminary in vivo data revealed a stronger local inflammatory response after 56 days and a sustained increase of the IL-2 serum concentration. Thus, the hypothesis that an additional PPAAm film on Cu-PIII-treated Ti6Al4V samples could reduce these Cu-induced inflammatory reactions was tested in another study in rats. The results demonstrated that Cu-PIII-treated Ti6Al4V plates with an additional PPAAm coating induced local inflammatory tissue reactions comparable with untreated samples, while Cu-PIII-treated samples without PPAAm caused significantly stronger reactions in the chronic phase for several inflammatory cells [31].

Furthermore, the serum profile of different pro- and anti-inflammatory cytokines after implantation of Ti plates with PPAAm films or plasma polymerized acrylic acid films (PPAAc) in rats was examined to characterize the systemic inflammatory response. It was found that the different plasma modifications caused distinct serum cytokine profiles, which were as a whole comparable between the PPAAm samples and the untreated controls, while the PPAAc samples differed markedly from both PPAAm and controls [32]. The serum cytokine profile for the PPAAm samples also indicated two distinct phases of the systemic inflammatory response, possibly caused by time-dependent changes in the physico-chemical properties of PPAAm as described earlier [30]. The associations between the cytokine serum concentrations and different inflammatory cell populations were additionally examined by a multivariate correlation approach, revealing that high IFNγ concentrations in the early phase were associated with a high number of pro-inflammatory $CD68^+$ monocyte/macrophages in the late phase [33]. This observation indicates that IFNγ could possibly be a serum marker to predict the local tissue response after implantation and associated implant-related complications.

In another in vivo approach using the rat femur, the osseointegration of Ti alloyed implants modified by PPAAm as well as plasma polymerized ethylenediamine (PPEDA) were evaluated [25]. Whereas uncoated Ti alloys showed the lowest bone-to-implant contact zone (BIC) (40.4%), the PPAAm and the PPEDA coatings revealed a clear increase of the BIC with 58.5% and 63.7%, respectively, indicating enhanced bone on growth [25].

We suggest that this amino-group-containing plasma polymer nanolayer (PPAAm) improves the cell–material interaction at the interface of diverse biomaterial surfaces, e.g., metals, polymers, calcium phosphates. Thus, we expect an improvement of the clinical outcome of permanent implants.

In this regard, we wanted to ascertain if PPAAm is also suitable to increase the attractiveness of a ceramic surface for dental implants. In recent years, these ceramic substrates were moved further into the center of healthcare, replacing metallic implant materials especially for patients with allergies. Building on our findings on PPAAm surface coatings of diverse bulk materials, the aim of our paper was to describe the interaction of MG-63 osteoblasts with very thin PPAAm films deposited on zirconia ceramic surfaces.

## 2. Materials and Methods

### *2.1. Substrates*

Titanium: Disks of polished titanium (Ti), technical purity, cp grade 2 (Ra 0.2 µm) or titanium alloy (Ti6Al4V; Ra 0.4 µm), 11 mm in diameter and a height of 1 mm were used for comparison purposes as reference materials and for the chemical surface characteristics.

Furthermore, planar silicon (Si)-wafers (1 × 1 cm) were sputter-coated with 100 nm titanium (Ti, ZfM, Chemnitz, Germany) [10]. The resulting average surface roughness (Ra) was 0.774 nm, measured by atomic force microscopy (JPK Instruments, Berlin, Germany, [10]). The planar Si/Ti wafers were used to evaluate the optimal PPAAm plasma process duration and its resulting layer thickness on cell attachment.

Ceramics: Yttria-stabilized tetragonal zirconia polycrystals (Y-TZP, see patent) as a source material for dental implants were produced according to the same standard ISO 13356:1997. The material parameters such as density, the ratios of $ZrO_2$, $Y_2O_3$, $HfO_2$, and $Al_2O_3$, grain size, and the minimum bending strength are defined precisely by that norm. In this way, identical Y-TZP ceramic materials are ensured. Disks of Y-TZP, 13–20 mm in diameter and 2 mm thick with smooth or rough topographies (root-mean-squared-roughness Rq 273 ± 40 nm and Rq 1320 ± 20 nm, respectively) were utilized for the chemical functionalization, physico-chemical analysis, and in vitro cell culture. The roughnesses were determined with the profiler Dektak 3ST (Veeco Instruments, Santa Barbara, CA, USA; radius of the standard diamond stylus 2.5 mm, stylus force 30 mg, scan length 500 mm; 100 measurements/sample) (see Patent, chapter 5).

### *2.2. Deposition of Plasma Polymerized Allylamine (PPAAm)*

Titanium: To determine the minimal possible layer thickness that allows cells to spread optimally, we evaluated the preconditions for the plasma deposition on the planar Ti wafers. The Ti wafers were coated by plasma polymerized allylamine (PPAAm) for 60 s (layer thickness <10 nm) or 480 s gross (layer thickness ~25 nm). Further preparation details are found in the following section. Ceramics: The microwave (MW) plasma reactor V55G (2.45 GHz; 60 L, Plasma Finish, Wertheim, Germany) was used for the deposition of the PPAAm films of different coating thicknesses. The substrates were in a downstream position 9 cm below the MW coupling window. First, the substrates were decontaminated and activated by continuous wave (cw) oxygen plasma (500 W, 50 Pa, 100 sccm $O_2$, 300 s cw) and subsequently followed, without breaking the vacuum, by coating with PPAAm using allylamine as a precursor. A MW gas-discharge plasma (500 W) with a pulsed deposition regime (0.3 s on/1.7 s off) at low pressure ($p$ = 50 Pa) was used for the coating. All samples were prepared under these identical standard plasma process conditions. Only the gross treatment time was varied from 960, 480, 240, 180, 120, 90, 60, 30, to 15 s [34]. Thin and very thin PPAAm films were realized dependent on the treatment time. A calibrated needle valve (0.125 ± 0.009 mL/min) allowed exact dosing of the monomer allylamine ($H_2C$=CH-$CH_2$-$NH_2$) (VWR International GmbH, Darmstadt, Germany). Argon was used as a carrier gas (50 sccm).

### *2.3. Surface Characterization*

#### 2.3.1. Grazing Incidence X-ray Diffraction (GIXRD), X-ray Photoelectron Spectroscopy (XPS), Fourier-Transform Infrared Spectroscopy FT-IR

GIXRD using a Siemens D5000 AXS diffractometer with Cu Kα radiation at 40 kV and 40 mA was carried out in order to study the crystallographic structure of the untreated and plasma-treated ceramic samples used. The measurements were performed at a constant incident angle of ω = 0.5° relative to the sample surface, over a range of 2 θ from 10° to 60°, with a step width of 0.02° and data collection time of 5 s per step.

The elemental chemical surface composition of the PPAAm thin films were determined by high-resolution scanning X-ray photoelectron spectroscopy (XPS). The Axis Ultra DLD electron spectrometer (Kratos Analytical, Manchester, UK) runs with monochromatic Al Kα radiation (1486 eV; 150 W), implemented charge neutralization, and a pass energy of 80 eV for estimating the chemical elemental composition. The spot size was 250 µm. On each sample, three spots were measured and averaged in different positions. The takeoff angle was 90° in all cases.

Data acquisition and processing was carried out with the "vision 2.1.3" software (operating software Kratos) [13]. The labeling of primary amino groups was performed with 4-trifluoromethyl-benzaldehyde (TFBA, Alfa Aesar, Haverhill, MA, USA) at 40 °C over a saturated gas phase of 2 h. The density of the amino groups $NH_2$/C was determined from the fluorine elemental fraction [35].

The chemical composition and molecular structure of PPAAm thin films were analyzed by means of FT-IRRAS (FT-IR Type: Spectrum One, PerkinElmer, Waltham, MA, USA) [36]. The spectra were obtained at the spectral resolution of 4 $cm^{-1}$, with the number of scans at 32 in the wavenumber region 4000 to 600 $cm^{-1}$.

### 2.3.2. Film Thickness, PPAAm Roughness

The thickness of the deposited films was determined by surface profilometry. The film thickness can be measured solely on very smooth surfaces; therefore, silicon wafers were used and coated in the same plasma process together with the ceramic samples. For this purpose, before coating, very thin strips of cellulose acetate were deposited across the substrate surfaces. After film deposition, the acetate strip was removed. The height of the step obtained between the coated and uncoated surface area was determined with the help of the surface profiler (Dektak3ST, Veeco Instruments, Santa Barbara, CA, USA). Every sample was measured at a minimum of three different positions. Tests by spectroscopic ellipsometry (SE 850 spectroscopic ellipsometer, SENTECH Instruments, Berlin, Germany) confirmed the correctness of this method.

Surface roughness was determined using the scanning probe microscope diCP2 (Veeco Instruments) in non-contact mode (cantilever MPP111, Veeco Instruments) with a tip radius of 10 nm before and after PPAAm film deposition on silicon wafers (Universitywafers.com). The roughness Rq was calculated on a 10 µm × 10 µm wide area.

### 2.3.3. Surface Free Energy, Contact Angle, Zeta Potential

The surface energy with its polar and disperse components was calculated from measurements of contact angles of three different liquids: Water, ethylene glycol, and methylene iodide. The contact angles were measured by the sessile drop method (drop volume ~0.5 µL) using the measuring system OCA30 (Data Physics Instruments GmbH, Filderstadt, Germany) and the software SCA 20. The surface energy was calculated using the methods of Owens, Wendt, and Rabel [37,38]. These measurements were always performed within 30–60 min after sample preparation at five different positions along the ceramic surface [39].

Existing surface charges can be estimated by determining the so-called zeta potential. Streaming potential measurements were carried out for various pressures using the Electrokinetic Analyzer SurPass (Anton Paar Germany GmbH, Ostfildern, Germany) to determine the streaming potentials dependent on the pressure. The measurements were performed in a 0.001 mol/L KCl solution ranging from pH 6.0 to 8.0 with a gap height of 100 µm. The streaming current was determined depending on the pressure (max. 300 mbar). Finally, the surface charge was calculated according to the method of Helmholtz–Smoluchowski. Measurements were performed in quadruplicate on two independent samples.

*2.4. Cell Culture Experiments*

The experiments were performed with the human osteoblast-like cell line MG-63 (CRL1427™, ATCC®, American Type Culture Collection, Manassas, VA, USA). MG-63 cells are a suitable in vitro-model for basic bone-related research, as the cell morphology, expression of adhesion receptors (e.g., $\alpha$1-5, $\alpha$v, $\beta$1-3, $\beta$5, CD44, syndecans), cell cycle phases (G0, S, G2/M), and intracellular signaling molecules (e.g., p-p38 MAPK, pERK, p-Akt, and intracellular $Ca^{2+}$) are stable over the passages 5 to 30, as Staehlke et al. discovered recently [40].

Titanium: For the experiments with Ti samples, the cells were cultured in Dulbecco's Modified Eagle's Medium (DMEM) (Life Technologies, Thermo Fischer Scientific, Waltham, MA, USA, #31966021) containing 10% fetal calf serum (FCS) (Biochrom FCS Superior, Merck KGaA, Darmstadt, Germany, #S0615) and 1% gentamicin (Ratiopharm GmbH, Ulm, Germany).

Ceramic: For the experiments with ceramic samples, the cells were cultured in DMEM (high glucose, Gibco Invitrogen, Karlsruhe, Germany), with 10% FCS (Gold, PAA, Pasching, Austria) for passaging or serum-free for the experiments and 1% gentamicin. Serum-free medium was used to avoid masking of the PPAAm-coated ceramic surface with proteins (soluble fibronectin) as described earlier [18]. The culture conditions were at 37 °C in a humidified atmosphere with 5% $CO_2$.

2.4.1. Cell Morphology

Titanium: The morphology of MG-63 cells on Ti samples after 1 h cell culture (30,000 cells/1 × 1 cm-wafer, in DMEM + 10% FCS) was analyzed by field emission scanning electron microscopy (FE-SEM, Merlin VP compact, Carl Zeiss Microscopy GmbH, Jena, Germany). The samples were fixed with 2.5% glutaraldehyde (Merck KGaA, Darmstadt, Germany) at 4 °C for at least 1 h. Samples were rinsed with 0.1% sodium phosphate buffer, dehydrated through a graded series of acetone (30% 5 min, 50% 5 min, 75% 15 min, 90% 10 min, 100% 2 × 10 min), and dried in a critical point dryer (K 850, EMITECH, Taunusstein, Germany), then gold sputtered with a coater (20 nm, SCD 004, BAL-TEC AG, Balzers, Liechtenstein). To image the cell morphology on the FE-SEM, an acceleration voltage of 5 kV, and a high-efficiency secondary electron detector were used.

Ceramic: The morphology of MG-63 cells on ceramic samples (series no. BK050, BK052) after 24 h of cell culture (serum-free DMEM) was examined using the SEM DSM 960A (Carl Zeiss). The samples were fixed with 4% glutaraldehyde (1 h), dehydrated through a graded series of acetone, dried in the critical point dryer, and sputtered with the coater as described above (see also patent, Chapter 5).

2.4.2. Actin Cytoskeleton

Titanium samples: The actin cytoskeleton organization (30,000 cells/well) was observed using the inverted confocal laser scanning microscope LSM 780 (Carl Zeiss Microscopy GmbH, Jena, Germany) equipped with an He–Ne laser (excitation: 543 nm), and ZEISS 63× Plan Neofluar oil immersion objective (1.25 oil/0.17). The MG-63 cells were grown on Ti samples for 1 h (DMEM + 10% FCS), and then fixed with 4% paraformaldehyde (PFA, Sigma-Aldrich, St Louis, MO, USA) at room temperature (RT) for 10 min and permeabilized with 0.1% Triton-X 100 (Merck) at RT for 10 min. For actin staining, cells were incubated with phalloidin-tetramethyl-rhodamine (TRITC, dilution 1:15 in phosphate buffer saline, Sigma-Aldrich) in the dark at RT for 30 min. Samples were embedded in the mounting medium Fluoroshield™ (Sigma-Aldrich) on a cover slip and stored in the dark at 4 °C. The software ZEN 2.3 software (ZEISS Efficient Navigation, ZEN 2.3, black edition, Carl Zeiss) was used for image acquisition.

Cell spreading: To quantify the cell area (in $\mu m^2$), we measured 40 TRITC-stained cells/sample using the software ImageJ 1.48a (Wayne Rasband, National Institutes of Health, Bethesda, MD, USA).

2.4.3. Cell Adhesion

Ceramic: Suspended MG-63 cells in serum-free DMEM were seeded onto the ceramic plates (Ø 20 mm; series no. BK034) at a density of $1 \times 10^4$/specimen for 10 min, and non-adherent cells in the

supernatant were counted and analyzed by flow cytometry (FACSCalibur, software CellQuest Pro 4.0.1, BD Biosciences, Franklin Lakes, NJ, USA). Cell adhesion was then calculated as a percentage of the cell number at 0 min. Three independent experiments were carried out.

### *2.5. Statistics*

Titanium samples: Statistics were performed by GraphPad Prism 7 software for Windows (GraphPad Software Inc., La Jolla, CA, USA). The spreading data (not normally distributed) were evaluated by non-parametric Kruskal–Wallis test post uncorrected Dunn's test.

Ceramic samples: The cell adhesion data were statistically evaluated by SPSS software 14.0 for Windows (SPSS Inc., Chicago, IL, USA). The differences were evaluated with Student's *t*-test.

All: In general, the normal distribution was established using the Kolmogorov–Smirnov test. Data were presented as mean ± standard error of mean (s.e.m.). Statistical significance was established at $p \leq 0.05$.

## 3. Results and Discussion

Plasma polymerized allylamine was deposited and investigated by us on a variety of materials (see Table 1). In recent years, we extended our work to anorganic oxide ceramic materials that should replace metallic implants for persons with allergies. So far, the influence of the plasma radiation on these ceramics was unknown.

The ceramic utilized for dental implants is a special yttrium-stabilized, tetragonal zirconia polycrystal (Y-TZP). The tetragonal crystal structure must be guaranteed for dental applications. It is known that the tetragonal crystallites can be transformed into their monoclinic modification under a volume expansion of ca. 3–5% followed by crack formation or break off of smaller particles; this can happen, for instance, via the influence of manual grinding or chemical manipulations [41,42]. Transformation toughening is responsible for the unique failure behavior of Y-TZP. Mechanical and/or chemical manipulations after sintering influence local phase transformations near the surface and reduce the toughness and crack resistance of the ceramic. The stability of the tetragonal crystal phase seems to be a problem [41].

Our aim was to determine both the applicability of the PPAAm layer on these crystalline zirconia ceramics and also the minimal possible film thickness that would allow cells to spread optimally. We carried out the standard plasma deposition process in dependence on the treatment time and described, among other things, the interaction of MG-63 cells with the PPAAm film deposited in different thicknesses on the Y-TZP ceramic.

### *3.1. Physico-Chemical Surface Properties of PPAAm-Treated Y-TZP Ceramic*

As a precondition for our further investigations, we studied the crystallographic structure of the ceramic substrate by X-ray diffraction analysis before and after plasma treatment to determine the influence of the plasma process.

The GIXRD analysis of the untreated and PPAAm-treated ceramic samples confirmed clearly, in agreement with the data file JCPDS 42-1164, the tetragonal crystal modification of Y-TZP (Figure 4). The undesired monoclinic phase was not detectable. The MW plasma process for the deposition of PPAAm has no influence on the tetragonal crystal structure of Y-TZP present.

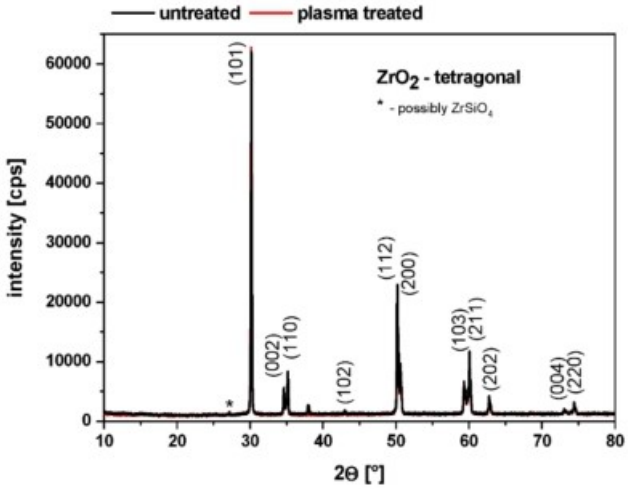


**Figure 4.** Grazing incidence X-ray diffraction (GIXRD) patterns of untreated and plasma polymerized allylamine (PPAAm) plasma-treated (960 s gross) tetragonal zirconia polycrystal (Y-TZP) ceramic.

The chemical composition and molecular structure of PPAAm thin films on ceramic (not shown) could be confirmed by means of FT-IRRAS. The FT-IRRAS spectra of PPAAm showed a high retention of the structural properties of the monomer allylamine $H_2C$=CH-$CH_2$-$NH_2$ for the MW plasma deposition method used here in accordance with [13].

A further approach in our investigations was the gradual reduction of the PPAAm film thickness. We searched for the minimal possible film thickness, which would allow cells to behave optimally. For all samples (Si-wafer), one and the same standard plasma process parameter was used, only the gross treatment times varied (see Section 2.2) and, therefore, the film thickness. A quasi-linear film growth could be found from 15 s until about 480 s (Figure 5). At 960 s, etching processes more frequently accompany the deposition process, followed by a greater degree of cross-linking of the plasma polymer, reduced film thickness, a loss of surface functional groups, and increasing WCA

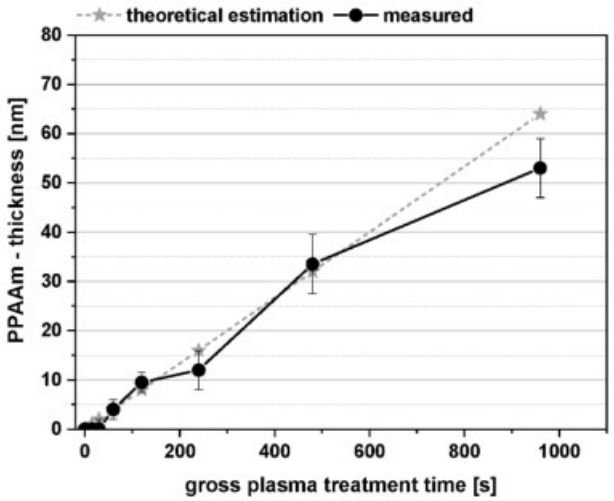


**Figure 5.** PPAAm film thickness dependent on the plasma treatment time determined on Si-wafers.

Layer formation and growth of the plasma polymer film PPAAm are of particular interest and can be explained by the results of Michelmore et al. [9] and Akhavan et al. [23]. They shed some light on the growth mechanisms of the very first layers of plasma polymer films, also for PPAAm. Michelmore et al. [9] verified a very smooth PPAAm film growth, and a continuous layer formation even for very thin films (<2 nm) from the very earliest stages on a silicon surface. The double bond in

the precursor allylamine encourages a better cross-linking in PPAAm and seems to contribute to the smooth layer formation. Island-like structures could be excluded for PPAAm. These results confirm our observations of very smooth PPAAm films (480 s: Rq = 1.9 ± 0.2 nm; 960 s: Rq = 3.8 ± 0.9 nm). Akhavan et al. were, again, able to demonstrate that the formation of metallic (zirconium/titanium-) carbide and oxycarbide bonds in the initial stages of the film formation led to the excellent film adhesion of the plasma polymer. A 2D-like, layer-by-layer (Frank-van der Merve mechanism) manner of growth was observed [23].

Plasma-treated surfaces are very reactive upon completion of the plasma deposition process. So-called post plasma processes, especially oxidation and hydrolysis, take place after storage in ambient air, influencing the wettability and surface energy by changing the surface chemical compositions. The wettability is determined by the charge and polarity of the surface functional groups. Therefore, the water contact angle (WCA) measurements were always carried out 30–60 min after the plasma process in each case, to get comparable results.

Figure 6 shows the WCA of untreated (time point 0 s) and PPAAm-coated smooth and rough ceramic surfaces as a function of the plasma treatment time. In the case of the smooth ceramic (Rq ~273 ± 40 nm), the WCA are in a range between 50° and 60° (54.9 ± 4.4°), whereas the WCA values of the rough ceramic (Rq~1320 ± 20 nm) vary more strongly between 40° and 60° (46.5 ± 12°) and are more hydrophilic than the smooth ceramic surfaces. For both roughnesses, the WCA are in the hydrophilic region in which the wettability is optimal for cell responses [24]. Even a very short plasma treatment time of 15 s is sufficient to shift the WCA of the untreated samples into the hydrophilic region, here especially apparent for the rough surfaces.

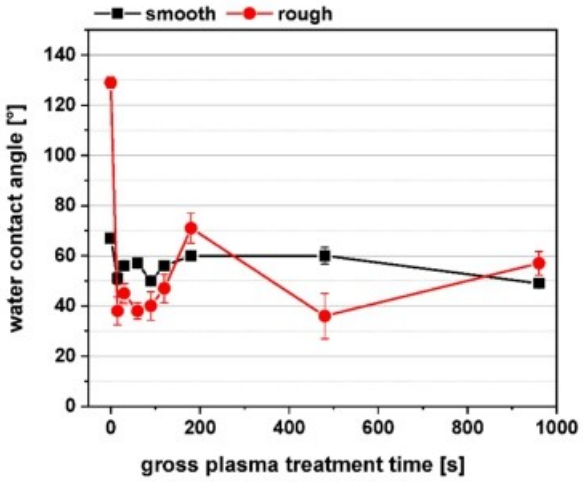


**Figure 6.** Water contact angles of untreated (time point 0 s) and PPAAm-coated smooth and rough ceramic. Note: Even a very short plasma treatment time of 15 s is sufficient to shift the water contact angles (WCA) of the untreated samples into the hydrophilic region. (Plasma treatment times: 15, 30, 60, 90, 120, 180, 480, and 960 s; $n = 5$).

The high WCA values of the untreated rough ceramic may be contributed to the enlargement of the effective surfaces area combined with higher hydrocarbon content. Our recent experiments by Rebl et al. [15] using polished and machined Ti showed similar tendency concerning WCA and roughness: For Ti-P (Ra 0.045 µm) and Ti-M (Ra 0.315 µm), the WCA values results in ca. 60° vs. 80°, respectively.

The zeta potential measured at pH 7 for the untreated rough zircon oxide ceramic is strongly negative at −53.1 ± 1.4 mV. The PPAAm nanofilm (480 s; on Si-Ti wafer) led to a positively charged surface (pH 6) at +32.8 ± 12 mV immediately after the deposition process and +35.5 ± 2 mV after 180 d storage in ambient air. The trend is consistent with our results in [13].

The surface energy and water contact angle of untreated and PPAAm-coated (120 and 960 s) smooth ceramic surfaces demonstrated that the PPAAm treatment led to an enhancement of the total

surface energy, including their polar and disperse parts (Figure 7A) and to decreasing WCA (Figure 7B). The total surface energy of the untreated smooth ceramic increased from about 37 ± 2 mN/m to about 50 ± 0.5 mN/m for both PPAAm coated surfaces (for 120 s and 960 s brutto, respectively). Also, the disperse and polar part of the surface energy increased on PPAAm. The disperse part of the untreated ceramic 24 ± 3 mN/m rose to 30 and 33 mN/m and the polar part of the untreated ceramic 14 ± 5 mN/m to 20 and 16 mN/m for 120 s and 960 s PPAAm. Furthermore, the shorter PPAAm treatment time of 120 s has a higher polar and lower disperse part than 960 s PPAAm. Possible reasons for this may be a lower influence of the etching processes or more surface functional groups through a lesser degree of cross-linking.

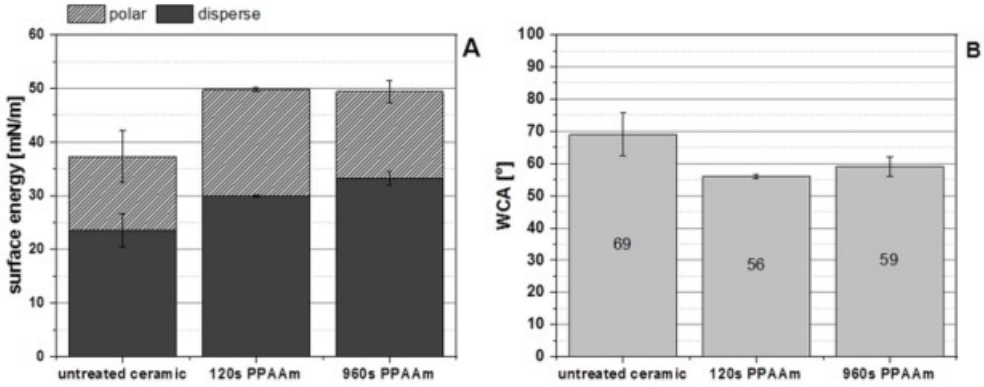


**Figure 7.** Surface energy (**A**) and water contact angle (**B**) of the untreated and PPAAm-coated smooth ceramic surface ($n$ = 3). Note the tendency toward enhanced surface energy (dispersed and polar part) and a reduced water contact angle (i.e., higher hydrophilicity) on PPAAm.

The XPS surface composition, as a function of the plasma treatment time (Figure 8) for smooth and rough ceramic surfaces shows that, with increasing treatment time, the ceramic surface will be covered systematically by the plasma polymer film PPAAm. The elements of the ceramic substrate Zr, Y, in slight traces Al, Si, Na, and also O disappeared; meanwhile, the components of PPAAm C and N increased. A complete covering by PPAAm is reached at about 200 s. The significantly higher roughness of the rough ceramic led to higher standard deviations in C, O, and N. Zr and Y are in the same dimensions as is the case for smooth ceramic surfaces.

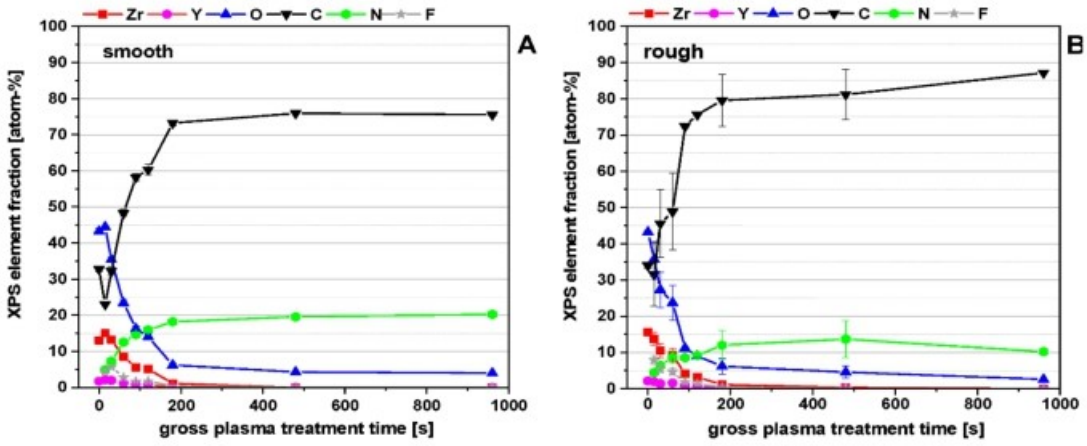


**Figure 8.** X-ray photoelectron spectroscopy (XPS) elemental content of PPAAm coating on a smooth (**A**) and rough (**B**) ceramic surface dependent on the treatment time. For a clearer presentation, the trace elements Al, Si, and Na were omitted.

The bar diagram (Figure 9) illustrates the surface composition of selected ceramic samples that were used in cell culture. The N/C ratios of PPAAm coatings for as little as 15 s is at 20% (not shown here) and

increases continuously: at 60 s to 26%, 120 s to 26.4%, 480 s to 25.8%, and 960 s to 26.8%, whereby the theoretical N/C value of the precursor allylamine is 33%. The PPAAm films formed until about 120 s of treatment time already contain a considerable number of nitrogen functional groups at the surface.

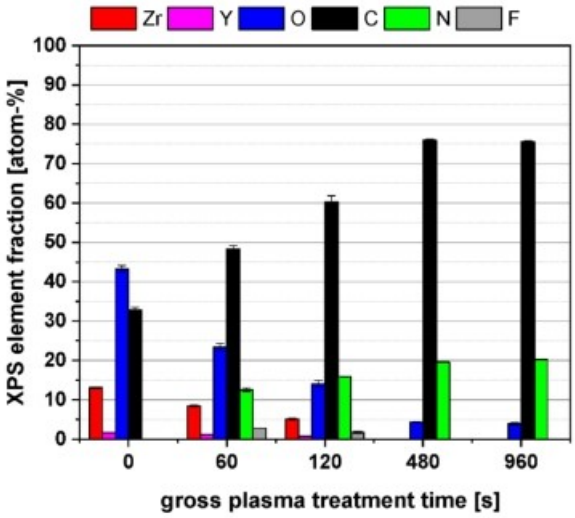


**Figure 9.** XPS elemental content after PPAAm coating of smooth ceramic dependent on the treatment time. The trace elements Al, Si, and Na were omitted.

Y-TZP ceramic surfaces that are negatively charged can be modified by the plasma polymer PPAAm under retention of the tetragonal crystal structure. Very smooth, positively charged PPAAm films could be deposited. In accordance with Michelmore et al. [9] and Akhavan et al. [23], a 2D-like, layer-by-layer (Frank-van der Merve mechanism) manner of growth can be assumed from the very earliest stages. Even short plasma treatment times led to PPAAm films with relatively high N/C ratios of about 20–26%. The WCA are optimal, lying in the hydrophilic range, and the total surface energy including their polar and disperse parts are enhanced on PPAAm. Thinner PPAAm films (<10 nm) seem to be beneficial in every respect and showed optimal conditions for adhesion and spreading of osteoblasts.

For future dental applications it is essential to evaluate the long-term stability of the PPAAm nanolayer on these Yttria-stabilized, tetragonal zirconia polycrystal ceramics (at least one year) as well as the in vivo effectiveness in the jawbone.

### *3.2. Cell Behavior on Titanium (Ti) and Ceramic Surfaces Bioactivated with Plasma Polymer (PPAAm)*

The plasma nanolayer PPAAm is convincing in its cell attractiveness. The 480 s plasma process on Ti, which results in a homogeneous nanolayer, allowed the cells to spread significantly in comparison with the uncoated Ti control, which we had already observed earlier [20]. In this work, it was of interest to determine whether a reduced plasma process time on Ti could induce the same spreading behavior. The PPAAm plasma treatment time of 60 s and 480 s gross, which corresponds to a layer thickness of about <10 nm and ~30 nm resp., revealed for both N/Cs ratios of about 26%. However, the cell-attractive characteristic of this nanolayer was obvious (Figure 10). After 1 h, cells on Ti PPAAm spread well and reached values of 1085.4 ± 55.5 $\mu m^2$ and 1365.6 ± 68.7 $\mu m^2$ for the PPAAm processes 60 s and 480 s, respectively (control: 713.8 ± 51.0 $\mu m^2$). The actin cytoskeleton is already more pronounced in stress fibers after a 60 s deposition time of plasma polymerized allylamine.

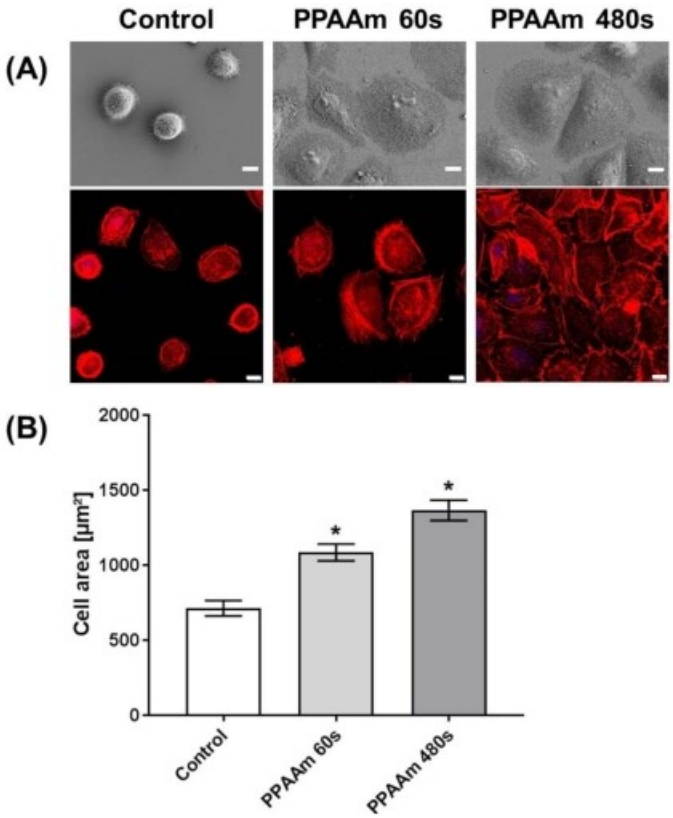


**Figure 10.** Impact of PPAAm plasma process duration and resulting nanolayer thickness on MG-63 cell morphology after 1 h on plane Ti. (**A**) Cell morphology (first row; FE-SEM Merlin VP compact, Carl Zeiss) and actin cytoskeleton (second row; LSM 780, Carl Zeiss); scale bars 10 µm. Note that the plasma process at 60 s gross is sufficient to significantly increase the cell area. (**B**) Cell area measurements (1 h) from the LSM actin images. ($n$ = 40 cells, mean ± s.e.m., Kruskal–Wallis test post hoc uncorrected Dunn´s test, * $p < 0.05$ vs. control).

Analogous to our investigations of PPAAm coatings on different materials (see Table 1), we prepared and analyzed the effects of conditioning ceramic surfaces with PPAAm, especially with regard to their further use as dental materials. The well-spread morphology also on PPAAm-coated ceramic surfaces is obvious (Figure 11). Ceramic on its own provides the cells with a surface characteristic, which leads to cell spread. In addition, the coating allows the cells to melt into the ceramic surface structure. The cells mimic the topography and the underlying structure appears through the flattened cell. These phenomena could also be observed with cells on metal surfaces, especially on corundum-blasted sharp-edged Ti coated with PPAAm, process duration 960 s gross resulting in a 50 nm layer [15]; or on plasma chemical oxidized surfaces additionally coated with PPAAm [11]. On PPAAm-modified ceramic, the cells are able to adhere immediately in the first 10 min and to a great degree of more than 80% compared with the untreated ceramic and the TCPS control at 81.4 ± 9.9%, 19.3 ± 2.9%, and 30.6 ± 4.7%, respectively (Figure 12).

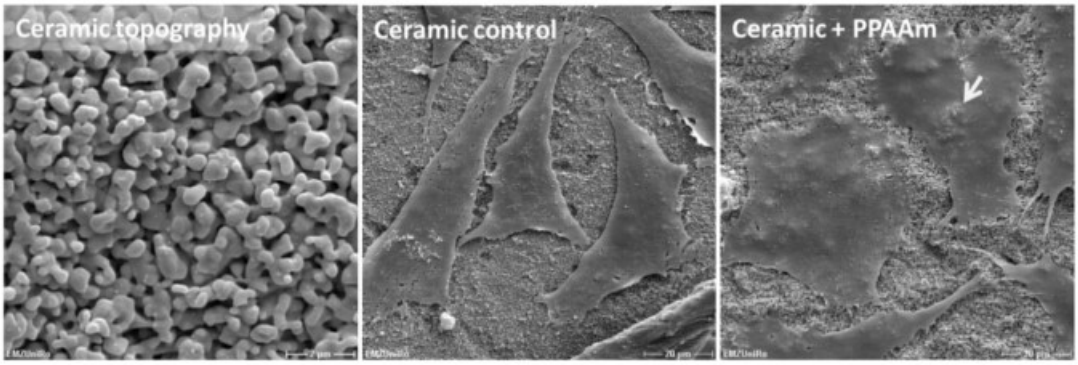


**Figure 11.** Cell morphology on plasma polymer (PPAAm)-modified rough ceramic after 24 h. The cell area on PPAAm (960 s gross) is increased and the cells melt into the underlying ceramic topography (arrow) in a way that the surface structures can be seen on the cell surface. (SEM DSM 960A, scale bars: left = 2 µm; middle and right = 20 µm, no. BK052).

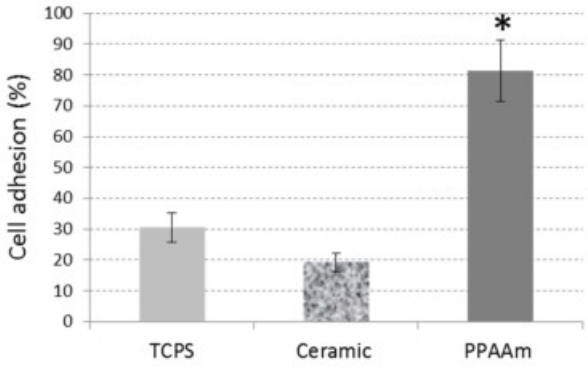


**Figure 12.** Initial cell adhesion (10 min) on plasma polymer modified smooth ceramic (PPAAm, 960 s gross). Flow cytometry, Student's *t*-test: PPAAm vs. bare ceramic (no. BK034) * $p < 0.01$, PPAAm vs. tissue culture plastic (TCPS) * $p < 0.05$; mean ± s.e.m., $n = 3$ independent experiments.

Summarizing all results with ceramic surfaces as well as other biomaterials tested (see Table 1), we can say that the moderately positively charged plasma polymerized allylamine (PPAAm) nanolayer is very cell attractive. This phenomenon can be seen in many cell biological concerns: (i) On PPAAm-modified materials, the cell spreading is very fast, cells are flattened, and cells melt into the surface structure [15], and (ii) this cell attractiveness leads to the next phenomenon that cells "forget" the underlying surface structure. This could be observed for the first time by our group. Normally, on material topographies, cells feel the underlying topography, i.e., cells are aligned on micro-grooves or machined Ti. But if these materials additionally PPAAm-modified, the cells not only adhere better and spread faster, but also override the topography [10,15].

## 4. Conclusions

Yttria-stabilized tetragonal zirconia polycrystal (Y-TZP) ceramic surfaces can be modified by the plasma polymer PPAAm under retention of the tetragonal crystal structure. The ceramic surface is negatively charged. Very smooth, positively charged PPAAm films could be deposited and a two-dimensional-like, layer-by-layer manner of growth can be assumed from the very earliest stages. Even short plasma treatment times led to PPAAm films with relatively high N/C ratios of about 20–26%. The WCA are in the optimal hydrophilic range. The surface energy is enhanced at ~50 mN/m independent from the plasma deposition time (120, 960 s) on ceramic. XPS revealed that components of PPAAm C and N reached their maximum already after a short plasma process. Thinner PPAAm films (<10 nm) seem to be beneficial in every respect and showed optimal conditions for adhesion

and spreading of human osteoblasts. Finally, we suggest that PPAAm as a cell-attractive nanolayer is also suitable for the bioactivation of dental implant surfaces.

## 5. Patent

A process for preparing ceramic implants for medical purposes. European patent specification. Vita Zahnfabrik H. Rauter GmbH & Co. KG, 79713 Bad Saeckingen (DE). Date of publication and mention of the grant of the patent: 22.03.2017, Bulletin 2017/12, Application number: 12753522.7, Date of filing: 05.09.2012. International application number: PCT/EP2012/067286. US14/236,740, US9, 241, 795, 26.01.2016.

**Author Contributions:** Conceptualization, J.B.N., B.F., M.S. and H.R.; methodology, B.F., J.B.N., M.S., H.R., S.S., M.G. and U.W.; investigations, B.F., J.B.N., M.S., U.W., H.R., S.S. and M.G.; data curation, B.F., M.S., H.R., U.W., S.S. and M.G.; Writing—Original Draft preparation, J.B.N., B.F., M.S., S.S., H.R., M.G. and U.W.; Writing—Review and Editing, J.B.N., B.F., H.R., S.S. and M.S.; visualization, B.F., H.R., S.S., M.S., U.W., M.G. and J.B.N.; supervision, J.B.N., B.F. and K.-D.W.; project administration, J.B.N., K.-D.W., M.S. and B.F.; funding acquisition, K.-D.W., J.B.N. and M.S.

**Funding:** The founding sponsors had no role in either the design of the study, the collection, analyses, or interpretation of data, the writing of the manuscript, or in the decision to publish the results.

**Acknowledgments:** This work was kindly supported by (i) the Federal Ministry of Education and Research (BMBF, Grants 13N9779, 13N9775, 13N11183, and 13N11188, Campus PlasmaMed), (ii) the Helmholtz Association in Germany (UR 0402210, VH-MV1), (iii) the German Research Foundation (DFG) priority program (SPP3221100, DFG NE560/3-4) as well as by (iv) the DFG Collaborative Research Centre (CRC) ELAINE 1270 for MG. We would also like to thank the VITA Zahnfabrik H. Rauter GmbH & Co. KG Bad Saeckingen for providing us with the ceramic samples and for the financial support. We are grateful to Urte Kellner, Dagmar Jasinski, Uwe Lindemann, Gerd Friedrichs, Andre Schella, Antje Quade and Katja Fricke from INP e.V. Greifswald for plasma-technical assistance. We acknowledge the technical support for SEM from the Electron Microscopic Center of the Rostock University Medical Center (Marcus Frank). We acknowledge being given the possibility of measuring the zeta potential in the Department Life, Light & Matter of the University of Rostock.

**Conflicts of Interest:** The authors declare there are no conflict of interest.

## References


1. Rebl, H. Osteoblast Physiology and Morphology on Cell Adhesive Plasma-Polymerized Allylamine and Ethylenediamine Layers. Ph.D. Thesis, University of Rostock, Rostock, Germany, 2014; p. 51.
2. Nebe, J.B.; Luethen, F. Integrin- and hyaluronan-mediated cell adhesion on titanium—Hyaluronan-mediated adhesion. In *Metallic Biomaterial Interfaces*, 1st ed.; Breme, J., Kirkpatrick, C.J., Thull, R., Eds.; WILEY-VCH: Weinheim, Germany, 2008; pp. 179–182, ISBN 978-3-527-31860-5.
3. Finke, B.; Lüthen, F.; Schröder, K.; Nebe, B.; Rychly, J.; Ohl, A. Amino functionalized titanium—A surface for improved osteoblast´s function. In Proceedings of the 18th International Symposium on Plasma Chemistry (ISPC-18), Kyoto, Japan, 26–31 August 2007; p. 692.
4. Goreham, R.V.; Mierczynska, A.; Smith, L.E.; Sedev, R.; Vasilev, K. Small surface nanotopography encourages fibroblast and osteoblast cell adhesion. *RSC Adv.* **2013**, *3*, 10309.
5. Liu, X.; Feng, Q.; Bachhuka, A.; Vasilev, K. Surafce modification by allylamine plasma polymerization promotes osteogenic differentiation of human adipose—Derived stem cells. *ACS Appl. Mater. Interfaces* **2014**, *6*, 9733.
6. Griffin, M.F.; Ibrahim, A.; Seifalian, A.M.; Butler, P.E.M.; Kalaskar, D.M.; Ferretti, P. Chemical group-dependent plasma polymerization preferentially directs adipose stem cell differentiation towards osteogenic or chondrogenic lineages. *Acta Biomater.* **2017**, *50*, 450.
7. Chaves, C.; Alshomer, F.; Palgrave, R.G.; Kalaskar, D.M. Plasma surface modification of polyhedral oligomeric silsequioxane-poly(carbonate-urea) urethane with allylamine enhances the response and osteogenic differentiation of adipose-derived stem cells. *ACS Appl. Mater. Interfaces* **2016**, *8*, 18701.
8. Macgregor, M.; Sinha, U.; Visalakshan, R.M.; Cavallaro, A.; Vasilev, K. Preserving the reactivity of coatings plasma deposited from oxazoline precursors—An in depth study. *Plasma Process Polym.* **2018**, doi:10.1002/ppap.201800130.
9. Michelmore, A.; Martinek, P.; Sah, V.; Short, R.D.: Vasilev, K. Surface morphology in the early stages of plasma polymer film growth from amine containing monomers. *Plasma Process Polym.* **2011**, *8*, 367–372, doi:10.1002/ppap.201000140.
10. Moerke, C.; Rebl, H.; Finke, B.; Dubs, M.; Nestler, P.; Airoudj, A.; Roucoules, V.; Schnabelrauch, M.; Koertge, A.; Anselme, K.; et al. Abrogated cell contact guidance on amino-functionalized micro-grooves. *ACS Appl. Mater. Interfaces* **2017**, *9*, 10461–10471, doi:10.1021/acsami.6b16430.
11. Rebl, H.; Finke, B.; Schmidt, J.; Mohamad, H.S.; Ihrke, R.; Helm, C.A.; Nebe, J.B. Accelerated cell-surface interlocking on plasma polymer-modified porous ceramics. *Mater. Sci. Engin. C* **2016**, *69*, 1116–1124, doi:10.1016/j.msec.2016.08.016.
12. Bergemann, C.; Cornelsen, M.; Quade, A.; Laube, T.; Schnabelrauch, M.; Rebl, H.; Weißmann, V.; Seitz, H.; Nebe, B. Continuous cellularization of calcium phosphate hybrid scaffolds induced by plasma polymer activation. *Mater. Sci. Eng. C* **2016**, *59*, 514–523, doi:10.1016/j.msec.2015.10.048.
13. Finke, B.; Rebl, H.; Hempel, F.; Schäfer, J.; Liefeith, K.; Weltmann, K.-D.; Nebe, J.B. Ageing of plasma-polymerised allylamine nanofilms and the maintenance of their cell adhesion capacity. *Langmuir* **2014**, *30*, 13914–13924, doi:10.1021/la5019778.
14. Schnabelrauch, M.; Wyrwa, R.; Rebl, H.; Bergemann, C.; Finke, B.; Schlosser, M.; Walschus, U.; Lucke, S.; Weltmann, K.-D.; Nebe, J.B. Surface-coated polylactide fiber meshes as tissue engineering matrices with enhanced cell integration properties. *Int. J. Polym. Sci.* **2014**, *2014*, 439784, doi:10.1155/2014/439784.
15. Rebl, H.; Finke, B.; Lange, R.; Weltmann, K.-D.; Nebe, B. Impact of plasma chemistry versus titanium surface topography on osteoblast orientation. *Acta Biomater.* **2012**, *8*, 3840–3851. doi:10.1016/j.actbio.2012.06.015.
16. Rebl, H.; Finke, B.; Rychly, J.; Schröder, K.; Nebe, J.B. Positively charged material surfaces generated by plasma polymerized allylamine enhance vinculin mobility in vital human osteoblasts. *Adv. Eng. Mater.* **2010**, *12*, 356–364, doi:10.1002/adbi.200900070.
17. Rebl, H.; Finke, B.; Schroeder, K.; Nebe, J.B. Time-dependent metabolic activity and adhesion of human osteoblast-like cells on sensor chips with a plasma polymer nanolayer. *Int. J. Artif. Org.* **2010**, *33*, 738–748.
18. Finke, B.; Luethen, F.; Schroeder, K.; Mueller, P.D.; Bergemann, C.; Frant, M.; Ohl, A.; Nebe, J.B. The effect of positively charged plasma polymerization on initial osteoblastic focal adhesion on titanium surfaces. *Biomaterials* **2007**, *28*, 4521–4534, doi:10.1016/j.biomaterials.2007.06.028.
19. Kunz, F.; Rebl, H.; Quade, A.; Matschegewski, C.; Finke, B.; Nebe, J.B. Osteoblasts with impaired spreading capacity benefit from the positive charges of plasma polymerized allylamine. *Eur. Cell Mater.*

**2015**, *29*, 177–189, doi:10.22203/eCM.v029a13.
20. Nebe, B.; Lüthen, F.; Finke, B.; Bergemann, C.; Schröder, K.; Rychly, J.; Liefeith, K.; Ohl, A. Improved initial osteoblast's functions on amino-functionalized titanium surfaces. *Biomol. Eng.* **2007**, *24*, 447–454, doi:10.1016/j.bioeng.2007.07.004.
21. Fritsche, A.; Haenle, M.; Zietz, C.; Mittelmeier, W.; Neumann, H.G.; Heidenau, F.; Finke, B.; Bader, R. Mechanical characterization of anti-infectious, anti-allergic, and bioactive coatings on orthopedic implant surfaces. *J. Mater. Sci.* **2009**, *44*, 5544–5551, doi:10.1007/s10853-009-3776-1ö.
22. DIN EN 582. Thermal spraying; determination of tensile adhesive strength; German Version EN 582: 1993.
23. Akhavan, B.; Wise, S.G.; Bilek, M.M.M. Substrate regulated growth of plasma polymerized films on carbide-forming metals. *Langmuir* **2016**, *32*, 10835–10843, doi:10.1021/acs.langmuir.6b02901.
24. van Wachem, P.B.; Beugeling, T.; Feijen, J.; Bantjes, A.; Detmers, J.P.; van Aken, W.G. Interaction of cultured human endothelial cells with polymeric surfaces of different wettabilities. *Biomaterials* **1985**, *6*, 403–408.
25. Gabler, C.; Zietz, C.; Göhler, R.; Fritsche, A.; Lindner, T.; Haenle, M.; Finke, B.; Meichsner, J.; Lenz, S.; Frerich, B.; et al. Evaluation of osseointegration of titanium alloyed implants modified by plasma polymerization. *Int. J. Mol. Sci.* **2014**, *15*, 2454–2464, doi:10.3390/ijms15022454.
26. Moerke, C.; Staehlke, S.; Rebl, H.; Finke, B.; Nebe, J.B. Restricted cell functions on micropillars are alleviated by surface-nanocoating with amino groups. *J. Cell Sci.* **2017**, doi:10.1242/jcs.207001.
27. Staehlke, S.; Henrike Rebl, H.; Finke, B.; Mueller, P.; Gruening, M.; Nebe, J.B. Enhanced calcium ion mobilization in osteoblasts on amino group containing plasma polymer nanolayer. *Cell Biosci.* **2018**, *8*, 22, doi:10.1186/s13578-018-0220-8.
28. Staehlke, S.; Koertge, A.; Nebe, B. Intracellular calcium dynamics dependent on defined microtopographical features of titanium. *Biomaterials* **2015**, *46*, 48–57, doi:10.1016/j.biomaterials.2014.12.016.
29. Xia, Z.; Triffitt, T. A review on macrophage responses to biomaterials. *Biomed. Mater.* **2006**, *1*, R1–9, doi:10.1088/1748-6041/1/1/R01.
30. Hoene, A.; Walschus; U.; Patrzyk, M.; Finke, B.; Lucke, S.; Nebe, B.; Schroeder, K.; Ohl, A.; Schlosser, M. In vivo investigation of the inflammatory response against allylamine plasma polymer coated titanium implants in a rat model. *Acta Biomater.* **2010**, *6*, 676–683, doi:10.1016/j.actbio.2009.09.003.
31. Walschus, U.; Hoene, A.; Patrzyk, M.; Lucke, S.; Finke, B.; Polak, M.; Lukowski, G.; Bader, R.; Zietz, C.; Podbielski, A.; et al. A cell-adhesive plasma polymerized allylamine coating reduces the in vivo inflammatory response induced by Ti6Al4V plates modified with plasma immersion ion implantation of copper. *J. Funct. Biomater.* **2017**, *8*, pii: E30, doi:10.3390/jfb8030030.
32. Walschus, U.; Hoene, A.; Patrzyk, M.; Finke, B.; Polak, M.; Lucke, S.; Nebe, B.; Schroeder, K.; Podbielski, A.; Wilhelm, L.; et al. Serum profile of pro- and anti-inflammatory cytokines in rats following implantation of low-temperature plasma-modified titanium plates. *J. Mater. Sci. Mater. Med.* **2012**, *23*, 1299–1307, doi:10.1007/s10856-012-4600-z.
33. Hoene, A.; Patrzyk, M.; Walschus, U.; Finke, B.; Lucke, S.; Nebe, B.; Schröder, K.; Schlosser, M. Systemic IFNγ predicts local implant macrophage response. *J. Mater. Sci. Mater. Med.* **2015**, *23*, 131, doi:10.1007/s10856-015-5476-5.
34. Schröder, K.; Finke, B.; Ohl, A.; Lüthen, F.; Bergemann, C.; Nebe, B.; Rychly, J.; Walschus, U.; Schlosser, M.; Liefeith, K.; et al. Capability of differently charged plasma polymer coatings for control of tissue interactions with titanium surfaces. *J. Adhes. Sci. Technol.* **2010**, *24*, 1191–1205, doi:10.1163/016942409X12619870771501.
35. Everheart, D.E.; Reilly, C.N. Chemical derivatization in electron-spectroscopy for chemical analysis of surface functional groups introduced on low-density polyethylene film. *Anal. Chem.* **1981**, *53*, 665–676.
36. Greenler, R.G. Infrared study of adsorbed molecules on metal surfaces by reflection techniques. *J. Chem. Phys.* **1966**, *44*, 310–315.
37. Owens, D.K.; Wendt, R.C. Estimation of surface free energy of polymers. *J. Appl. Polym. Sci.* **1969**, *13*, 1741–1747.
38. Rabel, W. Einige Aspekte der Benetzungstheorie und ihre Anwendungen auf die Untersuchung und Veränderung der Oberflächeneigenschaften von Polymeren. *Farbe Lack* **1971**, *77*, 997–1005.
39. Schröder, K.; Finke, B.; Jesswein, H.; Lüthen, F.; Diener, A.; Ihrke, R.; Ohl, A.; Weltmann, K.D.; Rychly, J.; Nebe, B. Similarities between plasma amino functionalized PEEK and titanium surfaces concerning

enhancement of osteoblast cell adhesion. *J. Adhes. Sci. Technol.* **2010**, *24*, 905–923, doi:10.1163/016942409X12598231567989.
40. Staehlke, S.; Rebl, H.; Nebe, J.B. Phenotypic stability of the human MG-63 osteoblastic cell line at different passages. *Cell Biol. Int.* **2018**, doi:10.1002/cbin.11073.
41. Mochales, C.; Maerten, A.; Rack, A.; Cloetens, P.; Mueller, W.D.; Zaslansky, P.; Fleck, C. Monoclinic phase transformations of zirconia-based dental prostheses, induced by clinically practised surface manipulations. *Acta Biomater.* **2011**, *7*, 2994–3002, doi:10.1016/j.actbio.2011.04.007.
42. Wongkamhaeng, K.; Dawson, D.V.; Holloway, J.A.; Denry, I. Effect of Surface Modification on In-Depth Transformations and Flexural Strength of Zirconia Ceramics. *J. Prosthodont.* **2019**, *28*, e364–e375, doi:10.1111/jopr.12908.

*Publikation II*:
Staehlke et al. Cell Biosci (2018) 8:22
https://doi.org/10.1186/s13578-018-0220-8

Cell & Bioscience

Open Access

# Enhanced calcium ion mobilization in osteoblasts on amino group containing plasma polymer nanolayer

Susanne Staehlke[1], Henrike Rebl[1], Birgit Finke[2], Petra Mueller[1], Martina Gruening[1] and J. Barbara Nebe[1*]

## Abstract

**Background:** Biomaterial modifications—chemical and topographical—are of particular importance for the integration of materials in biosystems. Cells are known to sense these biomaterial characteristics, but it has remained unclear which physiological processes bio modifications trigger. Hence, the question arises of whether the dynamic of intracellular calcium ions is important for the characterization of the cell–material interaction. In our prior research we could demonstrate that a defined geometrical surface topography affects the cell physiology; this was finally detectable in a reduced intracellular calcium mobilization after the addition of adenosine triphosphate (ATP).

**Results:** This new contribution examines the cell physiology of human osteoblasts concerning the relative cell viability and the calcium ion dynamic on different chemical modifications of silicon–titanium (Ti) substrates. Chemical modifications comprising the coating of Ti surfaces with a plasma polymerized allylamine (PPAAm)-layer or with a thin layer of collagen type-I were compared with a bare Ti substrate as well as tissue culture plastic. For this purpose, the human osteoblasts (MG-63 and primary osteoblasts) were seeded onto the surfaces for 24 h. The relative cell viability was determined by colorimetric measurements of the cell metabolism and relativized to the density of cells quantified using crystal violet staining. The calcium ion dynamic of osteoblasts was evaluated by the calcium imaging analysis of fluo-3 stained vital cells using a confocal laser scanning microscope. The positively charged nano PPAAm-layer resulted in enhanced intracellular calcium ion mobilization after ATP-stimulus and cell viability. This study underlines the importance of the calcium signaling for the manifestation of the cell physiology.

**Conclusions:** Our current work provides new insights into the intracellular calcium dynamic caused by diverse chemical surface compositions. The calcium ion dynamic appears to be a sensitive parameter for the cell physiology and, thus, may represent a useful approach for evaluating a new biomaterial. In this regard, reliable in vitro-tests of cell behavior at the interface to a material are crucial steps in securing the success of a new biomaterial in medicine.

**Keywords:** Chemical surface modifications, Titanium, Plasma polymer, Tissue culture plastic, Collagen type-I, Human osteoblasts, Zeta potential, Cell viability, Signaling, Calcium ion dynamic

## Background

Nowadays, there is an increasing demand for permanent, temporary and biodegradable orthopedic devices developed for bone repair and regeneration [1–3]. The cell–biomaterial interaction is a major challenge for tissue engineering. Both the topographical and chemical surface stimuli of the biomaterials can affect cellular behavior, either detrimentally or favorably, at the interface [4–7]. The physico–chemical stimuli of biomaterial surfaces control complex molecular mechanisms responsible for cell function [4, 8–10] by mechanotransduction—translating external signals and forces into intracellular biochemical signals [1]. As a result, initial processes like cell adhesion [8, 11], spreading [9, 12] and the mechanical attachment of cells to the biomaterial surface [5]

*Correspondence: barbara.nebe@med.uni-rostock.de
[1] Dept. of Cell Biology, University Medical Center Rostock, Schillingallee 69, 18057 Rostock, Germany
Full list of author information is available at the end of the article

further influence other cell activities such as proliferation, differentiation [2] and intracellular signaling [4, 10]. There is limited information on whether altered cellular responses by external mechanical stimuli affect intracellular signal transmission via an intracellular calcium ion dynamic. Many cellular functions, like proliferation or differentiation, are regulated by changes of cytosolic free calcium ions ($Ca^{2+}$) [13–15]. The cations ($Ca^{2+}$) act like common intracellular signaling molecules, which function as a "second messenger" [14, 16, 17]. Cytosolic free $Ca^{2+}$-concentration ($10^{-7}$ M) is strictly regulated [16]. A short-term rise of $Ca^{2+}$ is important for signal transmission, and intracellular calcium dynamic is triggered by a variety of factors like adenosine triphosphate (ATP) [14, 17, 18] or mechanical forces [10, 13]. The ligand ATP typically activates the cell-surface G protein-coupled receptor (GPCR) which generates inositol-1,4,5-triphosphate (IP3); this induces transient and rapid $Ca^{2+}$-release through activation of its receptor which is located in the membrane of the internal $Ca^{2+}$-store, the smooth endoplasmic reticulum (ER) [14, 15, 19]. Intracellular $Ca^{2+}$ as a second messenger system is responsible for signal transduction [14] e.g. the transmission of external signals and forces in adaptation to the changed environment [10, 18]. So, external signals provide a distinct $Ca^{2+}$ dynamic that selectively controls long-term cellular responses like proliferation [20] and differentiation [10, 14, 15] by, e.g. binding and activation of other downstream signal proteins and transcription factors [13, 17, 19]. To study the role of the intracellular $Ca^{2+}$ dynamic on different chemical surface compositions, osteoblasts were stained with a very common non-ratiometric (single wavelength) $Ca^{2+}$ indicator fluo-3 [16, 21] and analyzed using confocal laser scanning microscopy. The variation of fluorescence intensity in vital fluo-3-labeled osteoblasts was recorded over the time of 240 cycles of 2 s each [10]. To stimulate the intracellular calcium dynamic, ATP was added after the 90th cycle [10].

The complex interplay between modified biomaterials and cell behavior has not yet been fully understood and elucidated. Therefore, it is important to determine parameters that reflect the cell physiological behavior of the cells in interaction with the physico–chemical properties of the biomaterial surface. Titanium (Ti) or titanium alloys (like Ti6Al4V) as implant materials in medicine fulfill highly demanding biological conditions, being both inert and biocompatible, having excellent mechanical and physical properties, and being corrosion-resistant [2]. A layer of titanium dioxide ($TiO_2$) forms spontaneously when titanium is exposed to air [22]. For an improved interaction of cells on titanium materials, surfaces were endowed with modified chemical as well as physical properties [5, 7, 23]. It is known that cells sense and respond sensitively to the topographical features of surfaces [4]. In this regard, Staehlke et al. [10] found out that osteoblasts on Ti microstructures with impaired cell physiology (cell growth, actin cytoskeleton organization and synthesis of fibronectin) showed significantly reduced intracellular calcium mobilization compared to planar controls. To create new bioactive materials, in addition to the topographic modification, chemical surface properties are of significance for the cell substrate interface [24, 25]. It is reported that the ideal cell adhesion is mediated by positively charged as well as hydrophilic surfaces [2]. The allylamine, polymerized by a low-pressure physical plasma process, generates positively charged amino groups on the wet surface [8, 11]. The advantage of positively charged surfaces is the adsorption of molecules and proteins which mediate cell adhesion [2]. It has been shown that a PPAAm coating causes osteoblasts to respond with, in addition to improved adhesion and increased spreading [7–9], also an improved organization of the actin cytoskeleton with typically long stress fibers and enhanced focal adhesion kinase (FAK) protein expression [11, 12] which finally enhanced cell function [26]. Collagen type-I is one main organic part of the extracellular matrix (ECM), e.g. in skeletal [27] and dental bone [22]. Collagen functions as a ligand for cell adhesion receptors like integrins [6, 10] and is therefore a cell-attractive surface [22]. Collagen type-I layer as a biochemical surface modification supports the cell physiology, including adhesion and differentiation [27, 28]. The objectives of this in vitro-study on human osteoblasts was to investigate the cell physiological effects of two chemically modified Ti surfaces—PPAAm and collagen type-I—compared with a bare Ti substrate, as well as with standard tissue culture plastic (ibiTreat, IBIDI) (see Fig. 1). The zeta potentials on these different chemical compositions of the surface modifications were determined in order to analyze the influence of the surface charge on the cell behavior. Furthermore, this study focused on the intracellular calcium ion dynamic with its importance in the regulation of cell physiology. We have identified the intracellular calcium ion mobilization as a sensitive parameter to observe the cellular behavior on different biomaterials. Reliable in vitro-tests

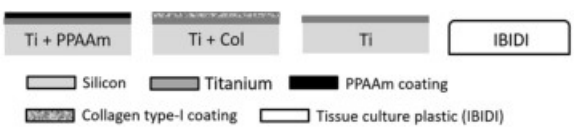


**Fig. 1** Scheme of the chemical surface composition. The silicon–titanium (Ti) substrates were modified by amino functionalization with plasma polymerized allylamine (Ti + PPAAm) as well as immobilization of a bioactive collagen type-I layer (Ti + Col). These modifications were compared with bare Ti substrates and tissue culture plastic (IBIDI)

for the description of cell–material interactions are the precondition for the design of new biomaterial surfaces in medicine.

## Results

### Surface characterization reveals a positive surface charge on the PPAAm-nanolayer

In order to evaluate the existing surface charges of the different chemical surface compositions, the zeta potential at pH 6.0–8.0 was determined (Fig. 2). Table 1 represents the values of the zeta potential at the cell physiological pH 7.4 [7]. These results indicated that only the PPAAm coating on Ti (Ti + PPAAm) exhibits a positive surface charge. In contrast, the immobilized collagen type-I layer on Ti (Ti + Col) revealed a slight negative surface charge, and Ti as well as the tissue culture plastic (IBIDI) surfaces showed a strong negative zeta potential (Table 1).

The measurements of water contact angle (WCA, distilled water) indicated that all chemical surface compositions (Ti + PPAAm, 68.4°; Ti + Col, 60.8°) as well as the IBIDI (72.8°) were more hydrophilic compared with Ti (85°) (Table 1).

**Table 1 Water contact angle and zeta potential (mean ± s.e.m.)**

| Surface | Water contact angle (in °) | Zeta potential at pH 7.4 (in mV) |
|---|---|---|
| Ti | 85.0 ± 0.7 | − 82.3 ± 3.9 [7] |
| Ti + PPAAm | 68.4 ± 1.7 | + 8.6 ± 1.4 [7] |
| Ti + Col | 60.8 ± 2.2 | − 18.5 ± 3.2 [7] |
| IBIDI | 72.8 ± 1.6 | − 81.7 ± 2.5 |

### The positively charged PPAAm nanolayer displayed increased relative cell viability

The relative cell viability after 24 h was confirmed by colorimetric measurements of the cell metabolism (MTS) and relativized to the density of cells (crystal violet staining). We found a significantly higher relative cell viability of MG-63 cells on Ti + PPAAm (3.66 ± 0.27) in contrast to all negatively charged surfaces after 24 h. A similar cell viability per cell number could be observed for Ti + Col (2.91 ± 0.24), Ti (3.08 ± 0.18) and IBIDI (2.87 ± 0.47) (Fig. 3).

### The positively charged PPAAm nanolayer triggered an enhanced intracellular $Ca^{2+}$ dynamic in MG-63 osteoblasts and HOB

Fluorescence measurements of vital fluo-3/acetoxymethyl ester (AM)-stained osteoblasts were recorded on the confocal laser scanning microscope (LSM780). The mean fluorescence intensity (MFI) of 10 defined regions of the cells (one region per cell, see Fig. 4) was analyzed

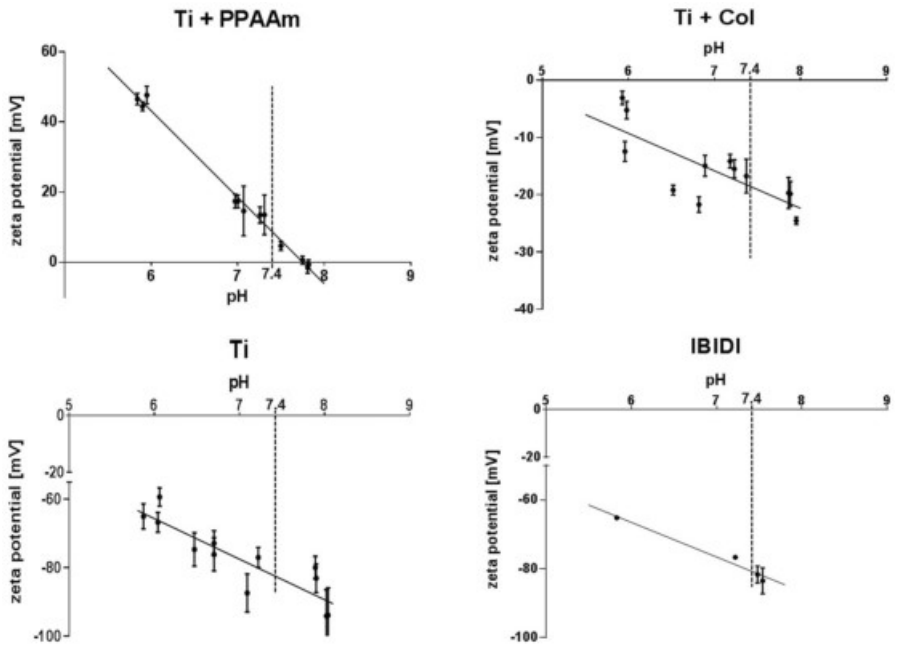


**Fig. 2** Surface characterization—the zeta potential—of different chemical compositions. Note that the zeta potential of the Ti + PPAAm indicated a positive surface charge, whereas collagen type-I coating (Ti + Col) and the control surfaces (Ti and IBIDI) exhibited a negative charge. The cell physiological pH 7.4 is indicated. (SurPASS™ system, Anton Paar, n = 3)

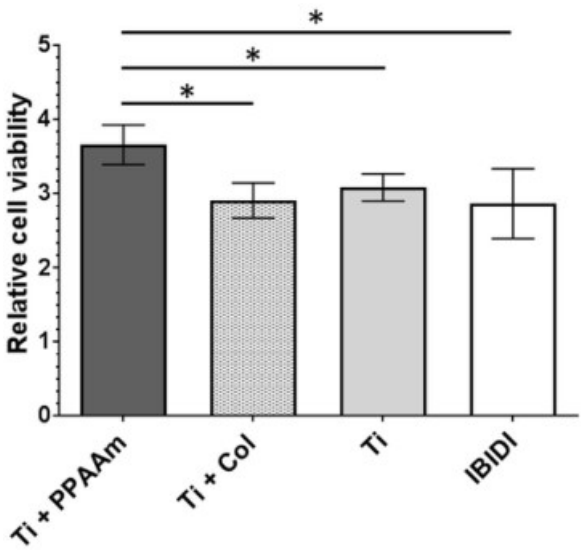


**Fig. 3** Relative cell viability of MG-63 osteoblasts on the chemical surface compositions after 24 h. Relative cell viability: values from the cell metabolism (MTS) related to the values of the cell density (crystal violet). Note that osteoblasts on Ti + PPAAm indicated an increase in relative cell viability compared with Ti + Col and bare Ti as well as IBIDI. (Anthos reader, mean ± s.e.m., adjusted Mann-Whitney U-Test, *$p < 0.05$, $n = 5$ independent experiments)

per cycle over a time series (240 cycles every 2 s, total 480 s). To stimulate the cytoplasmic $Ca^{2+}$ rise from the endoplasmic reticulum (ER), ATP was added after the 90th cycle (180 s). The recorded fluorescence signal of the stained cells over time was evaluated as a (i) basal calcium level (without ATP stimulation, 0–180 s), and (ii) the calcium ion mobilization (after ATP stimulation, 182–480 s). The individual values can be found in Table 2. MG-63 cells on Ti + PPAAm showed a significantly increased intracellular $Ca^{2+}$-mobilization after stimulation with ATP in contrast to Ti + Col, Ti and IBIDI (Fig. 5). The results indicated that the $Ca^{2+}$ dynamic in MG-63 osteoblasts was influenced by a positively charged surface.

It has often been discussed that the tumor cell lines (e.g. the MG-63 cells) are different in its sensitivity to primary cells.

In order to confirm the influence of chemical modifications on intracellular $Ca^{2+}$ signaling also in human primary osteoblasts (HOB), experiments were done in direct comparison. MG-63 and HOB cells were cultured for 24 h only on the most noticeable chemical modification, the positively charged Ti + PPAAm, compared with bare Ti. The fluorescence intensity of these fluo-3-stained osteoblasts at the 120th cycle was higher in both HOB and MG-63 cells on Ti + PPAAm (Fig. 6a). A significantly increased cytosolic free $Ca^{2+}$ mobilization after ATP stimulation was found in HOB as well as in MG-63 cells on Ti + PPAAm compared with Ti (Fig. 6b, c). The fluorescence signals are indicated in Table 3. Thus, the primary osteoblasts confirm increased calcium signaling on Ti + PPAAm.

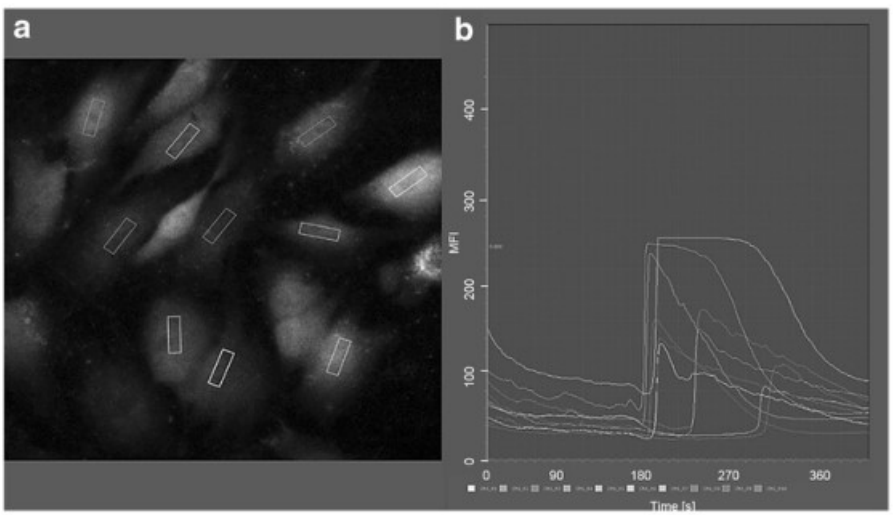


**Fig. 4** Fluorescence intensity of the $Ca^{2+}$-mobilization in osteoblasts over a time series using confocal laser scanning microscopy (LSM780, Carl Zeiss) and the software ZEN2 (blue edition, Carl Zeiss) in the mode "mean region of interest (ROI)". **a** In the first fluorescence image of the time series, the defined areas in 10 cells (one area per cell) are fixed. **b** Graphical representation of the mean fluorescence intensity (MFI) of the 10 defined areas over the entire time series.

**Table 2 Mean fluorescence intensity of mobilized $Ca^{2+}$ in MG-63 cells on Ti substrates (mean ± s.e.m.)**

| $Ca^{2+}$ signal | Ti | Ti + PPAAm | Ti + Col | IBIDI |
|---|---|---|---|---|
| Basal level (0–180 s) | 38.7 ± 0.8 | 51.9 ± 0.6 | 38.6 ± 0.2 | 23.6 ± 0.8 |
| After ATP (182–480 s) | 49.9 ± 1.1 | 89.1 ± 1.9 | 44.8 ± 1.6 | 17.2 ± 0.1 |

## Discussion

In the present study, osteoblast behavior (viability and calcium signaling) was correlated to different chemical surface compositions on titanium—plasma polymerized allylamine (Ti + PPAAm) and a collagen type-I coating (Ti + Col)—in comparison with the bare substrate (Ti) and tissue culture plastic (IBIDI). Using in vitro approaches, we showed clearly that chemical surface modifications of biomaterials affect the relative cell viability and, further, the intracellular $Ca^{2+}$ dynamic in osteoblasts. In addition, we found a biological analysis method—calcium imaging—to determine cell regulatory mechanisms which reflect the cell behavior on different materials.

Titanium is the biomaterial of choice in medical devices due to its mechanical and biological compatibility [22, 28]. Today, new biomaterials in medicine should be biocompatible and furthermore actively promote cellular functions [2]. Bioactive material surfaces are developed by physico–chemical modification for better osseointegration [4]. Different studies investigated the influence of surface modifications on cell–material interaction [4, 5]. The research and evaluation of new materials requires additional in vitro tests, also for the assessment of signal transduction.

The interaction between materials and osteoblasts is dependent on surface characteristics like wettability, surface charge or surface energy [3]. First of all, we analyzed the surface charge (at pH 7.4) of the different chemical compositions [7]. The zeta potential is of importance for biological responses like adhesion and spreading [4, 8, 9]. The zeta potential of surfaces modified with a Ti + PPAAm showed the only positive surface charge of all surfaces used in the study. The other chemical titanium modification Ti + Col indicated a slight negative surface charge. Our comparative surfaces—bare Ti substrate as well as IBIDI—revealed a highly negative zeta potential [7].

Previous studies, which characterized the PPAAm coating, examined the positive zeta potential in addition to hydrophilicity of this nanolayer [8, 11]. Interestingly, a greater hydrophilic potential was also observed for a collagen type-I coating, but in contrast to the PPAAm-nanolayer, a negative surface charge was measured [7]. Rebl et al. [9] reported a negative surface charge for a

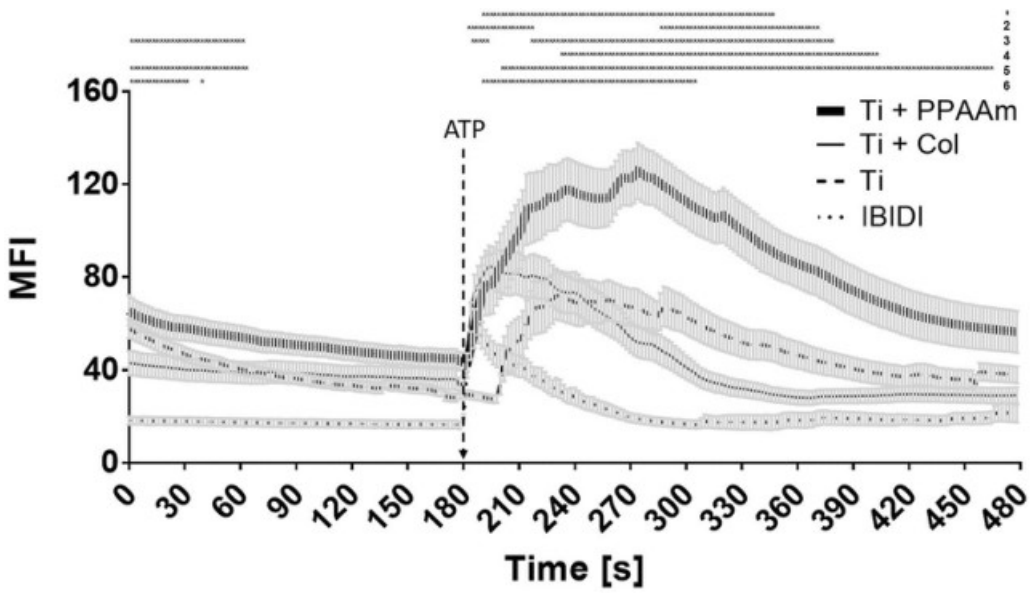


**Fig. 5** Time courses of $Ca^{2+}$-fluorescence signals of vital fluo-3 loaded MG-63 cells growing on different chemical surface compositions. The addition of ATP is highlighted at the time point 180 s (90th cycle). Note that cells on Ti + PPAAm showed significantly increased intracellular calcium signals after ATP stimulation. Cells on the control IBIDI indicated not only a weaker basal calcium signal (without ATP) but also a significantly weaker calcium ion mobilization after ATP compared with osteoblasts on Ti, Ti + PPAAm, and Ti + Col. (LSM780, Carl Zeiss; 3 independent approaches for 10 defined areas each of 10 cells per time point, polygon line as the mean ± s.e.m., multiple t-test, *p < 0.05). Explanations: 1 = Ti vs. Ti + PPAAm, 2 = Ti vs. Ti + Col, 3 = Ti vs. IBIDI, 4 = Ti + PPAAm vs. Ti + Col, 5 = Ti + PPAAm vs. IBIDI, 6 = Ti + Col vs. IBIDI

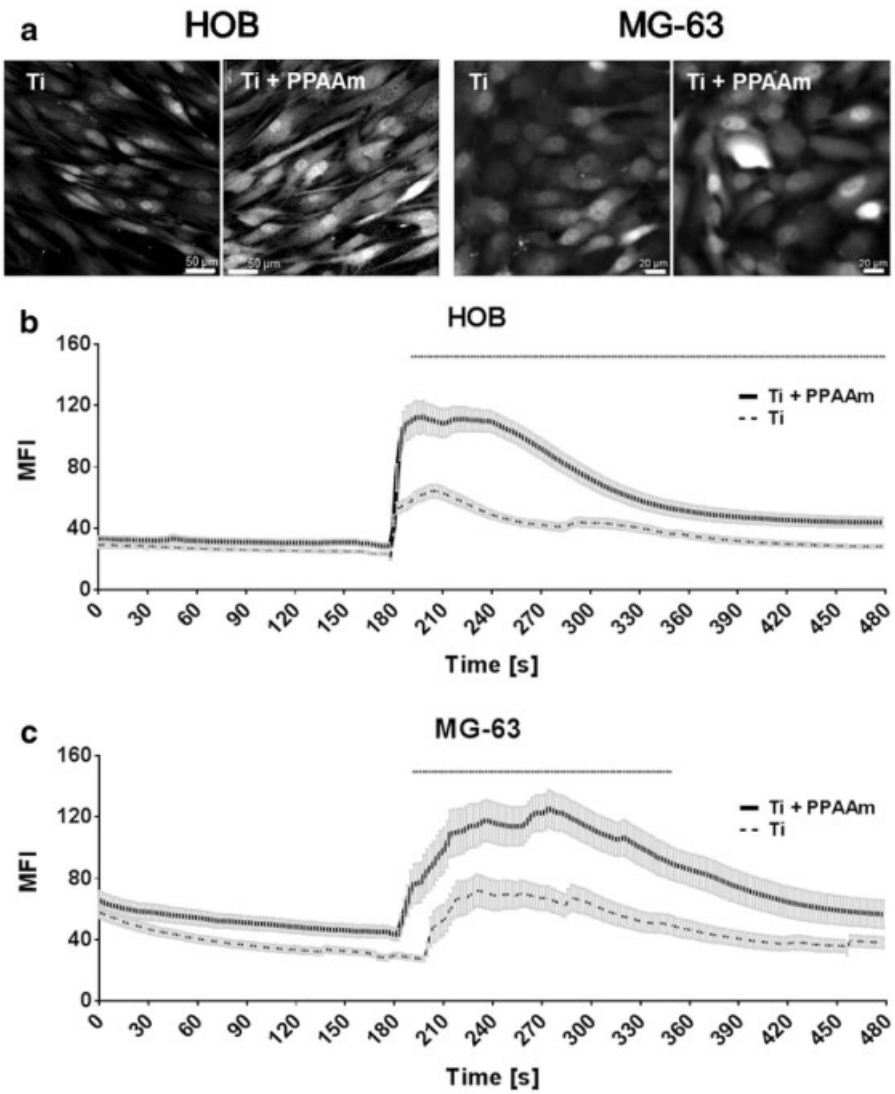


**Fig. 6** Calcium imaging in vital fluo-3 loaded human osteoblasts—cell line (MG-63) and primary osteoblasts (HOB). Changes in fluorescence intensities of the cells were detected using confocal laser scanning microscopy (LSM780, Carl Zeiss, ZEN-software). **a** The representative fluorescence images, after ATP stimulation (240 s = 120th cycle), show the $Ca^{2+}$ increase on Ti + PPAAm surfaces compared with bare Ti in MG-63 as well as HOB cells. (Scale bar MG-63: 20 µm, HOB: 50 µm). **b** Intracellular $Ca^{2+}$ dynamics in vital primary osteoblasts (HOB) over 480 s (= 240 cycles) every 2 s on Ti + PPAAm compared with Ti. Note the significantly enhanced intracellular calcium ion signal in HOB cells after ATP stimulus (180 s) on Ti + PPAAm. **c** Intracellular $Ca^{2+}$ signal of MG-63 cells over time on Ti + PPAAm compared with Ti. Significant differences in the intracellular $Ca^{2+}$ dynamic of MG-63 after ATP stimulation was detectable (see explanation in **b**). MG-63 and HOB established the same cellular reactivity in calcium signaling on Ti + PPAAm and bare Ti. (MG-63 = 3, and HOB = 5 independent approaches each for 10 defined areas of 10 cells per time point, 240 cycles, polygon line as mean ± s.e.m., multiple t-test, *$p < 0.05$)

collagen type-I layer on glass as well. Likewise, IBIDI dishes, with their high negative charge, exhibit hydrophilic properties [29]. It is known that biomaterial surfaces with moderate hydrophilicity improve cell growth and biocompatibility [2]. In addition, improved initial cell adhesion on positively charged surfaces was previously observed [7–9]. The extracellular matrix (ECM) molecules, which are synthesized by osteoblasts and important for cell adhesion and regeneration [22], are negatively charged, e.g. hyaluronan or collagen type-I [12]. The collagen type-I is, on the basis of the abundant presence in human tissue, the stability and as part of the ECM, a potential, organic bioactive coating for titanium surfaces [22]. The positively charged PPAAm nanolayer is capable of attracting negatively charged biomolecules of the ECM [12], and therefore particularly suitable as a

**Table 3 Comparison of $Ca^{2+}$ signals in HOB and MG-63 cells on Ti and Ti ± PPAAm (mean ± s.e.m.)**

| $Ca^{2+}$ signal | Primary osteoblasts—HOB | | Osteoblast cell line—MG-63 | |
|---|---|---|---|---|
| | Ti | Ti + PPAAm | Ti | Ti ± PPAAm |
| Basal level (0–180 s) | 26.3 ± 0.3 | 31.2 ± 0.1 | 38.7 ± 0.8 | 51.9 ± 0.6 |
| ATP peak maximum (182–300 s) | 50.5 ± 1.0 | 99.2 ± 1.7* | 59.3 ± 1.9 | 106.6 ± 2.5* |
| Slope after ATP (302–480 s) | 33.4 ± 0.5 | 50.3 ± 0.8* | 43.8 ± 0.8 | 77.8 ± 1.8 |

* Statistically significant, $p < 0.05$, multiple t-test

coating for biofunctionalized implant surfaces. Anselme et al. [4] described the electric charge, existing at the interface of biomaterials, as a significant factor in protein adsorption and integrin binding. It is postulated that for the best cell attachment a positively charged surface should be used, since cell adhesion and spreading are influenced by chemical composition and surface potential [2]. The initial cell reaction controls further cellular responses like signaling events and finally cell viability [2]. Major regulators of cell viability and proliferation are cell adhesion and cell spreading [5]. Prior investigations on surfaces coated with PPAAm indicated a significant increase in initial osteoblast adhesion and spreading [9, 11, 12], and thus an enhanced cell–material contact which finally improved the proliferation rate [26]. The positively charged modification with a nanolayer of PPAAm seems to be attractive for cells and stabilizes the adhesion of cells on the biomaterial surface, resulting, in addition, in better implant osseointegration [8, 12, 26].

The new findings of this study confirm this assumption. In this study, osteoblasts which were cultured for 24 h on surfaces with a positively charged PPAAm nanolayer showed a significant increase of relative cell viability compared with negatively charged surfaces. Cell viability on Ti + Col appears to be unchanged compared with the Ti and IBIDI. It is postulated in the literature that a bioactive protein coating with collagen type-I acts as a ligand for cell adhesion receptors [4, 6] and therefore will be a cell attractive surface [25]. In this regard, in in vitro- and in vivo-studies Avila et al. [22] presented enhanced cellular behavior on collagen type-I coated implants. Also, in long-term experiments (8 weeks) Sverzut et al. [25] showed that collagen type-I coatings led to improved osseointegration and differentiation in vivo. In the proximal tibial metaphysis of rats, Reyes et al. [30] compared bone-to-implant contact of machined titanium surfaces (Ti) with e.g. bovine type I collagen (Col I). After 4 weeks of healing the mean bone-to-implant contact percentages were 58% for Col I and 43% for Ti. Col I was statistically higher compared with Ti. The authors concluded that Col I enhanced bone repair and implant integration.

Further literature showed inconsistent results in in vitro approaches. Also, Morra et al. [28] postulated that the osteoblast growth rate on collagen-modified biomaterials is lower and cell viability is similar compared with pure titanium. Regarding our study, Rebl et al. [9] were also able to show that the positive charges of a PPAAm coating enhanced the cell physiology (initial cell adhesion and spreading), and were more effective than the collagen type-I coated surfaces. Thus, the zeta potential seems to be an important surface characteristic for cell physiology, as demonstrated in this study with the relative cell viability.

This feature of cell physiology—relative cell viability—is also reflected in the intracellular calcium dynamic after stimulation with ATP. In this study, an adapted cytosolic calcium signal was found corresponding to the relative cell viability in MG-63 osteoblasts on the different chemical compositions. It is known from the literature that intracellular $Ca^{2+}$ is a component of downstream signaling cascades [13, 14, 17] and regulates characteristics of cell physiology such as proliferation [15, 20]. The analysis of the intracellular $Ca^{2+}$ dynamic in fluo-3 stained osteoblasts on different chemical surface compositions presented here were performed using confocal laser scanning microscopy. The fluorescence changes over the time of 240 cycles were recorded every 2 s and evaluated. The basal calcium level (without stimulation), and the calcium dynamic after stimulation with ATP (even at the 90th cycle) were determined [10]. Interestingly, the cells on positively charged PPAAm reacted with a significantly higher calcium signal after ATP-stimulus compared with cells on negatively charged surfaces. Some studies showed a similar cellular reaction of the cell line MG-63 and primary osteoblasts (HOB) on biomaterials concerning the expression of integrin subunits and signaling, and declared MG-63 cells to be useful in in vitro models [31]. Nevertheless, they intend to verify appropriate functional studies with human primary cells [31]. Therefore, we placed HOB on the most noticeable chemical modification (Ti + PPAAm) compared with bare Ti and analyzed the intracellular calcium signal. Not only in the MG-63 cell line, but also in HOB, we were able to demonstrate this phenomenon of increased $Ca^{2+}$ mobilization on Ti + PPAAm. Also, Ravenscroft et al. [24] showed that chemical surface features of self-assembled monolayers on coverslips (DETA) can influence the calcium dynamic after an electrical stimulation (1 HZ, 6 V signal, 5 ms per pulse), as demonstrated with fura 2-stained chicken embryonic cardiac myocytes. Cells on the hydrophilic silanes showed a significant higher excitation-induced $Ca^{2+}$ concentration and dynamic (i.e. calcium transients, amplitude and duration).

Due to good spreading and adhesion properties, adhesion receptors such as integrins mediated stronger calcium signals [13]. Furthermore, cytoskeletal organization and formation of a cytoskeletal signaling complex affects the intracellular calcium mobilization [13]. In previous studies it was found that osteoblasts grown on the PPAAm nanolayer displayed improved osteoblast adhesion and spreading as well as a strong actin filament network [11, 12]. This new, further study shows accordingly the significantly increased calcium ion dynamic in osteoblasts on this positively charged surface.

In another earlier study we indicated altered cellular behavior on the topography of a defined micro-structured surface (micro pillars): changed actin organization resulting in short fiber formation on the top of the pillars [10] and, as a consequence, a significant decrease in the intracellular calcium signal [10, 16]. These topography-dependent reactions finally led to inhibited cell function [10]. Thus, we suggest that osteoblasts transmitted external signals and forces from the environment into the cell via calcium signaling. The stringent regulation of the intracellular $Ca^{2+}$ dynamic plays an important role in cell function [10, 13, 15]. It seems to be a correlation between the increased viability of MG-63 cells and the enhanced calcium ion dynamic detected on Ti + PPAAm. In this regard, it has been shown that the intracellular $Ca^{2+}$ dynamic plays an important role, and thus can be an indicator for the behavior of cells on different biomaterials.

## Conclusion

The material surface functionalization with positively charged plasma-polymerized allylamine (PPAAm) resulted in increased cell viability and, furthermore, in an enhanced calcium ion mobilization after ATP stimulation. We conclude that the calcium ion dynamic reflects the behavior of the cells on different surfaces accordingly. To develop new biomaterials it is of importance to understand the interaction of cells with the underlying material.

We have found an in vitro-method—calcium imaging—to assess the cell response to functionalized surface modifications. This study is one of the first to examine the intracellular calcium ion level and stimulus-dependent dynamic of intracellular calcium ions on chemically different coatings. These new results support our hypothesis that the calcium ion dynamic in cells is important in the transmission of external signals into the cell, which finally regulate the cell physiology.

## Methods

### Surfaces and chemical composition

The bare substrate was silicon with a final 100 nm titanium (Ti) coating. The surfaces thus had a native titanium-oxide layer ($TiO_2$) at which the cells interact. The Ti wafers, which measured 1 × 1 cm (length x width), were obtained from the Center for Microtechnologies (ZFM, University of Technology Chemnitz, Germany). To sterilize the bare material, samples were incubated in 70% ethanol for 15 min and rinsed with phosphate buffer saline (PBS, Sigma Aldrich, Munich, Germany).

One of the modifications of the bare Ti substrate was the wet chemical coating with collagen type-I (Ti + Col). For this purpose, 200 µl of a collagen work solution (Col, type I, rat tail tendon, BD Bioscience, Heidelberg, Germany, 200 µg/ml in acetic acid) was dripped onto the Ti sample under sterile conditions (laminar flow box) and allowed to adhere for 3 h. To remove the acetic acid from the working solution, the surfaces were rinsed 3 times with PBS before use.

Another chemical modification of the bare Ti was the coating with plasma polymerized allylamine (PPAAm) (Ti + PPAAm). The preparation was carried out in a low-pressure microwave plasma reactor (2.45 GHz; 500 W, 50 Pa) V55G (Plasma Finish, Germany, V = 60 l). The samples underwent a two-step procedure: at first they were decontaminated and activated in pulsed oxygen plasma (10 ms on/90 ms off; 30 s effective) and then, without breaking the vacuum, coated with the monomer allylamine by the pulsed plasma polymerization process (300 ms on, 1700 ms off, 72 s effective, gross 480 s). Prior to use, the allylamine was carefully purified of air by evacuating and purging with $N_2$. A liquid handling system allowed for the exact dosing of allylamine. Argon was used as a carrier gas (50 sccm Ar). The substrate was located in the plasma reactor in a downstream position [11]. The thickness of the deposited coatings was around 25 nm. Before the experiments started, these surfaces were rinsed with PBS.

The following control surfaces were used for the experiments—a bare Ti wafer (see above) and a tissue culture plastic (IBIDI). The tissue culture plastic ibidi µ-dishes with polymer coverslip (ibiTreat, Ø 35 mm; ibidi GmbH, Martinsried, Germany) are appropriate for microscopy and cell-based assays and fulfill optical requirements [29].

### Surface characterization—surface charge

Zeta-potential measurements were performed using SurPASS™ system (Anton Paar, Ostfildern, Germany) to determine the surface charge. Smooth samples with a size of 2 × 1 cm were mounted pairwise in the chamber with a gap height of 100 µm. The measurements were performed in a 0.001 mol/l KCl solution ranging from pH 6.0 to 8.0. The streaming current was determined depending on the pressure (max. 400 mbar). Finally, the zeta potential was calculated according to the method of Helmholtz–Smoluchowski. Measurements were

performed in quadruplicate on three independent pairs of samples (except for IBIDI, where only two samples were measured).

**Surface characterization—wettability**

The water contact angle (WCA) was determined by the sessile drop method using the Drop Shape Analyzer—DSA25 (Krüss GmbH, Hamburg, Germany) and 2 µl distilled water. Drop images were acquired with the digital camera of the DSA25, and the contact angles were determined with the included software by the fit method ellipse (ADVANCE, V.1.7.2.1). The measurements were done with three sessile drops on one sample (technical triplicates), and 3 independent samples were used for each surface (n = 3).

**Cell culture**

For the main part of the experiments, MG-63 cells, a human osteoblast-like cell line from ATCC (American Type Culture Collection ATCC®, CRL1427™ were used. The MG-63 cell line has similar characteristics concerning morphological behavior, adhesion, integrin receptor expression and signaling properties to primary human osteoblasts [31]. For comparison and confirmation of the intracellular calcium ion dynamic we used human primary osteoblasts (HOB, PromoCell GmbH, Heidelberg, Germany, C-12720) as well. Both cell types were cultured at 37 °C in a humidified atmosphere (5% $CO_2$). MG-63 cells were grown in Dulbecco's modified eagle medium (DMEM; Life Technologies GmbH, Darmstadt, Germany), with 10% fetal calf serum (FCS, Biochrom FCS Superior, Merck KGaA, Darmstadt, Germany) and 1% antibiotic (gentamicin, Ratiopharm GmbH, Ulm, Germany). Experiments were performed in passages 5–25. The HOB cells were cultivated in osteoblast growth medium with SupplementMix (PromoCell) and 1% antibiotic–antimycotic (Anti-Anti 100×, Life Technologies). Investigations with HOB were done in low passages (two to four). All cell cultures were examined prior to further examination on the one hand for mycoplasma, and on the other hand for density and growth. Cells in the near-confluent state (70–80% of confluency) were used for the corresponding in vitro-experiments.

**Relative cell viability assay**

To estimate the relative viability of cells growing on different chemical surface compositions, MTS assay was used. MTS ((3-(4,5-dimethylthiazol-2-yl)-5-(3-carboxymethoxyphenyl)-2-(4-sulfophenyl)-2H-tetrazolium salt), a yellow tetrazolium, is reduced to purple formazan in living cells by mitochondrial metabolic activity. The absorbance of this colored solution could be measured. For this, MG-63 cells (50,000 cells/$cm^2$) were seeded onto the 1 × 1 cm surfaces in 24-well plates (Thermo Fisher Scientific, Roskilde, Denmark) and cultivated for 24 h. Thereafter, materials with adherent cells were transferred into a fresh 24-well plate. Here, cells were incubated for 2-3 h in 500 µl culture medium containing 100 µl of MTS reagent (CellTiter 96 Aqueous ONE-Solution Cell Proliferation Assay, Promega, USA) at 37 °C. Supernatants were transferred into a 96-well plate (for each experimental group 4 × 100 µl were analyzed). The absorbance was recorded at 490 nm with a microplate reader (Anthos, Mikrosysteme, Krefeld, Germany). A background measurement was taken at 650 nm. To quantify the cell number, crystal violet staining was performed. Crystal violet binds to the negatively charged DNA in a linear fashion via ionic attraction. Staining was done on the basis of a protocol published previously [32]. Briefly, cells were fixed in 2-propanol (Walter CMP GmbH, Kiel, Germany) after washing with PBS. The permeabilization of the cell membrane was achieved by washing with 0.05% Tween 20 (VWR Chemicals, Leuven, Belgium). After shaking with 0.1% crystal violet solution (Serva, Heidelberg, Germany) for 20 min at room temperature, cells were washed with double-distilled (dd) $H_2O$. The bound crystal violet was re-dissolved using 33% acetic acid (J. T. Baker, Deventer, Netherlands). The optical density of the transferred supernatants was quantified with a microplate reader at 620 nm. The relative cell viability of osteoblasts will be presented as a quotient of MTS and crystal violet data.

**Intracellular $Ca^{2+}$ dynamic analysis by calcium imaging**

For the live cell calcium imaging, 80,000 cells/$cm^2$ osteoblasts were cultured on 1 × 1 cm samples with different chemical compositions for 24 h, and afterwards washed with pre-warmed PBS (+ Ca/Mg, Sigma) and stained with the calcium indicator fluo-3/AM (Life Technologies Corporation, Eugene, Oregon, US, 5 µM) according to Staehlke et al. [10]. Briefly, cells were transferred to a slightly hypotonic 4-(2-hydroxyethyl)-1-piperazineethanesulfonic acid (HEPES) buffer and loaded with fluo-3/AM. Fluo-3 is engineered with acetoxymethyl (AM) ester to load the dye into the osteoblasts [21]. In order to completely incorporate the dye in the osteoblasts for the best fluorescence signal, the method of hypo-osmotic shock treatment was additionally applied [16]. After incubation of the fluo-3/AM (40 min at 37 °C), the cells were cultured further in an isotonic HEPES buffer. Vital fluo-3/AM-labeled osteoblasts were visualized by a confocal laser scanning microscope (LSM780, Carl Zeiss AG, Oberkochen, Germany) with a C Apochromat 40× water immersion objective (Carl Zeiss, 1.20 W Korr M27) and an excitation at 488 nm by the argon ion laser (emission

at 515 nm). To record the global $Ca^{2+}$ fluorescence signal from single cells, the mode "time series" of the ZEN software (ZEISS efficient navigation, ZEN 2011 SP4, black edition, Carl Zeiss) of one cycle every 2 s for 240 cycles was applied. In order to stimulate the intracellular $Ca^{2+}$ release from the endoplasmic reticulum and thus the intracellular calcium dynamic, ATP (adenosine 50-triphosphate, 10 µM, SERVA Electrophoresis GmbH, Heidelberg, Germany) was added to the experiment always at the same time point—after the 90th cycle—during the recording of the time series. At least three independent samples were analyzed for each experimental group to assess the chemical surface influence on the calcium ion dynamic. Samples were exposed with the same settings (Gain, Digital Offset) as well as with a pinhole of maximal airy units (15 AU, 13.5 µm section). The measurement of the mean fluorescence intensity (MFI) of the global $Ca^{2+}$ signal from the separate images of the time series was done by ZEN2 (blue edition, version 2.0.0.0, Carl Zeiss). Ten defined areas of cells (one area per cell) for each time point (240 cycles = 240 time points) were analyzed using the function "mean ROI" (mean region of interest). For this, the corresponding defined areas were selected in the first image of a time series and the software analyzed the mean fluorescence intensity (MFI) of these areas in each cycle (one cycle = one image) of the entire time series (Fig. 4). Fluorescence images were acquired at a resolution of 512 × 512 pixels.

### Statistical evaluation

The statistical evaluation was conducted at least three times in independent tests. Results for the in vitro-investigations are expressed as mean ± standard error of the mean (s.e.m.). For the relative cell viability, we used the Mann–Whitney U-test. For the intracellular $Ca^{2+}$ dynamic experiments, a multiple t-test was done. Significant differences were reported as adjusted p-values < 0.05 (two-sided). All statistical analyses were performed with GraphPad Prism7 software (GraphPad Software Inc., La Jolla, CA USA).

#### Abbreviations

AM: acetoxymethyl ester; ATCC: American type culture collection; ATP: adenosine triphosphate; AU: airy unit; $Ca^{2+}$: calcium ions; Col: collagen type-I; DMEM: Dulbecco's modified eagle medium; ER: endoplasmic reticulum; ECM: extracellular matrix; FACS: fluorescence-activated cell scanning; FCS: fetal calf serum; HEPES: 4-(2-hydroxyethyl)-1-piperazine-ethanesulfonic acid; HOB: human primary osteoblasts (PromoCell); ibidi: Integrated BioDiagnostics (tissue culture plastic); LSM: laser scanning microscope; MFI: mean fluorescence intensity; MTS: 3-(4,5-dimethylthiazol-2-yl)-5-(3-carboxymethoxyphenyl)-2-(4-sulfophenyl)-2H-tetrazolium salt; PBS: phosphate buffered saline; PPAAm: plasma polymerized allylamine; s.e.m.: standard error of the mean; Si: silicon; Ti: titanium; WCA: water contact angle; ZEN: ZEISS efficient navigation.

#### Authors' contributions

SS conceived the study, participated in its design and drafted the manuscript. SS carried out cell culturing, collagen coating and the calcium experiments as well as statistical analyses. HR carried out the zeta potential analyses and statistics, drafted and revised the manuscript. PM carried out the investigation of cell viability and drafted the manuscript. MG examined the wettability and reviewed the manuscript. BF coated the titanium with the PPAAm-layer and drafted the manuscript. BN supervised the project, and formed the idea for the concept and critically revised the manuscript. All authors read and approved the final manuscript.

#### Author details

[1] Dept. of Cell Biology, University Medical Center Rostock, Schillingallee 69, 18057 Rostock, Germany. [2] Leibniz-Institute for Plasma Science and Technology (INP), Felix-Hausdorff-Str. 2, 17489 Greifswald, Germany.

#### Acknowledgements

We thank Norbert Zichner (Center for Microtechnologies ZFM, Chemnitz University of Technology, Germany) for the production of the Si–Ti-coated wafers.

#### Competing interests

The authors declare that they have no competing interests.

#### Availability of data and materials

The datasets generated and analysed during the current study are not publicly available due to their location on the local file server of an active directory of the University Medical Center Rostock (Rostock, Germany) but are available from the corresponding author on reasonable request.

#### Consent for publication

Not applicable.

#### Ethics approval and consent to participate

Not applicable.

#### Funding

We appreciate the financial support of the German Research Foundation (DFG) graduate school welisa (No. 1505/2) and the DFG ELAINE (No. 1270/1). SS is grateful to the KarriereWegeMentoring-Programme of the University Medical Center Rostock (European Social Fund for Germany and the state of Mecklenburg-Vorpommern, ESF/14-SM-A41-0005/15). HR is currently supported by the German Ministry of Education and Research (BMBF; FKZ 13GW0109D).

## Publisher's Note



Received: 27 November 2017 Accepted: 14 March 2018
Published online: 21 March 2018

#### References

1. Guo CL, Harris NC, Wijeratne SS, Frey EW, Kiang CH. Multiscale mechanobiology: mechanics at the molecular, cellular, and tissue levels. Cell Biosci. 2013;3(1):25. https://doi.org/10.1186/2045-3701-3-25.
2. Bacakova L, Filova E, Parizek M, Ruml T, Svorcik V. Modulation of cell adhesion, proliferation and differentiation on materials designed for body implants. Biotechnol Adv. 2011;29:739–67.
3. Sanz-Herrera JA, Reina-Romo E. Cell–biomaterial mechanical interaction in the framework of tissue engineering: insights, computational modeling and perspectives. Int J Mol Sci. 2011;12(11):8217–44. https://doi.org/10.3390/ijms12118217.
4. Anselme K, Ponche A, Bigerelle M. Relative influence of surface topography and surface chemistry on cell response to bone implant materials. Part 2: biological aspects. Proc Inst Mech Eng H. 2010;224(12):1487–507.

5. Ismail FS, Rohanizadeh R, Atwa S, Mason RS, Ruys AJ, Martin PJ, et al. The influence of surface chemistry and topography on the contact guidance of MG63 osteoblast cells. J Mater Sci Mater Med. 2007;18:705–14.
6. Petrie TA, Raynor JE, Reyes CD, Burns KL, Collard DM, García AJ. The effect of integrin-specific bioactive coatings on tissue healing and implant osseointegration. Biomaterials. 2008;29(19):2849–57. https://doi.org/10.1016/j.biomaterials.2008.03.036.
7. Moerke C, Rebl H, Finke B, Dubs M, Nestler P, Airoudj A, et al. Abrogated cell contact guidance on amino-functionalized microgrooves. ACS Appl Mater Interfaces. 2017;9(12):10461–71. https://doi.org/10.1021/acsami.6b16430.
8. Finke B, Rebl H, Hempel F, Schäfer J, Liefeith K, Weltmann K-D, et al. Ageing of plasma-polymerised allylamine nanofilms and the maintenance of their cell adhesion capacity. Langmuir. 2014;30(46):13914–24. https://doi.org/10.1021/la5019778.
9. Rebl H, Finke B, Rychly J, Schröder K, Nebe JB. Positively charged material surfaces generated by plasma polymerized allylamine enhance vinculin mobility in vital human osteoblasts. Adv Biomat. 2010;12:356–64. https://doi.org/10.1002/adem.200980070.
10. Staehlke S, Koertge A, Nebe B. Intracellular calcium dynamics in dependence on topographical features of titanium. Biomaterials. 2015;46:48–57. https://doi.org/10.1016/j.biomaterials.2014.12.016.
11. Finke B, Luethen F, Schroeder K, Mueller PD, Bergemann C, Frant M, et al. The effect of positively charged plasma polymerization on initial osteoblastic focal adhesion on titanium surfaces. Biomaterials. 2007;28:4521–34.
12. Rebl H, Finke B, Schmidt J, Mohamad HS, Ihrke R, Helm CA, et al. Accelerated cell-surface interlocking on plasma polymer-modified porous ceramics. Mater Sci Eng C Mater Biol Appl. 2016;69:1116–24. https://doi.org/10.1016/j.msec.2016.08.016.
13. Pommerenke H, Schmidt C, Dürr F, Nebe B, Lüthen F, Müller P, et al. The mode of mechanical integrin stressing controls intracellular signaling in osteoblasts. J Bone Min Res. 2002;17(4):603–11.
14. Berridge MJ. Calcium signalling remodelling and disease. Biochem Soc Trans. 2012;40(2):297–309. https://doi.org/10.1042/BST20110766.
15. Labelle D, Jumarie C. Moreau R. Capacitative calcium entry and proliferation of human osteoblast-like MG-63 cells. Cell Prolif. 2007;40(6):866–84.
16. Takahashi A, Camacho P, Lechleiter JD, Herman B. Measurement of intracellular calcium. Physiol Rev. 1999;79(4):1089–125.
17. Izquierdo JH, Bonilla-Abadía F, Cañas CA, Tobón GJ. Calcium, channels, intracellular signaling and autoimmunity. Reumatol Clin. 2014;10:43–7. https://doi.org/10.1016/j.reuma.2013.05.008.
18. Liedert A, Kaspar D, Blakytny R, Claes L, Ignatius A. Signal transduction pathways involved in mechanotransduction in bone cells. Biochem Biophys Res Commun. 2006;349(1):1–5.
19. Kim JM, Choi S, Kwack KH, Kim SY, Lee HW, Park K. G protein-coupled calcium-sensing receptor is a crucial mediator of MTA-induced biological activities. Biomaterials. 2017;127:107–16. https://doi.org/10.1016/j.biomaterials.2017.02.038.
20. Whitaker M. Calcium microdomains and cell cycle control. Cell Calcium. 2006;40(5e6):585–92.
21. Paredes RM, Etzler JC, Watts LT, Zheng W, Lechleiter JD. Chemical calcium indicators. Methods. 2008;46(3):143–51. https://doi.org/10.1016/j.ymeth.2008.09.025.
22. Avila G, Misch K, Galindo-Moreno P, Wang HL. Implant surface treatment using biomimetic agents. Implant Dent. 2009;18(1):17–26. https://doi.org/10.1097/ID.0b013e318192cb7d.
23. Nebe JB, Moerke C, Staehlke S, Finke B, Schnabelrauch M, Anselme K, et al. Complex cell physiology on topographically and chemically designed material surfaces. Mater Sci Forum. 2017;879:78–83. https://doi.org/10.4028/www.scientific.net/MSF.879.78.
24. Ravenscroft-Chang MS, Stohlman JM, Molnar P, Natarajan A, Canavan HE, Teliska M, et al. Altered calcium dynamics in cardiac cells grown on silanemodified surfaces. Biomaterials. 2010;31(4):602–7. https://doi.org/10.1016/j.biomaterials.2009.09.084.
25. Sverzut AT, Crippa GE, Morra M, de Oliveira PT, Beloti MM, Rosa AL. Effects of type I collagen coating on titanium osseointegration: histomorphometric, cellular and molecular analyses. Biomed Mater. 2012;7(3):035007. https://doi.org/10.1088/1748-6041/7/3/035007.
26. Nebe B, Lüthen F, Finke B, Bergemann C, Schröder K, Rychly J, et al. Improved initial osteoblast's functions on amino-functionalized titanium surfaces. Biomol Eng. 2007;24(5):447–54. https://doi.org/10.1016/j.bioeng.2007.07.004.
27. Schulz MC, Korn P, Stadlinger B, Range U, Möller S, Becher J, et al. Coating with artificial matrices from collagen and sulfated hyaluronan influences the osseointegration of dental implants. J Mater Sci Mater Med. 2014;25(1):247–58. https://doi.org/10.1007/s10856-013-5066-3.
28. Morra M, Cassinelli C, Cascardo G, Cahalan P, Cahalan L, Fini M, et al. Surface engineering of titanium by collagen immobilization. Surface characterization and in vitro and in vivo studies. Biomaterials. 2003;24(25):4639–54. https://doi.org/10.1016/S0142-9612(03)00360-0.
29. Lab on a Slide, Solutions for BioMicroscopy. Ibidi GmbH, Martinried, Germany. 2007. http://www.zenonbio.hu/catalogues/ibidi_catalog_01_07.pdf. p. 14–5. Accessed 19 Oct 2017.
30. Reyes CD, Petrie TA, Burns KL, Schwartz Z, Garcia AJ. Biomolecular surface coating to enhance orthopaedic tissue healing and integration. Biomaterials. 2007;28:3228–35.
31. Czekanska EM, Stoddart MJ, Ralphs JR, Richards RG, Hayes JS. A phenotypic comparison of osteoblast cell lines versus human primary osteoblasts for biomaterials testing. J Biomed Mater Res A. 2014;102(8):2636–43. https://doi.org/10.1002/jbm.a.34937.
32. Van Kooten TG, Klein CL, Wagner M, Kirkpatrick CJ. Focal adhesions and assessment of cytotoxicity. J Biomed Mater Res. 1999;46(1):33–43.

LANGMUIR

*Publikation III*: pubs.acs.org/Langmuir

Article

# Comparison of Protein-Repellent Behavior of Linear versus Dendrimer-Structured Surface-Immobilized Polymers

Jutta Lehnfeld, Martina Gruening, Matthias Kronseder, and Rainer Mueller*

Cite This: https://dx.doi.org/10.1021/acs.langmuir.0c00625

Read Online

ACCESS | Metrics & More | Article Recommendations | Supporting Information

**ABSTRACT:** For many biomedical applications, material surfaces should not only prevent unspecific protein adsorption and bacterial attachment as in many other applications in the food, health, or marine industry, but they should also promote the adhesion of tissue cells. In order to take a first step toward the challenging development of protein and bacteria-repelling and cell-adhesion-promoting materials, polyamine and poly(amido amine) surface coatings with terminal amine groups and varying structure (dendrimer, oligomer, polymer) were immobilized on model surfaces via silane chemistry. Physicochemical analysis showed that all modifications are hydrophilic (contact angles <60°) and possess similar surface free energies (SFEs, ~46−54 mN/m), whereas their amine group densities and zeta potentials at physiological conditions (pH 7.4) varied greatly (−50 to +75 mV). In protein adsorption experiments with single proteins (human serum albumin (HSA) and lysozyme) as well as complex physiological fluids (fetal bovine serum (FBS) and human saliva), the amounts of adsorbed protein were found to correlate strongly with the zeta potential of the surface coatings. Both modifications based on linear polymers exhibited good protein repellency toward all proteins examined and are thus promising for testing in cell adhesion studies.

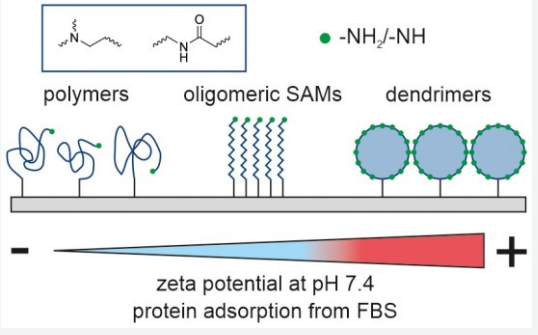


## INTRODUCTION

Surface fouling is a usually undesirable process, affecting, for example, the food industry,[1] the marine industry and sensoring,[2] and particularly health care.[3] In the medical field, the performance of medical devices or orthopedic implants strongly depends on the adsorption of proteins on the material surface because the attachment of proteins occurs rapidly after the first contact of the biomaterial with the human body and subsequent processes are mediated by this initial layer of proteins.[4] The colonization of bacteria and biofilm formation, for example, are enhanced by specific interactions between the protein film and the bacterial surface.[5] The attachment of tissue cells to a biomaterial surface was found to be influenced by adsorbed proteins as well.[4] Thus, it is vital to control protein adsorption as well as to prevent unspecific protein deposition. So far, many attempts have been made both to understand the correlation between physicochemical surface properties and the adsorption of proteins[6−8] and also to develop homogeneous or nanostructured nonfouling surface coatings.[9−13] Poly(ethylene glycol) (PEG)-based surface functionalizations exhibit excellent protein-repellent properties and have been used in a variety of applications,[14−17] but PEG coatings lack stability, especially under oxidative conditions.[18,19] Thus, novel protein-resistant and more stable functionalizations must be found, which, ideally, also inhibit bacterial attachment and, in the case of orthopedic implants, promote the attachment of tissue cells and the integration in the surrounding tissue.

In this context, some requirements for surface modifications can be described if they are supposed to show the aforementioned properties.

As unspecific protein adsorption is mainly entropy-driven and thus observed on hydrophobic surfaces, hydrophilic surfaces exhibit better protein-repellent properties in general.[20−22] Coatings withstanding protein adsorption also often share some additional similarities: They are swellable, moderately flexible, and possess polar functional groups with hydrogen bond-accepting moieties but lack hydrogen bond-donating groups as well as net charges.[23−25] Positively charged surface coatings, however, promote cell adhesion due to the interaction with the negatively charged eukaryotic cell surfaces and exhibit antibacterial properties, although bactericidal properties of cationic groups are reduced by previously adsorbed proteins.[26,27]

In our workgroup, poly(amido amine) (PAMAM) dendrimers, which are symmetrically branched macromolecules that are comparable to proteins with respect to their size and physicochemical properties, have been studied as surface

**Received:** March 4, 2020
**Revised:** April 30, 2020
**Published:** May 4, 2020



https://dx.doi.org/10.1021/acs.langmuir.0c00625
*Langmuir* XXXX, XXX,XXX−XXX

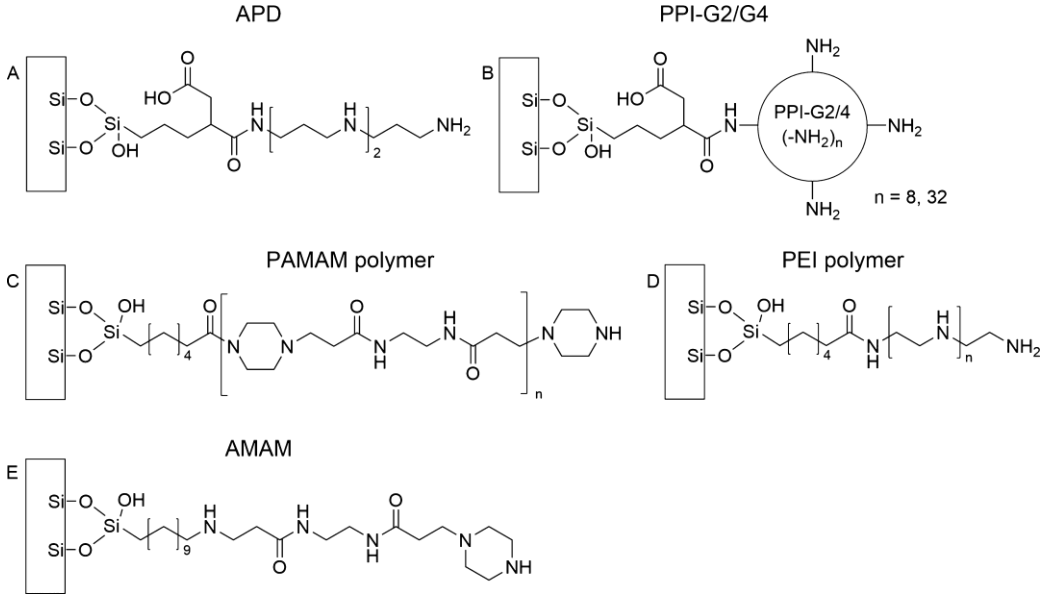


**Figure 1.** Overview of the synthesized surface modifications with (A) *N*,*N*′-bis(3-aminopropyl)-1,3-propanediamine, an oligo(propylene imine), (B) second- or fourth-generation poly(propyleneimine) dendrimers, (C) a linear poly(amido amine) polymer, (D) a linear poly(ethylene imine) polymer, and (E) an amidoamine structure from *N*,*N*′-ethylenebis(acrylamide) and piperazine.

modifications and were found to reduce unspecific protein adsorption and bacterial attachment but promote the adhesion of osteoblast cells.[28,29] Continuing this approach of combining surface amine groups, which are positively charged under physiological conditions, with varying, flexible structures, a systematic investigation of the surface properties of and protein adsorption on novel surface functionalizations of silicon and silica-based model substrates is presented. Via initial silane-based self-assembled monolayers (SAMs), surface modifcations with terminal amine groups were immobilized on the surfaces. The structure and the chemical functionalities within the molecules of the modifications were varied. Polyamines and PAMAMs were examined as dendrimers, linear polymers, or short oligomer-like species. The only exception in this systematic study is the PAMAM dendrimer which has been examined in detail in previous works.[28−30] These surface modifications were investigated thoroughly with respect to both their physicochemical characteristics (zeta potential, static and dynamic wetting behavior, and SFE) and their performance in protein adsorption experiments, determining unspecific protein adsorption with the bicinchoninic acid (BCA) assay.

We hypothesized that sufficiently flexible and hydrophilic coatings can exhibit protein-repellent properties despite possessing positively charged amine groups and thus may be suitable for further experiments regarding bacterial adhesion and cell attachment.

## EXPERIMENTAL SECTION

**Chemicals.** Nonporous sintered silica beads (diameter 250−315 μm, surface area 0.19 $m^2/g$ from gas adsorption experiment) were obtained from Brace GmbH (Germany), and nonporous silica particles (diameter 1 μm) were purchased from micromod Partikeltechnologie GmbH (Germany). In addition, 10 mm × 10 mm single-side-polished silicon wafers as well as 10 mm × 25 mm double-side-polished silicon wafers (Si-Mat Silicon Materials, Germany, cut by Disco Hi-Tec Europe GmbH, Germany) were used as substrates. Silanes 11-bromoundecyltrichlorosilane (95%), 7-oct-1-enyltrichlorosilane (95%), and 3-(triethoxysilyl)propylsuccinic acid anhydride (TESPSA, 95%) were purchased from ABCR Gelest (Germany). The poly(propylene imine) (PPI) dendrimers of generations 2 (PPI-G2, MW 773.3 g/mol, $C_{40}H_{96}N_{14}$, eight terminal primary amine groups) and 4 (PPI-G4, MW 3513.8 g/mol, $C_{184}H_{432}N_{62}$, 32 terminal primary amine groups) were obtained from SyMO-Chem (The Netherlands) (structure in Figure S1), whereas *N*,*N*′-bis(3-aminopropyl)-1,3-propanediamine (APD, 97%), *N*,*N*′-ethylenebis(acrylamide) (96%), piperazine (anhydrous, 99%), and poly(ethylene imine) (PEI) polymer (linear, MW 25 000 g/mol) were purchased from ABCR Gelest (Germany).

Sulfosuccinimidyl-4-*O*-(4,4′-dimethoxytrityl) butyrate (sulfo-SDTB) was purchased from Bioworld (USA). HSA (≥96%) and lysozyme (≥90%) were obtained from Sigma-Aldrich Chemie GmbH (Germany), and FBS was purchased from PAN-Biotech GmbH (Germany). Human saliva was prepared as published previously.[28] Unless otherwise stated, all further solvents and reagents were obtained from Sigma-Aldrich Chemie (Germany), VWR International GmbH (Germany), or Carl Roth GmbH (Germany) in the highest purity available. Sterile-filtered water was obtained by the filtration of purified water (ϱ ≥ 18 MΩcm, by means of an ultrafiltration apparatus from Millipore Corp., USA) with a bottle top vacuum filtration system with a 0.2 μm poly(ether sulfone) membrane (VWR, Germany).

**Oxidation of the Substrates.** As described in previous publications,[28−30] wafer substrates were cleaned by sonication in acetone for 15 min. After that, substrates (precleaned wafers and previously untreated beads) were oxidized in half-concentrated nitric acid (38% w/w) via sonication for 30 min and stored in $HNO_3$ for at least 2 weeks. Prior to functionalization, nitric acid was removed via rinsing repeatedly with sterile-filtered water (until pH 5−6 was reached), and the substrates were dried in a desiccator equipped with silica gel as the drying agent under vacuum.

**Modification of Silicon and Silica Substrates.** *Synthesis of Siloxane Monolayers.* Unless stated otherwise, silanizations as well as successive functionalization steps were carried out under the exclusion of water (use of dried solvents and glassware) under an argon atmosphere, as described previously.[30]

The synthesis of the of 6-carboxyhexanylsiloxane monolayer (SAM-COOH) was performed according to Liu et al.[31] and has been explained in previous publications.[28,30] Silanization was achieved with a 7-oct-1-enyltrichlorosilane solution in anhydrous toluene for 2 h at room temperature under a protective nitrogen atmosphere. After rinsing multiple times with toluene and drying, the oxidation of the

https://dx.doi.org/10.1021/acs.langmuir.0c00625

terminal alkene groups was performed with $KMnO_4$ (25 mmol/L in 0.1 mol/L sulfuric acid) for 15 min at room temperature. The removal of manganese dioxide and excess permanganate was achieved by rinsing multiple times with 0.1 mol/L $H_2SO_4$, 0.1 mol/L sodium bisulfite ($NaHSO_3$) solution, 0.1 mol/L HCl solution, and repeatedly with water until a neutral pH was reached.

The preparation of the 11-aminoundecylsiloxane monolayers (SAM-$NH_2$) was derived from the protocol by Balachander and Sukenik[32] and has already been published previously.[28,30] Summarized shortly, silanization was carried out in a 11-bromoundecyltrichlorosilane solution in anhydrous toluene for at least 2 h at room temperature. The bromine-terminated SAM was rinsed with toluene for excess silane removal and dimethyl sulfoxide (DMSO). Substitution of the bromine with azide groups was performed with a solution of sodium azide ($NaN_3$) in anhydrous DMSO for at least 24 h. After rinsing with DMSO and tetrahydrofuran (THF), reduction of the azide groups was performed with a lithium aluminum hydride ($LiAlH_4$) solution in anhydrous THF for at least 24 h. Wafer substrates were then rinsed once with 10% hydrochloric acid (HCl), once with 0.1 mol/L HCl, and repeatedly with water until neutralization was reached. Silica beads and particles, however, were first rinsed with anhydrous THF and then several times with diluted HCl solution (0.1 mol/L) and repeatedly with water (until pH 6 was reached).

The silanization of substrates with a TESPSA monolayer was achieved as described previously[28−30] with a solution of TESPSA and anhydrous acetic anhydride (molar ratio 1:3) in anhydrous toluene at elevated temperatures (110 °C for 30 min, 130 °C for 10 min) under an argon atmosphere. Excess silane was removed by rinsing with toluene.

*Further Modification of SAMs with Amine-Group-Containing Reagents.* APD as well as second- and fourth-generation PPI dendrimers were immobilized on TESPSA-modified substrates via the formation of an amide bond, similar to previously described immobilization proecdures.[30] After the rinsing steps with toluene, the TESPSA-coated substrates were sonicated once with anhydrous DMSO and immersed in the respective APD or PPI dendrimer solution in anhydrous DMSO for 2 days at room temperature. (See Supporting Information Table S1 for details.) Excessive reagent was removed by rinsing at least once with DMSO and multiple times with methanol before drying.

A linear poly(amido amine) (PAMAM) polymer was synthesized similar to the procedure described by Dey and Ray.[33] *N*,*N*′-Ethylenebis(acrylamide) and piperazine were dissolved in water in a 1:1 molar ratio, and the solution was stirred under an argon atmosphere at 30 °C. After 2 days, a 20% molar excess of piperazine was added to the solution and stirred for 5 h in order to guarantee piperazine end groups. After a total reaction time of 48 h, the solution was poured into excess acetone, and the slightly yellow and viscous precipitate was filtered. The crude product was separated from oligomeric species by dialysis against water overnight and subsequently freeze-dried and analyzed via HPLC-ESI-MS, reflective IR, and $^1H$ and $^{13}C$ NMR spectroscopy (Figures S2−S4 in the Supporting Information).

The obtained linear PAMAM polymer and a linear PEI polymer were immobilized on SAM-COOH-modified substrates. Therefore, the carboxylic acid groups were converted to active esters via reaction with a solution containing *N*-(3-(dimethylamino)propyl)-*N*′-ethylcarbodiimide hydrochloride and *N*-hydroxysuccinimide in 0.1 mol/L 2-(*N*-morpholino)ethanesulfonic acid buffer (pH 5.4) for 2 h at room temperature. After reagent removal via rinsing with buffer and water, immobilization of the PAMAM polymer was performed via immersion in a 10 mg/mL solution in water for 1 h at room temperature. Excess polymer was removed by rinsing with water. For the modification with PEI polymer, the substrates with activated carboxylic acid esters were rinsed with buffer, water, and methanol before immersion in a 10 mg/mL PEI solution in a methanol/water mixture (9:1 v/v) for 1.5 h at room temperature. Removal of excess polymer was achieved by rinsing with the methanol/water mixture and methanol.

The synthesis of an amidoamine (AMAM) SAM (with structure analogous to that of the PAMAM polymer) was carried out with the SAM-$NH_2$. The substrates were immersed in a 200 mmol/L solution of *N*,*N*′-ethylenebis(acrylamide) in DMSO overnight at room temperature. After the removal of excess *N*,*N*′-ethylenebis-(acrylamide) by rinsing with DMSO several times, the substrates were transferred to a 200 mmol/L solution of piperazine in DMSO and the reaction was performed at room temperature overnight. Excess reagent was removed by rinsing with DMSO and methanol.

**Analysis of the Modified Substrates.** *Verification of Successful Surface Modification.* In order to confirm successful surface modification diffuse reflectance infrared Fourier transform (DRIFT) spectra were recorded from functionalized silica particles, using a diffuse reflectance accessory from Pike Technologies Inc. (USA) and a FT/IR-610 infrared spectrometer from Jasco Inc. (Japan). Spectra of unmodified particles were used as background.

Furthermore, X-ray photoelectron (XPS) spectra of modified silicon wafers were recorded with a PHI 5700 electron spectrometer from Physical Electronics Co. (USA) using monochromatic Al Kα radiation (1486.6 eV).

The density of surface amino groups was determined with the colorimetric sulfo-SDTB assay on functionalized silica beads.[34] Beads were incubated in 0.1 mol/L sulfo-SDTB in 50 mmol/L $NaHCO_3$ buffer (pH 8.5, 2% (v/v) dimethylformamide (DMF)) for 30 min at room temperature. After removal of the unbound analyte by rinsing with water, 4,4′-dimethoxytrityl cations were released upon treatment with 35% perchloric acid for 20 min. The absorbance of the supernatant solution at 495.6 nm was recorded with a Lambda 18 UV/vis spectrometer from PerkinElmer (USA).

*Physicochemical Analysis.* The hydrophilicity of functionalized silicon wafers was obtained from static contact angle measurements with water via a sessile drop technique using a P1 goniometer from Erna Inc. (Japan). Droplets of 2.5 μL were placed on the wafer surface with an automated dispenser from Hamilton Company (USA). For the calculation of the SFE, static contact angles were measured with water, formamide, and diiodomethane. The SFE was calculated using the Lifshitz−van der Waals/acid−base approach.[35] Dynamic wetting behavior was analyzed on double-side-coated silicon wafers via the Wilhelmy balance technique using a K100 tensiometer from Kruess (Germany). After the determination of the surface tension of the wetting liquid (water or phosphate-buffered saline solution (PBS)) via the Wilhelmy plate method, for each wafer 10 immersion cycles were recorded with a maximum immersion depth of 12 mm and a progression speed of 10 mm/min. The respective advancing and receding contact angles were obtained by extrapolation of the linear parts of the force/length lines to zero immersion depth.

The zeta potential of modified substrates was examined using two different techniques via either electrophoretic measurements of functionalized silica particles with a Zetasizer Nano ZS from Malvern Inc. (U.K.) or by means of streaming current measurements of single-side-coated wafers with a SurPass electrokinetic analyzer from Anton Paar (Austria). Measurements were performed in 1 mmol/L KCl solution, and the pH was adjusted with HCl and KOH or NaOH solutions.

*Quantification of Protein Adsorption.* Quantification of protein adsorption on modified silica beads was performed via the BCA assay according to the procedure described previously.[28,29] Protein adsorption was tested with undiluted physiological fluids FBS and human saliva as well as 10 mg/mL solutions of HSA or lysozyme in PBS buffer (150 mmol/L, pH 7.4). The protein content of the physiological fluids was determined before adsorption experiments by means of the BCA assay. After the incubation of functionalized beads with protein solution for 60 min at 25 °C, unadsorbed protein was removed by rinsing thoroughly with PBS. (See the Supporting Information for details on the procedure.) Dried protein-covered beads and the BCA working solution (prepared according to the manufacturer's instructions) were mixed while cooling in an ice bath. Functionalized beads without protein (HSA, lysozyme) or oxidized but otherwise unmodified beads (saliva, FBS) served as controls for blank samples and the standard curve. For each BCA assay, a standard

curve was recorded, adding dilutions with known concentration of the respective protein solution to BCA working solution in the presence of functionalized or oxidized beads, respectively. After incubation for 30 min in a water bath at 40 °C, the reaction was stopped by cooling in an ice bath, and the extinction of the supernatant solution was recorded at 562 nm with the Lambda 18 UV/vis spectrophotometer from PerkinElmer (USA).

*Statistics.* For the protein adsorption experiments, pairwise comparisons were performed with the Mann−Whitney-U-Test with considered $p$ values of <0.05 (IBM SPSS Statistics, version 25, USA). Unless otherwise stated, results are provided as medians with 25 and 75% quartiles (interquartile range).

## RESULTS AND DISCUSSION

**Verification of Successful Surface Modification.** Successful immobilization of the surface modifications could be proven by XPS (on silicon wafers), IR spectroscopy (on silica particles, see Supporting Information Figure S5), and the sulfo-SDTB assay (on silica beads) (Table 1). Compared to the XPS data from the intermediate siloxane SAMs,[30] a decreased silicon content but increased carbon content could be detected for all surface modifications, which is a consequence of the formation of a thicker organic layer. In addition, a higher nitrogen content was measured due to the introduction of amine groups. This result was supported by the data obtained from the sulfo-SDTB assay, an assay detecting amine groups. For all surface modifications, an increase in the amine group density could be observed compared to that of previous silane SAMs without amine groups (Table 1). The only exception is the AMAM surface, where no change in the amine group density was observed, compared to the SAM-$NH_2$ monolayer, as the number of surface amine groups remained constant.

**Table 1.** Characterization of the Surface Modifications via XPS and a Sulfo-SDTB Assay (Providing Amine Group Density)[a]

| | XPS [atom %] | | | | |
|---|---|---|---|---|---|
| | Si | C | O | N | amine group density [nmol/m$^2$] |
| oxidized[b] | 49 | 19 | 31 | 1 | 104 (33−127) |
| TESPSA[b] | 22 | 42 | 35 | 0 | 186 (128−188) |
| APD | 17 | 47 | 29 | 6 | 504 (362−680) |
| PPI-G2 | 12 | 56 | 24 | 8 | 2100 (2031−2935) |
| PPI-G4 | 10 | 58 | 20 | 11 | 3784 (3155−4092) |
| SAM-COOH[b] | 41 | 26 | 33 | 0 | 164 (136−170) |
| PAMAM polymer | 23 | 40 | 27 | 10 | 472 (427−569) |
| PEI polymer | 30 | 33 | 31 | 6 | 717 (660−776) |
| SAM-$NH_2$[b] | 38 | 32 | 28 | 2 | 2553 (2036−3038) |
| AMAM | 30 | 37 | 29 | 4 | 2581 (2295−2606) |

[a]For XPS measurements, at least two wafers were measured ($n \geq 2$). The amine group density was determined from at least two independent experiments with three replicates each ($n \geq 6$) for each surface modification. Medians are provided (with 25 and 75% quartiles in brackets). [b]XPS data for oxidized substrates, TESPSA, SAM-COOH, and SAM-$NH_2$ from Katzur et al.[30]

An interpretation of the results of the sulfo-SDTB assay in terms of the grafting density of the different coatings should be made very carefully. The assay is broadly applied for the quantification of primary amine groups on solid substrates (e.g., of immobilized peptides[36,37]) but not for modifications containing only secondary amine groups as reactive species. As secondary amines have been proven to be more nucleophilic than primary amine groups,[38] it can be assumed that these groups may also contribute to the formation of the trityl cation in the sulfo-SDTB assay despite possible steric hindrance. This effect can be seen in the positive signal of the PAMAM polymer coating of the present study which carries only secondary and tertiary groups. Although no direct comparison between surface modifications with varying compositions of primary, secondary, and tertiary amines can be made, the results allow a rough estimate of the surface density of the immobilized molecules. We can state that the dendrimers are immobilized at high surface densities, while all linear molecules are immobilized at considerably lower surface densities.

**Analysis of the Physicochemical Properties.** The different surface modifications were further analyzed with respect to their physicochemical properties, namely, static wetting behavior, SFE, dynamic wetting behavior, and zeta potential. The results are summarized in Table 2, Figures 2 and 3, and the Supporting Information (Table S3, Figure S6).

*Wettability and SFE.* All surface modifications exhibit increased water contact angles compared to those of oxidized but uncoated wafers.[29] Nevertheless, they can be considered to be hydrophilic because they exhibit water contact angles of

**Table 2.** Static Contact Angles, SFE, and Zeta Potential Data (Isoelectric Point (IEP) and Zeta Potential at pH 7.4) for the Surface Modifications[a]

| | contact angle [deg] | | | | zeta potential | | | |
|---|---|---|---|---|---|---|---|---|
| | | | | | electrophoresis | | streaming current | |
| | water | formamide | $CH_2I_2$ | SFE [mN/m] | IEP | at pH 7.4 [mV] | IEP | at pH 7.4 [mV] |
| oxidized[b] | 14 (12−16) | 9 (6−12) | 41 (40−45) | 56.8 (56.5−57.2) | 2.5 | −50 | 2.7 | −90 |
| APD | 46 (41−53) | 34 (33−35) | 26 (24−28) | 50.2 (49.7−50.5) | 6.0 | −50 | | |
| PPI-G2 | 45 (39−54) | 31 (29−32) | 32 (29−33) | 51.3 (51.2−51.6) | 7.9 | +25 | 8.29 | +31 |
| PPI-G4 | 39 (31−47) | 30 (24−32) | 40 (39−42) | 50.4 (49.7−52.8) | 9.1 | +75 | 8.87 | +48 |
| PAMAM polymer | 27 (22−36) | 19 (16−23) | 37 (27−40) | 54.3 (53.7−54.5) | 5.7 | −35 | | |
| PEI polymer | 35 (33−41) | 31 (29−33) | 39 (34−40) | 49.3 (48.8−50.3) | 5.9 | −30 | 7.46 | +2 |
| AMAM | 57 (46−60) | 40 (38−40) | 45 (43−48) | 46.0 (45.5−46.6) | 9.0 | +50 | | |

[a]For each surface coating, contact angles were measured on at least 5 wafers per liquid (four drops per wafer, $n \geq 20$). Zeta potential measurements were performed in 1 mmol/L KCl solution. Electrophoresis data was obtained from at least four measurements at each pH value, each consisting of two measurements in triplicate ($n \geq 24$). Three streaming current measurements were carried out for each modification ($n = 3$). Medians are provided (with 25 and 75% quartiles in brackets). [b]Results for contact angles, SFE, and zeta potentials of oxidized substrates are taken from Staehlke et al.[29]

https://dx.doi.org/10.1021/acs.langmuir.0c00625

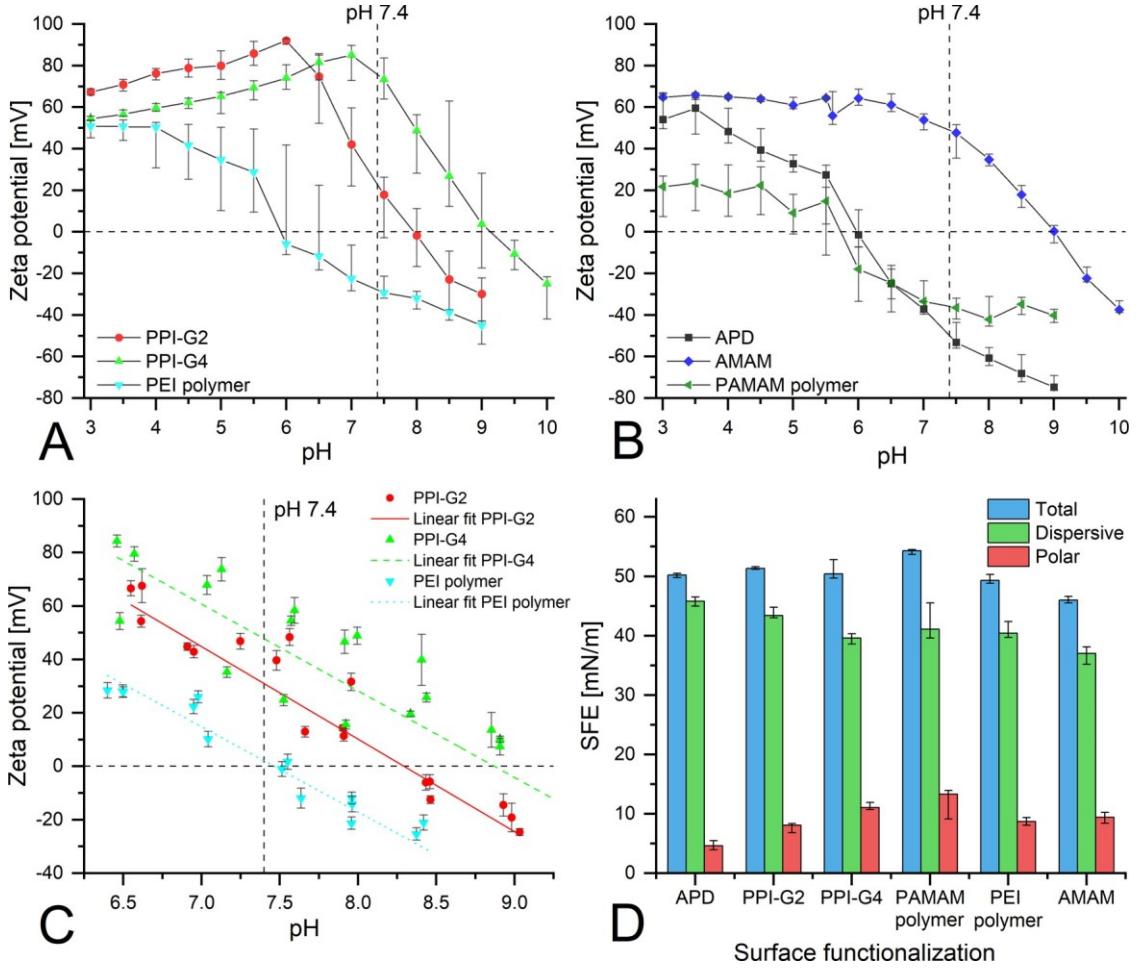


**Figure 2.** Zeta potential determined via electrophoresis of silica particles functionalized with (A) PPI-G2, PPI-G4, or PEI polymer or (B) APD, AMAM, or PAMAM polymer. (C) Zeta potential of PPI-G2-, PPI-G4-, or PEI-polymer-coated silicon wafers, obtained from streaming current measurements (mean average ± standard deviation). All zeta potential measurements were performed in 1 mmol/L KCl solution. (D) SFE as well as polar and dispersive components of the different surface coatings. For (A), (B), and (D), medians (with the interquartile range shown as error bars) are provided.

<60°. The lowest angles can be found for the polymers (27° for the PAMAM polymer and 35° for the PEI polymer), which are thus the most hydrophilic surface modifications. Contact angles of between 39 and 46° were measured for PPI-G4-, PPI-G2-, and APD-functionalized surfaces. The least hydrophilic surface modification was the AMAM structure with a contact angle of 57°. In all cases, the contact angles of the terminal modification were lower than those of the intermediate SAMs, again indicating successful surface modification.[30]

From contact angle measurements with formamide and diiodomethane (in addition to water), the SFE (as well as its polar and dispersive component, see Figure 2D) was calculated. (Components of surface tensions used for calculation are provided in Table S2 of the Supporting Information.) No major differences could be determined between the different surface modifications with SFEs ranging from 46.0 to 54.3 mN/m, which are all lower than the SFE of oxidized wafers. The lowest SFE was determined for the AMAM surface, also exhibiting the lowest dispersive component (37 mN/m), whereas the highest SFE (and the largest polar component) was obtained for the PAMAM- polymer-covered substrates (54.3 and 13.3 mN/m, respec- tively). This modification also exhibited the highest content of polar interactions at 24%. The lowest content of polar interactions was found for the APD modification of 9%.

The results for the SFE are in good accordance with previous results. The SFE obtained for the PPI-G4 dendrimer is comparable to those on amine-terminated PAMAM dendrimer surfaces, measured by Katzur et al.,[30] which were characterized by total and polar SFEs of ~45 and ~12 mN/m. The magnitudes of the polar components of PAMAM-G5-$NH_2$- and PPI-G4-functionalized surfaces are thus quite similar, whereas the dispersive component of the latter is significantly higher, leading to a higher total SFE. This difference can probably be explained by the absence of inner amide groups of PPI dendrimers.

Comparing structurally related modifications APD, PPI-G2, and PPI-G4 which bear only amine groups as functional groups, no differences can be seen for the total SFE. Two clear tendencies, however, can be observed for the polar as well as the dispersive component. The former is increasing from APD via PPI-G2 to PPI-G4, and the latter is decreasing, both caused by the increasing number of inner and surface amine groups. In general, surfaces which contain both amine and amide groups seem to possess larger polar contributions to the SFE, as both the PAMAM polymer and AMAM-functionalized surfaces exhibit polar contributions of >20% (24 and 21%,

https://dx.doi.org/10.1021/acs.langmuir.0c00625

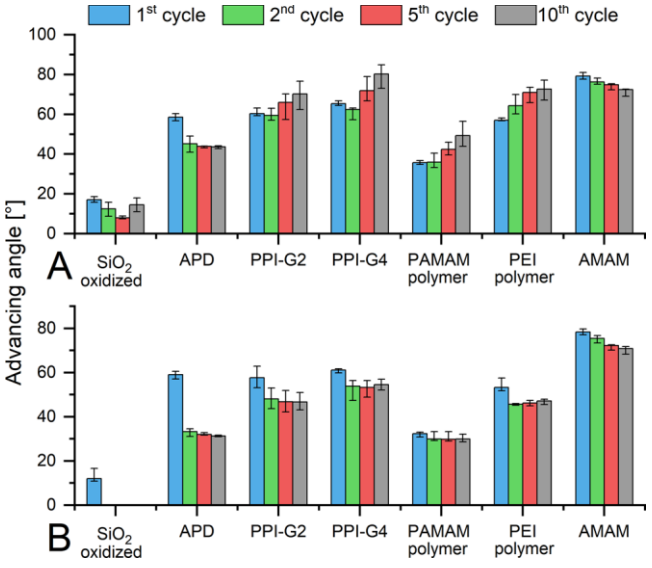


**Figure 3.** Advancing contact angles obtained from dynamic contact angle measurements with (A) water and (B) PBS buffer. Results for cycles 1, 2, 5, and 10 are given as medians (with the interquartile range as error bars). For each surface modification, six wafers were analyzed ($n$ = 6).

respectively), which is higher than the polar component of any other surface coating except PPI-G4 (22% polar component).

*Zeta Potential.* In contrast to the SFEs, zeta potentials varied strongly among the different surface coatings. Zeta potential measurements were performed via the electrophoresis of functionalized silica particles and, if necessary, were supported by streaming current measurements of modified single-side-polished wafers. This was the case for surface coatings with PPI dendrimer or PEI polymer coatings, as particles with these modifications were prone to aggregation close to the IEP, leading to large experimental errors (Figure 2A). For the electrophoresis experiments, the range from pH 3 to pH 9 or pH 10 was investigated (Figure 2A,B). In addition to the complete potential curves, the isoelectric points (IEPs) as well as the zeta potentials at pH 7.4 were extracted (Table 2). At first, all surface modifications drastically increased the zeta potential of the surfaces, indicated by a shift of the IEP from 2.5 or 2.7 for unmodified substrates[29] to at least 5.7 for the PAMAM polymer. Surfaces with PAMAM polymer, PEI polymer, or APD modification exhibited IEPs at pH 5.7, 5.9, or 6.0, respectively, in electrophoretic measurements. This correlates with negative zeta potentials (−30 to −50 mV) under physiological conditions. The low IEPs of the coatings with linear polymers (PEI polymer and PAMAM polymer) might be explained by the properties of the initial SAM. The intermediate SAM-COOH possesses an IEP of <2[28] and thus carries negative charges over the complete pH range from 3 to 10. The grafting-to approach, used for both polymers, might lead to an incomplete conversion of these carboxylic groups to amide groups as well as to a low-density surface coverage with polymers in the mushroom regime.[39,40] The IEP of the APD-modified surfaces is slightly higher (at pH 6.0). This value is significantly lower than the results obtained for amine-terminated SAMs as an IEP at pH 7.3 was obtained for SAM-$NH_2$-modified substrates from streaming current experiments in our group.[30] A higher zeta potential is expected because the immobilized APD molecule contains a terminal primary group as well as inner secondary amine groups. Their p$K_a$ values in dilute solution are expected to be ∼10. This protonation behavior, however, was shown to be altered completely for surface-immobilized amines in a SAM. Shyue et al.[41] demonstrated that, due to the dense packing of the functional groups in a SAM, deprotonation is a gradual process, starting below pH 0 and having a p$K_a$ value of approximately 3 because as soon as some surface groups are protonated, further protonation is hindered due to the unfavorable electrostatic interactions. Thus, the IEP of the APD surface is lowered. This trend may be enhanced by the immobilization procedure. Due to the ring opening of the succinic anhydride during amide formation, one negatively charged carboxyl group is formed for each immobilized APD molecule, decreasing the zeta potential even further. This might serve as an explanation of why the IEP of the APD surface is lower than the IEP measured by Sugimura et al.,[42] who obtained an IEP of 7.5 to 8.0 for a silane monolayer in which each silane molecule carried one inner secondary and one surface primary amine group.

The surface modifications with PPI dendrimers possess a high density of amine groups that leads to surfaces with high IEPs (7.9 to 9.1 in electrophoretic measurements). These zeta potentials are even higher than the results obtained for measurements of silica particles with amine-terminated PAMAM dendrimers (IEP 7.6[29]) due to their increased amine group density. The PPI coatings all exhibit strongly positive zeta potentials under physiological conditions. The strongly positive zeta potentials over a large pH range and the steep decrease in the zeta potential at high pH values correspond to the protonation behavior that van Duijvenbode et al.[43] observed. Due to its unique shell-like deprotonation behavior, one-third of the dendrimer's amine groups are deprotonated at around pH 6, whereas the other two-thirds remain protonated until pH 10.[43] A result obtained for the PPI dendrimer surfaces which was not observed for any other surface modification was the increase in zeta potential with increasing pH in the range between pH 3 and pH 6, which may lead to the conclusion that the dendrimer conformation changes, causing a larger number of exposed and protonated amine groups. This, however, is not supported by theoretical calculations of the radial density distribution profiles of PPI dendrimers under different pH conditions. Jain et al.[44] found very similar distributions at pH 4 and 7.4 which changed completely upon an increase in the pH to 10.

A behavior comparable to that of the PPI dendrimer surfaces was observed for the AMAM coating with an IEP at approximately pH 9.0 and a highly positively charged surface (+50 mV) at pH 7.4. This strongly positive surface charge is the additive result of the underlying amine SAM (with an IEP of 7.3[30]) as well as of the modification with a terminal piperazine molecule which possesses a p$K_a$ value of 9.71 in solution.[45]

The results obtained from electrophoresis measurements are supported by the data from streaming current experiments of the PPI dendrimer or PEI-polymer-functionalized surfaces.

*Dynamic Contact Angle Measurements.* In order to gain more detailed information about the dynamic behavior of the surface coatings in solution, tensiometric experiments were performed. In addition to water (unbuffered, pH ∼5.5), PBS solution (pH 7.4, 150 mM NaCl) was used in order to investigate the properties of the modifications under physiological conditions. The advancing angles are shown in

https://dx.doi.org/10.1021/acs.langmuir.0c00625

Figure 3, and further information is provided in the Supporting Information (Table S3, Figure S6). Comparing all surface modifications, advancing angles of the different coatings are higher than those of oxidized substrates and vary greatly, ranging from ~30° (APD and PAMAM polymer with PBS buffer) to 80° (PPI-G4 with sf-water). Receding angles, by contrast, are very similar and usually <10°, with AMAM being the only exception (receding angles 26−37°). Larger hysteresis was observed for substrates with PPI dendrimers or a PEI polymer coating (~40−60°), in contrast to smaller hysteresis values for APD, PAMAM polymer, and AMAM (~20−40°). The results for PPI dendrimer coatings are in good accordance with the results by Zhang et al.[46]

Measurements in pure water revealed decreasing advancing contact angles and hysteresis for AMAM- and APD-modified surfaces with an increasing number of cycles. The opposite was observed for PPI dendrimer or PAMAM- or PEI-polymer-functionalized surfaces. Increasing hysteresis (with an increasing number of immersion cycles) has also been observed by Katzur et al.[30] for PAMAM-G5-$NH_2$ dendrimers. The large and increasing hysteresis values for the polymer and dendrimer modifications can possibly be explained by the higher flexibility and swellability of the polymer molecules compared to those of the short-chain analogues.[47] Both the dendrimer branches and the polymer chains are probably able to reorient themselves,

exposing hydrophobic $-CH_2-$ groups to the air interface or amine or amide groups to the water interface, respectively. Kobayashi et al.[48] proposed similar properties for polymer brushes with hydrophobic and hydrophilic moieties. The flexibility required for reorientation at the interface not only is given for linear polymers but also has been proven for PPI dendrimers.[49]

Comparing tensiometric data from immersion in pure water with measurements in PBS, the observed advancing angles in PBS are in general lower and decrease with an increasing number of immersion cycles (i.e., the hydrophilicity of the surface coatings increases). This observation is surprising at first glance because other studies found that the static contact angles of amine group bearing surface modifications increase with increasing pH due to the deprotonation of charged functional groups.[50] The surface modifications in this study, however, bear charges at pH 5.5 and 7.4 (Figure 2), although the zeta potential may vary in sign and amplitude. If the reduced advancing angles are not caused by the higher pH of PBS buffer, then the ions present must be responsible for this observation. Although in the literature no evidence has been found for any influence of the salt content on the dynamic contact angles of uncharged polymers,[51] it was demonstrated in simulations by Welch and Muthukumar[52] that high ionic strengths lead to a dense and more crowded conformation of the PPI dendrimer in solution. Similar behavior might be observed here as the higher ionic strength can reduce the flexibility and swelling of the surface coating and thus the contact angle hysteresis due to charge screening.

**Protein Adsorption.** Quantitative analysis of protein adsorption was performed with the BCA assay, investigating adsorption from HSA or lysozyme solutions and from undiluted physiological fluids human saliva and FBS (Figure 4). The total protein content of the physiological fluids was also quantified with a BCA assay to be 0.92 (0.88−0.97) mg/mL for saliva or 36.1 (34.8−37.7) mg/mL for FBS.

As a rule, protein adsorption was lower from lysozyme than from HSA solutions as well as from saliva than from FBS. This

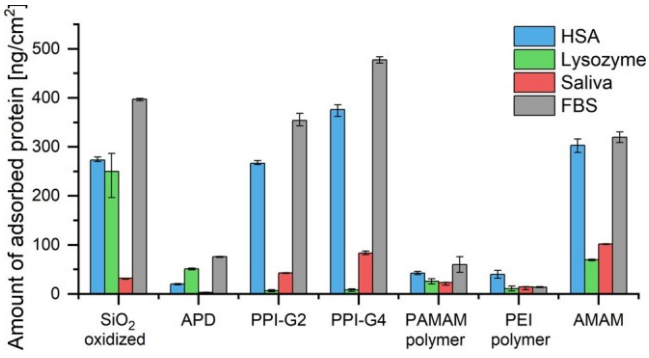


**Figure 4.** Amount of adsorbed proteins from HSA or lysozyme solution (each 10 mg/mL in PBS buffer), undiluted human saliva, or undiluted FBS on differently functionalized silica beads, determined with the BCA assay. Protein adsorption was analyzed in at least two independent experiments with three replicates each ($n \geq 6$) for each surface modification. Medians (with the interquartile range as error bars) are provided. For improved clarity, the results of the Mann−Whitney-U test are not included in the figure. All pairwise comparisons showed significance, with the exception of the following: HSA: $SiO_2$ − PPI-G2, PAMAM polymer − PEI polymer; lysozyme: PPI-G2 − PPI-G4, PPI-G2 − PEI polymer, PPI-G4 − PEI polymer; and FBS: APD − PAMAM polymer.

observation can be explained by the differences between the model proteins and physiological solutions used in the assay. HSA is a medium-sized protein with a molecular weight of 66.5 kDa, which is negatively charged under physiological conditions (IEP 4.7).[53] Lysozyme, however, is a small protein (14.6 kDa) carrying a positive charge at pH 7.4 (IEP 11.1).[20] These two proteins further differ in their susceptibility to denaturation. Whereas HSA possesses a low internal stability and thus easily denatures upon adsorption and can be classified as a "soft" protein, lysozyme is an example of a "hard" protein, exhibiting comparably high stability toward denaturation.[20] Thus, HSA is more prone to adsorption, which is reflected in the fact that the amounts of adsorbed HSA were higher than the amounts of lysozyme on all surfaces (except APD). FBS is a physiological fluid (pH 7.7 ± 0.1 measured, ionic strength 0.15 mol/L[54]) with a protein content of between 32 and 42 mg/mL and a large number of different proteins, with albumin being the most abundant among them (approximately two-thirds of the total protein content).[55] Therefore, adsorption from FBS led to higher amounts of the same magnitude of adsorbed protein compared to adsorption from HSA, with the PEI polymer modification being the only exception. Human saliva (pH 8.3 ± 0.1 measured), in contrast to FBS, contains fewer ions (ionic strength ~40−90 mmol/L[56]) and only 0.3% proteins with IEPs which mainly range from 4 to 8.[57,58] The rather low protein content of saliva (total content of approximately 1−2 mg/mL[57]) serves as an explanation for the overall low protein adsorption from saliva compared to adsorption experiments with HSA or FBS. Furthermore, the surface modifications can be divided into two groups, with respect to their performance in protein adsorption experiments. Enhanced protein adsorption for at least two of the four tested solutions (compared to the $SiO_2$ reference) could be observed for coatings with PPI dendrimer or AMAM, whereas protein adsorption is strongly reduced on APD-, PEI-polymer-, or PAMAM-polymer-functionalized substrates. The lowest protein fouling was obtained for the PEI-polymer-functionalized surface. In this case, the amount of adsorbed proteins

https://dx.doi.org/10.1021/acs.langmuir.0c00625

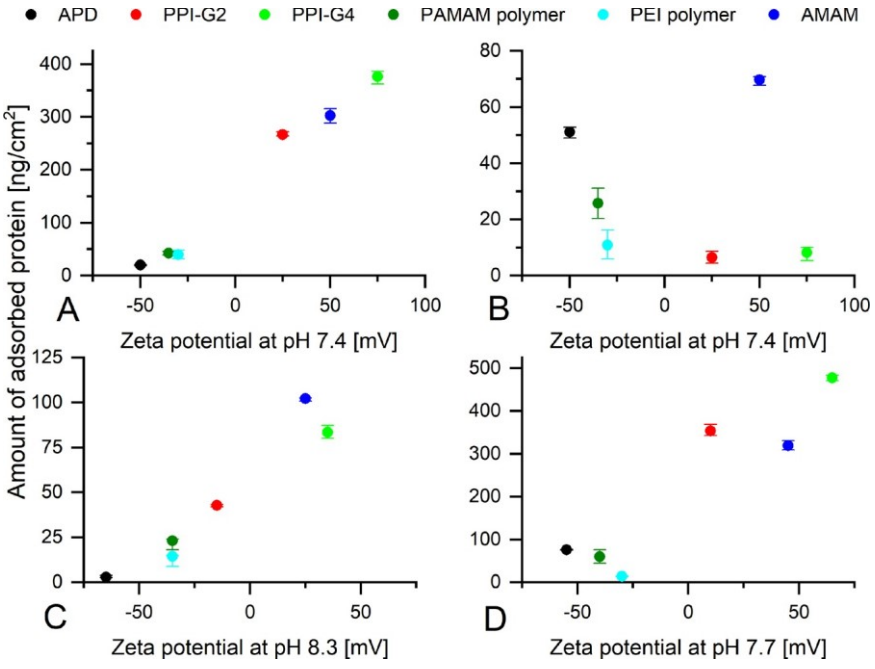


**Figure 5.** Dependence of the protein from solutions of (A) HSA or (B) lysozyme as well as (C) saliva and (D) FBS on the zeta potential of the surface modifications at the pH of the respective protein solution. Medians are depicted (with the interquartile range as error bars).

was reduced to values of between 3.5% (FBS) and 14.7% (HSA) of the amounts of protein on the $SiO_2$ reference.

In the following section, protein adsorption will be discussed with respect to the properties of the different surface modifications, such as wettability, SFE, and zeta potential. Figures displaying protein adsorption of the different investigated proteins or protein solutions as a function of the aforementioned surface properties are provided in Figure 5 or in the Supporting Information (Figures S7−S11).

Regarding surface wettability and SFE, no correlation can be observed in our study. This might be caused by the fact that the wettability and SFE of the surfaces do not exhibit large differences among each other. Other studies, however, demonstrated correlations between measured contact angles and protein adsorption. In the majority of the cases, increased protein adsorption on hydrophobic surfaces was observed. Detailed studies investigating the adhesion forces between model proteins (also including lysozyme and serum albumin) and surface modifications with varying contact angles were performed by Sethuraman et al.[59] and Xu and Siedlecki.[22] They observed stepwise behavior with strong adhesive interactions for hydrophobic surfaces (water contact angles >60−65°) and significantly weaker interactions for hydrophilic surfaces (contact angles <60°).

Considering these results, all surface modifications in this study can be classified as part of the hydrophilic and protein-repellent group. Less-detailed studies are available for the adsorption of serum or saliva proteins, although also here higher protein adsorption from saliva was observed on hydrophobic surfaces,[60] whereas Staehlke et.al.[29] found no correlation for FBS adsorption. In contrast to the results presented here, a correlation could be established between the substrate's SFE (or components thereof) and the amounts of adsorbed protein in other studies. Decreasing adsorption of bovine serum albumin on cellulose-based surface modifications with increasing SFE was detected by Czibula et al.[61] Similarly, Michiardi et al.[6] observed a linear correlation between the polar component of the SFE and the amount of adsorbed HSA, which was not found in this study either.

In contrast to the results for SFE and wettability, a strong correlation could be found for the dependence of protein adsorption on the zeta potential of the substrates at the pH of the respective protein solution. For HSA, saliva, and FBS, an almost linear increase in adsorbed protein with an increasing zeta potential can be observed. With the exception of the comparably hydrophobic AMAM modification, an opposite behavior (i.e., decreasing adsorption) can be assumed for lysozyme (Figure 5).

Thus, the adsorption of the proteins is mainly mediated by electrostatic interactions because HSA and a majority of the salivary proteins are negatively charged at pH 7.4 or pH 8.3, respectively, whereas lysozyme carries a positive net charge. These results are in accordance with previously published studies. Also, Patil et al.[8] found an increase in adsorbed HSA with increasing zeta potential. FBS was found to adsorb less on more negatively charged surfaces whereas lysozyme adsorbed more to negatively charged surfaces.[62,63]

In summary, the protein adsorption on the surface modifications presented in this study is mainly dominated by electrostatic effects due to the broad scope of surface charges caused by the amine groups.

Comparing the properties of the novel amine-based surface functionalizations, examined in this study, with the initially stated requirements for protein-resistant surface coatings,[20−24] they possess some of the necessary characteristics because they are hydrophilic, flexible, and possibly swellable. They also contain polar groups, which can act as hydrogen bond acceptors; however, they also exhibit unfavorable net charges and hydrogen bond donors. Thus, it has to be expected that they do not perform as well as established protein-repelling surface coatings, such as PEG. On surfaces with oligomeric or polymeric ethylene glycol, albumin and lysozyme adsorption could be prevented to unmeasurable amounts.[64] In addition, adsorption from complex physiological fluids, such as human

https://dx.doi.org/10.1021/acs.langmuir.0c00625

saliva, was severely reduced to a very low amount of 2 ng/cm$^2$.[28] Nevertheless, the polymer-based coatings (PEI and PAMAM polymer) examined in this study performed very well, reducing adsorption from saliva to 14 and 23 ng/cm$^2$, respectively. The adsorption of HSA was decreased to ~40 ng/cm$^2$, which is significantly lower than the amount of protein related to surface coverage with an HSA monolayer (~250−600 ng/cm$^2$, depending on protein orientation[21]). Their good performance may be explained by their advantageous physicochemical properties (e.g., their hydrophilicity) but also by their flexibility, which might lead to the steric repulsion of approaching proteins, as observed for PEG coatings.[65] In order to confirm this, further investigation of the flexibility of the polymer coatings is required.

## CONCLUSIONS

In order to develop protein-resistant materials, polyamine and poly(amido amine) surface coatings with terminal amine groups and varying structure (dendrimer, oligomer, and polymer) were immobilized on model surfaces. All coatings were moderately hydrophilic and exhibited similar SFEs but differed strongly with respect to their zeta potential. The adsorption of different types of proteins almost did not correlate with the surface free energy but was strongly affected by the surface charge formation. Positively charged model proteins adsorbed to a higher extent to surfaces with negative zeta potentials and vice versa, with the complex physiological protein solutions saliva and serum behaving similarly to the negatively charged model protein. Protein repellency was higher for polymers with linear structure compared to those with dendrimer structure. The strongest effect was found for PEI and PAMAM polymers, both of which had not the highest and lowest values for surface free energy and zeta potential but showed the most prominent structural changes during dynamic wetting. Thus, we conclude that sufficiently flexible and hydrophilic coatings can resist protein adsorption despite possessing positively charged amine groups. Further experiments, investigating the kinetics of protein adsorption as well as the behavior of cells on those surfaces, are now underway in order to gain further insight into the protein adsorption process and to test their ability to promote cell adhesion and proliferation.

## ASSOCIATED CONTENT

### Supporting Information

The Supporting Information is available free of charge at https://pubs.acs.org/doi/10.1021/acs.langmuir.0c00625.

Further details on the experimental procedure; IR and $^1$H and $^{13}$C NMR spectra of the PAMAM polymer; DRIFT spectra of functionalized silica particles; detailed results from dynamic contact angle measurements of coated wafers with sf-water and PBS; and dependence of protein adsorption on the physicochemical surface properties (water contact angle, SFE, and polar and dispersive component of SFE) (PDF)

## AUTHOR INFORMATION


### Corresponding Author

**Rainer Mueller** − *Institute of Physical and Theoretical Chemistry, University of Regensburg, 93053 Regensburg, Germany;* orcid.org/0000-0001-9641-7780; Phone: +49-941 943-4521; Email: rainer.mueller@chemie.uni- regensburg.de

### Authors

**Jutta Lehnfeld** − *Institute of Physical and Theoretical Chemistry, University of Regensburg, 93053 Regensburg, Germany*

**Martina Gruening** − *Department of Cell Biology, Rostock University Medical Center, 18057 Rostock, Germany*

**Matthias Kronseder** − *Physics Department, University of Regensburg, 93053 Regensburg, Germany*

Complete contact information is available at: https://pubs.acs.org/10.1021/acs.langmuir.0c00625


### Notes

The authors declare no competing financial interest.

## ACKNOWLEDGMENTS

J.L. thanks the Chemical Industry Fund (Fonds der Chemischen Industrie (FCI)) of the Chemical Industry Association (Verband der Chemischen Industrie (VCI)) for the chemistry fond fellowship (Chemiefonds-Stipendium) and the Bavarian State Ministry of Science and the Arts for their scholarship (Promotionsabschluss-Stipendium) within the Bavarian program for the advancement of women in science (Bayerisches Programm zur Realisierung der Chancengleichheit für Frauen in Forschung und Lehre). We also thank Gudrun Deigele, Jonas Blahnik, Andreas Jungwirth, Fiona Kappaun, and Friederike Reinhoff for excellent technical assistance.

## ABBREVIATIONS

AMAM, amidoamine; APD, *N*,*N*′-bis(3-aminopropyl)-1,3-propanediamine; BCA, bicinchoninic acid; DRIFT, diffuse reflectance infrared Fourier transform; FBS, fetal bovine serum; G2/G4, second/fourth generation; HSA, human serum albumin; IEP, isoelectric point; PAMAM, poly(amido amine); PBS, phosphate-buffered saline; PEG, poly(ethylene glycol); PEI, poly(ethylene imine); PPI, poly(propylene imine); SAM, self-assembled monolayer; SAM-COOH, 6-carboxyhexanylsiloxane monolayer; SAM-$NH_2$, 11-amino-undecylsiloxane monolayer; SFE, surface free energy; sulfo-SDTB, sulfosuccinimidyl-4-*O*-(4,4′-dimethoxytrityl) butyrate; TESPSA, 3-(triethoxysilyl)propyl succinic acid anhydride; XPS, X-ray photoelectron spectroscopy

## REFERENCES


(1) Merian, T.; Goddard, J. M. Advances in Nonfouling Materials: Perspectives for the Food Industry. *J. Agric. Food Chem.* 2012, *60*, 2943−2957.

(2) Whelan, A.; Regan, F. Antifouling strategies for marine and riverine sensors. *J. Environ. Monit.* 2006, *8*, 880−886.

(3) Bryers, J. D. Medical Biofilms. *Biotechnol. Bioeng.* 2008, *100*, 1−18.

(4) Jäger, M.; Zilkens, C.; Zanger, K.; Krauspe, R. Significance of Nano- and Microtopography for Cell-Surface Interactions in Orthopaedic Implants. *J. Biomed. Biotechnol.* 2007, *2007*, 69036.

(5) Pidhatika, B.; Möller, J.; Benetti, E. M.; Konradi, R.; Rakhmatullina, E.; Mühlebach, A.; Zimmermann, R.; Werner, C.; Vogel, V.; Textor, M. The role of the interplay between polymer architecture and bacterial surface properties on the microbial adhesion to polyoxazoline-based ultrathin films. *Biomaterials* 2010, *31*, 9462−9472.


https://dx.doi.org/10.1021/acs.langmuir.0c00625

(6) Michiardi, A.; Aparicio, C.; Ratner, B. D.; Planell, J. A.; Gil, J. The influence of surface energy on competitive protein adsorption on oxidized NiTi surfaces. *Biomaterials* 2007, *28*, 586−594.

(7) Gessner, A.; Lieske, A.; Paulke, B.-R.; Müller, R. H. Functional groups on polystyrene model nanoparticles: Influence on protein adsorption. *J. Biomed. Mater. Res., Part A* 2003, *65A*, 319−326.

(8) Patil, S.; Sandberg, A.; Heckert, E.; Self, W.; Seal, S. Protein adsorption and cellular uptake of cerium oxide nanoparticles as a function of zeta potential. *Biomaterials* 2007, *28*, 4600−4607.

(9) Chang, Y.; Chen, S.; Zhang, Z.; Jiang, S. Highly Protein-Resistant Coatings from Well-Defined Diblock Copolymers Containing Sulfobetaines. *Langmuir* 2006, *22*, 2222−2226.

(10) Bellassai, N.; Marti, A.; Spoto, G.; Huskens, J. Low-fouling, mixed-charge poly-L-lysine polymers with anionic oligopeptide side-chains. *J. Mater. Chem. B* 2018, *6*, 7662−7673.

(11) Perrino, C.; Lee, S.; Choi, S. W.; Maruyama, A.; Spencer, N. D. A Biomimetic Alternative to Poly(ethylene glycol) as an Antifouling Coating: Resistance to Nonspecific Protein Adsorption of Poly(L-lysine)-graft-dextran. *Langmuir* 2008, *24*, 8850−8856.

(12) Lowe, S.; O'Brien-Simpson, N. M.; Connal, L. A. Antibiofouling polymer interfaces: poly(ethylene glycol) and other promising candidates. *Polym. Chem.* 2015, *6*, 198−212.

(13) Niegelhell, K.; Süßenbacher, M.; Sattelkow, J.; Plank, H.; Wang, Y.; Zhang, K.; Spirk, S. How Bound and Free Fatty Acids in Cellulose Films Impact Nonspecific Protein Adsorption. *Biomacromolecules* 2017, *18*, 4224−4231.

(14) Holmberg, K.; Bergström, K.; Brink, C.; Österberg, E.; Tiberg, F.; Harris, J. M. Effects on protein adsorption, bacterial adhesion and contact angle of grafting PEG chains to polystyrene. *J. Adhes. Sci. Technol.* 1993, *7*, 503−517.

(15) Jo, S.; Park, K. Surface modification using silanated poly(ethylene glycol)s. *Biomaterials* 2000, *21*, 605−616.

(16) Dalsin, J. L.; Lin, L.; Tosatti, S.; Vörös, J.; Textor, M.; Messersmith, P. B. Protein Resistance of Titanium Oxide Surfaces Modified by Biologically Inspired mPEG-DOPA. *Langmuir* 2005, *21*, 640−646.

(17) Hlídková, H.; Horák, D.; Proks, V.; Kučerová, Z.; Pekárek, M.; Kuča, K. PEG-Modified Macroporous Poly(Glycidyl Methacrylate) and Poly(2-Hydroxyethyl Methacrylate) Microspheres to Reduce Non-Specific Protein Adsorption. *Macromol. Biosci.* 2013, *13*, 503−511.

(18) Pidhatika, B.; Rodenstein, M.; Chen, Y.; Rakhmatullina, E.; Mühlebach, A.; Acikgöz, C.; Textor, M.; Konradi, R. Comparative Stability Studies of Poly(2-methyl-2-oxazoline) and Poly(ethylene glycol) Brush Coatings. *Biointerphases* 2012, *7*, 1−15.

(19) Qin, G.; Cai, C. Oxidative degradation of oligo(ethylene glycol)-terminated monolayers. *Chem. Commun.* 2009, No. 34, 5112−5114.

(20) Norde, W.; Lyklema, J. Why proteins prefer interfaces. *J. Biomater. Sci., Polym. Ed.* 1991, *2*, 183−202.

(21) Sigal, G. B.; Mrksich, M.; Whitesides, G. M. Effect of Surface Wettability on the Adsorption of Proteins and Detergents. *J. Am. Chem. Soc.* 1998, *120*, 3464−3473.

(22) Xu, L.-C.; Siedlecki, C. A. Effects of surface wettability and contact time on protein adhesion to biomaterial surfaces. *Biomaterials* 2007, *28*, 3273−3283.

(23) Wörz, A.; Berchtold, B.; Moosmann, K.; Prucker, O.; Rühe, J. Protein-resistant polymer surfaces. *J. Mater. Chem.* 2012, *22*, 19547−19561.

(24) Chapman, R. G.; Ostuni, E.; Takayama, S.; Holmlin, R. E.; Yan, L.; Whitesides, G. M. Surveying for Surfaces that Resist the Adsorption of Proteins. *J. Am. Chem. Soc.* 2000, *122*, 8303−8304.

(25) Beckner, W.; He, Y.; Pfaendtner, J. Chain Flexibility in Self-Assembled Monolayers Affects Protein Adsorption and Surface Hydration: A Molecular Dynamics Study. *J. Phys. Chem. B* 2016, *120*, 10423−10432.

(26) Finke, B.; Luethen, F.; Schroeder, K.; Mueller, P. D.; Bergemann, C.; Frant, M.; Ohl, A.; Nebe, B. J. The effect of positively charged plasma polymerization on initial osteoblastic focal adhesion on titanium surfaces. *Biomaterials* 2007, *28*, 4521−4534.

(27) Müller, R.; Eidt, A.; Hiller, K.-A.; Katzur, V.; Subat, M.; Schweikl, H.; Imazato, S.; Ruhl, S.; Schmalz, G. Influences of protein films on antibacterial or bacteria-repellent surface coatings in a model system using silicon wafers. *Biomaterials* 2009, *30*, 4921−4929.

(28) Eichler, M.; Katzur, V.; Scheideler, L.; Haupt, M.; Geis-Gerstorfer, J.; Schmalz, G.; Ruhl, S.; Müller, R.; Rupp, F. The impact of dendrimer-grafted modifications to model silicon surfaces on protein adsorption and bacterial adhesion. *Biomaterials* 2011, *32*, 9168−9179.

(29) Staehlke, S.; Lehnfeld, J.; Schneider, A.; Nebe, J. B.; Müller, R. Terminal chemical functions of polyamidoamine dendrimer surfaces and its impact on bone cell growth. *Mater. Sci. Eng., C* 2019, *101*, 190−203.

(30) Katzur, V.; Eichler, M.; Deigele, E.; Stage, C.; Karageorgiev, P.; Geis-Gerstorfer, J.; Schmalz, G.; Ruhl, S.; Rupp, F.; Müller, R. Surface-immobilized PAMAM-dendrimers modified with cationic or anionic terminal functions: Physicochemical surface properties and conformational changes after application of liquid interface stress. *J. Colloid Interface Sci.* 2012, *366*, 179−190.

(31) Liu, Q.; Ding, J.; Mante, F. K.; Wunder, S. L.; Baran, G. R. The role of surface functional groups in calcium phosphate nucleation on titanium foil: a self-assembled monolayer technique. *Biomaterials* 2002, *23*, 3103−3111.

(32) Balachander, N.; Sukenik, C. N. Monolayer Transformation by Nucleophilic Substitution: Applications to the Creation of New Monolayer Assemblies. *Langmuir* 1990, *6*, 1621−1627.

(33) Dey, R. K.; Ray, A. R. Synthesis, characterization, and blood compatibility of polyamidoamines copolymers. *Biomaterials* 2003, *24*, 2985−2993.

(34) Cook, A. D.; Pajvani, U. B.; Hrkach, J. S.; Cannizzaro, S. M.; Langer, R. Colorimetric analysis of surface reactive amino groups on poly(lactic acid-co-lysine):poly(lactic acid) blends. *Biomaterials* 1997, *18*, 1417−1424.

(35) Shalel-Levanon, S.; Marmur, A. Validity and accuracy in evaluating surface tension of solids by additive approaches. *J. Colloid Interface Sci.* 2003, *262*, 489−499.

(36) Lim, K.; Chua, R. R. Y.; Saravanan, R.; Basu, A.; Mishra, B.; Tambyah, P. A.; Ho, B.; Leong, S. S. J. Immobilization Studies of an Engineered Arginine-Tryptophan-Rich Peptide on a Silicone Surface with Antimicrobial and Antibiofilm Activity. *ACS Appl. Mater. Interfaces* 2013, *5*, 6412−6422.

(37) He, W.; McConnell, G. C.; Schneider, T. M.; Bellamkonda, R. V. A Novel Anti-inflammatory Surface for Neural Electrodes. *Adv. Mater.* 2007, *19*, 3529−3533.

(38) Brotzel, F.; Chu, Y. C.; Mayr, H. Nucleophilicities of Primary and Secondary Amines in Water. *J. Org. Chem.* 2007, *72*, 3679−3688.

(39) Prucker, O.; Rühe, J. Synthesis of Poly(styrene) Monolayers Attached to High Surface Area Silica Gels through Self-Assembled Monolayers of Azo Initiators. *Macromolecules* 1998, *31*, 592−601.

(40) Szleifer, I. Statistical thermodynamics of polymers near surfaces. *Curr. Opin. Colloid Interface Sci.* 1996, *1*, 416−423.

(41) Shyue, J.-J.; De Guire, M. R.; Nakanishi, T.; Masuda, Y.; Koumoto, K.; Sukenik, C. N. Acid-Base Properties and Zeta Potentials of Self-Assembled Monolayers Obtained via in Situ Transformations. *Langmuir* 2004, *20*, 8693−8698.

(42) Sugimura, H.; Hozumi, A.; Kameyama, T.; Takai, O. Organosilane self-assembled monolayers formed at the vapour/solid interface. *Surf. Interface Anal.* 2002, *34*, 550−554.

(43) van Duijvenbode, R. C.; Borkovec, M.; Koper, G. J. M. Acid-base properties of poly(propylene imine)dendrimers. *Polymer* 1998, *39*, 2657−2664.

(44) Jain, V.; Maingi, V.; Maiti, P. K.; Bharatam, P. V. Molecular dynamics simulations of PPI dendrimer-drug complexes. *Soft Matter* 2013, *9*, 6482−6496.

(45) Hamborg, E. S.; Versteeg, G. F. Dissociation Constants and Thermodynamic Properties of Amines and Alkanolamines from (293 to 353) K. *J. Chem. Eng. Data* 2009, *54*, 1318−1328.

https://dx.doi.org/10.1021/acs.langmuir.0c00625

(46) Zhang, C.; Luo, N.; Hirt, D. E. Surface Grafting Polyethylene Glycol (PEG) onto Poly(ethylene-co-acrylic acid) Films. *Langmuir* 2006, *22*, 6851−6857.
(47) Rupp, F.; Scheideler, L.; Geis-Gerstorfer, J. Effect of Heterogenic Surfaces on Contact Angle Hysteresis: Dynamic Contact Angle Analysis in Material Sciences. *Chem. Eng. Technol.* 2002, *25*, 877−882.
(48) Kobayashi, M.; Terayama, Y.; Yamaguchi, H.; Terada, M.; Murakami, D.; Ishihara, K.; Takahara, A. Wettability and Antifouling Behavior on the Surfaces of Superhydrophilic Polymer Brushes. *Langmuir* 2012, *28*, 7212−7222.
(49) Scherrenberg, R.; Coussens, B.; van Vliet, P.; Edouard, G.; Brackman, J.; de Brabander, E.; Mortensen, K. The Molecular Characteristics of Poly(propyleneimine) Dendrimers As Studied with Small-Angle Neutron Scattering, Viscosimetry, and Molecular Dynamics. *Macromolecules* 1998, *31*, 456−461.
(50) Holmes-Farley, S. R.; Bain, C. D.; Whitesides, G. M. Wetting of Functionalized Polyethylene Film Having Ionizable Organic Acids and Bases at the Polymer-Water Interface: Relations between Functional Group Polarity, Extent of Ionization, and Contact Angle with Water. *Langmuir* 1988, *4*, 921−937.
(51) Welzel, P. B.; Rauwolf, C.; Yudin, O.; Grundke, K. Influence of Aqueous Electrolytes on the Wetting Behavior of Hydrophobic Solid Polymers-Low-Rate Dynamic Liquid/Fluid Contact Angle Measurements Using Axisymmetric Drop Shape Analysis. *J. Colloid Interface Sci.* 2002, *251*, 101−108.
(52) Welch, P.; Muthukumar, M. Tuning the Density Profile of Dendritic Polyelectrolytes. *Macromolecules* 1998, *31*, 5892−5897.
(53) Oliva, F. Y.; Avalle, L. B.; Cámara, O. R.; De Pauli, C. P. Adsorption of human serum albumin (HSA) onto colloidal $TiO_2$ particles, Part I. *J. Colloid Interface Sci.* 2003, *261*, 299−311.
(54) Wardlaw, A. C. The complement-dependent bacteriolytic activity of normal human serum. I. The Effect of pH and Ionic Strength and the Role of Lysozyme. *J. Exp. Med.* 1962, *115*, 1231−1249.
(55) Zheng, X.; Baker, H.; Hancock, W. S.; Fawaz, F.; McCaman, M.; Pungor, E., Jr. Proteomic Analysis for the Assessment of Different Lots of Fetal Bovine Serum as a Raw Material for Cell Culture. Part IV. Application of Proteomics to the Manufacture of Biological Drugs. *Biotechnol. Prog.* 2006, *22*, 1294−1300.
(56) Lagerlöf, F.; Ekstrand, J. The Effect of Flow Rate on the Ionized Calcium Concentration of Human Parotid Saliva. *Caries Res.* 1982, *16*, 123−128.
(57) Schipper, R. G.; Silletti, E.; Vingerhoeds, M. H. Saliva as research material: Biochemical, physicochemical and practical aspects. *Arch. Oral Biol.* 2007, *52*, 1114−1135.
(58) Denny, P.; Hagen, F. K.; Hardt, M.; Liao, L.; Yan, W.; Arellanno, M.; Bassilian, S.; Bedi, G. S.; Boontheung, P.; Cociorva, D.; Delahunty, C. M.; Denny, T.; Dunsmore, J.; Faull, K. F.; Gilligan, J.; Gonzalez-Begne, M.; Halgand, F.; Hall, S. C.; Han, X.; Henson, B.; Hewel, J.; Hu, S.; Jeffrey, S.; Jiang, J.; Loo, J. A.; Ogorzalek Loo, R. R.; Malamud, D.; Melvin, J. E.; Miroshnychenko, O.; Navazesh, M.; Niles, R.; Park, S. K.; Prakobphol, A.; Ramachandran, P.; Richert, M.; Robinson, S.; Sondej, M.; Souda, P.; Sullivan, M. A.; Takashima, J.; Than, S.; Wang, J.; Whitelegge, J. P.; Witkowska, H. E.; Wolinsky, L.; Xie, Y.; Xu, T.; Yu, W.; Ytterberg, J.; Wong, D. T.; Yates, J. R., III; Fisher, S. J. The proteomes of Human Parotid and Submandibular/Sublingual Gland Salivas Collected as the Ductal Secretions. *J. Proteome Res.* 2008, *7*, 1994−2006.
(59) Sethuraman, A.; Han, M.; Kane, R. S.; Belfort, G. Effect of Surface Wettability on the Adhesion of Proteins. *Langmuir* 2004, *20*, 7779−7788.
(60) Lindh, L.; Arnebrant, T.; Isberg, P.-E.; Glantz, P.-O. Concentration Dependence of Adsorption from Human Whole Resting Saliva at Solid/Liquid Interfaces: An Ellipsometric Study. *Biofouling* 1999, *14*, 189−196.
(61) Czibula, C.; Teichert, G.; Nau, M.; Hobisch, M.; Palasingh, C.; Biesalski, M.; Spirk, S.; Teichert, C.; Nypelö, T. Design of Friction, Morphology, Wetting, and Protein Affinity by Cellulose Blend Thin Film Composition. *Front. Chem.* 2019, *7*, 239−248.
(62) El-Ghannam, A.; Hamazawy, E.; Yehia, A. Effect of thermal treatment on bioactive glass microstructure, corrosion behavior, ζ potential, and protein adsorption. *J. Biomed. Mater. Res.* 2001, *55*, 387−395.
(63) Rezwan, K.; Meier, L. P.; Gauckler, L. J. Lysozyme and bovine serum albumin adsorption on uncoated silica and AlOOH-coated silica particles: the influence of positively and negatively charged oxide surface coatings. *Biomaterials* 2005, *26*, 4351−4357.
(64) Lee, S.-W.; Laibinis, P. E. Protein-resistant coatings for glass and metal oxide surfaces derived from oligo(ethylene glycol)-terminated alkyltrichlorosilanes. *Biomaterials* 1998, *19*, 1669−1675.
(65) Harder, P.; Grunze, M.; Dahint, R.; Whitesides, G. M.; Laibinis, P. E. Molecular Conformation in Oligo(ethylene glycol)-Terminated Self-Assembled Monolayers on Gold and Silver Surfaces Determines Their Ability To Resist Protein Adsorption. *J. Phys. Chem. B* 1998, *102*, 426−436.

https://dx.doi.org/10.1021/acs.langmuir.0c00625

American Journal of
Biomedical Science & Research

www.biomedgrid.com
ISSN: 2642-1747

*Publikation IV*: Opinion



# Cell-Material Interaction - Spreading Course Correlates with Surface Charge

**Martina Gruening[1], Sven Neuber[2], Katja Fricke[3], Christiane A. Helm[2] and Barbara Nebe[1,4] ***

[1]*Department of Cell Biology, Rostock University Medical Center, Germany*

[2]*Soft Matter and Biophysics, Institute of Physics, University of Greifswald, Germany*

[3]*Leibniz Institute for Plasma Science and Technology, e. V., Greifswald, Germany*

[4]*Department Science and Technology of Life, Light and Matter, Interdisciplinary Faculty, University of Rostock, Germany*

***Corresponding author:** Barbara Nebe, Department of Cell Biology, Rostock University Medical center, Schillingallee 69, 18057 Rostock, Germany.

***To Cite This Article:*** *Gruening M, Neuber S, Fricke K, Helm C and Nebe B. Cell-Material Interaction - Spreading Course correlates with Surface Charge. 2020 - 9(1). AJBSR.MS.ID.001341.* DOI: 10.34297/AJBSR.2020.09.001341.

**Received:** May 14, 2020; **Published:** May 26, 2020

## Abstract

To design appropriate materials for tissue engineering, a profound understanding of the cell-material interaction is essential. We are of the opinion that the zeta (ζ) potential has a decisive role in the cell behaviour, outshining wettability. Here we present a comparative analysis of the MG-63 osteoblastic cell spreading behaviour on negatively and positively charged surfaces in the hydrophilic range. The results indicate a correlation of the cells' spreading area with the surface charge. Thus, the ζ-potential should be considered as a key parameter for cell interactions at the biomaterial interface.

**Keywords:** Cell-Material Interaction, Zeta Potential, Wettability, Surface Modification, Polyelectrolyte Multilayer, Amino Polymer, MG-63, Osteoblasts, Cell Spreading

**Abbreviations:** DMEM-Dulbecco's Modified Eagle Medium; PAH-Poly (allylamine hydrochloride); PAMAM-Poly (amidoamine); PDADMA-Poly (diallyl dimethylammonium chloride); PEI-Poly (ethylene imine); PPAAm-Plasma Polymerized Allylamine; PSS-Poly (styrene sulfonate); Ti-Titanium; WCA-Water contact angle; ζ-Zeta Potential.

## Introduction

Materials that are coated with polymers are currently being widely used in biomedical applications. This involves a high degree of interaction at the cell-material interface. Depending on time and distance of cells to the material surface the four initial adhesion phases were described as surface recognition, early attachment stage, intermediate attachment or membrane adhesion, and late adhesion or spreading phase [1], profoundly influencing the further cell viability, growth and cell function. To select appropriate materials for tissue engineering, a sound understanding of this cell-material interaction is indispensable [2]. Considering the biological relevance of these interactions, numerous research groups are focusing on this issue. However, as Vendre et al. [1] stated, the "cell-material communication code" is still not fully deciphered to define precise principles that govern the cell-material crosstalk.

Although a variety of material surface properties (chemical, topographical or mechanical [1]) have been reported to contribute to the nature of cell-material interactions, no general rules could yet be developed allowing predictions of cell attachment, spreading, or growth [3]. Considering for example the wettability of a surface, several studies indicate that hydrophilic surfaces promote the cell adhesion [4], while hydrophobic surfaces often inhibit the crosstalk between cells and materials [5]. However, there are also exceptions to the rules [6].

Accordingly, to our opinion, Spriano et al. [7] claimed that systematic studies of diverse materials in the same investigative conditions are still lacking in literature. We assume that not the wettability but the surface charge via ζ-potential strongly affects the cellular behaviour at the interface. Here, we focused on the

spreading course, as the cell area and morphology have been accepted as good indicators of the occupation of materials by cells [1,3]. Human MG-63 osteoblasts were cultured on Titanium (Ti) coated with the positively charged plasma polymerized allylamine (PPAAm) nanolayer and with polyelectrolyte nanofilms terminated with negatively charged poly(styrene sulfonate) (PSS) and positively charged poly(diallyldimethylammonium chloride) (PDADMA).

## Materials and Methods

### Surface Modification and Characterization

Planar silicon wafers sputtered with 100nm Ti particles obtained from the Centre for Micro technologies (ZFM, University of Technology Chemnitz, Germany) served as base material and negative control [8]. Ti was modified with (i) PPAAm [9] (parameters: continuous wave oxygen/argon plasma; 500W, 50Pa, 1000-sccm O2, 5sccm Ar, 60s; 480s PPAAm deposition time) and (ii) polyelectrolyte multilayers [10] terminated with PDADMA (sequence: PEI/PSS/(PDADMA/PSS)$_9$/PDADMA) or PSS (sequence: PEI/PSS/(PAH/PSS)$_2$).

The surface charge via ζ-potentials at pH 7.4 were assessed by the SurPASS™ system (Anton Paar, Ostfildern, Germany) in a 1mM KCl solution [8] (n = 3, three pairs of samples). Wettability via Water Contact Angles (WCA) was assessed by the sessile drop method using the Drop Shape Analyzer-DSA25 (Krüss, Hamburg, Germany) [8] (n = 3 at 3 drops each).

### Cellular Spreading Course

For analysing the spreading behaviour, we used the human osteoblast-like cell line MG-63 (ATCC®, CRL1427™, Bethesda, USA; for more information see [11-13]. The cells were cultured in complete DMEM (31966-021, Life Technologies Limited, Paisley, UK), with 10% fetal calf serum (Biochrom FCS Superior, Merck, Darmstadt, Germany) [8].

Cell membranes were stained with the PKH-26 General Cell Linker Kit (Sigma-Aldrich Chemie, Taufkirchen, Germany) for 5min at 37°C in suspension [14]. 50,000 vital stained cells/cm² were seeded onto the substrates and cultivated for 1, 3 and 12h. Cell areas after 24h were assessed by fluoro-3-acetoxymethyl ester stained cells (fluo-3, Life Technologies Corporation, Eugene, Oregon, US) [8,15]. Microscopic images were obtained using a confocal laser scanning microscope LSM780, a C-Apochromat 40x/1.20W Korr M27 objective and the ZEN black software 2011 SP4 (Carl Zeiss, Jena, Germany). The cell area in µm² of 45 cells per surface and per independent experiment was determined using the ''measurement report'' of the software Photoshop CC 2017 (Adobe, San Jose, CA, USA) (n = 3 for 1 and 24h, n = 2 for 3 and 12h).

## Results and Discussion

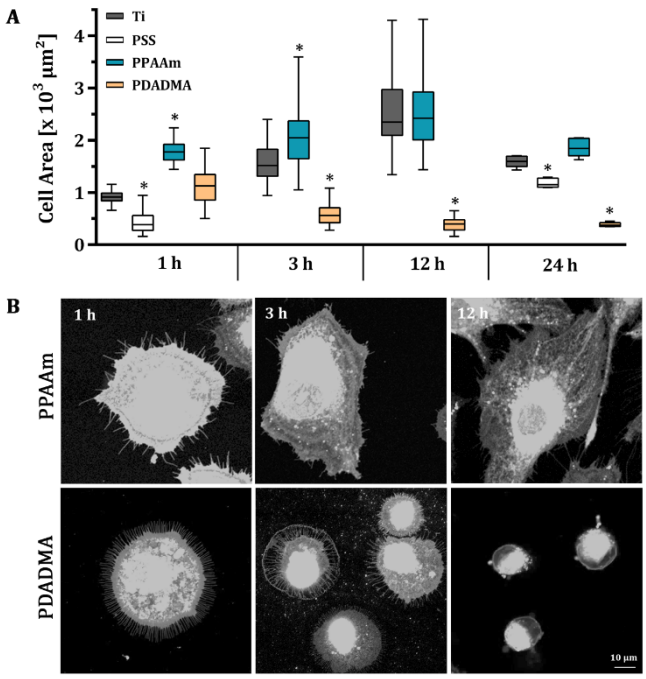


**Figure 1:** Spreading course of MG-63 osteoblastic cells on a plasma polymer nanolayer (PPAAm) and on polyelectrolyte nanofilms (PSS, PDADMA) vs. Ti. (A) Time-dependent spreading course over 24h. (B) Exemplary microscopic images of PKH-26 stained cells on PPAAm and PDADMA after 1, 3 and 12h. Note that in the early phase of cell spreading the positive charges dominates the negative charges. However, observing the time-dependent spreading the PDADMA surface with a very high positive ζ-potential (~ +50 mV) impeded dynamic cell spreading from 3h on although the surface is hydrophilic. (Statistics: Kruskal-Wallis and Dunn's multiple comparison test, $p < 0.05$, *indicates significance to the Ti control; medians ± interquartile ranges with maximum and minimum; n = 3 á 45 cells for 1 and 24h; n = 2 for 3 and 12h; LSM780).

In our experiments the wettability seemed not to play a decisive role for cell spreading. PSS surfaces were hydrophilic with a WCA similar to PPAAm (68°) [8], but negatively charged as the Ti surface (-82mV [16]). However, the hydrophilic PPAAm with a positive ζ-potential of +8mV [16] displayed the highest initial cell area (Figure 1); spreading course 1, 3, 12 and 24 h: Ti 913 -1518-2347-1592µm², PPAAm 1778-2047- 2425-1840µm², PDADMA 1127-559-397-374µm², respectively; spreading 1 and 24h: PSS 385-1151µm², respectively). Related observations have been reported in literature where cell adhesion, morphology and apoptosis of MG-63 cells on poly(amidoamine) (PAMAM) polymer thin coatings with different terminal functions were examined. Hydrophilic PAMAM-$NH_2$ surfaces with a positive ζ-potential of +22mV evoked increased cell attachment and spreading with a well-organized actin cytoskeleton within 24h. In contrast, on hydrophilic PAMAM-$CO_2H$ and -$CH_3$ surfaces with a negative ζ-potential, cells were impaired in their spreading and revealed an increased number of apoptotic cells, although both were hydrophilic (WCA: 33° and 44°, respectively) [17].

Our positively charged PDADMA surfaces were hydrophilic with WCA values of ~ 40°, but cells ignored this hydrophilic environment and exhibited an impaired spreading behaviour after an initial tendency to spread better than Ti. A reduction of the cell area occurred, demonstrating the additional strong influence of a very high positive ζ-potential with ~ +50mV for PDADMA on the spreading behaviour. Interestingly, the cells seem to favour only a certain spectrum of ζ-potentials, being neither in the negative nor in the highly positive range - independent of the hydrophilicity.

## Conclusion

The ζ-potential appears to be of great importance for the cellular spreading as indicator of the cell-material interaction and should be considered as a key parameter when designing and investigating new materials for medical applications.

## Acknowledgements

We appreciate the funding by the Deutsche Forschungsgemein - schaft (DFG, German Research Foundation)-Collaborative Research Centre (CRC) 1270/1-299150580. The authors thank Dipl.-Ing. Norbert Zichner (Center for Microtechnologies, TU Chemnitz) concerning the production of the titanium base materials.

## Conflict of Interest

The authors declare that no conflicts of interest exist.

## References

1. Ventre M, Causa F, Netti PA (2012) Determinants of cell-material crosstalk at the interface: towards engineering of cell instructive materials. J R Soc Interface 9(74): 2017-2032.
2. Tsimbouri PM, McNamara LE, Alakpa EV, Dalby MJ, Turner LA (2014) Cell-Material Interactions. Tissue Eng (2014): 217-251.
3. Saltzman WM, Kyriakides TR (2014) Cell Interactions with Polymers. Princ Tissue Eng (2014): 385-406.
4. Bcakova L, Filova E, Parizek M, Ruml T, Svorcik V (2011) Modulation of cell adhesion, proliferation and differentiation on materials designed for body implants. Biotechnol Adv 29(6): 739-767.
5. Faucheux N, Schweiss R, Lützow, Werner C, Groth T (2004) Self-assembled monolayers with different terminating groups as model substrates for cell adhesion studies. Biomaterials 25(14): 2721-2730.
6. Gentleman MM, Gentleman E (2014) The role of surface free energy in osteoblast-biomaterial interactions. Int Mater Rev 59(8): 417-429.
7. Spriano S, Sarath Chandra V, Cochis A, Uberti F, Rimondini L, et al. (2017) How do wettability, zeta potential and hydroxylation degree affect the biological response of biomaterials? Mater Sci Eng C 74: 542-555.
8. Staehlke S, Rebl H, Finke B, Mueller P, Gruening M, et al. (2018) Enhanced calcium ion mobilization in osteoblasts on amino group containing plasma polymer nanolayer. Cell Biosci 8: 22.
9. Rebl H, Finke B, Lange R, Weltmann KD, Nebe JB (2012) Impact of plasma chemistry versus titanium surface topography on osteoblast orientation, Acta Biomater 8(10): 3840-3851.
10. Mohamad HS, Neuber S, Helm CA (2019) Surface Forces of Asymmetrically Grown Polyelectrolyte Multilayers: Searching for the Charges. Langmuir 35(48): 15491-15499.
11. Staehlke S, Rebl H, Nebe B (2019) Phenotypic stability of the human MG-63 osteoblastic cell line at different passages. Cell Biol Int 43(1): 22-32.
12. Czekanska EM, Stoddart MJ, Ralphs JR, Richards RG, Hayes JS (2014) A phenotypic comparison of osteoblast cell lines versus human primary osteoblasts for biomaterials testing. J Biomed Mater Res Part A 102(8): 2636-2643.
13. Clover J, Gowen M (1994) Are MG-63 and HOS TE85 human osteosarcoma cell lines representative models of the osteoblastic phenotype? Bone 15(6): 585-591.
14. Matschegewski C, Staehlke S, Loeffler R, Lange R, Chai F, et al. (2010) Cell architecture-cell function dependencies on titanium arrays with regular geometry. Biomaterials 31(22): 5729-5740.
15. Staehlke S, Koertge A, Nebe B (2015) Intracellular calcium dynamics dependent on defined micro topographical features of titanium, Biomaterials 46: 48-57.
16. Mörke C, Rebl H, Finke B, Dubs M, Nestler P, et al. (2017) Abrogated Cell Contact Guidance on Amino-Functionalized Microgrooves. ACS Appl Mater Interfaces 9(12): 10461-10471.
17. Staehlke S, Lehnfeld J, Schneider A, Nebe JB, Müller R (2019) Terminal chemical functions of polyamidoamine dendrimer surfaces and its impact on bone cell growth. Mater Sci Eng C 101: 190-203.

frontiers in Bioengineering and Biotechnology

ORIGINAL RESEARCH
published: 08 September 2020
doi: 10.3389/fbioe.2020.01016

*Publikation V*

# Enhancement of Intracellular Calcium Ion Mobilization by Moderately but Not Highly Positive Material Surface Charges

*Martina Gruening[1], Sven Neuber[2], Peter Nestler[2], Jutta Lehnfeld[3], Manuela Dubs[4], Katja Fricke[5], Matthias Schnabelrauch[4], Christiane A. Helm[2], Rainer Müller[3], Susanne Staehlke[1] and J. Barbara Nebe[1,6]**

*[1] Department of Cell Biology, Rostock University Medical Center, Rostock, Germany, [2] Soft Matter and Biophysics, Institute of Physics, University of Greifswald, Greifswald, Germany, [3] Colloid and Interface Chemistry, Institute of Physical and Theoretical Chemistry, University of Regensburg, Regensburg, Germany, [4] Department of Biomaterials, INNOVENT e.V., Jena, Germany, [5] Leibniz Institute for Plasma Science and Technology e.V. (INP), Greifswald, Germany, [6] Department Science and Technology of Life, Light and Matter, Faculty of Interdisciplinary, University of Rostock, Rostock, Germany*

OPEN ACCESS

**Edited by:**
*Masoud Mozafari, University of Toronto, Canada*

**Reviewed by:**
*Thomas Michael Groth, Martin Luther University Halle-Wittenberg, Germany*
*Bogdan Parakhonskiy, Ghent University, Belgium*

***Correspondence:**
*J. Barbara Nebe*
*barbara.nebe@med.uni-rostock.de*

**Specialty section:**
*This article was submitted to Biomaterials, a section of the journal Frontiers in Bioengineering and Biotechnology*

**Received:** *19 May 2020*
**Accepted:** *03 August 2020*
**Published:** *08 September 2020*

**Citation:**
*Gruening M, Neuber S, Nestler P, Lehnfeld J, Dubs M, Fricke K, Schnabelrauch M, Helm CA, Müller R, Staehlke S and Nebe JB (2020) Enhancement of Intracellular Calcium Ion Mobilization by Moderately but Not Highly Positive Material Surface Charges. Front. Bioeng. Biotechnol. 8:1016. doi: 10.3389/fbioe.2020.01016*

Electrostatic forces at the cell interface affect the nature of cell adhesion and function; but there is still limited knowledge about the impact of positive or negative surface charges on cell-material interactions in regenerative medicine. Titanium surfaces with a variety of zeta potentials between −90 mV and +50 mV were generated by functionalizing them with amino polymers, extracellular matrix proteins/peptide motifs and polyelectrolyte multilayers. A significant enhancement of intracellular calcium mobilization was achieved on surfaces with a moderately positive (+1 to +10 mV) compared with a negative zeta potential (−90 to −3 mV). Dramatic losses of cell activity (membrane integrity, viability, proliferation, calcium mobilization) were observed on surfaces with a highly positive zeta potential (+50 mV). This systematic study indicates that cells do not prefer positive charges in general, merely moderately positive ones. The cell behavior of MG-63s could be correlated with the materials' zeta potential; but not with water contact angle or surface free energy. Our findings present new insights and provide an essential knowledge for future applications in dental and orthopedic surgery.

Keywords: human osteoblasts, calcium ion signaling, titanium surface modification, amino polymer, polyelectrolyte multilayer, zeta potential, surface charge, wettability

**Abbreviations:** AM, acetoxymethyl ester; APTES, (3-aminopropyl)triethoxysilan; ATP, adenosine 5'-triphosphate; Col I, collagen-type I; Col IV, collagen-type IV; DAPI, 4′,6-diamidino-2-phenylindole; DETA, (3-trimethoxysilylpropyl)diethylenetriamine; DMEM, Dulbecco's Modified Eagle Medium; DMSO, dimethyl sulfoxide; ECM, extracellular matrix; EDC, *N*-(3-dimethylaminopropyl)-*N′*-ethylcarbodiimide hydrochloride; Ent, entactin; EthD-1, Ethidium Homodimer 1; HSPG, heparan sulfate proteoglycans; Lam, laminin; MES, 2-(*N*-morpholino) ethanesulfonic acid; $MFI_C$, mean fluorescence intensity of cells; $MFI_B$, basal mean fluorescence intensity; $MFI_A$, mean fluorescence intensity after ATP stimulation; MTS, 3-(4,5-dimethylthiazol-2-yl)-5-(3-carboxymethoxyphenyl)-2-(4-sulfophenyl)-2H-tetrazolium salt; NHS, *N*-hydroxysuccinimide; OeTS, 7-octenyltrichlorosilane solution; PAH, poly(allylamine hydrochloride); PAMAM, poly(amidoamine); PBS, phosphate buffered saline; PDADMA, poly(diallyldimethyl ammonium chloride); PEI, poly(ethylene imine); PEM, polyelectrolyte multilayer; PES, polyethersulfone; PFA, paraformaldehyde; PP, proliferative phase; PPAAm, plasma polymerized allylamine; PPI-G4, poly(propylene imine) dendrimer generation 4; PSS, poly(styrene sulfonate); RGD, peptide sequence Arg-Gly-Asp; ROI, region of interest; ROS, reactive oxygen species; RT, room temperature; SAM, self-assembled monolayer; SEM, scanning electron microscope; SFE, surface free energy; SPDP, *N*-succinimidyl-3-(2-pyridyldithio) propionate; TESPSA, 3-(triethoxysilyl)propyl succinic acid anhydride; Ti, titanium; WCA, water contact angle; XPS, X-ray photoelectron spectroscopy; ζ, zeta potential.

## INTRODUCTION

Bone defects due to fractures, infections or tumor resections are one of the main causes of disability in an aging society, leading to a loss of quality of life (Akter and Ibanez, 2016). In orthopedic applications, titanium (Ti) has been and still is the material of choice due to properties such as high strength and corrosion resistance (Hanawa, 2019). To improve the bioactivity of Ti-based materials, several strategies are used, including physical treatments to modify the topography (Wennerberg and Albrektsson, 2009; Nikkhah et al., 2012; Kumar et al., 2019) or chemical treatments to modify the bioactivity (Kokubo and Yamaguchi, 2015; Muderrisoglu et al., 2018; Devgan and Sidhu, 2019) all aiming to optimize the interaction with osteoblastic cells.

Surface properties are one of the main factors influencing the cells' fate by guiding cellular processes at the interface from the very beginning (Felgueiras et al., 2018; Ferrari et al., 2019). As a result, the advanced cell-material interaction is a pivotal step determining the success of osseointegration, ultimately, the success of implants. Initial processes driven by the surface properties involve cellular attachment, adhesion and spreading (von der Mark and Park, 2013), which further affect other cell activities such as proliferation, differentiation (Bacakova et al., 2011), and intracellular signaling (Anselme et al., 2010; Staehlke et al., 2015, 2018). Stimulating cellular behavior at the interface by acting on surface physico-chemical properties, especially roughness, stiffness, wettability, and surface charge via surface functionalization can be an effective way to improve bone regeneration (Ferrari et al., 2019).

Previous research has shown that osteoblasts favor a certain range of roughness, pore size, wettability, specific biomacromolecules or their biomimetic motifs (Chen et al., 2018) and also stiffness (Abalymov et al., 2020). It could be demonstrated that cells prefer moderately hydrophilic surfaces displaying contact angles between 40° and 65° (Bacakova et al., 2011; Rebl et al., 2012; Mörke et al., 2017). However, other studies have shown that this is not always the case; for instance MG-63 osteoblasts exhibited increased cell attachment and spreading on methylated silicon surfaces with decreasing wettability (Padial-Molina et al., 2011). Similarly, Kennedy et al. (2006) reported that MC3T3-E1 cells displayed improved cell proliferation with increased hydrophobicity and the lowest spreading on the most hydrophilic SAM (self-assembled monolayers) surface. Thus, the contact angle is not a good predictor of cell behavior (Gentleman and Gentleman, 2014).

Furthermore, it has been proven that extracellular matrix (ECM) proteins (mainly collagen, fibronectin, laminin and vitronectin) (Müller et al., 2006; Rico et al., 2009; Chen et al., 2018), their RGD sequence (Arg-Gly-Asp) (Mörke et al., 2017) and cytokines [e.g., basic fibroblast growth factor (bFGF)] (Cao et al., 2015) have the capacity to promote cell attachment.

Some explanations have also been suggested for the surface charge and its effect on the cell-material interaction. Surface charges can generate electrical cues necessary to regulate cell function (De Aza et al., 2003; Finke et al., 2007; Fernández-Yagüe et al., 2019). As human osteoblasts are negatively charged (Rebl et al., 2016), positive surface charges significantly influence cell adhesion (Rebl et al., 2010; Dhowre et al., 2015; Mörke et al., 2017), spreading and proliferation (Staehlke et al., 2019), particularly in the early stages of cell responses. The most detailed study on the effect of surface charges to date is that of Metwally and Stachewicz (2019), indicating a great importance in the development of functionally implantable biomaterials. They reviewed that surface charges determine protein adsorption and thus the subsequent cell adhesion process. Referring to Goldenberg and Steinberg (2010) surface charge seems to be also important for the correct protein localization of signaling molecules in the cell membrane; it has been documented that proteins like GTPases of the Ras, Rho, Arf, and Rab protein families target the plasma membrane through electrostatic interactions (Heo et al., 2006).

The measurement of zeta (ζ) potentials is a suitable technique for characterizing the charging behavior at the solid-liquid interface of modified biomaterial surfaces (Ferraris et al., 2018). There are few papers that address materials such as hydrogels (Schulz et al., 2018), polyelectrolyte multilayers (PEM) (Guo et al., 2018) or metals (Ponsonnet et al., 2003; Nebe et al., 2007) exhibiting a positive ζ-potential enhancing cell processes like cell adhesion, spreading, viability and proliferation. And yet present understanding of the mechanism involved in controlling cell activities via surface charge in tissue engineering is still limited.

In order to gain deeper insights into the impact of surface charges on the cell-material interaction, systematic experiments are required. Our previous work has shown that a plasma polymerized nanolayer of allylamine (PPAAm) provides positive charges on an otherwise negatively charged Ti surface that can boost cell behavior (reviewed in Nebe et al., 2019). The question arose whether a positive ζ-potential is generally considered to be a decisive factor for the cellular outcome.

In the present study, we generated a broad range of surface charges to investigate in detail their influence on osteoblastic cell response via intracellular calcium ion ($Ca^{2+}$) mobilization, cell viability and proliferation. For this purpose, we deposited nine different top layers on Ti substrates from the following three categories: (i) amino polymers, (ii) ECM/peptide motifs, and (iii) PEM. We determined the physico-chemical characterization of these surfaces via water contact angles (WCA), surface free energies (SFE), X-ray photoelectron spectroscopy (XPS) and layer thicknesses, and employed ζ-potential measurements to determine surface charges.

We hypothesize that cell physiology can be improved by material surfaces featuring a certain range of positive ζ-potential.

## MATERIALS AND METHODS

### Functionalization of Titanium Arrays

The following section describes the methods for the diverse Ti surface modifications used for surface charge determination and in the cell biological experiments shown in **Figure 1**. They are categorized in modifications with amino polymers, ECM/peptide motifs, as well as in PEM. As base material and negative control we used planar silicon arrays sputtered

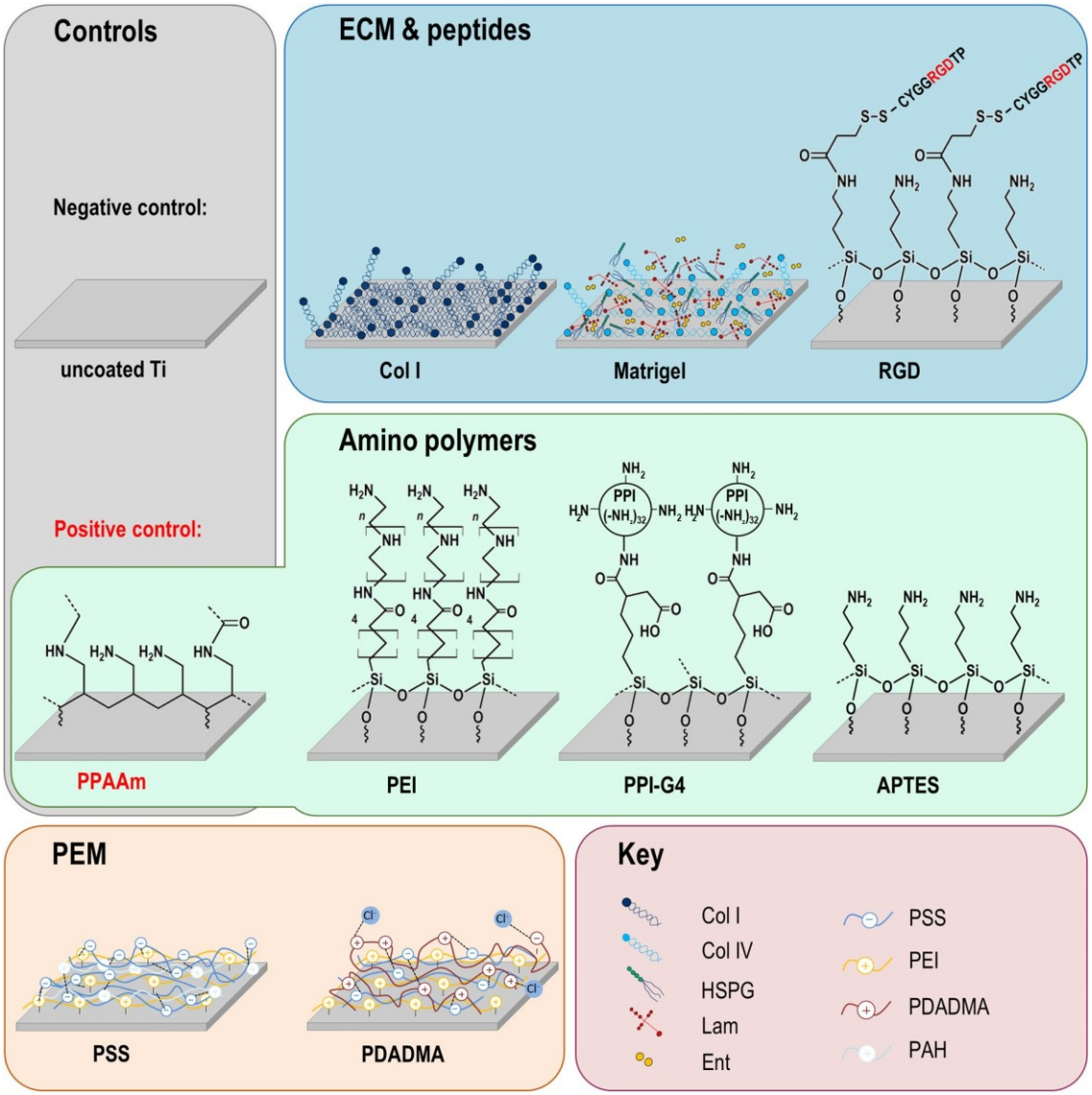


**FIGURE 1** | Chemical surface modifications of plane Ti arrays. The modifications can be classified into three groups: amino polymers, extracellular matrix (ECM)/peptide motifs and polyelectrolyte multilayers (PEM). Please note that the molecular structures are schematic formula drawings (created using the freeware ACD/ChemSkretch 2018.2.5, Advanced Chemistry Development, Toronto, ON, Canada), which do not necessarily allow conclusions about the molecular length of the individual layers. Ti, titanium; Col I, collagen-type I; RGD, peptide sequence Arg-Gly-Asp; PPAAm, plasma polymerized allylamine; PEI, poly(ethylene imine); PPI-G4, poly(propylene imine) dendrimer generation 4; APTES, (3-aminopropyl)triethoxysilan; PSS, poly(styrene sulfonate); PDADMA, poly(diallyldimethylammonium chloride); HSPG, heparan sulfate proteoglycans; Lam, laminin; Ent, entactin; Col IV, collagen-type IV; PAH, poly(allylamine hydrochloride).

with 100 nm Ti particles obtained from the Center for Microtechnologies (ZFM, University of Technology Chemnitz, Germany) at 1 x 1 x 0.075 cm in size (length width depth) for cell analysis, or 2 x 1 x 0.075 cm for ζ-potential analysis as previously reported (Staehlke et al., 2018).

## Amino Polymers

### *Plasma polymerized allylamine (PPAAm)*

As it is known that the positively charged plasma polymerized allylamine (PPAAm) layer can improve several cell functions (Rebl et al., 2012; Mörke et al., 2017; Staehlke et al., 2018; Nebe et al., 2019), this plasma functionalization of Ti was used as a positive control in all experiments. The specimens were coated with the PPAAm nanolayer by using a low-pressure plasma reactor (V55G, Plasma Finish, Germany) (Rebl et al., 2012) with the following parameters: continuous wave oxygen/argon plasma (500 W, 50 Pa, 1000-sccm $O_2$, 5 sccm Ar, 60 s), 480 s PPAAm deposition time. PPAAm films have proven to be very robust according to DIN EN 582 (1993), mechanically stable (Fritsche et al., 2009) and can be used for cell experiments for up to 200 days when stored in ambient air (Finke et al., 2014).

### *(3-Aminopropyl)triethoxysilane (APTES)*

Ti surfaces were modified with the linker (3-aminopropyl)triethoxysilane (APTES) (Mörke et al., 2017). Prior to modification, the substrates were cleaned and pre-activated by water vapor plasma treatment for 15 s at 0.1 mbar in a microwave. Then, Ti surfaces were coated with 100 mM APTES (abcr, Karlsruhe, Germany) in toluene (Alfa Aesar/Fisher Scientific, Kandel, Germany) for 3 h at 60°C in an incubator (GFL 3032, Burgwedel, Germany) turning at 35 rpm. After carefully washing with ultrapure water, the samples were dried under a stream of pure nitrogen (ultra-high purity 5.0 grade) in a laminar flow box (Herasafe KS 12, Kendro, Langenselbold, Germany). APTES layers are stable up to 1 year when stored under exclusion of light and oxygen.

### *Poly(ethylene imine) (PEI)*

Before functionalization, contaminants were removed from the substrate surface by sonicating in acetone (p.a., Sigma-Aldrich Chemie, Taufkirchen, Germany), followed by oxidation of the substrates in a semi-concentrated $HNO_3$ solution (38%, 1:1 v/v from concentrated ($\geq$65%) nitric acid, obtained from Carl Roth, Karlsruhe, Germany) for 1 week. The wafers were rinsed with ultrapure and sterile water multiple times until a neutral pH was obtained, then dried in a vacuum desiccator (Carl Roth). As described in previous publications, further modification steps were performed under an argon atmosphere in anhydrous solvents (dried with a molecular sieve from Carl Roth) (Eichler et al., 2011; Katzur et al., 2012). The synthesis of carboxylic acid-terminated SAM (SAM-COOH) is based on the protocol by Liu et al. (2002) and was described previously (Katzur et al., 2012). Here, the silanization in a 7-octenyltrichlorosilane solution was carried out for 2 h, the conversion of the terminal alkene groups in a $KMnO_4$ solution for 15 min.

For the immobilization of the poly(ethylene imine) (PEI) polymer, the SAM-COOH-modified substrates were first activated via immersion in a solution containing 100 mmol/l *N*-(3-dimethylaminopropyl)-*N′*-ethylcarbodiimide hydrochloride (EDC) and 100 mmol/l *N*-hydroxysuccinimide (NHS) in 0.1 mol/l 2-(N-morpholino) ethanesulfonic acid (sodium salt) (MES) buffer (pH adjusted to 5.4) for 2 h at room temperature (RT). EDC, NHS and MES were purchased from Sigma-Aldrich Chemie of analytical grade. After rinsing once with MES buffer, twice with water and once with methanol (p.a., Fischer Scientific, Schwerte, Germany), the immobilization of the polymer was carried out in a 10 mg/ml PEI solution (linear, Mw = 25 kDa, abcr, Karlsruhe, Germany) in a methanol/water mixture (9:1 v/v) for 1.5 h at RT. Excess polymer was removed by rinsing twice with the methanol/water mixture and once with methanol before the specimens were dried in a desiccator. PEI layers are stable for up to 8 weeks when stored in the dark and under argon atmosphere.

### *Poly(propylene imine) dendrimer (PPI-G4)*

In respect to the functionalization with PEI described above, the surfaces were first cleaned by sonication and then oxidized for 1 week. Then a silanization of substrates with 3-(triethoxysilyl)propyl succinic acid anhydride (TESPSA, abcr, Karlsruhe, Germany) was performed according to previously published protocols (Eichler et al., 2011) at elevated temperatures (110°C for 30 min, followed by 130°C for 10 min) under an argon atmosphere. Excess silane was removed by rinsing twice with dry toluene. The specimens were sonicated once with dry dimethyl sulfoxide (DMSO, Fisher Scientific, Schwerte, Germany) and immersed in a 0.5 mmol/l poly(propylene imine) dendrimer generation 4 (PPI-G4, SyMO-Chem, Eindhoven, Netherlands) solution in anhydrous DMSO. The reaction was performed for at least 40 h at RT. Rinsing was performed by sonicating once with DMSO and at least three times with methanol before drying the wafers in a desiccator. PPI-G4 layers are stable for up to 8 weeks when stored in the dark and under argon atmosphere.

## Extracellular Matrix (ECM) Proteins and Peptide Motifs

### *Collagen type-I (Col I)*

Ti substrates were chemically wet-coated with 40 µg/cm$^2$ collagen type-I (Col I; rat tail, Corning, Discovery Labware, Bedford, MA, United States) and dried overnight at RT (Rebl et al., 2010). Residues of acetic acid were removed by rinsing twice with sterile ultrapure water. Col I coatings were produced prior to cell experiments and used directly.

### *Basement membrane matrix (Matrigel)*

Ti arrays were coated with basement membrane matrix (Matrigel) containing laminin, collagen type-IV, heparan sulfate proteoglycans, entactin and growth factors (Corning, Discovery Labware, Bedford, MA, United States) using a thin-film coating method. For this purpose, Matrigel was thawed on ice and diluted to a concentration of 1 mg/ml using serum-free ice-cold Dulbecco's Modified Eagle Medium (DMEM, 21063-029, Life Technologies Limited, Paisley, United Kingdom). 200 µl of the solution was added to the Ti substrates (200 µg/cm$^2$) with pre-cooled pipette tips and incubated at RT for 1 h under sterile conditions. Unbound material was aspirated and substrates were rinsed gently using serum-free DMEM. Matrigel coatings were produced prior to cell experiments and used directly.

### *Arginine-glycine-aspartic sequence (RGD)*

Ti surfaces were modified with a nonapeptide containing the arginine-glycine-aspartic acid (RGD)-tripeptide (complete amino acid sequence C-Y-G-G-R-G-D-T-P, kindly provided by Dr. K. Rischka, Fraunhofer IFAM Institute Bremen, Germany) as reported in Mörke et al. (2017). Prior to peptide coupling Ti substrates was coated with APTES as described above. RGD layers are stable up to 1 year when stored under exclusion of light and oxygen.

## Polyelectrolyte Multilayers (PEM)

Polyelectrolyte multilayer films were created by dip-coating of oppositely charged polyelectrolytes with a deposition robot (Riegler & Kirstein, Potsdam, Germany) according to Mohamad et al. (2019). Here, we used PEI [branched, Mw = 750 kDa, polydispersity (PDI) = 12.5], polyallylamine hydrochloride (PAH, Mw = 50–60 kDa) and poly(diallyldimethylammonium chloride) (PDADMA, Mw = 322 kDa, PDI = 2.19) as polycations and

poly(styrene sulfonate) sodium salt (PSS, Mw = 666 kDa, PDI < 1.2) as polyanion.

PSS-terminated PEM consisted of three double layers with the sequence PEI/PSS/$(PAH/PSS)_2$. PDADMA-terminated polyelectrolyte brushes were composed of 10.5 double layers with the sequence PEI/PSS/$(PDADMA/PSS)_9$/PDADMA. The layer stability of prepared PEM was verified by AFM measurements [DI Multimode AFM using NanoScope IIIa software from Veeco (Santa Barbara, CA, United States)]. Layers are stable in the range of pH 3–11, in solutions up to 1 M NaCl and after storage in ambient air up to 1 year unchanged.

# Surface Characterization

## Zeta Potential

ζ-potentials were assessed with the SurPASS$^{TM}$ system (Anton Paar, Ostfildern, Germany) and the associated software Attract 2.1 as previously published (Staehlke et al., 2018). Streaming potentials were measured at pH 6.5–8.0 in a 1 mM KCl solution (VWR International, Darmstadt, Germany) and ζ-potentials at pH 7.4 were calculated via a linear regression using the software GraphPad Prism version 6.05 ($n$ = 3, three pairs of samples).

## Surface Wettability

Surface free energies of the substrate/air interface and WCA were determined by the sessile drop method using the Drop Shape Analyzer—DSA25 (Krüss, Hamburg, Germany) (Staehlke et al., 2018). One µl drops of distilled water and diiodomethane (Sigma-Aldrich Chemie, Taufkirchen, Germany) were deposited on the sample surface ($n$ = 3 at 3 drops each). WCA values were calculated with the supplied software (ADVANCE, V.1.7.2.1, Krüss, Hamburg, Germany) via the Young's equation and the SFE according to Owens, Wendt, Rabel und Kaelble (OWRK).

## Layer Thickness

Layer thickness was measured with null ellipsometry (Multiskop; Optrel GbR, Sinzing, Germany) as described before (Mörke et al., 2017). Each sample was modeled by 6 slabs in order to account for oxide layers (Si, $SiO_2$, Ti, $TiO_2$, layer of interest and ambient air). The thickness of the Ti and $TiO_2$ layer was determined independently prior to deposition of the layer of interest. Additionally, uncoated samples were measured and served as a reference. Each measurement was carried out at several angles of incidence (50°− 80° in 1° steps) in two different ellipsometric zones (Nestler et al., 2012).

## Chemical Composition

The elemental composition of the modified surfaces was analyzed by using an AXIS Supra X-ray photoelectron spectrometer from Kratos Analytical Ltd. (Manchester, United Kingdom). Measurements were performed using a monochromatic Al Ka X-ray source (1486.6 eV) operated at 150 W. Survey and core-level spectra were acquired using a pass energy of 80 eV. For each sample, an area of 250 µm was analyzed in duplicates on three different positions. During the analysis, the integrated charge neutralization system was activated for charge compensation. XPS measurements for PEI and PPI-G4 were performed with a PHI 5700 (Physical Electronics, United States). Here, survey and core-level spectra were acquired using pass energies of 117–187 eV. Charge neutralization was not necessary.

# Cell Biological Investigations

## Cell Culture

Human osteoblast-like MG-63 cells (American Type Culture Collection ATCC®, CRL1427$^{TM}$, Bethesda, MD, United States) were used; this cell line has been successfully applied as a model for studying cell-material interactions (Staehlke et al., 2019) and has similar characteristics to primary human osteoblasts (Clover and Gowen, 1994; Czekanska et al., 2014). The cells were cultured in Dulbecco's Modified Eagle Medium (DMEM, 31966-021, Life Technologies Limited, Paisley, United Kingdom), with 10% fetal calf serum (FCS, Biochrom FCS Superior, Merck, Darmstadt, Germany) and 1% antibiotics (gentamicin, Ratiopharm, Ulm, Germany) at 37°C with 5% $CO_2$/95% air atmosphere (Staehlke et al., 2018). All experiments were performed in passages 5–30, as the MG-63 cell physiology is known to remain stable over the entire range of these passages (Staehlke et al., 2019).

## Cell Morphology

### *Scanning electron microscopy (SEM)*

MG-63s (15,000 cells/$cm^2$) were cultured for 24 h on the Ti arrays, washed three times with phosphate buffered saline (PBS, Sigma-Aldrich Chemie, Taufkirchen, Germany), fixed with 2.5% glutardialdehyde (Merck, Darmstadt, Germany) at 4°C overnight and rinsed with 0.1% sodium phosphate buffer (according to Sørensen, Merck, Darmstadt, Germany). The samples were then dehydrated through an ethanol series of 30, 50, 75, 90 and twice 100% (for 5, 5, 15, 10, and 10 min, respectively) and dried in a critical point dryer (K 850, EMITECH, Taunusstein, Germany). The samples were sputtered with gold for 50 s (15 nm, SCD 004, BAL-TEC, Wetzlar, Germany) and field emission scanning electron microscopy (FE-SEM, ZEISS Merlin VP compact, Carl Zeiss, Oberkochen, Germany) observations were taken with an acceleration voltage of 5 kV, a working distance of 5.6 mm and a high efficiency secondary electron detector (InlenseDuo for 2,000x, HE-SE2 detector for 100, 500x, and 5,000x).

### *Circularity*

The circularity of the cells after 24 h could be evaluated with Photoshop CC 2017 using fluorescence microscopic images of fluoro-3-acetoxymethyl ester (fluo-3) stained cells ($n \geq 3$ independent experiments á 15 cells). These images were also used for determining the cell area as basic values for the $Ca^{2+}$ mobilization experiments (**Supplementary Table S1**). For the staining procedure see section "Intracellular $Ca^{2+}$ mobilization." A circularity value of 1.0 represents a perfect circle, whereas a value converging toward 0 indicates an elongated polygon.

## Cell Viability

Cell viability was analyzed by an MTS assay, flow cytometry (both described in the **Supplementary Material**) and live/dead staining for selective surfaces representing negative, moderately and 2x highly positive surface charges (Ti, PPAAm, PPI-G4, and PDADMA, respectively). For live/dead staining a cell viability kit (L3224, Molecular Probes, Eugene, OR, United States)

was used. This two-color fluorescence assay is based on the measurement of intracellular esterase activity of living cells (Calcein-acetoxymethyl ester, Calcein-AM) and the abrogation of the plasma membrane integrity of dead cells (Ethidium homodimer-1, EthD-1). While EthD-1 is excluded by the intact plasma membrane of living cells, it can enter cells with damaged cell membrane and binds to nucleic acids. After a cultivation period of 24 h MG-63s (80,000 cells/$cm^2$) were washed carefully with PBS and incubated with a Calcein-AM/EthD-1 solution (1:1, 2 µM Calcein-AM, 4 µM EthD-1) for 20 min at 37°C in the dark. The cells were then rinsed with PBS and fixed with 4% paraformaldehyde (PFA, Sigma-Aldrich Chemie, Taufkirchen, Germany) at RT for 10 min. Samples were embedded on a coverslip with mounting medium Fluoroshield™ (Sigma-Aldrich Chemie, Taufkirchen, Germany) containing 4′,6-diamidino-2-phenylindole (DAPI) and examined using the confocal laser scanning microscope LSM780 (Carl Zeiss, Jena, Germany) with a Plan-Apochromat 63x oil immersion objective (Carl Zeiss; zoom 1 and 2.5) and the ZEN software (ZEISS efficient navigation, ZEN 2011 SP4, black edition, Carl Zeiss).

### Intracellular $Ca^{2+}$ Mobilization

#### *Pre-screening study*

The $Ca^{2+}$ mobilization process in MG-63s was specified with respect to the adenosine 5′-triphosphate (ATP) concentration for cell stimulation, $Ca^{2+}$ origin and the presence of ATP receptors as provided in the **Supplementary Material**. The basal $Ca^{2+}$ signal of MG-63s on Ti and PPAAm controls was validated by immunofluorescence. Therefore, 50,000 cells/$cm^2$ were stained after 1 h with the $Ca^{2+}$ indicator fluo-3 (5 µM, Life Technologies Corporation, Eugene, OR, United States) (Staehlke et al., 2015, 2018), Hoechst 33342 (1:1000, Life Technologies Corporation) and for images after 24 h additionally with 20 µl BacMam 2.0 reagent (CellLight™ actin-RFP, Life Technologies Corporation) at 37°C in isotonic 4-(2-hydroxyethyl)-1-piperazineethanesulfonic acid buffer (HEPES) (Staehlke et al., 2015, 2018). Confocal laser scanning microscopy (LSM780, Carl Zeiss, Jena, Germany) was carried out with a Plan-Apochromat 63x oil immersion objective (Carl Zeiss, 1.40. Oil DIC M27) and the ZEN software (ZEISS efficient navigation, ZEN 2011 SP4, black edition, Carl Zeiss).

#### *$Ca^{2+}$ mobilization*

$Ca^{2+}$ mobilization experiments on different Ti surface modifications were performed according to Staehlke et al. (2015, 2018). In brief, 80,000 cells/$cm^2$ were seeded onto the samples for 24 h and then loaded with 5 µM fluo-3 in $Ca^{2+}$ containing HEPES buffer via a hypo-osmotic shock treatment. $Ca^{2+}$ fluorescence signals of 10 single cells per surface over a time span of 480 s were recorded with a confocal laser scanning microscope LSM780 and the ZEN software (ZEN 2011 SP4, black edition) with the following settings: scan mode ‘time series‘ (1 frame every 2 s, 240 frames in total), maximum pinhole (15 airy unit, 13.5 µm section), gain 632, digital offset −3. First, the basal $Ca^{2+}$ signal was recorded for 180 s. Then, the cells were stimulated with ATP (0.5 mM, SERVA Electrophoresis, Heidelberg, Germany), which indicates the reactivity of vital cells in dependence of the underlying chemical layer. At least three independent experiments per modification with 10 cells each for 240 analysis points per cell were investigated (=7,200 records per surface modification). The mean fluorescence intensity of the single cells ($MFI_C$) was evaluated with the ZEN2 software (blue edition, version 2.0.0.0, Carl Zeiss). For this purpose, ten defined boxes were positioned on randomly chosen cells in the first image of the time series (one box per cell). Using the function ‘mean ROI’ (region of interest), the software analyzed the MFI of the boxes ($MFI_{ROI}$) for 240 time points per cell. However, the $MFI_{ROI}$ represents only a small sub-area of a cell (**Supplementary Figure S4**). Compared with a flat expanded cell, the $Ca^{2+}$ signal of a spherical cell (more cell volume under limited area as cell height is larger) is concentrated on a smaller area, which leads to increased $MFI_{ROI}$ values. Therefore, the $MFI_{ROI}$ values were normalized to the mean area of cells after 24 h ($A_C$) and the defined area of ROI ($A_{ROI}$), assuming that $MFI_{ROI}$ is independent of the ROI position in the cell. Accordingly, the $A_C$ of 15 fluo-3 stained cells per surface were measured with the software Photoshop CC 2017 ($n$ = 3 independent experiments, **Supplementary Table S1**). The $MFI_C$ is described in the form:

$$MFI_c = MFI_{ROI} \times \frac{A_c}{A_{ROI}}$$

where $MFI_C$ is the mean fluorescence intensity of cells at 0–480 s, $MFI_{ROI}$ is the mean fluorescence intensity of the region of interest (ROI), $A_C$ is the mean area of cells after 24 h (µm²), and $A_{ROI}$ is the defined area of ROI (100 µm²). To calculate the mean *basal* fluorescence intensity of a cell ($MFI_B$), $MFI_{ROI}$ values of 0–170 s were used. In order to determine the MFI *after* ATP stimulation ($MFI_A$), $MFI_{ROI}$ values of 190–240 s were employed. The $Ca^{2+}$ mobilization (increase of the $Ca^{2+}$ signal = slope) was calculated by subtracting the $MFI_B$ from $MFI_A$.

## Statistics

Non-parametric Kruskal–Wallis followed by Dunn’s multiple comparisons test (or non-parametric Wilcoxon matched pairs signed-rank test) with the software GraphPad Prism version 6.05 for Windows (GraphPad Software, La Jolla, CA, United States) was conducted on the $p$-values $< 0.05$. Results are presented in (i) mean ± sem (standard error of the mean) for $MFI_C$ values of the $Ca^{2+}$ mobilization, (ii) in mean ± SD (standard deviation) for proliferation and cell area values, as well as for WCA, SFE, ζ-potential and XPS analyses, and (iii) in median with interquartile ranges (IQR) for cell circularity and MTS values.

# RESULTS

## Physico-Chemical Characterization of Ti Surface Coatings

Results regarding layer thickness, wettability and surface charge (deduced from ζ-potentials) are given in **Table 1**. The chemical surface composition determined by XPS measurements is listed in **Supplementary Table S2**.

**TABLE 1** | Surface characteristics of chemically modified Ti (mean ± SD, *n* = 3).

| Surface | | Layer thickness [nm] | WCA [°] | SFE [mN/m]<br>*dispersive*<br>*polar* | ζ at pH 7.4 [mV] |
|---|---|---|---|---|---|
| Controls | Ti | 9.0 + $TiO_2$ (5.0) | 87.4 ± 0.8 | 37.6 ± 1.4<br>*35.6 ± 1.1*<br>*2.1 ± 0.3* | **−87.5 ± 1.6** |
| | PPAAm | 24.5 | 66.9 ± 1.7 | 46.2 ± 1.5<br>*36.2 ± 0.6*<br>*10.0 ± 1.0* | **+7.1 ± 2.7** |
| Amino Polymers | APTES | 5.0 | 88.1 ± 4.1 | 37.0 ± 2.7<br>*35.1 ± 1.6*<br>*1.9 ± 1.0* | **+1.9 ± 1.5** |
| | PEI | 18.0 | 27.6 ± 2.4 | 74.3 ± 2.1<br>*48.8 ± 0.9*<br>*25.5 ± 1.1* | **+9.1 ± 2.6** |
| | PPI-G4 | 23.0 | 47.2 ± 4.3 | 62.4 ± 3.6<br>*45.0 ± 1.2*<br>*17.4 ± 2.4* | **+50.2 ± 6.2** |
| ECM and Peptides | Col I | 165.0 | 50.5 ± 4.3 | 58.6 ± 3.5<br>*41.6 ± 1.1*<br>*17.0 ± 2.5* | **−2.8 ± 1.5** |
| | Matrigel | 5.5 | 69.6 ± 6.9 | 46.7 ± 5.4<br>*38.9 ± 2.1*<br>*7.8 ± 3.3* | **−43.3 ± 1.0** |
| | RGD | 5.6 | 74.9 ± 1.2 | 43.0 ± 1.8<br>*37.0 ± 1.2*<br>*6.0 ± 0.6* | **+1.7 ± 1.0** |
| Polyelectrolyte Multilayers | PSS | 7.0 | 62.3 ± 2.7 | 49.3 ± 2.3<br>*37.2 ± 0.8*<br>*12.1 ± 1.5* | **−88.8 ± 11.8** |
| | PDADMA | 38.0 | 38.7 ± 3.2 | 62.0 ± 3.3<br>*34.6 ± 1.3*<br>*27.3 ± 2.0* | **+51.4 ± 3.6** |

### Layer Thickness

The layer thickness of all modifications was less than or equal to 165 nm. The oxide layer of titanium surfaces was found to be 5 nm. The thinnest layer was achieved with RGD (0.6 nm) with an underlying APTES layer of 5.0 nm (in total 5.6 nm). The thickest layer was measured for Col I at 165 nm.

### Wettability

The analysis demonstrated a change to more hydrophilic surfaces for all modifications except APTES, indicated by a decrease in WCA and an increase in SFE. Uncoated Ti surfaces as well as APTES-functionalized surfaces showed the highest WCA (with Ti 87.4° < APTES 88.1°), the lowest SFE under 40 mN/m and the lowest content of polar interactions with ≤2 mN/m. PEI-functionalized surfaces displayed the lowest WCA (27.6°) and consequently were the most hydrophilic surfaces showing the highest SFE values (74.3 mN/m) with polar interactions of 25.5 mN/m.

### Zeta Potential

A less negative ζ-potential was achieved on almost all surfaces compared with uncoated Ti at −87.5 mV. Only the ζ-potential of PSS (-88.8 mV) was slightly lower. Further negative surface potentials were found for Matrigel (-43.3 mV). Col I substrates exhibit only a slightly negative ζ-potential (-2.8 mV). All other surfaces present a positive ζ-potential and can be classified as moderately and highly positive. Moderately positively charged surfaces include PPAAm, APTES, PEI and RGD (+7.1, +1.9, +9.1, and +1.7 mV, respectively), whereas highly positively charged surfaces comprise PPI-G4 and PDADMA (+50.2 and +51.4 mV, respectively). Here we sorted the investigated surfaces starting with the most negative ζ-potential: PSS < Ti < Matrigel < Col I < RGD < APTES < PPAAm < PEI < PPI-G4 < PDADMA.

## Cell Biological Investigations

The effect of positive and negative ζ-potential of chemically modified Ti surfaces on MG-63s behavior was observed and correlated.

### Cell Morphology

The cell morphology on highly positively charged PPI-G4 and PDADMA surfaces was significantly changed to a more round shape (circularity 0.74 and 0.77, respectively) compared to

A

Circularity

| Surface | Ti | PPAAm | APTES | PEI | PPI-G4 | Col I | Matrigel | RGD | PSS | PDADMA |
|---|---|---|---|---|---|---|---|---|---|---|
| Median | 0.36 | 0.44 | 0.45 | 0.38 | **0.74** * | 0.37 | 0.50 | 0.46 | 0.50 | **0.77** * |
| 25th Quartile | 0.28 | 0.37 | 0.36 | 0.32 | 0.67 | 0.26 | 0.38 | 0.40 | 0.36 | 0.74 |
| 75th Quartile | 0.45 | 0.54 | 0.66 | 0.49 | 0.77 | 0.50 | 0.65 | 0.64 | 0.57 | 0.81 |

B

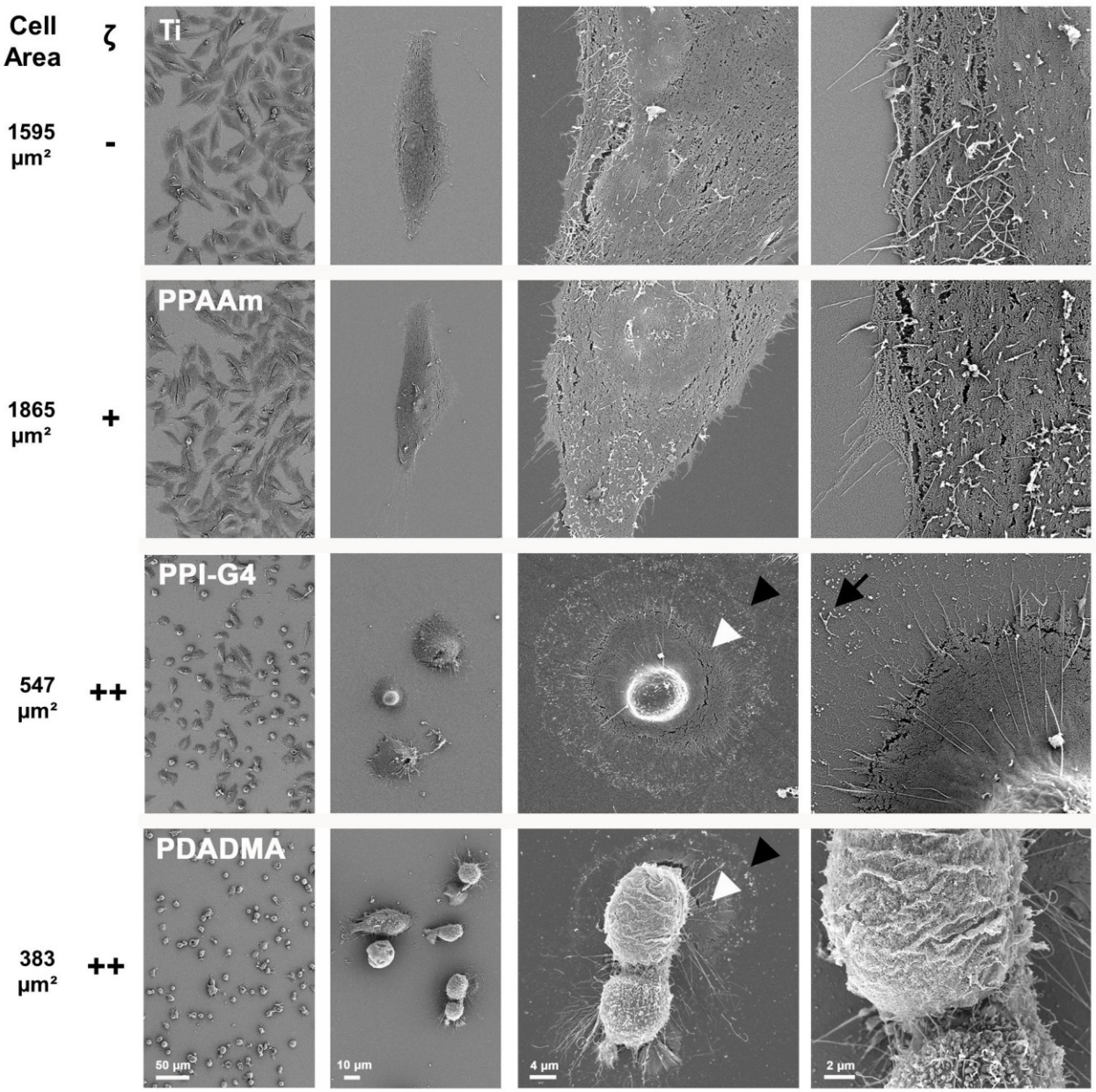


**FIGURE 2** | Morphology of MG-63s after 24 h on bare and functionalized Ti with negative (–), moderately positive (+) and highly positive (++) ζ-potential. **(A)** The cell circularity on highly positive surface charges reveals a morphologically significant difference to the other surfaces (*). A circularity value of 1.0 represents a perfect circle. (Statistics: Kruskal–Wallis and Dunn's multiple comparison test, *$p < 0.05$; median ± IQR; $n = 3$ independent experiments). **(B)** Note the enormous decrease in cell area (from black arrowhead to white) on PPI-G4 and PDADMA. The PPI-G4 image (right) shows filopodia residues after the cell has retracted (arrow). On PDADMA different membrane structures with and without microvilli are visible (right image). (SEM images, magnification from left to right 100, 500, 2,000 and 5,000x, scale bars 50, 10, 4, and 2 µm, respectively, FE-SEM Merlin VP compact; mean cell area, $n = 3$ independent approaches, fluo-3 staining, LSM780).

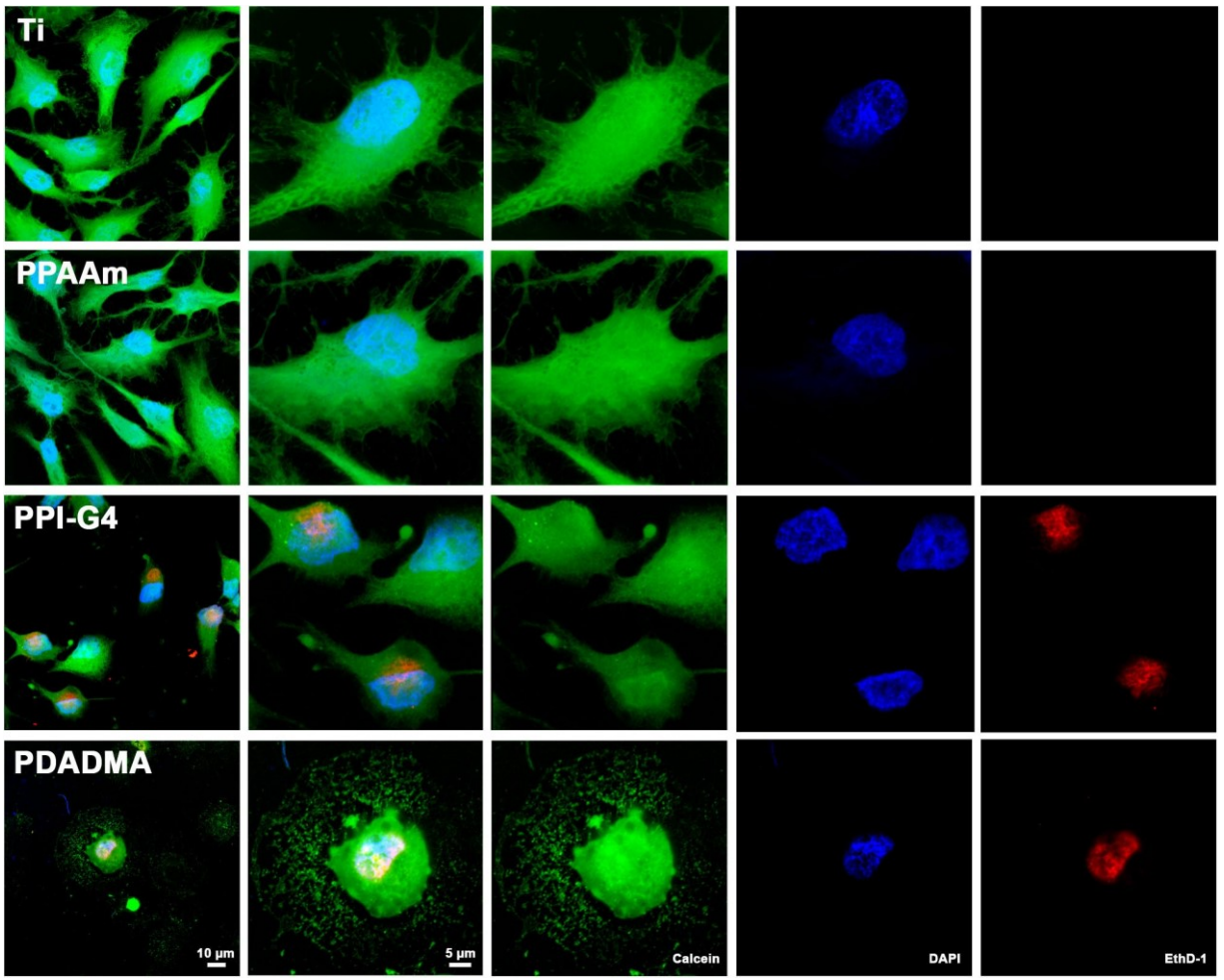


**FIGURE 3** | Cell viability of MG-63s after 24 h on Ti and PPAAm arrays representing negatively and moderately positive surface charges, as well as PPI-G4 and PDADMA, representing highly positive surface charges. Cells on PPI-G4 and PDADMA surfaces are stained with both calcein and EthD-1, indicating damaged plasma membranes. (Immunofluorescence images of live/dead staining; 63x objective with 1x and 2.5x zoom, scale bar 10 and 5 µm; nucleus in blue (DAPI), esterase activity of living cells in green (calcein), DNA of cells with abrogated membrane integrity in red (EthD-1); LSM780).

all other surfaces with a polygonal shape (**Figure 2A**). High resolution SEM images revealed a decrease in cell area of MG-63s on PPI-G4 and PDADMA (**Figure 2B**, indicated by arrowheads), showing impaired cell morphology in contrast to well spread phenotypes on Ti and PPAAm. At 5,000x magnification, filopodia and membrane residues of cells on PPI-G4 are visible (arrow), whereas cells on PDADMA also show an altered membrane structure, as no microvilli are presented in individual cells.

## Cell Viability

Fluorescence live/dead images displayed several cells on highly positively charged PPI-G4 and PDADMA surfaces that were positive for both Calcein and EthD-1 in contrast to Ti and PPAAm, suggesting a damaged plasma membrane (**Figure 3**). These images also confirmed the reduced cell area and circular shape on PPI-G4 and PDADMA after 24 h. In addition, we observed a decreased relative cell viability (**Supplementary Figure S1**) and cell proliferation (**Supplementary Figure S2**) on these surfaces compared with Ti and PPAAm, with a greater extent on PDADMA surfaces. While the amount of proliferative cells declined (with 64.1, 66.8, 51.8, and 24.6% for Ti, PPAAm, PPI-G4 and PDADMA, respectively), the cells increasingly remained in the G1 phase (34.0, 32.2, 47.5, and 73.7% for Ti, PPAAm, PPI-G4 and PDADMA, respectively).

## Intracellular $Ca^{2+}$ Mobilization

The intracellular basal $Ca^{2+}$ signals on the control surfaces Ti and PPAAm are depicted in **Figure 4**. The fluorescence images reveal an increased cell area on PPAAm after 1 h compared with the uncoated Ti control (white dotted lines), while cells are equally spread after 24 h (insert top right). The basal $Ca^{2+}$ level was found elevated after 1 h as well as after 24 h on PPAAm compared with Ti. Consequently, these control surfaces were consistently included in the following $Ca^{2+}$ mobilization experiments.

The influence of the individual Ti modifications on $Ca^{2+}$ mobilization in vital cells is presented in **Figure 5** (an overview

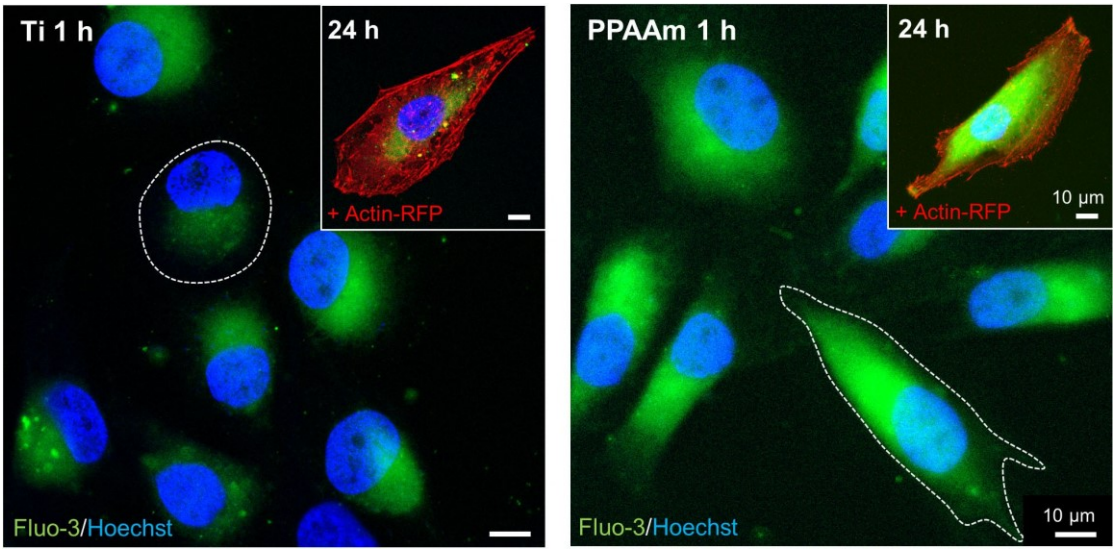


**FIGURE 4** | Basal $Ca^{2+}$ signals in living MG-63s after 1 h and 24 h on the control surfaces Ti (left) and PPAAm (right). The intracellular basal $Ca^{2+}$ level on PPAAm is increased both after 1 and 24 h, suggesting higher cell function. While cells on PPAAm exhibit a larger cell area after 1 h (white dotted line), the area is balanced after 24 h. (Immunofluorescence images; 63x objective, scale bar 10 µm; nucleus in blue (Hoechst), $Ca^{2+}$ ions in green (fluo-3), cytoskeleton in red (actin-RFP); LSM780).

of the time series with fluorescence images can be found in the **Supplementary Figure S5**). Shown are the whole time series of $Ca^{2+}$ mobilization in MG-63 osteoblasts cultured 24 h on Ti modifications (blue curves) and the corresponding controls (gray curves = Ti, green/red curves = PPAAm). The exact values for $MFI_B$, $MFI_A$ and slope can be found in **Table 2**. Stimulation with ATP after 180 s resulted in a significantly lower $Ca^{2+}$ mobilization in cells on PSS and PDADMA compared with their Ti controls, whereas the $MFI_A$ of cells on Col I and PEI exceeded the Ti control significantly (**Figure 5**). Cells on Matrigel could not display a significantly different $Ca^{2+}$ level upon stimulation than Ti. The $MFI_A$ in cells on RGD-functionalized surfaces was significantly elevated compared with Ti, but below PPAAm. The highest $Ca^{2+}$ mobilization after ATP stimulation was found in cells on APTES. Cells cultured on PDADMA surfaces exhibited the lowest mobilization rate, while cells on PPI-G4 surfaces could not mobilize $Ca^{2+}$ ions at all.

These results could be correlated with the ζ-potential of the substrates, as shown in **Figure 6**. Here, the sections 5A-C are classified into negative, moderately and highly positive according to ζ-potential values, starting with the most negative and ending with the most positive value. With this alignment the diminished $Ca^{2+}$ mobilization in cells on surfaces with negative (**Figure 6A**) and highly positive ζ-potential (**Figure 6C**) compared with surfaces with moderately positive ζ-potential (**Figure 6B**) could be clearly demonstrated. Cells on surfaces with negative ζ-potentials of −88.8 to −43.3 mV displayed significantly lower $Ca^{2+}$ levels after ATP stimulation than PPAAm, the positively charged control (red line in highlighted area = $MFI_A$ of PPAAm) (**Figure 6A**). Exclusively, Col I-functionalized surfaces with an almost neutral ζ-potential of − 2.8 mV lacked significance to PPAAm. The absolute slope from basal $Ca^{2+}$ level to the level after ATP stimulation reached a maximum of 594.9 $MFI_C$ on negatively charged surfaces (**Table 2**).

Materials revealing a moderately positive ζ-potential of ~ 1 to 10 mV consistently exhibited significantly higher $Ca^{2+}$ levels after stimulation than Ti, the negatively charged control (black line in highlighted area = $MFI_A$ of Ti, **Figure 6B**). Here, the $Ca^{2+}$ mobilization ranged between 800.7 and 1392.4 $MFI_C$ (**Table 2**).

On substrates presenting highly positive ζ-potentials (~ + 50 mV), MG-63s indicated an impaired $Ca^{2+}$ mobilization with $MFI_A$ values significantly lower than PPAAm and Ti (**Figure 6C**). The maximum $Ca^{2+}$ level increase was 79.1 $MFI_C$ (**Table 2**).

Furthermore, a correlation of $Ca^{2+}$ mobilization data with the measured surface properties for wettability (WCA and SFE) could not be identified (**Table 2**). There were both less and more hydrophilic surfaces in the range of cells showing a stronger ability to mobilize intracellular $Ca^{2+}$ (e.g., ~ 90° for APTES and ~ 30° for PEI) as well as a lower ability for $Ca^{2+}$ mobilization (e.g., ~ 90° for Ti and ~40° for PDADMA). However, osteoblasts behave differently with respect to their $Ca^{2+}$ dynamics. A similar statement can be formulated regarding the SFE values. Here, the highest SFE values (Col I < PDADMA < PPI-G4 < PEI with 58.6, 62.0, 62.4, and 74.3 mN/m, respectively) did not automatically lead to the best $Ca^{2+}$ mobilization results, especially noticeable for PPI-G4 and PDADMA, which displayed the lowest slope.

## DISCUSSION

Cells in living bone tissue are surrounded by an electrically charged, organic/inorganic solid that is permeated by a flow of ionic solution through an intricate channel system

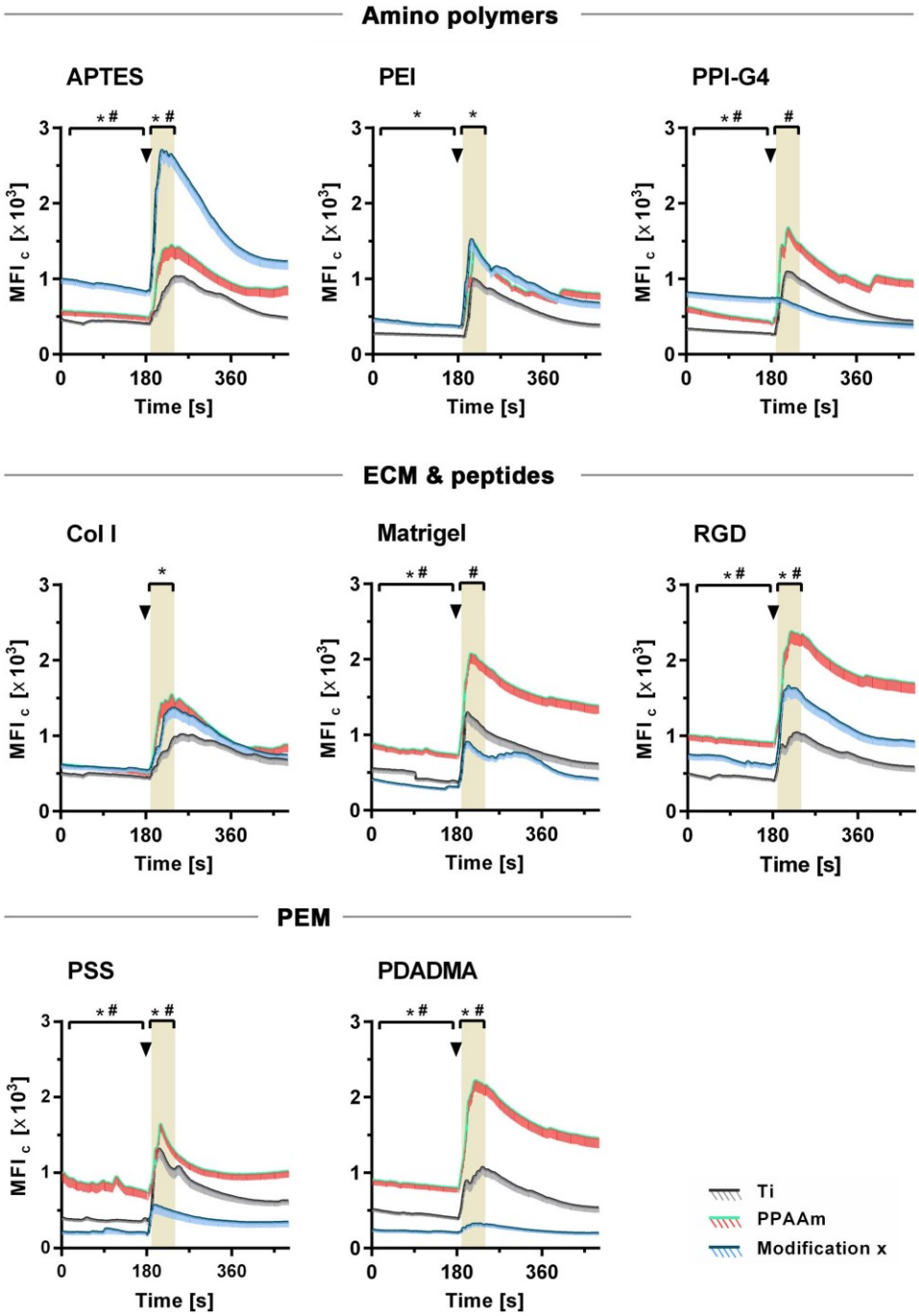


**FIGURE 5** | Dynamic $Ca^{2+}$ mobilization in vital fluo-3 loaded MG-63s growing on amino polymers, extracellular matrix (ECM)/peptide motifs and polyelectrolyte multilayers (PEM) in the time frame 0–480 s. The positive control PPAAm (also an amino polymer) and the negative control Ti are embedded for the respective experiment. Shown are time courses of the mean fluorescence intensity of cells ($MFI_C$) over 8 min: First, the basal $Ca^{2+}$ signal is recorded for 180 s. At 180 s the cells are stimulated with ATP (arrowheads) and the $Ca^{2+}$ signal is detected (LSM780, Carl Zeiss; ZEN-software). For statistical analyses of the basal MFI, values of the time points 0–170 s are used. For analyses of the MFI after ATP stimulation, values of the time points 190–240 s are used (highlighted in grey). $MFI_C$ values are normalized to the mean cell area after 24 h. (Statistics: Kruskal–Wallis and Dunn's multiple comparison test, $p < 0.05$; mean ± sem; $n \geq 3$ independent approaches, per time point ≥ 30 cells; * indicates significance of modification x to Ti and # significance to PPAAm).

(Chakkalakal, 1989). Consequently, it is not surprising that bone cell physiology is also affected by electrical cues when cultivating cells on artificial material surfaces. Cell-material interactions are highly complex and require more systematic investigations regarding surface charge. It is certain that electrostatic forces are crucial for cellular attachment via focal adhesion to material

surfaces (Metwally and Stachewicz, 2019) influencing the further fate of cells. Earlier studies have mostly dealt with a limited number of surface charges [e.g., only negative surfaces (Altankov et al., 2003), one positive compared with several negative surfaces (Chang et al., 2014), or only one negative, neutral and positive surface charge (Iwai et al., 2013)] disallowing detailed statements. It has been reported that materials with positive surface potentials have a beneficial effect on cell viability as well as on adhesion and spreading. But most studies lacked a clear determination of the surface potential (Lee et al., 1994; Bacakova et al., 1996; Webb et al., 1998; Lesný et al., 2006). Hence, the underlying mechanism controlling cell activities using the materials' surface charge is still not fully understood in bone tissue engineering.

In the present study, the behavior of osteoblastic MG-63s via intracellular $Ca^{2+}$ mobilization was systematically investigated on different Ti modifications and correlated with the materials' ζ-potential as a parameter for the electric surface property. We used unmodified Ti (- 87.5 mV) and PPAAm coated Ti (+7.1 mV) as controls with negative and positive ζ-potential, respectively, as published before (Mörke et al., 2017; Nebe et al., 2019), knowing that the PPAAm surface modification enhances cell physiology concerning adhesion, spreading, motility (Rebl et al., 2010), actin filament network (Rebl et al., 2016), viability and $Ca^{2+}$ mobilization (Moerke et al., 2018; Staehlke et al., 2018), as well as the implant osseointegration (Hoene et al., 2010). Cells bind to this positively charged plasma polymer layer via electrostatic forces, as it is known that osteoblasts (Finke et al., 2007), epithelial cells and chondrocytes (Cohen et al., 2004) express i.a. the negatively charged hyaluronan as a spherical shell around the cells (Zimmerman et al., 2002). However, the question arose whether positive ζ-potentials generally lead to a beneficial cellular outcome.

## Physico-Chemical Characterization of Ti Surface Coatings

Therefore, we successfully prepared nine chemical modifications of Ti substrates with (i) amino polymers, (ii) ECM/peptide motifs, and (iii) PEM, resulting in a broad range of ζ-potentials. The materials' characteristic ζ-potential, WCA, SFE, layer thickness (**Table 1**) and chemical composition (**Supplementary Table S2**) were evaluated.

The layer thickness was in the nanometer range (max. 165 nm). The APTES-modified surface layer was similar in thickness to the PEI and PPI-G4 layers. These layers are SAM arrangements, whereby the smaller thickness of the APTES layer correlates with the shorter molecular length of the APTES molecule compared with both the PEI and PPI-G4 molecule lengths. The molecular length of the RGD-conjugated APTES molecule is slightly longer than the APTES molecule itself. However, it is unlikely that an RGD molecule is coupled to every amino group on APTES. It therefore seems possible that individual RGD molecules are not necessarily aligned completely orthogonal to the surface as it is the case in a perfect SAM arrangement. In addition, interactions like hydrogen bonding between amino groups on APTES and residual amino acids of the RGD may possibly lead to a "bending" of the RGD molecules and consequently to a

**TABLE 2** | $Ca^{2+}$ mobilization results related to surface characteristics of chemically modified Ti (mean ± SD, $n = 3$ for surface characteristics; mean ± sem, $n \leq 3$ for $Ca^{2+}$ values).

| Surface | PSS | Ti | Matrigel | Col I | RGD | APTES | PPAAm | PEI | PPI-G4 | PDADMA |
|---|---|---|---|---|---|---|---|---|---|---|
| ζ [mV] | −88.8 ± 12 | −87.5 ± 2 | −43.3 ± 1 | −2.8 ± 1 | 1.7 ± 1 | 1.9 ± 1 | 7.1 ± 3 | 9.1 ± 3 | 50.2 ± 6 | 51.4 ± 4 |
| $MFI_B$ | 216.4 ± 40 | 445.1 ± 18 | 329.6 ± 20 | 575.3 ± 44 | 683.6 ± 60 | 918.5 ± 72 | 656.6 ± 32 | 412 ± 35 | 769.8 ± 63 | 221.5 ± 28 |
| $MFI_A$ | 523.4 ± 107 | 1040 ± 53 | 791 ± 72 | 1037.5 ± 97 | 1484.3 ± 123 | 2310.9 ± 157 | 1461.4 ± 58 | 1232.4 ± 104 | 691.8 ± 54 | 300.6 ± 37 |
| Slope | 307.1 ± 134 | 594.9 ± 71 | 461.3 ± 104 | 462.2 ± 105 | 800.7 ± 126 | 1392.4 ± 169 | 804.8 ± 53 | 820.4 ± 138 | −78.0 ± 17 | 79.1 ± 18 |
| WCA [°] | 62.3 ± 3 | 87.4 ± 1 | 69.6 ± 7 | 50.5 ± 4 | 74.9 ± 1 | 88.1 ± 4 | 66.9 ± 2 | 27.6 ± 2 | 47.2 ± 4 | 38.7 ± 3 |
| SFE [mN/m] | 49.3 ± 2 | 37.6 ± 1 | 46.7 ± 5 | 58.6 ± 3 | 43.0 ± 2 | 37.0 ± 3 | 46.2 ± 1 | 74.3 ± 2 | 62.4 ± 4 | 62.0 ± 3 |

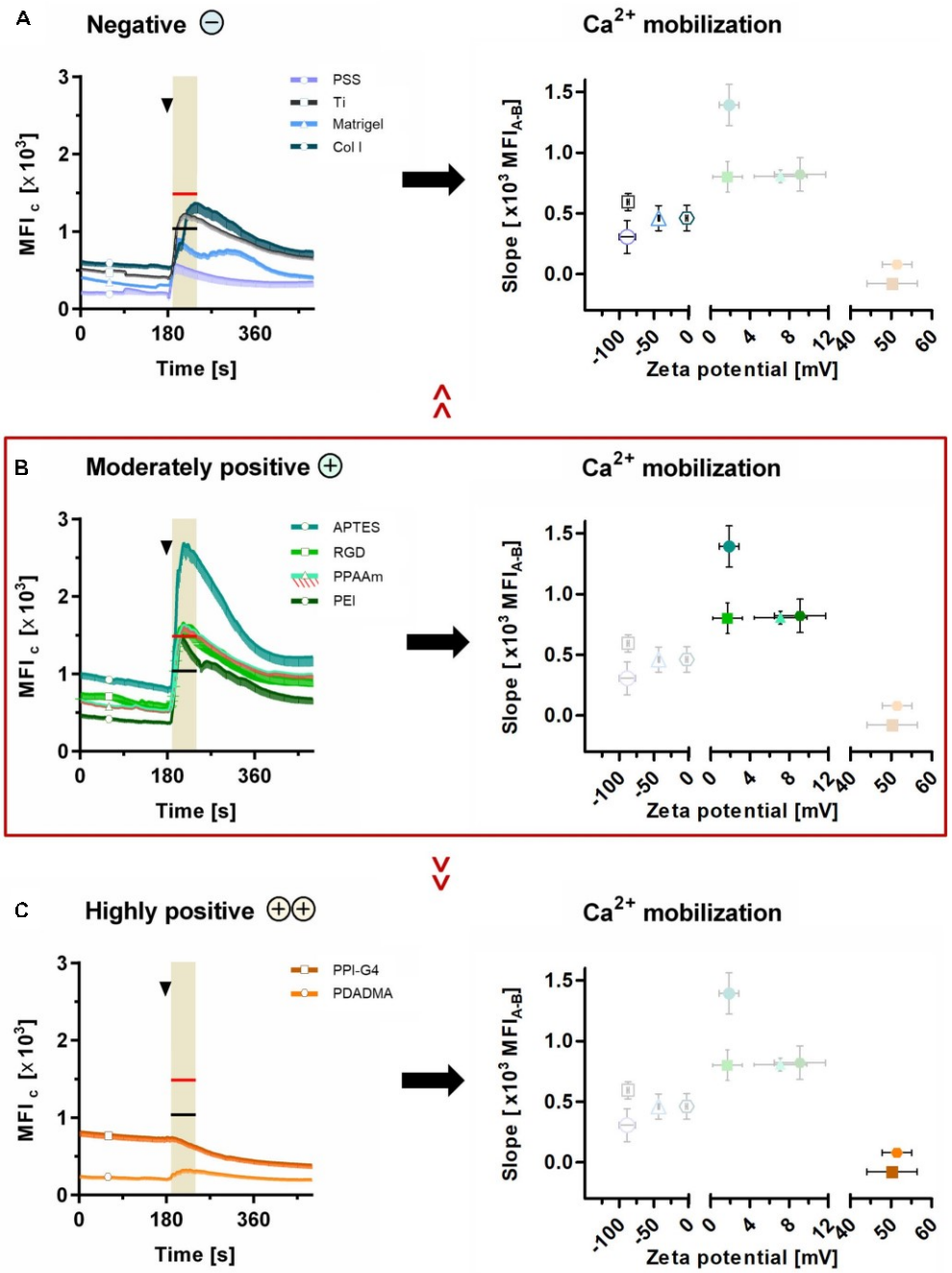


**FIGURE 6** | $Ca^{2+}$ mobilization results related to ζ-potential. Presented are (i) the mean fluorescence intensity of cells ($MFI_C$) after 24 h on surfaces with **(A)** negative, **(B)** moderately positive and **(C)** highly positive ζ-potentials compared with the mean fluorescence intensity after ATP stimulation ($MFI_A$) of cells on Ti (black lines at time points 170–240 s in highlighted area) and PPAAm (red lines at time points 170–240 s in highlighted area), and (ii) the correlation of the $Ca^{2+}$ mobilization (slope) with the materials' ζ-potentials. Note that the slope of the $Ca^{2+}$ mobilization curve is strongly dependent on ζ-potential values. Here, the surfaces with moderately positive ζ-potentials indicate a beneficial impact. ($Ca^{2+}$ signaling: mean ± sem, $n \geq 3$ independent approaches, per time point ≥ 30 cells for modifications and 190 cells for Ti and PPAAm controls, arrowheads at 180 s indicate ATP stimulation). PSS, poly(styrene sulfonate); Ti, titanium; Col I, collagen-type I; APTES, (3-aminopropyl)triethoxysilan; RGD, peptide sequence Arg-Gly-Asp; PPAAm, plasma polymerized allylamine; PEI, poly(ethylene imine); PPI-G4, poly(propylene imine) dendrimer generation 4; PDADMA, poly(diallyldimethylammonium chloride).

reduction of the overall layer thickness. Regarding PPAAm coatings, it must be emphasized that PPAAm is a very complex, highly cross-linked structure, which was presented here only in a very simplified and model-like schematic manner (see **Figure 1**). The thickness of PPAAm, as well as Col I, Matrigel, and the polyelectrolyte multilayer coatings is mainly

determined by the individual material properties and the process parameters.

The wettability analysis demonstrated a change to more hydrophilic surfaces. There is evidence that mammalian cells favor modestly hydrophilic surfaces displaying water contact angles between 40° and 65° (Rebl et al., 2012; Ahn et al., 2014; Gentleman and Gentleman, 2014). However, Gentleman and Gentleman (2014) reviewed that studies often lack a clear trend of cell behavior with wettability. They rather assumed SFE to be the more relevant feature for cellular behavior. This could not, however, be confirmed here. We could neither find a connection between WCA and SFE to the surface charge which is consistent with Olsson et al. (1995), nor a correlation with the cell behavior.

The ζ-potential could rather be the pivotal parameter for controlling cell physiology in osteoblasts, as our results indicate. In whole bone tissue negative ζ-potentials could be determined (Skalak and Shu, 1986; Otter et al., 1988; Chakkalakal, 1989). In this study, ζ-potentials of the investigated surface modifications were identified in the range of −90 to −3 mV (PSS < Ti < Matrigel < Col I), +1 to +10 mV (RGD < APTES < PPAAm < PEI) and ~+50 mV (PPI-G4 < PDADMA). For the first time, we were able to classify the ζ-potential into three categories with regard to an improved cell response on the respective surfaces and introduce the following terms: negative < moderately positive > highly positive.

## ζ-Potential – A Parameter for Surface Charge – Can Strongly Influence Cellular Behavior

It is known that physiology features of MG-63s such as actin cytoskeleton organization (Staehlke et al., 2015), viability (Staehlke et al., 2018) or proliferation (Labelle et al., 2007) are reflected by intracellular $Ca^{2+}$ dynamics. However, to our knowledge there is no literature on intracellular $Ca^{2+}$ dynamics in the context of the ζ-potential of biomaterials other than our previously published study comparing surfaces with negative ζ-potential with positive charges of plasma polymer nanolayers (PPAAm). The question remained, if positive charges in general promote the cellular outcome.

In order to gain deeper insights into the effect of surface charges on $Ca^{2+}$ dynamics, we analyzed the intracellular $Ca^{2+}$ signals before ($MFI_B$) and after ATP stimulation ($MFI_A$) on surface modifications with various charges using confocal laser scanning microscopy (**Figure 5** and **Supplementary Figure S5**). Additionally, cell morphology (**Figure 2**), cell viability (**Figure 3** and **Supplementary Figure S1**) and cell proliferation (**Supplementary Figure S2**) were investigated on selected surfaces. In the following, our results are discussed regarding negative, moderately and highly positive ζ-potentials.

## Negative ζ-Potential (– 90 to – 3 mV)

On our surfaces with negative ζ-potential we found evidence of reduced $Ca^{2+}$ mobilization after 24 h compared with surfaces with moderately positive ζ-potential. On PSS terminated PEM surfaces, MG-63s showed one of the lowest $Ca^{2+}$ slopes after 24 h. Other studies documented that hMSC cell numbers after 2, 5, and 7 days were consistently lower on PSS terminated PEM films than on control surfaces (Liao et al., 2010). However, PSS ending films exhibited good biocompatibility, as shown for SaOS-2 cells (cytokine IL-8 production) (Tryoen-Tóth et al., 2002), at least for films consisting of not more than six polyelectrolyte layers (Arias et al., 2016).

## Moderately Positive ζ-Potential (+1 to +10 mV)

Surfaces in the moderately positively charged range were found to promote the cell physiology via $Ca^{2+}$ mobilization. Cells can access their intracellular $Ca^{2+}$ stores more effectively after an external stimulus (here: ATP) than cells on negatively charged substrates, suggesting higher cell activities.

Ravenscroft-Chang et al. (2010) loaded primary cardiac myocytes growing on (3-trimethoxysilylpropyl) diethylenetriamine (DETA) silane modified and fluorinated glass substrates with fura-2 AM and induced a $Ca^{2+}$ signal by electrical stimulation (1 HZ, 6 V, 5 ms/pulse). Cells exhibited a significantly higher $Ca^{2+}$ level, as shown in higher amplitude and duration. However, the authors did not determine the ζ-potential of their surfaces. But a slightly positive ζ-potential at pH 7.4 of such DETA amino silane treated glass surfaces was measured earlier by Metwalli et al. (2006) supporting the idea of higher cellular activity on the basis of moderately positive charges.

For PEI functionalized surfaces it is known that cytotoxicity can exist depending on the molecular weight and concentration (Brunot et al., 2007). However, in studies with surfaces derived from low molecular weight PEI, as used here (25 kDa), no cytotoxic effects were reported for fibroblasts up to 7 days (Hernandez-Montelongo et al., 2017). PEI modification could further improve proliferation and function of MG-63s (Liu et al., 2009), as indicated here by an increased $Ca^{2+}$ slope.

RGD peptide motifs covalently bonded to Ti surfaces promote osteoblast attachment and survival (Secchi et al., 2007). El-Ghannam et al. (2004) showed that APTES-RGD coatings provided the optimal surface for cell adhesion, spreading, and cytoskeletal organization for MC3T3-El cells, better than RGD and APTES alone. It must be taken into consideration that surfaces modified with RGD (as well as Col I and Col IV and laminin containing Matrigel) can trigger $Ca^{2+}$ mobilization through integrin mediated "outside-in" signal transduction during cell adhesion (Sjaastad and Nelson, 1997; Boraschi-Diaz et al., 2017). After 24 h cultivation, however, integrin signaling may no longer be that influential in this case, as no additional stimulus such as mechanical stress (Pommerenke et al., 2002) was applied. Otherwise an increased $Ca^{2+}$ mobilization on these ECM coated surfaces would be expected. Here, we found that APTES alone was capable of mobilizing $Ca^{2+}$ in MG-63s even more than PPAAm – surfaces that do not present integrin ligands.

Lee et al. (2018) presented ATPES-treated PDMS concave microwell surfaces to cortical neurons which revealed optimal surface conditions additionally supporting a spheroid formation. The authors also stimulated the cells with KCl for spontaneous calcium transients (fluo-4 AM), observing typical temporal $Ca^{2+}$ responses in all chemically modified microwells based on APTES (APTES, APTES-Laminin, APTES-poly-L-lysine, APTES-carbon nanotubes).

### Highly Positive ζ-Potentials (~ +50 mV)

On PPI-G4 and PDADMA surfaces with highly positive ζ-potentials we discovered a restricted cell viability, reflected in an impaired $Ca^{2+}$ mobilization and a disturbed cell morphology and proliferation after 24 h, indicating that cells cannot tolerate such ζ-potentials.

Koch et al. (2018) produced the 11-amino acid self-assembling peptides P11-8 and P11-28/29 hydrogels exhibiting ζ-potentials of ~ + 20 mV and ~ + 60 mV at pH 7.0, respectively. HPDLF and HCO cells on highly positive P11-28/29 surfaces showed reduced cell area after 24 h, while cells on P11-8 displayed also enhanced osteogenic differentiation (ALP activity) compared with hydrogels containing negatively charged glutamic acids. Similarly, Kidambi et al. (2004) reported that primary hepatocytes were unable to remain attached to PEM films with PDADMA as the outermost layer. Inactive cells completely lifted off the surface by day 7 where liver-specific functions approached zero. In our previous study (Gruening et al., 2020) we found an impeded cell spreading dynamic on PDADMA surfaces after an initial tendency to spread better than Ti. The longer the influence of strongly positive charges on the cells, the more the cells were hampered.

Guo et al. (2018) pointed out that on positively charged non-cross-linked PEI films (ζ-potential: + 50 and +62 mV) more fibroblasts could adhere within the first 24 h compared with negatively charged polymer films. But, on the second day, cells on the negatively charged surfaces proliferated well, in contrast to those on samples with high ζ-potentials. The authors argued that this was due to the reported cytotoxicity of PEI. But by cross-linking these PEI films, the high ζ-potential was reduced to ~ + 20 mV and cells proliferated on all surfaces.

During the cell cycle, checkpoints in G1 and G2 (gap) phases prevent cells from entering into the next phase in case of cell injury e.g., due to accumulation of reactive oxygen species (ROS) (Muller et al., 2007) or inadequate environmental conditions such as bacterial infection (Kato et al., 2008), hypoxia (Zou et al., 2015) or withdrawal of nutrition (Blagosklonny, 2011). Cells which do not pass the safety controls proceed with the non-proliferative G0/G1 phase in quiescence (cell cycle arrest) or even permanent senescence (Blagosklonny, 2011; Terzi et al., 2016). We found an increasing cell amount in the G1 phase on highly positive surfaces, leading to a decline of cellular proliferation. In further experiments it is to be examined whether the high surface charges lead to an elevated ROS production as stress response and thus to a cell cycle arrest, allowing cells to cope with their environment.

However, the high surface charge leads to an intense interaction with the negatively charged cell surface (Rebl et al., 2016), which is further considered to cause damaged lipid bilayers due to new vesicular structures around the cationic molecules which create holes in the cell membrane (Mecke et al., 2005). This could be supported by the live/dead staining, demonstrating an abolished membrane integrity in still vital cells on PPI-G4 and PDADMA.

The adverse effects of highly positive surface charges deduced from the ζ-potential might also be indirectly linked to protein adsorption, since it has been published that the protein adsorption is strongly affected by the ζ-potential (Krajewski et al., 1998; Lehnfeld et al., 2020) influencing the protein population (Shelton et al., 1988) and orientation (Norde and Lyklema, 1991; Antonini et al., 2014). Therefore, a further correlation between protein adsorption and ζ-potential of different surface modifications with well-defined effects on the cell behavior is of great interest.

## CONCLUSION

This is the largest systematic study so far documenting the importance of the materials' surface charge deduced from ζ-potential for the intracellular $Ca^{2+}$ dynamics and viability of human osteoblasts. Positive charges offer unique cues that induce an intensive cell response. But interestingly, we identified that cells favor only a certain range of moderately positive surface charges and not a positively charged surface in general. The ζ-potential appears to be a key property of biomaterial surfaces dominating the relevance of wettability (WCA, SFE), and should be considered in biomaterial coating design in tissue engineering and dental and orthopedic implantology.

## DATA AVAILABILITY STATEMENT

The datasets presented in this study can be found in online repositories. The names of the repository/repositories and accession number(s) can be found below: Mendeley data doi: 10.17632/h8rs6v4dgt.1.

## AUTHOR CONTRIBUTIONS

MG: conceptualization, investigation, validation, visualization, and original draft preparation. SN: PEM preparation. PN: layer thickness measurement and review and editing. KF: XPS measurement and PPAAm preparation. MD: APTES and RGD preparation. JL: PEI and PPI-G4 preparation and review and editing. MS: visualization and review and editing. CH and RM: review and editing and funding acquisition. SS: ATP receptor immunofluorescence and review and editing. JBN: conceptualization, review and editing, project administration, and funding acquisition. All authors contributed to the article and approved the submitted version.

## FUNDING

This project was supported by the Deutsche Forschungsgemeinschaft (DFG, German Research Foundation) – Collaborative Research Center (CRC) 1270/1 ELAINE – 299150580. JL was supported by the Fonds der Chemischen Industrie (FCI) with the Chemiefonds Fellowship.

## ACKNOWLEDGMENTS

We thank Dr. Marcus Frank and Dr. Armin Springer (Electron Microscopy Center, University Medical Center Rostock) concerning SEM sample preparation and the cooperation with Dipl.-Ing. Norbert Zichner (Center for Microtechnologies, TU Chemnitz) concerning the production of the titanium-coated materials. We acknowledge Petra Seidel (Cell Biology, University Medical Center Rostock) for her technical assistance concerning MTS assay, Dr. Matthias Kronseder (Physics, University of Regensburg) for XPS analyses of PEI and PPI-G4, and Dr. Frank Krueger (Communications Engineering, University of Rostock) for providing the digital laboratory book eLab-FTW within the CRC ELAINE.

## SUPPLEMENTARY MATERIAL

The Supplementary Material for this article can be found online at: https://www.frontiersin.org/articles/10.3389/fbioe.2020.01016/full#supplementary-material

## REFERENCES

Abalymov, A., Van der Meeren, L., Skirtach, A. G., and Parakhonskiy, B. V. (2020). Identification and analysis of key parameters for the ossification on particle functionalized composites hydrogel materials. *ACS Appl. Mater. Interf.* 2020:acsami.0c06641. doi: 10.1021/acsami.0c06641

Ahn, H., Lee, I., Lee, H., and Kim, M. (2014). Cellular behavior of human adipose-derived stem cells on wettable gradient polyethylene surfaces. *Int. J. Mol. Sci.* 15, 2075–2086. doi: 10.3390/ijms15022075

Akter, F., and Ibanez, J. (2016). Bone and cartilage tissue engineering. *Tissue Eng. Made Easy* 2016, 77–97. doi: 10.1016/B978-0-12-805361-4.00008-4

Altankov, G., Richau, K., and Groth, T. (2003). The role of surface zeta potential and substratum chemistry for regulation of dermal fibroblasts interaction. *Materwiss. Werksttech.* 34, 1120–1128. doi: 10.1002/mawe.200300699

Anselme, K., Ponche, A., and Bigerelle, M. (2010). Relative influence of surface topography and surface chemistry on cell response to bone implant materials. Part 2: biological aspects. *Proc. Inst. Mech. Eng. H* 224, 1487–1507. doi: 10.1243/09544119JEIM901

Antonini, V., Torrengo, S., Marocchi, L., Minati, L., Serra, M. D., Bao, G., et al. (2014). Combinatorial plasma polymerization approach to produce thin films for testing cell proliferation. *Coll. Surf. B Biointerf.* 113, 320–329. doi: 10.1016/J.COLSURFB.2013.09.020

Arias, C. J., Surmaitis, R. L., and Schlenoff, J. B. (2016). Cell adhesion and proliferation on the "living" surface of a polyelectrolyte multilayer. *Langmuir* 32, 5412–5421. doi: 10.1021/acs.langmuir.6b00784

Bacakova, L., Filova, E., Parizek, M., Ruml, T., and Svorcik, V. (2011). Modulation of cell adhesion, proliferation and differentiation on materials designed for body implants. *Biotechnol. Adv.* 29, 739–767. doi: 10.1016/J.BIOTECHADV.2011.06.004

Bacakova, L., Svorcik, V., Rybka, V., Micek, I., Hnatowicz, V., Lisa, V., et al. (1996). Adhesion and proliferation of cultured human aortic smooth muscle cells on polystyrene implanted with N+, F+ and Ar+ ions: correlation with polymer surface polarity and carbonization. *Biomaterials* 17, 1121–1126. doi: 10.1016/0142-9612(96)85914-X

Blagosklonny, M. V. (2011). Cell cycle arrest is not senescence. *Aging* 3, 94–101. doi: 10.18632/aging.100281

Boraschi-Diaz, I., Wang, J., Mort, J. S., and Komarova, S. V. (2017). Collagen Type I as a Ligand for receptor-mediated signaling. *Front. Phys.* 5:12. doi: 10.3389/fphy.2017.00012

Brunot, C., Ponsonnet, L., Lagneau, C., Farge, P., Picart, C., and Grosgogeat, B. (2007). Cytotoxicity of polyethyleneimine (PEI), precursor base layer of polyelectrolyte multilayer films. *Biomaterials* 28, 632–640. doi: 10.1016/J.BIOMATERIALS.2006.09.026

Cao, C., Song, Y., Yao, Q., Yao, Y., Wang, T., Huang, B., et al. (2015). Preparation and preliminary *in vitro* evaluation of a bFGF-releasing heparin-conjugated poly(ε-caprolactone) membrane for guided bone regeneration. *J. Biomater. Sci. Polym. Edn.* 26, 600–616. doi: 10.1080/09205063.2015.1049044

Chakkalakal, D. A. (1989). Mechanoelectric transduction in bone. *J. Mater. Res.* 4, 1034–1046. doi: 10.1557/JMR.1989.1034

Chang, H.-Y., Huang, C.-C., Lin, K.-Y., Kao, W.-L., Liao, H.-Y., You, Y.-W., et al. (2014). Effect of surface potential on NIH3T3 cell adhesion and proliferation. *J. Phys. Chem. C* 118, 14464–14470. doi: 10.1021/jp504662c

Chen, S., Guo, Y., Liu, R., Wu, S., Fang, J., Huang, B., et al. (2018). Tuning surface properties of bone biomaterials to manipulate osteoblastic cell adhesion and the signaling pathways for the enhancement of early osseointegration. *Coll. Surf. B Biointerf.* 164, 58–69. doi: 10.1016/J.COLSURFB.2018.01.022

Clover, J., and Gowen, M. (1994). Are MG-63 and HOS TE85 human osteosarcoma cell lines representative models of the osteoblastic phenotype? *Bone* 15, 585–591. doi: 10.1016/8756-3282(94)90305-0

Cohen, M., Joester, D., Geiger, B., and Addadi, L. (2004). Spatial and temporal sequence of events in cell adhesion: from molecular recognition to focal adhesion assembly. *Chembiochem* 5, 1393–1399. doi: 10.1002/cbic.200400162

Czekanska, E. M., Stoddart, M. J., Ralphs, J. R., Richards, R. G., and Hayes, J. S. (2014). A phenotypic comparison of osteoblast cell lines versus human primary osteoblasts for biomaterials testing. *J. Biomed. Mater. Res. Part A* 102, 2636–2643. doi: 10.1002/jbm.a.34937

De Aza, P. N., Luklinska, Z. B., Santos, C., Guitian, F., and De Aza, S. (2003). Mechanism of bone-like formation on a bioactive implant in vivo. *Biomaterials* 24, 1437–1445. doi: 10.1016/S0142-9612(02)00530-6

Devgan, S., and Sidhu, S. S. (2019). Evolution of surface modification trends in bone related biomaterials: a review. *Mater. Chem. Phys.* 233, 68–78. doi: 10.1016/J.MATCHEMPHYS.2019.05.039

Dhowre, H. S., Rajput, S., Russell, N. A., and Zelzer, M. (2015). Responsive cell-material interfaces. *Nanomedicine* 10, 849–871. doi: 10.2217/nnm.14.222 Eichler, M., Katzur, V., Scheideler, L., Haupt, M., Geis-Gerstorfer, J., Schmalz, G., et al. (2011). The impact of dendrimer-grafted modifications to model silicon surfaces on protein adsorption and bacterial adhesion. *Biomaterials* 32, 9168–9179. doi: 10.1016/J.BIOMATERIALS.2011.08.063

El-Ghannam, A. R., Ducheyne, P., Risbud, M., Adams, C. S., Shapiro, I. M., Castner, D., et al. (2004). Model surfaces engineered with nanoscale roughness and RGD tripeptides promote osteoblast activity. *J. Biomed. Mater. Res.* 68A, 615–627. doi: 10.1002/jbm.a.20051

Felgueiras, H. P., Antunes, J. C., Martins, M. C. L., and Barbosa, M. A. (2018). Fundamentals of protein and cell interactions in biomaterials. *Pept. Proteins Biomater. Tissue Regen. Repair* 88, 956–970. doi: 10.1016/B978-0-08-100803-4.00001-2

Fernández-Yagüe, M., Antoñanzas, R. P., Roa, J. J., Biggs, M., Gil, F. J., and Pegueroles, M. (2019). Enhanced osteoconductivity on electrically charged titanium implants treated by physicochemical surface modifications methods. *Nanomed. Nanotechnol. Biol. Med.* 18, 1–10. doi: 10.1016/J.NANO.2019.02.005

Ferrari, M., Cirisano, F., and Morán, M. C. (2019). Mammalian cell behavior on hydrophobic substrates: influence of surface properties. *Colloids Interf.* 3:48. doi: 10.3390/colloids3020048

Ferraris, S., Cazzola, M., Peretti, V., Stella, B., and Spriano, S. (2018). Zeta potential measurements on solid surfaces for in vitro biomaterials testing: surface charge, reactivity upon contact with fluids and protein absorption. *Front. Bioeng. Biotechnol.* 6:60. doi: 10.3389/fbioe.2018.00060

Finke, B., Luethen, F., Schroeder, K., Mueller, P. D., Bergemann, C., Frant, M., et al. (2007). The effect of positively charged plasma polymerization on initial osteoblastic focal adhesion on titanium surfaces. *Biomaterials* 28, 4521–4534. doi: 10.1016/J.BIOMATERIALS.2007.06.028

Finke, B., Rebl, H., Hempel, F., Schäfer, J., Liefeith, K., Weltmann, K.-D., et al. (2014). Aging of plasma-polymerized allylamine nanofilms and the maintenance of their cell adhesion capacity. *Langmuir* 30, 13914–13924. doi: 10.1021/la5019778

Fritsche, A., Haenle, M., Zietz, C., Mittelmeier, W., Neumann, H.-G., Heidenau, F., et al. (2009). Mechanical characterization of anti-infectious, anti-allergic, and bioactive coatings on orthopedic implant surfaces. *J. Mater. Sci.* 44, 5544–5551. doi: 10.1007/s10853-009-3776-1

Gentleman, M. M., and Gentleman, E. (2014). The role of surface free energy in osteoblast-biomaterial interactions. *Int. Mater. Rev.* 59, 417–429. doi: 10.1179/1743280414Y.0000000038

Goldenberg, N. M., and Steinberg, B. E. (2010). Surface charge: a key determinant of protein localization and function. *Cancer Res.* 70, 1277–1280. doi: 10.1158/0008-5472.CAN-09-2905

Gruening, M., Neuber, S., Fricke, K., Helm, C. A., and Nebe, B. (2020). Cell-material interaction - spreading course correlates with surface charge. *Am. J. Biomed. Sci. Res.* 9, 4–6. doi: 10.34297/AJBSR.2020.09.001341

Guo, S., Kwek, M. Y., Toh, Z. Q., Pranantyo, D., Kang, E.-T., Loh, X. J., et al. (2018). Tailoring polyelectrolyte architecture to promote cell growth and inhibit bacterial adhesion. *ACS Appl. Mater. Interf.* 10, 7882–7891. doi: 10.1021/acsami.8b00666

Hanawa, T. (2019). Titanium-tissue interface reaction and its control with surface treatment. *Front. Bioeng. Biotechnol.* 7:170. doi: 10.3389/fbioe.2019.00170

Heo, W., Do Inoue, T., Park, W. S., Kim, M. L., Park, B. O., Wandless, T. J., et al. (2006). PI(3,4,5)P3 and PI(4,5)P2 lipids target proteins with polybasic clusters to the plasma membrane. *Science* 314, 1458–1461. doi: 10.1126/SCIENCE.1134389

Hernandez-Montelongo, J., Lucchesi, E. G., Nascimento, V. F., França, C. G., Gonzalez, I., Macedo, W. A. A., et al. (2017). Antibacterial and non-cytotoxic ultra-thin polyethylenimine film. *Mater. Sci. Eng. C* 71, 718–724. doi: 10.1016/J.MSEC.2016.10.064

Hoene, A., Walschus, U., Patrzyk, M., Finke, B., Lucke, S., Nebe, B., et al. (2010). In vivo investigation of the inflammatory response against allylamine plasma polymer coated titanium implants in a rat model. *Acta Biomater.* 6, 676–683. doi: 10.1016/J.ACTBIO.2009.09.003

Iwai, R., Nemoto, Y., and Nakayama, Y. (2013). The effect of electrically charged polyion complex nanoparticle-coated surfaces on adipose-derived stromal progenitor cell behaviour. *Biomaterials* 34, 9096–9102. doi: 10.1016/J.BIOMATERIALS.2013.08.027

Kato, T., Tsuda, T., Inaba, H., Kawai, S., Okahashi, N., Shibata, Y., et al. (2008). Porphyromonas gingivalis gingipains cause G(1) arrest in osteoblastic/stromal cells. *Oral Microbiol. Immunol.* 23, 158–164. doi: 10.1111/j.1399-302X.2007.00405.x

Katzur, V., Eichler, M., Deigele, E., Stage, C., Karageorgiev, P., Geis-Gerstorfer, J., et al. (2012). Surface-immobilized PAMAM-dendrimers modified with cationic or anionic terminal functions: physicochemical surface properties and conformational changes after application of liquid interface stress. *J. Coll. Interf. Sci.* 366, 179–190. doi: 10.1016/J.JCIS.2011.09.029

Kennedy, S. B., Washburn, N. R., Simon, C. G., and Amis, E. J. (2006). Combinatorial screen of the effect of surface energy on fibronectin-mediated osteoblast adhesion, spreading and proliferation. *Biomaterials* 27, 3817–3824. doi: 10.1016/J.BIOMATERIALS.2006.02.044

Kidambi, S., Ilsoon, L., and Chan, C. (2004). Controlling primary hepatocyte adhesion and spreading on protein-free polyelectrolyte multilayer films. *J. Am. Chem. Soc.* 126, 16286–16287. doi: 10.1021/JA046188U

Koch, F., Wolff, A., Mathes, S., Pieles, U., Saxer, S., Kreikemeyer, B., et al. (2018). Amino acid composition of nanofibrillar self-assembling peptide hydrogels affects responses of periodontal tissue cells in vitro. *Int. J. Nanomed.* 13, 6717–6733. doi: 10.2147/IJN.S173702

Kokubo, T., and Yamaguchi, S. (2015). Growth of novel ceramic layers on metals via chemical and heat treatments for inducing various biological functions. *Front. Bioeng. Biotechnol.* 3:176. doi: 10.3389/fbioe.2015.00176

Krajewski, A., Piancastelli, A., and Malavolti, R. (1998). Albumin adhesion on ceramics and correlation with their Z-potential. *Biomaterials* 19, 637–641. doi: 10.1016/S0142-9612(97)00153-1

Kumar, P. S., Sathesh, K., Grandhi, V. V., and Gupta, V. (2019). The effects of titanium implant surface topography on osseointegration: literature review. *JMIR Biomed. Eng.* 4:e13237. doi: 10.2196/13237

Labelle, D., Jumarie, C., and Moreau, R. (2007). Capacitative calcium entry and proliferation of human osteoblast-like MG-63 cells. *Cell Prolif.* 40, 866–884. doi: 10.1111/j.1365-2184.2007.00477.x

Lee, G., Lim, J., Park, J., Lee, W., Yoon, D. S., Kim, S. H., et al. (2018). Construction of neurospheroids via surface modified concave microwells. *J. Ind. Eng. Chem.* 62, 341–351. doi: 10.1016/J.JIEC.2018.01.014

Lee, J. H., Jung, H. W., Kang, I.-K., and Lee, H. B. (1994). Cell behaviour on polymer surfaces with different functional groups. *Biomaterials* 15, 705–711. doi: 10.1016/0142-9612(94)90169-4

Lehnfeld, J., Gruening, M., Kronseder, M., and Mueller, R. (2020). Comparison of protein-repellent behavior of linear versus dendrimer-structured surface-immobilized polymers. *Langmuir* 2020:acs.langmuir.0c00625. doi: 10.1021/acs.langmuir.0c00625

Lesný, P., P˘rádný, M., Jendelová, P., Michálek, J., Vacík, J., and Syková, E. (2006). Macroporous hydrogels based on 2-hydroxyethyl methacrylate. Part 4: growth of rat bone marrow stromal cells in three-dimensional hydrogels with positive and negative surface charges and in polyelectrolyte complexes. *J. Mater. Sci. Mater. Med.* 17, 829–833. doi: 10.1007/s10856-006-9842-1

Liao, T., Moussallem, M. D., Kim, J., Schlenoff, J. B., and Ma, T. (2010). N-isopropylacrylamide-based thermoresponsive polyelectrolyte multilayer films for human mesenchymal stem cell expansion. *Biotechnol. Prog.* 26, 1705–1713. doi: 10.1002/btpr.471

Liu, Q., Ding, J., Mante, F. K., Wunder, S. L., and Baran, G. R. (2002). The role of surface functional groups in calcium phosphate nucleation on titanium foil: a self-assembled monolayer technique. *Biomaterials* 23, 3103–3111. doi: 10.1016/S0142-9612(02)00050-9

Liu, Z.-M., Lee, S.-Y., Sarun, S., Peschel, D., and Groth, T. (2009). Immobilization of poly (ethylene imine) on poly (l-lactide) promotes MG63 cell proliferation and function. *J. Mater. Sci. Mater. Med.* 20, 2317–2326. doi: 10.1007/s10856-009-3806-1

Mecke, A., Majoros, I. J., Patri, A. K., Baker, J. R., Banaszak Holl, M. M., and Orr, B. G. (2005). Lipid bilayer disruption by polycationic polymers:? the roles of size and chemical functional group. *Langmuir* 21, 10348–10354. doi: 10.1021/la050629l

Metwalli, E., Haines, D., Becker, O., Conzone, S., and Pantano, C. G. (2006). Surface characterizations of mono-, di-, and tri-aminosilane treated glass substrates. *J. Coll. Interf. Sci.* 298, 825–831. doi: 10.1016/J.JCIS.2006.03.045

Metwally, S., and Stachewicz, U. (2019). Surface potential and charges impact on cell responses on biomaterials interfaces for medical applications. *Mater. Sci. Eng. C* 104:109883. doi: 10.1016/J.MSEC.2019.109883

Moerke, C., Staehlke, S., Rebl, H., Finke, B., and Nebe, J. B. (2018). Restricted cell functions on micropillars are alleviated by surfacenanocoating with amino groups. *J. Cell Sci.* 131:jcs207001. doi: 10.1242/jcs.207001

Mohamad, H. S., Neuber, S., and Helm, C. A. (2019). Surface forces of asymmetrically grown polyelectrolyte multilayers: searching for the charges. *Langmuir* 35, 15491–15499. doi: 10.1021/acs.langmuir.9b01787

Mörke, C., Rebl, H., Finke, B., Dubs, M., Nestler, P., Airoudj, A., et al. (2017). Abrogated cell contact guidance on amino-functionalized microgrooves. *ACS Appl. Mater. Interf.* 9, 10461–10471. doi: 10.1021/acsami.6b16430

Muderrisoglu, C., Saveleva, M., Abalymov, A., Van der Meeren, L., Ivanova, A., Atkin, V., et al. (2018). Nanostructured biointerfaces based on bioceramic calcium carbonate/hydrogel coatings on titanium with an active enzyme for stimulating osteoblasts growth. *Adv. Mater. Interf.* 5:1800452. doi: 10.1002/admi.201800452

Muller, F. L., Lustgarten, M. S., Jang, Y., Richardson, A., and Van Remmen, H. (2007). Trends in oxidative aging theories. *Free Radic. Biol. Med.* 43, 477–503. doi: 10.1016/J.FREERADBIOMED.2007.03.034

Müller, R., Abke, J., Schnell, E., Scharnweber, D., Kujat, R., Englert, C., et al. (2006). Influence of surface pretreatment of titanium- and cobalt-based biomaterials on covalent immobilization of fibrillar collagen. *Biomaterials* 27, 4059–4068. doi: 10.1016/J.BIOMATERIALS.2006.03.019

Nebe, B., Finke, B., Lüthen, F., Bergemann, C., Schröder, K., Rychly, J., et al. (2007). Improved initial osteoblast functions on amino-functionalized titanium surfaces. *Biomol. Eng.* 24, 447–454. doi: 10.1016/J.BIOENG.2007.07.004

Nebe, J. B., Rebl, H., Schlosser, M., Staehlke, S., Gruening, M., Weltmann, K.-D., et al. (2019). Plasma polymerized allylamine—the unique cell-attractive nanolayer for dental implant materials. *Polymers* 11:1004. doi: 10.3390/polym11061004

Nestler, P., Block, S., and Helm, C. A. (2012). Temperature-induced transition from odd-even to even-odd effect in polyelectrolyte multilayers due to

interpolyelectrolyte interactions. *J. Phys. Chem. B* 116, 1234–1243. doi: 10.1021/jp208837m

Nikkhah, M., Edalat, F., Manoucheri, S., and Khademhosseini, A. (2012). Engineering microscale topographies to control the cell-substrate interface. *Biomaterials* 33, 5230–5246. doi: 10.1016/J.BIOMATERIALS.2012.03.079

Norde, W., and Lyklema, J. (1991). Why proteins prefer interfaces. *J. Biomater. Sci. Polym. Edn.* 2, 183–202. doi: 10.1080/09205063.1991.9756659

Olsson, J., Carlén, A., Burns, N. L., and Holmberg, K. (1995). Modified pellicle formation and reduced in vitro bacterial adherence after surface treatment with different siloxane polymers. *Coll. Surf. B Biointerf.* 5, 161–169. doi: 10.1016/0927-7765(95)01212-2

Otter, M., Goheen, S., and Williams, W. S. (1988). Streaming potentials in chemically modified bone. *J. Orthop. Res.* 6, 346–359. doi: 10.1002/jor.1100060306

Padial-Molina, M., Galindo-Moreno, P., Fernández-Barbero, J. E., O'Valle, F., Jódar-Reyes, A. B., Ortega-Vinuesa, J. L., et al. (2011). Role of wettability and nanoroughness on interactions between osteoblast and modified silicon surfaces. *Acta Biomater.* 7, 771–778. doi: 10.1016/J.ACTBIO.2010.08.024

Pommerenke, H., Schmidt, C., Dürr, F., Nebe, B., Lüthen, F., Muller, P., et al. (2002). The mode of mechanical integrin stressing controls intracellular signaling in osteoblasts. *J. Bone Miner. Res.* 17, 603–611. doi: 10.1359/jbmr.2002.17.4.603

Ponsonnet, L., Reybier, K., Jaffrezic, N., Comte, V., Lagneau, C., Lissac, M., et al. (2003). Relationship between surface properties (roughness, wettability) of titanium and titanium alloys and cell behaviour. *Mater. Sci. Eng. C* 23, 551–560. doi: 10.1016/S0928-4931(03)00033-X

Ravenscroft-Chang, M. S., Stohlman, J. M., Molnar, P., Natarajan, A., Canavan, H. E., Teliska, M., et al. (2010). Altered calcium dynamics in cardiac cells grown on silane-modified surfaces. *Biomaterials* 31, 602–607. doi: 10.1016/J.BIOMATERIALS.2009.09.084

Rebl, H., Finke, B., Ihrke, R., Rothe, H., Rychly, J., Schroeder, K., et al. (2010). Positively charged material surfaces generated by plasma polymerized allylamine enhance vinculin mobility in vital human osteoblastss. *Adv. Eng. Mater.* 12, B356–B364. doi: 10.1002/adem.200980070

Rebl, H., Finke, B., Lange, R., Weltmann, K.-D., and Nebe, J. B. (2012). Impact of plasma chemistry versus titanium surface topography on osteoblast orientation. *Acta Biomater.* 8, 3840–3851. doi: 10.1016/J.ACTBIO.2012.06.015

Rebl, H., Finke, B., Schmidt, J., Mohamad, H. S., Ihrke, R., Helm, C. A., et al. (2016). Accelerated cell-surface interlocking on plasma polymer-modified porous ceramics. *Mater. Sci. Eng. C* 69, 1116–1124. doi: 10.1016/J.MSEC.2016.08.016

Rico, P., Hernández, J. C. R., Moratal, D., Altankov, G., Pradas, M. M., and Salmerón-Sánchez, M. (2009). Substrate-induced assembly of fibronectin into networks: influence of surface chemistry and effect on osteoblast adhesion. *Tissue Eng. Part A* 15, 3271–3281. doi: 10.1089/ten.tea.2009.0141

Schulz, A., Katsen-Globa, A., Huber, E. J., Mueller, S. C., Kreiner, A., Pütz, N., et al. (2018). Poly(amidoamine)-alginate hydrogels: directing the behavior of mesenchymal stem cells with charged hydrogel surfaces. *J. Mater. Sci. Mater. Med.* 29:105. doi: 10.1007/s10856-018-6113-x

Secchi, A. G., Grigoriou, V., Shapiro, I. M., Cavalcanti-Adam, E. A., Composto, R. J., Ducheyne, P., et al. (2007). RGDS peptides immobilized on titanium alloy stimulate bone cell attachment, differentiation and confer resistance to apoptosis. *J. Biomed. Mater. Res. Part A* 83A, 577–584. doi: 10.1002/jbm.a.31007

Shelton, R. M., Rasmussen, A. C., and Davies, J. E. (1988). Protein adsorption at the interface between charged polymer substrata and migrating osteoblasts. *Biomaterials* 9, 24–29. doi: 10.1016/0142-9612(88)90065-8

Sjaastad, M. D., and Nelson, W. J. (1997). Integrin-mediated calcium signaling and regulation of cell adhesion by intracellular calcium. *Bioessays* 19, 47–55. doi: 10.1002/bies.950190109

Skalak, R., and Shu, C. (1986). *Electromechanical Effects in Bone. Handb. Bioeng*. Available online at: https://www.ideals.illinois.edu/handle/2142/25222 (accessed April 14, 2020).

Staehlke, S., Koertge, A., and Nebe, B. (2015). Intracellular calcium dynamics dependent on defined microtopographical features of titanium. *Biomaterials* 46, 48–57. doi: 10.1016/J.BIOMATERIALS.2014.12.016

Staehlke, S., Rebl, H., Finke, B., Mueller, P., Gruening, M., and Nebe, J. B. (2018). Enhanced calcium ion mobilization in osteoblasts on amino group containing plasma polymer nanolayer. *Cell Biosci.* 8:22. doi: 10.1186/s13578-018-0220-8

Staehlke, S., Rebl, H., and Nebe, B. (2019). Phenotypic stability of the human MG-63 osteoblastic cell line at different passages. *Cell Biol. Int.* 43, 22–32. doi: 10.1002/cbin.11073

Terzi, M. Y., Izmirli, M., and Gogebakan, B. (2016). The cell fate: senescence or quiescence. *Mol. Biol. Rep.* 43, 1213–1220. doi: 10.1007/s11033-016-4065-0

Tryoen-Tóth, P., Vautier, D., Haikel, Y., Voegel, J.-C., Schaaf, P., Chluba, J., et al. (2002). Viability, adhesion, and bone phenotype of osteoblast-like cells on polyelectrolyte multilayer films. *J. Biomed. Mater. Res.* 60, 657–667. doi: 10.1002/jbm.10110

von der Mark, K., and Park, J. (2013). Engineering biocompatible implant surfaces: Part II: cellular recognition of biomaterial surfaces: lessons from cell-matrix interactions. *Prog. Mater. Sci.* 58, 327–381. doi: 10.1016/J.PMATSCI.2012.09.002

Webb, K., Hlady, V., and Tresco, P. A. (1998). Relative importance of surface wettability and charged functional groups on NIH 3T3 fibroblast attachment, spreading, and cytoskeletal organization. *J. Biomed. Mater. Res.* 41, 422–430. doi: 10.1002/(SICI)1097-4636(19980905)41:3<422::AID-JBM12<3.0.CO;2-K

Wennerberg, A., and Albrektsson, T. (2009). Effects of titanium surface topography on bone integration: a systematic review. *Clin. Oral Implants Res.* 20, 172–184. doi: 10.1111/j.1600-0501.2009.01775.x

Zimmerman, E., Geiger, B., and Addadi, L. (2002). Initial stages of cell-matrix adhesion can be mediated and modulated by cell-surface hyaluronan. *Biophys. J.* 82, 1848–1857. doi: 10.1016/S0006-3495(02)75535-5

Zou, W., Yang, S., Zhang, T., Sun, H., Wang, Y., Xue, H., et al. (2015). Hypoxia enhances glucocorticoid-induced apoptosis and cell cycle arrest via the PI3K/Akt signaling pathway in osteoblastic cells. *J. Bone Miner. Metab.* 33, 615–624. doi: 10.1007/s00774-014-0627-1

**Conflict of Interest:** The authors declare that the research was conducted in the absence of any commercial or financial relationships that could be construed as a potential conflict of interest.

frontiers

# *Supplementary Material*

***Publikation V***

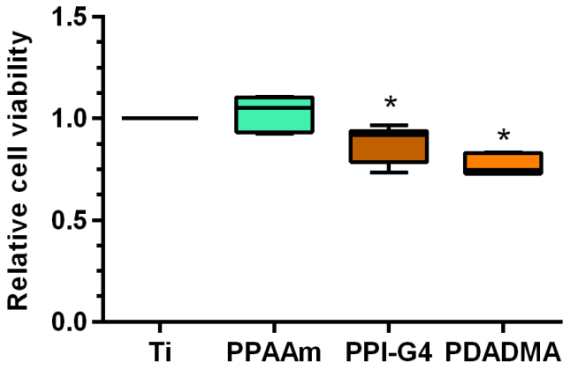


**Supplementary Figure S1.** Relative cell viability of MG-63s on highly positively charged PPI-G4 and PDADMA surfaces compared with Ti (negatively charged) and PPAAm (moderately positively charged) after 24 h. Presented are cell metabolism values based on MTS measurements. Values are related to the cell density deduced from crystal violet staining and normalized to the Ti control. Note that the relative cell viability of MG-63s on highly positively charged surfaces is significantly decreased in contrast to Ti and PPAAm. (Statistics: Nonparametric Wilcoxon matched pairs signed-rank test, *p > 0.05; median ± IQR with maximum and minimum; n = 3 independent experiments, Anthos reader).

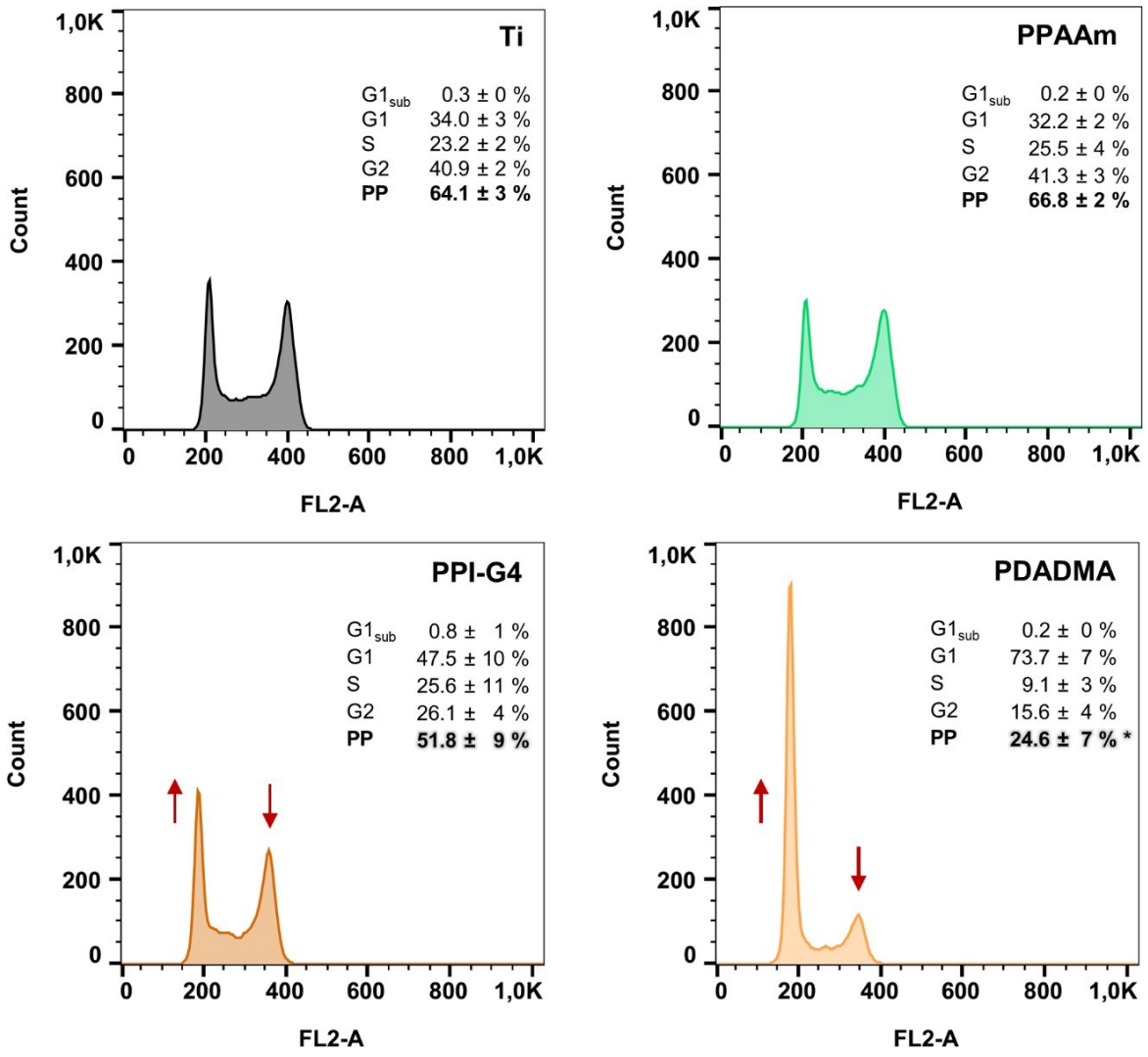


**Supplementary Figure S2.** Cell proliferation of MG-63 osteoblasts on highly positively charged PPI-G4 and PDADMA surfaces compared with the controls Ti (negatively charged) and PPAAm (moderately positively charged) after 24 h. Demonstrated are representative examples of cell cycle histograms of the respective surfaces and the proliferative phase (PP = S + G2), G1 and apoptosis peak ($G1_{sub}$) calculated from three independent experiments. Note the reduction of proliferative cells due to highly positive surface charges, while the cells increasingly remain in the G1 phase (indicated by red arrows). Late apoptotic events ($G1_{sub}$) could not be detected for all surfaces after 24 h. (Statistics: Nonparametric Kruskal-Wallis + Dunn´s multiple comparisons test, $p > 0.05$, * significant decrease compared with Ti and PPAAm; mean ± SD; n = 3, flow cytometer FACSCalibur).
(Abbreviations: PPI-G4, poly(propylene imine) dendrimer generation 4; PDADMA, poly(diallyldimethylammonium chloride, PPAAm, plasma polymerized allylamine; PP, proliferative phase, G, gap; S, synthesis phase).

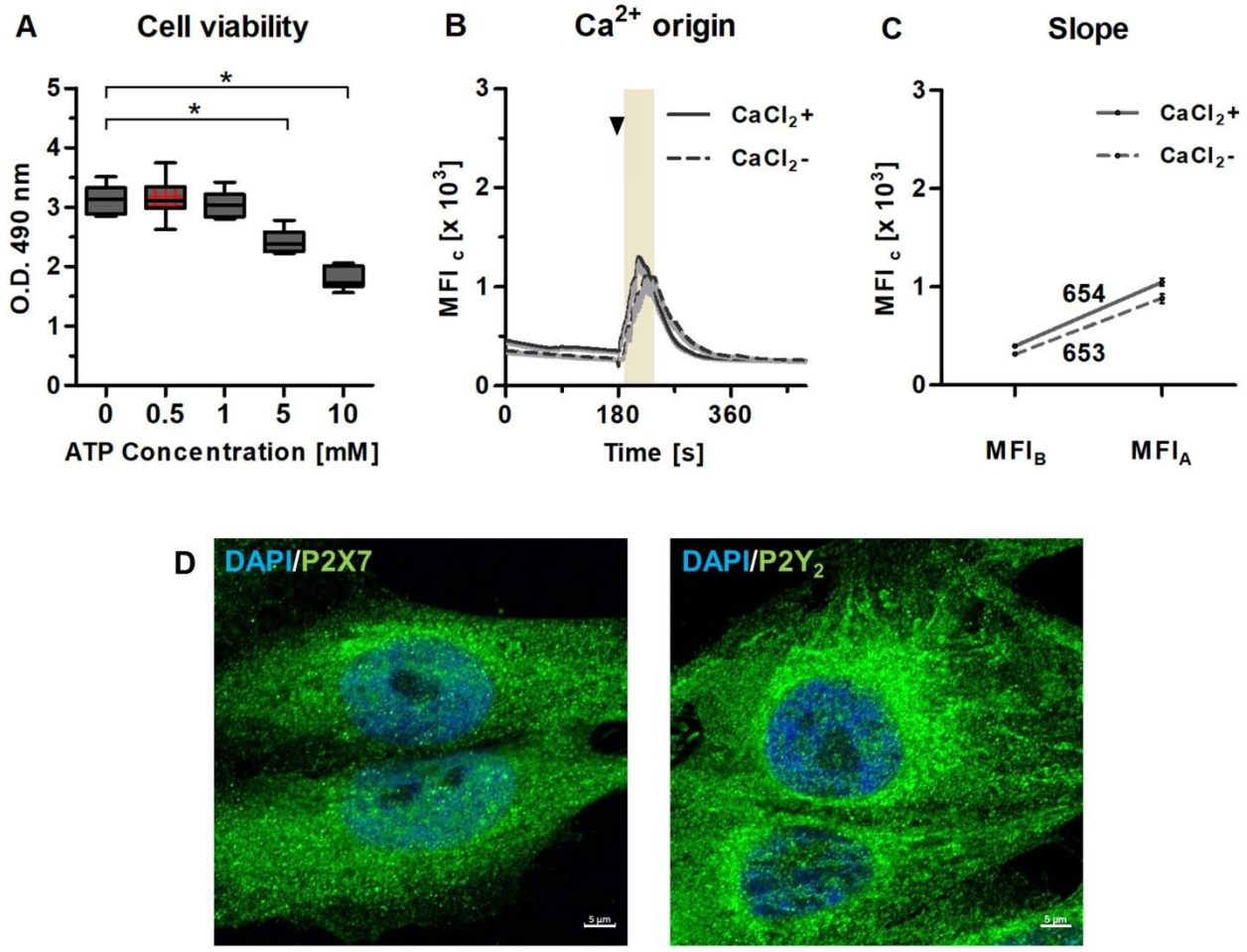


**Supplementary Figure S3.** Intracellular $Ca^{2+}$ mobilization via ATP receptors - a pre-screening study. (**A**) ATP concentration: Cell viability (MTS) of MG-63s after 20 min incubation with different ATP concentrations. A non-toxic concentration of 0.5 mM was used for all $Ca^{2+}$ mobilization experiments (red grid lines). (Statistics: Mann-Whitney U-test, *p < 0.05; median ± IQR and minimum and maximum; n = 3). (**B**) $Ca^{2+}$ source: $MFI_C$ (Mean fluorescence intensities of cells) of intracellular $Ca^{2+}$ in cells on Ti surfaces in $CaCl_2$ containing HEPES ($CaCl_2$ +) and HEPES without $CaCl_2$ ($CaCl_2$ - ).There is no significant difference between $CaCl_2$ + and $CaCl_2$ - for $MFI_B$ (basal MFI = 0–170 s) and $MFI_A$ (MFI after stimulation with ATP = 190–240 s, highlighted area). The arrow indicates the addition of ATP after 180 s. (Statistics: Mann-Whitney test, *p > 0.05; mean ± sem; n = 3, LSM780). (**C**) $Ca^{2+}$ mobilization: The slope from $MFI_B$ to $MFI_A$ is the same for $CaCl_2$ + (654 $MFI_C$) and $CaCl_2$ – (653 $MFI_C$). (**D**) ATP receptors: Fluorescence images of ATP receptor types $P2X_7$ (left) and $P2Y_2$ (right) (green) in MG-63s (cell nucleus, blue). (Magnification 63x, scale bars 5 µm, LSM780).

Role of ATP receptors: $P2Y_2$ is an ATP-sensitive G-protein coupled receptor. External ATP stimulation of MG-63s activates the phospholipase-C pathway, triggering the osteoblasts to mobilize their intracellular $Ca^{2+}$ storage from the endoplasmic reticulum, leading to increasing cytoplasmic $Ca^{2+}$ levels. An extracellular $Ca^{2+}$ influx via ATP-sensitive ligand-gated ion channels (e.g. $P2X_7$) appears to be of secondary importance in this case.

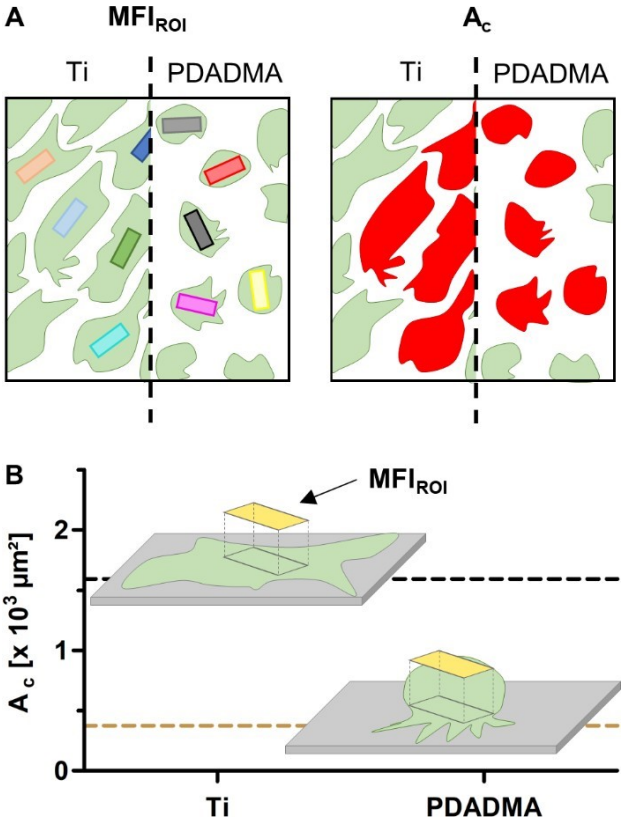


**Supplementary Figure S4.** Calculation example of the mean fluorescence intensity of cells ($MFI_C$) on Ti and PDADMA. (**A**) The MFI of the 'region of interest' ($MFI_{ROI}$) is determined by boxes (colored rectangles) with defined areas of 100 µm² ($A_{ROI}$) placed on randomly selected fluo-3 stained cells (green). The cell area $A_C$ (red) is measured from flat cells on Ti and spherical cells on PDADMA. (**B**) The $Ca^{2+}$-signal of a spherical cell on PDADMA is concentrated on a smaller area, which results in misleadingly high $MFI_{ROI}$ values.

**Supplementary Table S1.** Cell area of MG-63s after 24 h on chemically modified Ti: The basic values for $MFI_C$ calculation were determinated using microscopic images of fluo-3 stained cells (mean ± SD, n = 3).

| Surface | Ti | PPAAm | APTES | PEI | PPI-G4 | Col I | Matrigel | RGD | PSS | PDADMA |
|---|---|---|---|---|---|---|---|---|---|---|
| **Cell area [µm²]** | 1595 ± 108 | 1865 ± 175 | 1623 ± 131 | 1621 ± 169 | 547 ± 45 | 1836 ± 210 | 1553 ± 241 | 1568 ± 207 | 1181 ± 90 | 383 ± 42 |

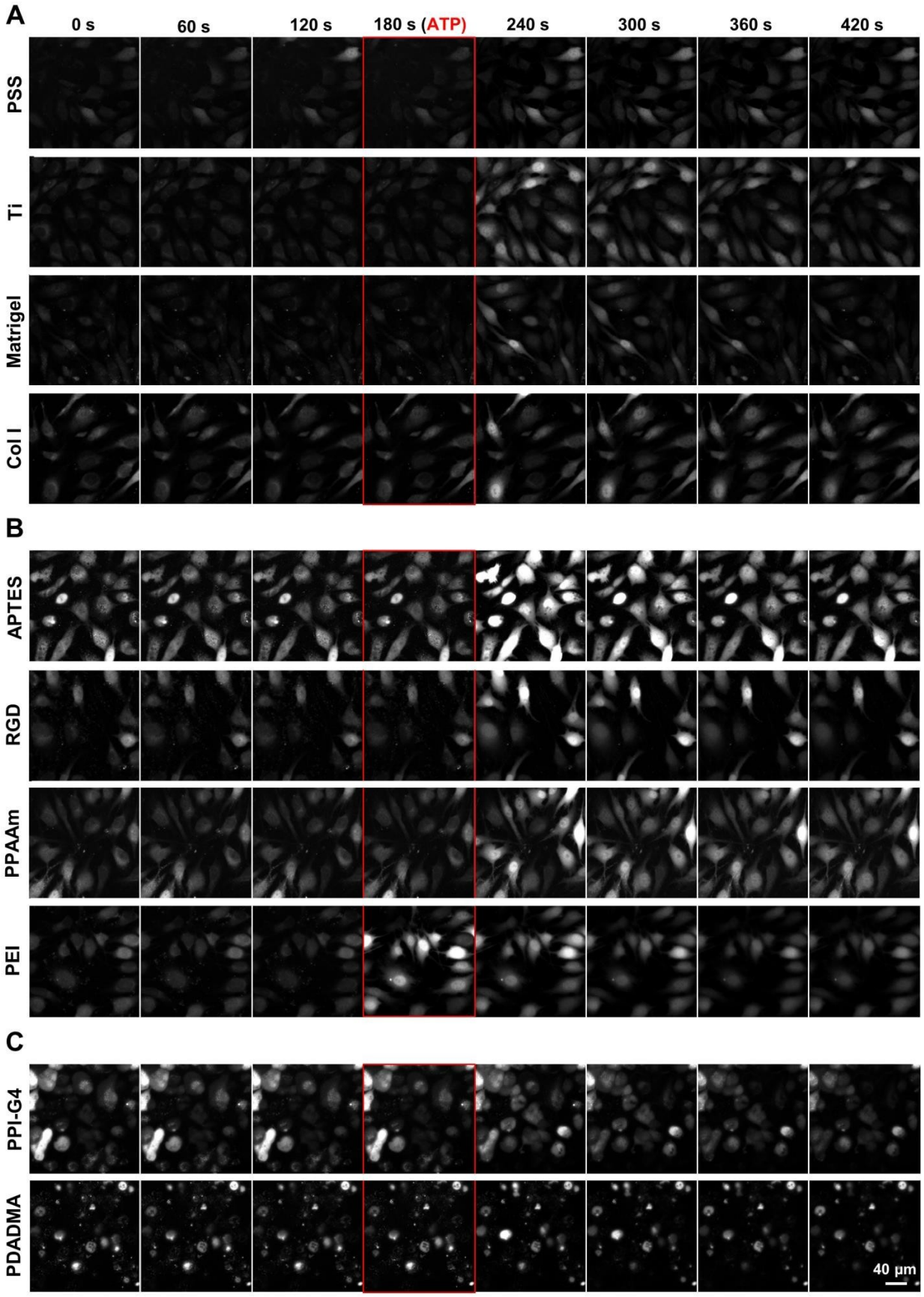
A
0 s
60 s
120 s
180 s (ATP)
240 s
300 s
360 s
420 s
PSS
Ti
Matrigel
Col I
B
APTES
RGD
PPAAm
PEI
C
PPI-G4
PDADMA
40 μm

**Supplementary Figure S5.** Representative example of the intracellular $Ca^{2+}$ mobilization in vital fluo-3 loaded MG-63s growing on (A) negatively, (B) moderately positively and (C) highly positively charged surfaces in the time frame 0-420 s. First, the basal $Ca^{2+}$ signal is recorded, and then the cells are stimulated with ATP at 180 s (marked by the red box). Note the impressively higher $Ca^{2+}$ signals after ATP stimulation in cells on moderately positively charged surfaces (240 and 300s). $Ca^{2+}$ mobilization in cells on highly positively charged surfaces is strongly impaired, accompanied by a spherical cell morphology and reduced cell area (magnification 40x, scale bars 40 µm; LSM780).

**Supplementary Table S2.** Chemical composition of modified Ti by XPS (mean ± SD, n = 3).

| Surface | | Ti | Si | C | O | N | Other |
|---|---|---|---|---|---|---|---|
| **Control** | PPAAm | 0.0 | 0.0 | 74.2 ± 0.4 | 1.6 ± 0.3 | 24.3 ± 0.1 | < 4 at-% |
| **Amino Polymers** | APTES | 8.1 ± 0.5 | 6.4 ± 0.1 | 40.9 ± 1.0 | 37.5 ± 0.6 | 6.4 ± 0.1 | < 4 at-% |
| | PEI | 16.8 ± 0.1 | 0.0 | 29.2 ± 0.5 | 49.3 ± 0.2 | 4.7 ± 0.8 | < 4 at-% |
| | PPI-G4 | 4.0 ± 2.5 | 1.5 ± 0.5 | 57.7 ± 3.4 | 23.7 ± 2.5 | 13.3 ± 1.4 | < 4 at-% |
| **ECM & Peptides** | Col I | 0.0 | 0.0 | 55.9 ± 1.4 | 25.8 ± 1.5 | 11.3 ± 1.1 | 7.1 at-%* |
| | Matrigel | 27.4 ± 0.6 | 0.0 | 16.2 ± 0.6 | 53.3 ± 0.4 | 2.1 ± 0.3 | < 4 at-% |
| | RGD | 7.6 ± 0.1 | 4.9 ± 0.2 | 40.6 ± 0.3 | 37.7 ± 0.3 | 7.0 ± 0.3 | < 4 at-% |
| **Polyelectrolyte Multilayers** | PSS | 0.0 | 12.5 ± 0.5 | 51.8 ± 2.1 | 19.8 ± 0.0 | 4.8 ± 0.1 | 11.2 at-%* |
| | PDADMA | 0.0 | 0.1 ± 0.0 | 77.9 ± 0.2 | 13.0 ± 0.2 | 5.2 ± 0.0 | < 4 at-% |

* Col I: mainly 4.5 ± 0.7 at-% Na, 1.6 ± 0.3 at-% S; PSS: mainly 4.3 ± 2.0 at-% Na, 5.4 ± 0.2 at-% S.

## Supplementary Methods

### Relative cell viability

As cells on the highly positively charged surfaces PPI-G4 and PDADMA exhibited altered morphology and disturbed $Ca^{2+}$ mobilization after 24 h, the relative cell viability of MG-63s on these surfaces was determined by MTS assay in comparison with the control surfaces Ti and PPAAm. This test utilizes the ability of NADH(P)H-dependent dehydrogenase enzymes in mitochondrial active and viable cells to reduce yellow MTS ((3-(4,5-dimethylthiazol-2-yl)-5-(3-carboxymethoxyphenyl)-2-(4-sulfophenyl)-2H-tetrazolium salt) to purple formazan. A detailed description of the procedure can be obtained from Staehlke et al. 2018. In brief, 50,000 cells/$cm^2$ were seeded onto the surfaces for 24 h and then incubated in a fresh 24-well plate for 2–3 h in 500 µl DMEM containing 100 µl of MTS reagent (CellTiter 96 ® Aqueous ONE-Solution Cell Proliferation Assay, Promega, USA) at 37 °C. The increase in color intensity in the media was quantified by measuring the absorbance of the supernatants in a 96-well plate at 490 nm with a microplate reader (Anthos, Mikrosysteme, Krefeld, Germany). A background measurement was recorded at 650 nm to be subtracted from the absorption values. Cell numbers were determined by crystal violet staining. Therefore, cells were fixed by shaking with methanol (J. T. Baker, Deventer, Netherlands) for 10 min at RT. The fixing solution was discarded, the cells covered with a Neißer solution (Carl Roth, Karlsruhe, Germany) and incubated for 10 min shaking at RT. Distilled water was then added and aspirated until the supernatant was clear. The crystal violet was re-dissolved by incubating the cells with 33% acetic acid (J. T. Baker, Deventer, Netherlands) for 10 min shaking at RT. The optical density of the transferred supernatants was quantified at 620 nm. The relative cell viability was calculated by the quotient of MTS and crystal violet values and normalized to the Ti control. Three independent experiments were carried out, each in duplicate (n = 3).

### Cell Proliferation

To investigate the cell proliferation, 80,000 cells were seeded onto Ti, PPAAm, PPI-G4 and PDADMA surfaces for 24 h and then trypsinated with 0.05% trypsin/0.02% EDTA (PAA Laboratories, Pasching, Austria) for 7 min. After centrifugation (10 min, 1200 rpm; Centrifuge 5702 R, Eppendorf AG, Hamburg, Germany) cells were fixed with 70% ethanol at -20 °C overnight. Subsequently, cells were washed once with PBS, treated with RNase (1 mg/ml, Sigma-Aldrich Chemie, Taufkirchen, Germany) at 37 °C for 25 min and incubated with propidium iodide (PI, 50 mg/ml, Sigma-Aldrich Chemie, Taufkirchen, Germany) at 4 °C overnight. Up to 10,000 events per sample were measured with the flow cytometer FACSCalibur (BD Biosciences, San Jose, CA, USA) using the software CellQuest Pro 4.0.1 (BD Biosciences). For the cell proliferation analysis the cell cycle phases $G1_{sub}$, G0/G1, S and G2/M were calculated in percent using FlowJo v10 (BD Biosciences, San Jose, CA, USA). In accordance with Staehlke et al. 2019, we defined the MG-63s in S- and G2/M-phase as proliferative cells and in the sub-G1 phase as apoptotic cells for statistical evaluation (n = 3 independent experiments).

### Cell viability for ATP concentration

To ensure that an adequate amount of adenosine 5`-triphosphate (ATP) was used to stimulate the intracellular calcium ($Ca^{2+}$) mobilization in MG-63 osteoblasts, an MTS assay was performed. For this purpose, 10,000 cells/well were seeded into 96-well plates (Greiner Bio-One, Frickenhausen, Germany) and cultivated for 24 h. The culture medium was then removed, and the cells incubated for 20 minutes with ATP concentrations of 0 (as control), 0.5, 1, 5 and 10 mM in isotonic HEPES (4-(2-hydroxyethyl)-1-piperazineethanesulfonic acid) buffer, as used for $Ca^{2+}$ mobilization. After the

addition of ATP, the cell morphology was observed with a light microscope (Axiovert 40 C, CP-Achromat 10x/0.25 Ph1, Carl Zeiss, Jena, Germany) and an eventual pH change in the HEPES buffer determined with a MicroFET pH-meter (Sentron Europe BV, Leek, The Netherlands). Thereafter, the HEPES buffer was replaced with 100 µl culture media containing 20 µl of MTS reagent (CellTiter 96 ® Aqueous ONE-Solution Cell Proliferation Assay, Promega, USA) and the cells were incubated for 1 h at 37 °C. The absorbance of the supernatants in a 96-well plate was measured with a microplate reader (Anthos, Mikrosysteme, Krefeld, Germany) at 490 nm. A background measurement was recorded at 650 nm to be subtracted from the absorption values. Three independent experiments were carried out, each in triplicate (n = 3).

**ATP receptor immunofluorescence staining**

MG-63 cells (30,000 cells/cm²) were cultured on the Ti arrays for 24 h and then fixed with 4% PFA (Sigma-Aldrich Chemie, Taufkirchen, Germany) at RT for 10 min. After washing three times in PBS, cells were permeabilized with 0.1% Triton X-100 (10 min, RT) (Merck, Darmstadt, Germany). ATP receptor staining was performed using the anti-$P2Y_2$ antibody (1:100, Alomone Labs, Jerusalem, Israel, APR-10) and the anti-$P2X_7$ antibody (1:200, Alomone Labs, Jerusalem, Israel, APR-04). Cells were incubated with the primary antibody for 60 min at RT. After washing with PBS, the cells were treated with goat-anti-rabbit-IgG-Alexa Fluor 488 (1:200, Invitrogen, Karlsruhe, Germany, A-11008) for 30 min at RT in the dark. Afterwards, samples were embedded with DAPI containing Fluoroshield™ on a cover slip and stored in the dark at 4 °C. The ATP receptors were examined using the LSM780 (Carl Zeiss) with a Plan-Apochromat 63x/1.40 Oil DIC M27 objective (Carl Zeiss) and the ZEN software (ZEISS efficient navigation, ZEN 2011 SP4, black edition, Carl Zeiss).

**Intracellular $Ca^{2+}$ mobilization**

Pilot test: In order to determine the origin of the $Ca^{2+}$ ions for their cytoplasmic increase in the cells, more general testing was carried out first. $Ca^{2+}$ ions either originate e.g. from the intracellular $Ca^{2+}$ storage – the endoplasmic reticulum (ER), which releases $Ca^{2+}$ into the cytoplasm after activation of the phospholipase-C signaling pathway – or they originate from extracellular sources and are transported into the cell via voltage-sensitive $Ca^{2+}$ channels/ ligand-gated ion channels, or a mixture of both. For this purpose, extracellular $Ca^{2+}$ sources had to be eliminated from the HEPES buffer. The HEPES buffer composition including 1 mM $CaCl_2$ was used, as previously published (Staehlke et al., 2015, 2018), as well as a HEPES buffer without $CaCl_2$. Washing and staining steps (fluo-3) were performed without $CaCl_2$ in PBS and HEPES buffer. The following recording of $Ca^{2+}$ signal and analysis of $Ca^{2+}$ time course was performed as described in the materials and methods section of the manuscript.

Staehlke, S., Koertge, A., and Nebe, B. (2015). Intracellular calcium dynamics dependent on defined microtopographical features of titanium. *Biomaterials* 46, 48–57. doi:10.1016/J.BIOMATERIALS.2014.12.016.

Staehlke, S., Rebl, H., Finke, B., Mueller, P., Gruening, M., and Nebe, J. B. (2018). Enhanced calcium ion mobilization in osteoblasts on amino group containing plasma polymer nanolayer. *Cell Biosci.* 8, 22. doi:10.1186/s13578-018-0220-8.

Staehlke, S., Lehnfeld, J., Schneider A., Nebe J. B., Müller R. Terminal chemical functions of polyamidoamine dendrimer surfaces and its impact on bone cell growth. *Mater. Sci. Eng. C* 101, 190–203. doi: 10.1016/j.msec.2019.03.073